Imperial College London

# Effects of Strain-Rate and Temperature on Ductile Damage and Fracture of Metallic Materials

*by*

Alexander Sancho García

Department of Mechanical Engineering, Imperial College London,
South Kensington Campus, London SW7 2AZ, United Kingdom

This thesis is submitted for the degree of
Doctor of Philosophy of Imperial College London

2019

# Abstract

Ductile damage appears in metallic materials when they undergo sufficiently high plastic strain. It is caused by voids and produces degradation on the mechanical properties that eventually leads to the ductile fracture of the material. Like other properties, this behaviour is affected by the temperature and velocity of material deformation. This thesis investigates the effects that temperature and strain-rate have on ductile damage from an experimental and a modelling point of view, and explores innovative experimental methods to quantify damage and models to represent it.

Experimental tests for the characterisation of plasticity, ductile damage and ductile fracture were conducted on stainless steel 304L and copper C110. The experiments were run at three temperatures ranging from $-80°C$ to $180°C$, and at three strain-rates from $10^{-3}$ $s^{-1}$ to $10^{4}$ $s^{-1}$. For the accurate representation of plasticity near fracture, a neck monitoring method was implemented from which local stresses and strains can be calculated once localisation occurs. The method was also employed to analyse the effect of stress triaxiality on fracture using notched samples. Ductile damage accumulation was obtained from the degradation of the elastic modulus and validated by a micrographic analysis of the samples.

The experiments at different temperatures were conducted following the same methodology inside an environmental chamber. To be able to apply the techniques to high-speed tests, an in-situ shadowgraph method was developed and a sub-pixel edge detection algorithm implemented, resulting in very high quality results, even at the highest strain-rate tested. An innovative experimental rig was also designed to perform high-speed interrupted tests from which damage accumulation was measured.

Making use of the experimental results, plasticity, ductile damage and fracture models were calibrated and their effectiveness assessed. Novel ductile fracture and damage accumulation models were developed, which include the effects of strain-rate and temperature. The models also include non-linear damage accumulation, and are capable of representing accurately the effects observed in the experiments.

# Declaration of originality

The work hereby presented is based on research carried out by the author at the Department of Mechanical Engineering of Imperial College London, and it is all the author's own work except where otherwise acknowledged. No part of the present work has been submitted elsewhere for another degree or qualification.

# Copyright declaration

The copyright of this thesis rests with the author. Unless otherwise indicated, its contents are licensed under a Creative Commons Attribution-Non Commercial 4.0 International Licence (CC BY-NC).

Under this licence, you may copy and redistribute the material in any medium or format. You may also create and distribute modified versions of the work. This is on the condition that: you credit the author and do not use it, or any derivative works, for a commercial purpose.

When reusing or sharing this work, ensure you make the licence terms clear to others by naming the licence and linking to the licence text. Where a work has been adapted, you should indicate that the work has been changed and describe those changes.

Please seek permission from the copyright holder for uses of this work that are not included in this licence or permitted under UK Copyright Law.

# Contents

**List of Figures** **xi**

**List of Tables** **xxi**

**Acknowledgements** **xxv**

**List of Publications** **xxvii**

**Acronyms and Abbreviations** **xxix**

**Notation** **xxxi**

**1 Introduction** **1**

1.1 Ductile Damage and Fracture of Metals . . . . . 2

1.2 Aim and Objectives . . . . . 4

1.3 Thesis Outline . . . . . 5

**2 Literature Review** **7**

2.1 Metal Plasticity . . . . . 7

2.1.1 Plasticity Modelling . . . . . 8

2.2 Ductile Damage and Ductile Fracture . . . . . 10

2.2.1 From the Early Studies to the Modern Developments on Ductile Damage . . . . . 11

2.2.2 Damage Modelling . . . . . 13

2.3 Experimental Techniques . . . . . 22

2.3.1 Tensile Testing . . . . . 22

2.3.2 Ductile Damage Quantification . . . . . 24

2.3.3 Temperature and High Strain-Rate Testing . . . . . 31

2.4 Summary . . . . . 32

**3 Methodology** **35**

3.1 Introduction . . . . . 35

3.2 Materials . . . 36
3.2.1 Austenitic Stainless Steel . . . 36
3.2.2 Electrolytic Tough Pitch Copper . . . 37
3.3 Experimental Procedure for Plasticity Modelling . . . 37
3.3.1 Test Description . . . 37
3.3.2 Specimens Design . . . 40
3.4 Experimental Procedure for Ductile Fracture Modelling . . . 42
3.4.1 Test Description . . . 43
3.4.2 Specimens Design . . . 45
3.5 Experimental Procedure for Ductile Damage Modelling . . . 46
3.5.1 Test Description . . . 47
3.5.2 Specimens Design . . . 50
3.6 Material Modelling and Implementation in Finite Elements . . . 51
3.6.1 Model Parameters Calibration . . . 51
3.6.2 Finite Elements Material Subroutines . . . 52

**4 Strain-Rate and Temperature Considerations 55**
4.1 Introduction . . . 55
4.2 Strain-Rate Considerations . . . 56
4.2.1 High-Speed Tests Considerations . . . 56
4.2.2 Tests and Equipment Set-up . . . 58
4.2.3 Strain Measurement . . . 60
4.2.4 Post-processing Algorithm . . . 65
4.2.5 Interrupted High-Speed Test . . . 68
4.3 Temperature Considerations . . . 79
4.3.1 Temperature Tests Challenges . . . 80
4.3.2 Tests and Equipment Set-up . . . 80

**5 Experimental Results in Quasi-Static and Room Temperature Conditions 83**
5.1 Introduction . . . 83
5.2 Plasticity Tests . . . 83
5.2.1 Neck Geometry . . . 84
5.2.2 Stress Triaxiality . . . 86
5.2.3 Equivalent Stress - Strain . . . 87
5.2.4 Stress - Strain Neck Correction . . . 88
5.3 Ductile Fracture Tests . . . 89
5.3.1 Fracture Surface . . . 90
5.3.2 Notch Geometry . . . 91
5.3.3 Equivalent Stress - Strain . . . 92

5.3.4 Effect of Stress Triaxiality on Ductility . . . 93
5.4 Damage Accumulation Tests . . . 95
5.4.1 Damage Accumulation Measurement Using Extensometer . . . 96
5.4.2 Damage Accumulation Measurement Using Digital Image Correlation . . . 98
5.5 Damage Validation and Comparison Tests . . . 99
5.5.1 Specimens Preparation . . . 100
5.5.2 Post-process Methodology . . . 101
5.5.3 Porosity Study of a Fractured Specimen . . . 103
5.5.4 Porosity Study of a Necked Specimen . . . 105
5.5.5 Porosity Study of Damaged Specimens . . . 108
5.6 Conclusions . . . 111

**6 Experimental Results - Strain-Rate Effect 113**
6.1 Introduction . . . 113
6.2 Strain-Rate Effect on Plasticity . . . 113
6.2.1 Neck Geometry . . . 115
6.2.2 Stress Triaxiality . . . 117
6.2.3 Equivalent Stress - Strain . . . 118
6.3 Strain-Rate Effect on Ductile Fracture . . . 120
6.3.1 Fracture Surface . . . 121
6.3.2 Equivalent Stress - Strain . . . 123
6.3.3 Effect of Stress Triaxiality on Ductility . . . 126
6.4 Strain-Rate Effect on Damage Accumulation . . . 127
6.4.1 Elastic Modulus Analysis . . . 128
6.4.2 Porosity Analysis . . . 130
6.5 Conclusions . . . 135

**7 Experimental Results - Temperature Effect 137**
7.1 Introduction . . . 137
7.2 Temperature Effect on Plasticity . . . 137
7.2.1 Neck Geometry . . . 138
7.2.2 Stress Triaxiality . . . 140
7.2.3 Equivalent Stress - Strain . . . 142
7.2.4 Stress - Strain Neck Correction . . . 144
7.3 Temperature Effect on Ductile Fracture . . . 144
7.3.1 Fracture Surface . . . 144
7.3.2 Equivalent Stress - Strain . . . 147
7.3.3 Effect of Stress Triaxiality on Ductility . . . 147
7.4 Temperature Effect on Damage Accumulation . . . 151

7.5 Conclusions . . . 153

**8 Material Models Development and Calibration 155**

8.1 Introduction . . . 155
8.2 Plasticity Modelling . . . 155
8.2.1 Johnson-Cook Model Fit . . . 156
8.3 Ductile Fracture Modelling . . . 162
8.3.1 Johnson-Cook Model Fit . . . 162
8.3.2 Proposed Ductile Fracture Model . . . 163
8.4 Ductile Damage Modelling . . . 170
8.4.1 Bonora Model . . . 170
8.4.2 Proposed Damage Model . . . 172
8.5 Conclusions . . . 178

**9 Conclusions 181**

9.1 Experimental Methodology . . . 181
9.2 Results in Standard Conditions . . . 185
9.3 Strain-Rate Effect . . . 186
9.4 Temperature Effect . . . 188
9.5 Material Models . . . 189
9.6 Further Work . . . 191

**References 195**

**A Drawings 207**

A.1 Sample Drawings . . . 207
A.2 Rig Drawings . . . 239

**B Additional Results 265**

B.1 Additional Strain-Rate Results . . . 265
B.2 Additional Temperature Results . . . 274
B.3 Additional Modelling Results . . . 282

**C User Subroutines 287**

C.1 UMAT Material model subroutine . . . 287
C.2 Example of Abaqus/Standard Input File . . . 311

# List of Figures

1.1 Falcon 9 rocket launch and Falcon Heavy rocket boosters landing for their reuse (Space X, Cape Canaveral, 2018); this is just an example of the current needs for life and operative limits extension, costs reduction and safety of materials operating even in the most extreme conditions (images from [3, 4]). 2

2.1 Phases of ductile damage. . . . . 11
2.2 SEM observations of the different types of void nucleation: a) by debonding of an inclusion from the matrix, b) by cracking of the inclusion or c) a combination of the previous two (image from [20]). . . . . 11
2.3 Coalescence of two voids following two different mechanisms: a)-e) plastic necking between voids and f)-j) shear localisation (image from [21]). . . . . 12
2.4 Typical fracture surface produced by ductile fracture. . . . . 12
2.5 Stress triaxiality ($\eta$) vs. normalised Lode angle ($\bar{\theta}$) map representing the different stress states and loading conditions that the material can undergo [55]. . . . . 17
2.6 Comparison of the fracture locus predicted by three phenomenological fracture models in the space of stress triaxiality, Lode angle parameter and equivalent fracture strain ($\eta$, $\bar{\theta}$, $\bar{\varepsilon}_f$) [55]. . . . . 19
2.7 CDM definition of ductile damage on a representative volume element (RVE). 20
2.8 Comparison of the uniform deformation assumption and the real behaviour used to calculate true stress - true strain. . . . . 23
2.9 Damage vs. local equivalent strain results obtained by metallographic evaluation of mechanically polished and electropolished samples of a dual-phase 600 steel (figure from [96]). . . . . 26
2.10 Load vs. indentation depth measurement in a hardness test and calcualtion of elastic modulus from the slope of the curve (figure from [98]). . . . . 27
2.11 3D void volumes of a high carbon steel grade obtained using CT X-Ray in-situ measurements at three different strain levels: (a) $\varepsilon = 0.02$, (b) $\varepsilon = 0.25$ and (c) $\varepsilon = 0.32$ (just before fracture), (figure from [104]). . . . . 29
2.12 Diagram of the potential drop test arrangement (figure from [110]). . . . . 30
2.13 Experimental techniques used to test different strain-rate ranges. . . . . 31

3.1 True stress - true strain ($\sigma_T$ - $\varepsilon_T$) measured using different methods. . . . . 38
3.2 Experimental arrangement used for the specimen's neck geometry monitoring. 39
3.3 Accuracy of the neck monitoring technique, thickness of the grey transition between dark and bright pixels of the image. . . . . 40
3.4 Necked specimen before and after applying the thresholding filter; the neck shape, minimum radius and osculating circles have been represented. . . . . 40
3.5 Round RB6 specimen geometry. . . . . 41
3.6 Hourglass round HGR6 specimen geometry. . . . . 41
3.7 Example of necking correction curves obtained from traditional and imaging methods. . . . . 42
3.8 Fracture equivalent plastic strain - stress triaxiality ($\bar{\varepsilon}_{pl,f}$ - $\eta$) analysis of RNB specimens. . . . . 43
3.9 Shadowgraph equipment used for post-fracture neck geometry measurement. 46
3.10 RNB6-4 specimen geometry ($2a = 5$ mm, $\rho = 3$ mm). . . . . 46
3.11 Ductile damage accumulation - equivalent plastic strain ($D$ - $\bar{\varepsilon}_{pl}$). . . . . 47
3.12 Engineering stress - engineering strain ($\sigma_e$ - $\varepsilon_e$) of a tensile test for elastic modulus monitoring. . . . . 48
3.13 Experimental setup used for damage monitoring on a HGR6 specimen. . . . 49
3.14 Equivalent stress - equivalent plastic strain ($\bar{\sigma}$ - $\bar{\varepsilon}_{pl}$) of one unloading-reloading cycle. . . . . 49
3.15 HGF6 specimen geometry. . . . . 50
3.16 Equivalent stress - time ($\bar{\sigma}$ - $t$) obtained using in-built and VUMAT Johnson-Cook plasticity models [1]. . . . . 53

4.1 Load - engineering strain ($P$ - $\varepsilon_e$) measured in a high-speed tensile test ($v \approx 17$ m/s). . . . . 57
4.2 High strain-rate tensile tests set-up; a) load chain schematic and b) picture of the actual test set-up. . . . . 59
4.3 Specimen preparation for video-extensometer technique. . . . . 60
4.4 Specimen preparation for DIC technique. . . . . 61
4.5 In-situ shadowgraph for high strain-rate tensile tests. . . . . 62
4.6 Necking images a) using the in-situ shadowgraph method and b) taking pictures of painted specimen. . . . . 63
4.7 Comparison of true equivalent stress - true equivalent strain curves ($\bar{\sigma}$ - $\bar{\varepsilon}$) obtained using different strain measurement methods. Strain-rate - true equivalent strain curves ($\dot{\varepsilon}$ - $\bar{\varepsilon}$) are also represented. . . . . 64
4.8 Specimen contour measurement using a thresholding algorithm. . . . . 65
4.9 Specimen contour measurement using a sub-pixel edge detection algorithm. 66
4.10 Comparison of the neck geometry obtained using thresholding and sub-pixel edge detection algorithms. . . . . 67

4.11 Comparison of the true equivalent stress - true equivalent strain curve ($\bar{\sigma}$ - $\bar{\varepsilon}$) obtained using thresholding and sub-pixel edge detection algorithms. . . 67
4.12 Hybrid method for ductile damage measurement at high strain-rates: a) first plastic deformation, b) first load-unload cycle, c) second plastic deformation, d) second load-unload cycle. . . . . 69
4.13 True equivalent stress - true equivalent strain ($\bar{\sigma}$ - $\bar{\varepsilon}$) measurements of hybrid test with plastic load applied in quasi-static conditions and comparison with continuous tests. . . . . 70
4.14 Ductile damage - true equivalent strain ($D$ - $\bar{\varepsilon}$) measurements of hybrid test with plastic load applied in quasi-static conditions and comparison with continuous tests. . . . . 70
4.15 Design model of the experimental rig for adjustable interrupted high strain-rate tensile tests. . . . . 73
4.16 Experimental set-up for adjustable interrupted high strain-rate tensile tests. 74
4.17 Load - time ($P$ - $t$) response of different shear pin designs. . . . . 75
4.18 Finite elements model of the main components of the experimental rig. . . . 76
4.19 Finite elements model detail of: a) shear pin and b) specimen. . . . . 76
4.20 Von Mises stress ($\bar{\sigma}$) in section through the pin, a) during the deformation of the specimen, b) before fracture, c) after fracture. . . . . 77
4.21 Load carried by the specimen and the shear pin ($P$ - $t$). . . . . 77
4.22 Equivalent plastic strain ($\bar{\varepsilon}_{pl}$) in the specimen after elongation of a) 0.5 mm, b) 1 mm, c) 1.5 mm and d) 2 mm. . . . . 78
4.23 Total equivalent strain and equivalent plastic strain on the centre of the specimen axis ($\bar{\varepsilon}$ - $t$ and $\bar{\varepsilon}_{pl}$ - $t$). . . . . 78
4.24 Experimental set-up for high and low temperature tensile tests with damage accumulation measurements. . . . . 81
4.25 Ice formation on the surface of the specimen in a low temperature damage accumulation test. . . . . 82

5.1 Evolution of the neck geometry (radius of curvature of the osculating circle and normalised minimum cross-sectional radius vs. equivalent plastic strain ($\rho$ - $\bar{\varepsilon}_{pl}$ and $a/a_0$ - $\bar{\varepsilon}_{pl}$)). . . . . 85
5.2 Evolution of the neck geometry (radius of curvature of the osculating circle and normalised minimum cross-sectional radius vs. time ($\rho$ - $t$ and $a/a_0$ - $t$)). 85
5.3 Variation of equivalent plastic strain - stress triaxiality throughout the tensile tests ($\bar{\varepsilon}_{pl}$ - $\eta$), vertical lines represent the average triaxiality of the test. 86
5.4 True equivalent stress - true equivalent strain ($\bar{\sigma}$ - $\bar{\varepsilon}$) obtained with the imaging method and "true" stress - "true" strain ($\sigma_T$ - $\varepsilon_T$) obtained with the traditional method. . . . . 87

5.5 Necking effect correction curves: strain correction ($(\bar{\varepsilon})_{imaging}$ - $(\varepsilon_e)_{extens.}$) and stress correction ($(\bar{\sigma})_{imaging}$ - $(\sigma_e)$). . . . . 88
5.6 Fracture surface of tensile specimens in quasi-static and room temperature conditions: stainless steel 304L at (a) 40x, (b) 150x and (c) 2000x magnification; copper C110 at (d) 40x, (e) 150x and (f) 1000x magnification. . . . 90
5.7 Evolution of the minimum radius of the notch cross-section with applied equivalent plastic strain for the different RNB tensile tests; the results are normalised with the initial radius of each sample ($a/a_0$ - $\bar{\varepsilon}_{pl}$). . . . . 92
5.8 Evolution of the radius of curvature of the notch with applied equivalent plastic strain for the different RNB tensile tests ($\rho$ - $\bar{\varepsilon}_{pl}$). . . . . 92
5.9 True equivalent stress - true equivalent strain of the RNB tensile tests ($\bar{\sigma}$ - $\bar{\varepsilon}$). . . . . 93
5.10 Variation of stress triaxiality with applied equivalent plastic strain for the different RNB tensile tests, the crosses represent the fracture equivalent plastic strain - average triaxiality ($\bar{\varepsilon}_{pl,f}$ - $\eta_{av}$). . . . . 94
5.11 Effective elastic modulus - equivalent plastic strain ($\tilde{E}$ - $\bar{\varepsilon}_{pl}$) experimental results. . . . . 96
5.12 Ductile damage - equivalent plastic strain ($D$ - $\bar{\varepsilon}_{pl}$) experimental results. . . 96
5.13 Ductile damage mean and standard deviation - equivalent plastic strain ($D$ - $\bar{\varepsilon}_{pl}$) experimental results. . . . . 97
5.14 Damage accumulation measurement in stainless steel 304L flat samples. . . 99
5.15 Ductile damage analysis of stainless steel 304L HGF6 samples. . . . . 99
5.16 Grid of locations analysed to obtain porosity maps in the sample (a) cross-section and (b) longitudinal-section. . . . . 101
5.17 Comparison of bright and dark field microscopy for porosity calculation of the same stainless steel 304L micrograph with a 50x magnification. . . . . 102
5.18 Thresholding process used to estimate porosity from micropgraphs ($\varphi = 0.0059$). . . . . 103
5.19 Size comparison of individual voids in the original and thresholded pictures for the calibration of the intensity threshold value; numbers represent size in pixels. . . . . 103
5.20 Porosity below the fracture cross-section of a stainless steel 304L specimen; porosity details in the centre and near the surface of the sample at 100x magnification. . . . . 104
5.21 Porosity analysis of a fractured stainless steel 304L specimen. . . . . 104
5.22 Porosity in the longitudinal mid-plane of a stainless steel 304L necked specimen ($\bar{\varepsilon}_{pl} = 0.993$); details A,B & C approximately in the specimen axis and details C, D & E in the central cross-section of the neck. . . . . 106
5.23 Contours of porosity in the longitudinal slice of a necked specimen ($\bar{\varepsilon}_{pl} = 0.993$). . . . . 106

5.24 Distributions of porosity in the longitudinal slice of a necked specimen ($\bar{\varepsilon}_{pl} = 0.993$). . . . . 107
5.25 100x magnification micrographs of the centre of the neck in a stainless steel 304L specimen strained to $\bar{\varepsilon}_{pl} = 0.993$. . . . . 107
5.26 Contours of porosity in the cross-section of the analysed specimens. . . . . 109
5.27 Radial distribution of porosity in the specimens studied in Figure 5.26. . . . 109
5.28 Analysis of the porosity and ductile damage evolution with equivalent plastic strain. . . . . 110

6.1 Effect of strain-rate on the normalised minimum cross-sectional radius - equivalent plastic strain ($a/a_0$ - $\bar{\varepsilon}_{pl}$). . . . . 115
6.2 Effect of strain-rate on the radius of curvature of the neck - equivalent plastic strain ($\rho$ - $\bar{\varepsilon}_{pl}$). . . . . 115
6.3 Effect of strain-rate on the equivalent plastic strain - stress triaxiality ($\bar{\varepsilon}_{pl}$ - $\eta$).117
6.4 Effect of strain-rate on true equivalent stress - true equivalent strain behaviour ($\bar{\sigma}$ - $\bar{\varepsilon}$); the evolution of strain-rate for increasing strain in each experiment is also represented ($\dot{\varepsilon}$ - $\bar{\varepsilon}$). . . . . 118
6.5 Effect of strain-rate on the fracture surface of stainless steel 304L (from left to right: $\dot{\varepsilon} \sim 10^{-3}$ s$^{-1}$, $\dot{\varepsilon} \sim 10^{2}$ s$^{-1}$ and $\dot{\varepsilon} \sim 10^{3}$ s$^{-1}$; from top to bottom: 40x, 150x and 1000x magnification. . . . . 121
6.6 Effect of strain-rate on the fracture surface of copper C110 (from left to right: $\dot{\varepsilon} \sim 10^{-3}$ s$^{-1}$, $\dot{\varepsilon} \sim 10^{2}$ s$^{-1}$ and $\dot{\varepsilon} \sim 10^{3}$ s$^{-1}$; from top to bottom: 40x, 150x and 1000x magnification. . . . . 122
6.7 Effect of strain-rate on true equivalent stress - true equivalent strain ($\bar{\sigma}$ - $\bar{\varepsilon}$) for the notched bar tests; the evolution of strain-rate for each experiment is also represented ($\dot{\varepsilon}$ - $\bar{\varepsilon}$). . . . . 124
6.8 Effect of strain-rate on maximum axial stress - true equivalent strain ($\sigma_{zz,MAX}$ - $\bar{\varepsilon}$) for the notched bar tests; the evolution of strain-rate for each experiment is also represented ($\dot{\varepsilon}$ - $\bar{\varepsilon}$). . . . . 125
6.9 Effect of strain-rate on fracture equivalent plastic strain - stress triaxiality ($\bar{\varepsilon}_f$ - $\eta$). . . . . 126
6.10 True equivalent stress - true equivalent strain ($\bar{\sigma}$ - $\bar{\varepsilon}$) of the interrupted tensile tests used for damage estimation at $\dot{\varepsilon} \sim 10^{2}$ s$^{-1}$. . . . . 128
6.11 Ductile damage accumulation of copper C110 at different strain-rates obtained using the elastic modulus reduction method ($D$ - $\bar{\varepsilon}$); mean and standard deviation values of damage are represented. . . . . 129
6.12 Ductile damage accumulation of stainless steel 304L at different strain-rates obtained using the elastic modulus reduction method ($D$ - $\bar{\varepsilon}$); mean and standard deviation values of damage are represented. . . . . 129

6.13 Contours of porosity in the cross-section of stainless steel 304L specimens deformed at high strain-rate. . . . . 132
6.14 Evolution of the porosity with equivalent plastic strain for stainless-steel 304L specimens deformed at high strain-rate ($\dot{\varepsilon} \sim 10^2$ s$^{-1}$). . . . . 132
6.15 Effect of strain-rate on the evolution of the porosity vs. equivalent plastic strain ($\varphi$ - $\bar{\varepsilon}_{pl}$) for stainless steel 304L. . . . . 133
6.16 Contours of porosity in the cross-section of copper C110 specimens deformed at high strain-rate. . . . . 134
6.17 Evolution of the porosity radial distribution for copper C110 specimens deformed at high strain-rate ($\dot{\varepsilon} \sim 10^2$ s$^{-1}$). . . . . 134
6.18 Evolution of the porosity with equivalent plastic strain for copper C110 specimens deformed at high strain-rate ($\dot{\varepsilon} \sim 10^2$ s$^{-1}$). . . . . 135
6.19 Pictures of the cross-section of copper C110 samples at 5x magnification. . 135

7.1 Effect of temperature on normalised minimum cross-sectional radius - equivalent plastic strain ($a/a_0$ - $\bar{\varepsilon}_{pl}$). . . . . 139
7.2 Effect of temperature on radius of curvature of the neck - equivalent plastic strain ($\rho$ - $\bar{\varepsilon}_{pl}$). . . . . 139
7.3 Effect of temperature on equivalent plastic strain - stress triaxiality ($\bar{\varepsilon}_{pl}$ - $\eta$). 141
7.4 Effect of temperature on true equivalent stress - true equivalent strain behaviour ($\bar{\sigma}$ - $\bar{\varepsilon}$). . . . . 142
7.5 Effect of temperature on the necking correction curves: strain correction ($(\bar{\varepsilon})_{imaging}$ - $(\varepsilon_e)_{extens.}$) and stress correction ($(\bar{\sigma})_{imaging}$ - $(\sigma_e)$). . . . . 143
7.6 Effect of temperature on the fracture surface of stainless steel 304L (from left to right: $T \sim -80$°C, $T \sim 20$°C and $T \sim 180$°C; from top to bottom: 40x, 150x and 1000x magnification. . . . . 145
7.7 Effect of temperature on the fracture surface of copper C110 (from left to right: $T \sim -80$°C, $T \sim 20$°C and $T \sim 180$°C; from top to bottom: 40x, 150x and 1000x magnification. . . . . 146
7.8 Effect of temperature on true equivalent stress - true equivalent strain ($\bar{\sigma}$ - $\bar{\varepsilon}$) for the notched bar tests. . . . . 148
7.9 Effect of temperature on maximum axial stress - true equivalent strain ($\sigma_{zz,MAX}$ - $\bar{\varepsilon}$) for the notched bar tests. . . . . 149
7.10 Effect of temperature on fracture equivalent plastic strain - stress triaxiality ($\bar{\varepsilon}_f$ - $\eta$). . . . . 150
7.11 Example of engineering stress - engineering strain ($\sigma_e$ - $\varepsilon_e$) of loading-unloading experiments run at different temperatures. . . . . 152
7.12 Effect of temperature on effective elastic modulus - equivalent plastic strain ($\tilde{E}$ - $\bar{\varepsilon}_{pl}$); mean and standard deviation values of elastic modulus represented. 153

7.13 Effect of temperature on ductile damage - equivalent plastic strain ($D$ - $\bar{\varepsilon}_{pl}$); mean and standard deviation values of damage represented. . . . . 153

8.1 Estimated temperature along the high-speed tests. . . . . 157
8.2 Johnson-Cook plasticity model fit to experimental results of stainless steel 304L; all results fitted together; the residuals of the fitting process have also been plotted. . . . . 158
8.3 Johnson-Cook plasticity model fit to experimental results of copper C110; all results fitted together; the residuals of the fitting process have also been plotted. . . . . 158
8.4 Johnson-Cook plasticity model fit to experimental results of stainless steel 304L; standard, strain-rate and temperature results fitted separately. . . . . 160
8.5 Johnson-Cook plasticity model fit to experimental results of copper C110; standard, strain-rate and temperature results fitted separately. . . . . 161
8.6 Johnson-Cook ductile fracture model fit to experimental results of stainless steel 304L; the residuals of the fitting process have also been plotted. . . . . 164
8.7 Johnson-Cook ductile fracture model fit to experimental results of copper C110; the residuals of the fitting process have also been plotted. . . . . 164
8.8 Analysis of the vertical displacement and slope change of the curve for varying strain-rate controlled by the parameters $\gamma_1$ and $\gamma_2$ in the proposed ductile fracture model. . . . . 166
8.9 Analysis of the vertical displacement and slope change of the curve for varying temperature controlled by the parameters $\psi_1$, $\psi_2$ and $\psi_3$ in the proposed ductile fracture model. . . . . 167
8.10 Proposed ductile fracture model fit to experimental results of stainless steel 304L; the residuals of the fitting process have also been plotted. . . . . 169
8.11 Proposed ductile fracture model fit to experimental results of copper C110; the residuals of the fitting process have also been plotted. . . . . 169
8.12 Bonora ductile damage model fit attempt of stainless steel 304L following the fitting process recomended in [90]. . . . . 171
8.13 Bonora ductile damage model fit attempt of stainless steel 304L fitting the damage accumulation shape firstly. . . . . 172
8.14 Analysis of the shape change of the damage accumulation curve controlled by the parameters $\nu_1$ and $\nu_2$ in the proposed ductile damage accumulation model ($\bar{\varepsilon}_{th} = 0.2$, $\bar{\varepsilon}_f = 2.0$ and $D_{cr} = 0.5$). . . . . 174
8.15 Threshold strain model fit to experimental results of copper C110. . . . . 176
8.16 Critical damage model fit to experimental results of stainless steel 304L. . . 177
8.17 Critical damage model fit to experimental results of copper C110. . . . . 177
8.18 Proposed ductile damage model fit to experimental results of stainless steel 304L. . . . . 179

8.19 Proposed ductile damage model fit to experimental results of copper C110. 179

B.1 Strain-rate effect on normalised minimum cross-sectional radius - equivalent plastic strain ($a/a_0$ - $\bar{\varepsilon}_{pl}$) for stainless steel 304L specimens with different notch acuities. . . . . 267
B.2 Strain-rate effect on notch curvature - equivalent plastic strain ($\rho$ - $\bar{\varepsilon}_{pl}$) for stainless steel 304L specimens with different notch acuities. . . . . 268
B.3 Strain-rate effect on equivalent strain - stress triaxiality ($\bar{\varepsilon}$ - $\eta$) for stainless steel 304L specimens with different notch acuities. . . . . 269
B.4 Strain-rate effect on normalised minimum cross-sectional radius - equivalent plastic strain ($a/a_0$ - $\bar{\varepsilon}_{pl}$) for copper C110 specimens with different notch acuities. . . . . 271
B.5 Strain-rate effect on notch curvature - equivalent plastic strain ($\rho$ - $\bar{\varepsilon}_{pl}$) for copper C110 specimens with different notch acuities. . . . . 272
B.6 Strain-rate effect on equivalent strain - stress triaxiality ($\bar{\varepsilon}$ - $\eta$) for copper C110 specimens with different notch acuities. . . . . 273
B.7 Temperature effect on normalised minimum cross-sectional radius - equivalent plastic strain ($a/a_0$ - $\bar{\varepsilon}_{pl}$) for stainless steel 304L specimens with different notch acuities. . . . . 275
B.8 Temperature effect on notch curvature - equivalent plastic strain ($\rho$ - $\bar{\varepsilon}_{pl}$) for stainless steel 304L specimens with different notch acuities. . . . . 276
B.9 Temperature effect on equivalent strain - stress triaxiality ($\bar{\varepsilon}$ - $\eta$) for stainless steel 304L specimens with different notch acuities. . . . . 277
B.10 Temperature effect on normalised minimum cross-sectional radius - equivalent plastic strain ($a/a_0$ - $\bar{\varepsilon}_{pl}$) for copper C110 specimens with different notch acuities. . . . . 279
B.11 Temperature effect on notch curvature - equivalent plastic strain ($\rho$ - $\bar{\varepsilon}_{pl}$) for copper C110 specimens with different notch acuities. . . . . 280
B.12 Temperature effect on equivalent strain - stress triaxiality ($\bar{\varepsilon}$ - $\eta$) for copper C110 specimens with different notch acuities. . . . . 281
B.13 Johnson-Cook plasticity model fit to experimental results of stainless steel 304L; all experimental data fitted together; low plasticity at low temperature has not been used in the fitting. . . . . 282
B.14 Johnson-Cook plasticity model fit to experimental results of stainless steel 304L; standard, strain-rate and temperature results fitted separately; low plasticity at low temperature has not been used in the fitting. . . . . 283
B.15 Johnson-Cook fracture model fit to experimental results of stainless steel 304L; standard, strain-rate and temperature results fitted separately. . . . . 284
B.16 Johnson-Cook fracture model fit to experimental results of copper C110; standard, strain-rate and temperature results fitted separately. . . . . 285

B.17 Bonora ductile damage model fit attempt of copper C110 following the fitting process recomended in [90]. . . . . 286
B.18 Bonora ductile damage model fit attempt of copper C110 fitting the damage accumulation shape firstly. . . . . 286

# List of Tables


3.1 Stainless steel 304L chemical composition. . . . . 36
3.2 Geometry and stress triaxiality of the specimens used for plastic fracture analysis. . . . . 45

4.1 Dimensions of the specimens used at low and high speed. . . . . 58
4.2 Specimens analysed for high-speed strain measurement methods comparison and validation. . . . . 64
4.3 Comparison of elastic modulus and damage values obtained with the continuous and interrupted techniques. . . . . 71

5.1 Specimens studied in the quasi-static room temperature plasticity analysis. 84
5.2 Neck onset strain ($\varepsilon_{onset}$), final neck radius of curvature ($\rho_f$) and final cross-sectional radius ($a_f$) measured with imaging method; final cross-sectional radius ($a_f$) measured with shadowgraph. . . . . 84
5.3 Specimens studied in the quasi-static room temperature ductile fracture analysis. . . . . 89
5.4 Stress triaxiality results of stainless steel 304L. Theoretical initial stress triaxiality ($\eta_0$) obtained using Equation 3.5; initial ($\eta_0$), final ($\eta_f$) and average ($\eta_{av}$) stress triaxiality throughout the test obtained using the proposed imaging method; and fracture equivalent strain ($\bar{\varepsilon}_f$) obtained using the proposed imaging technique and the shadowgraph measurements. . . . . 94
5.5 Stress triaxiality results of copper C110. Theoretical initial stress triaxiality ($\eta_0$) obtained using Equation 3.5; initial ($\eta_0$), final ($\eta_f$) and average ($\eta_{av}$) stress triaxiality throughout the test obtained using the proposed imaging method; and fracture equivalent strain ($\bar{\varepsilon}_f$) obtained using the proposed imaging technique and the shadowgraph measurements. . . . . 95
5.6 Specimens studied in the quasi-static room temperature damage accumulation analysis. . . . . 95
5.7 Specimens studied in the quasi-static room temperature damage validation analysis. . . . . 100
5.8 Details of the grinding and polishing stages followed to prepare specimens. . 101

6.1 Specimens studied in the analysis of strain-rate effects on plasticity. . . . . 114
6.2 Camera set-up for the plasticity analysis at varying strain-rate. . . . . 114
6.3 Effect of strain-rate on neck onset strain ($\varepsilon_{onset}$), final neck radius of curvature ($\rho_f$) and final cross-sectional radius ($a_f$) measured with imaging method; and final cross-sectional radius ($a_f$) measured with shadowgraph. . 116
6.4 Effect of strain-rate on stress triaxiality; the average ($\eta_{av}$), minimum ($\eta_{min}$) and maximum ($\eta_{max}$) values of triaxiality for each test are presented. . . . 117
6.5 Average ($\dot{\varepsilon}_{av}$), minimum ($\dot{\varepsilon}_{min}$) and maximum ($\dot{\varepsilon}_{max}$) values of strain-rate of the tensile tests. . . . . 119
6.6 Specimens studied in the analysis of strain-rate effects on ductile fracture. . 120
6.7 Specimens studied in the analysis of strain-rate effects on ductile damage accumulation. . . . . 128

7.1 Specimens studied in the analysis of temperature effects on plasticity. . . . 138
7.2 Effect of temperature on neck onset strain ($\varepsilon_{onset}$), final neck radius of curvature ($\rho_f$) and final cross-sectional radius ($a_f$) measured with imaging method; and final cross-sectional radius ($a_f$) measured with shadowgraph. . 140
7.3 Effect of temperature on stress triaxiality; the average ($\eta_{av}$), minimum ($\eta_{min}$) and maximum ($\eta_{max}$) values of triaxiality for each test are presented. 141
7.4 Specimens studied in the analysis of temperature effects on fracture strain. 145
7.5 Specimens studied in the analysis of temperature effects on ductile damage accumulation. . . . . 151

8.1 Reference parameters for Johnson-Cook model and adiabatic heating calculations. . . . . 156
8.2 $R^2$ values of Johnson-Cook model calibration using different fitting approaches. 161
8.3 Calibrated parameters of Johnson-Cook plastic hardening model. . . . . 162
8.4 Calibrated parameters of Johnson-Cook ductile fracture model. . . . . 163
8.5 $R^2$ values of Johnson-Cook and proposed ductile fracture models calibration using different fitting approaches. . . . . 168
8.6 Calibrated parameters of the proposed ductile fracture model. . . . . 168
8.7 Parameters involved in the damage modelling. . . . . 175
8.8 Calibrated parameters of the threshold strain part of the model. . . . . 176
8.9 Calibrated parameters of the critical damage part of the model. . . . . 176
8.10 Calibrated parameters of the damage accumulation part of the model. . . . 177

A.1 List of specimen drawings included in the appendix. . . . . 207
A.2 List of rig part drawings included in the appendix. . . . . 239

B.1 Stress triaxiality results of stainless steel 304L at different strain-rates. Theoretical initial stress triaxiality ($\eta_0$) obtained using Equation 3.5; initial ($\eta_0$), final ($\eta_f$) and average ($\eta_{av}$) stress triaxiality throughout the test obtained using the proposed imaging method; and fracture equivalent strain ($\bar{\varepsilon}_f$) obtained using the proposed imaging technique. . . . . 266
B.2 Stress triaxiality results of copper C110 at different strain-rates. Theoretical initial stress triaxiality ($\eta_0$) obtained using Equation 3.5; initial ($\eta_0$), final ($\eta_f$) and average ($\eta_{av}$) stress triaxiality throughout the test obtained using the proposed imaging method; and fracture equivalent strain ($\bar{\varepsilon}_f$) obtained using the proposed imaging technique. . . . . 270
B.3 Stress triaxiality results of stainless steel 304L at different temperatures. Theoretical initial stress triaxiality ($\eta_0$) obtained using Equation 3.5; initial ($\eta_0$), final ($\eta_f$) and average ($\eta_{av}$) stress triaxiality throughout the test obtained using the proposed imaging method; and fracture equivalent strain ($\bar{\varepsilon}_f$) obtained using the proposed imaging technique. . . . . 274
B.4 Stress triaxiality results of copper C110 at different temperatures. Theoretical initial stress triaxiality ($\eta_0$) obtained using Equation 3.5; initial ($\eta_0$), final ($\eta_f$) and average ($\eta_{av}$) stress triaxiality throughout the test obtained using the proposed imaging method; and fracture equivalent strain ($\bar{\varepsilon}_f$) obtained using the proposed imaging technique . . . . . 278

# Acknowledgements

I give my greatest thanks to my academic supervisors Professor John Dear, Dr. Paul Hooper and Dr. Catrin Davies, the three of them from Imperial College London. I am in debt to them for giving me the opportunity to undertake this project, for guiding me through the research and for igniting so many good ideas that have made this thesis possible. I also give my thanks to my industrial supervisor Dr. Mike Cox for the support provided throughout and to AWE Plc. for funding this project. The assistance received from Dr. Tim Cartwright and Dr. Giles Aldrich-Smith has been invaluable and is also greatly appreciated.

I also have to thank all the colleagues and friends that I have met in London during the last four years. Many thanks to Joël, James, Marco, Farnaz, Mitesh, Sherry, Ian, Emily, Alex, Geena, Xianyan, Tobias, Rob, Derek, Fabian and a huge etcetera for the support, for all the coffee breaks shared and for the time spent together at places like Eastside and Port Aventura. Leire, Ipi, Beñat, Serrano and Lore also deserve a special mention for proof reading this work. I also want to thank Professor Rafael Avilés from my former University of the Basque Country, who inspired me to become a doctor.

Last and certainly most important, the support of my family and friends has been invaluable throughout the last four years and without them I would not have gone this far. Thanks to my mum Begoña, my grandpa Angel, my cousins Mikel and Jorge, my uncle Angel and my aunt Marta, who was always a role model for all of us. Also thanks to my very good friends David and Beñat for the support in good and bad times. Finally, a very special mention to Loreain, for always being next to me whilst writing this thesis and for all her encouragement and affection when I needed it most.

# List of publications

Parts of the work presented in this thesis have been or are planned to be disseminated through a number of written publications; these are listed below, as of June 2020.

## Peer-reviewed journal publications

[p1] A. Sancho, M. J. Cox, T. Cartwright, G. D. Aldrich-Smith, C. M. Davies, P. A. Hooper, J. P. Dear, "Experimental techniques for ductile damage characterisation," *Procedia Structural Integrity*, vol. 2, pp. 966–973, 2016. (`https://doi.org/10.1016/j.prostr.2016.06.124`)

[p2] A. Sancho, M. J. Cox, T. Cartwright, C. M. Davies, P. A. Hooper, J. P. Dear, "An experimental methodology to characterise post-necking behaviour and quantify ductile damage accumulation in isotropic materials," *International Journal of Solids and Structures*, vol. 176-177, pp. 191–206, 2019. (`https://doi.org/10.1016/j.ijsolstr.2019.06.010`)

[p3] A. Sancho, M. J. Cox, J. P. Dear, C. M. Davies, P. A. Hooper, "An innovative methodology to characterise post-necking behaviour at high strain-rate and different temperatures in isotropic materials", *To be published.*

[p4] A. Sancho, M. J. Cox, P. A. Hooper, J. P. Dear, C. M. Davies, "A novel experimental technique to quantify damage accumulation at high strain-rate and different temperatures", *To be published.*

[p5] A. Sancho, M. J. Cox, C. M. Davies, J. P. Dear, P. A. Hooper, "A new strain-rate and temperature dependent fracture and non-linear ductile damage accumulation model", *To be published.*

## Peer-reviewed conference publications

[c1] A. Sancho, M. J. Cox, G. D. Aldrich-Smith, T. Cartwright, C. M. Davies, P. A. Hooper, J. P. Dear, "Experimental methodology for the measurement of plasticity on metals at high strain-rate", in *DYMAT2018, EPJ Web of Conferences*, vol. 183, 02063, 2018. (`https://doi.org/10.1051/epjconf/201818302063`)

[c2] A. Sancho, M. J. Cox, T. Cartwright, P. A. Hooper, J. P. Dear, C. M. Davies, "Effects of strain-rate and temperature on ductile damage of metals", in *PVP2018, ASME 2018 Pressure Vessels and Piping Conference*, PVP2018-85158, pp. V06AT06A029, 2018. (`https://doi.org/10.1115/PVP2018-85158`)

[c3] A. Sancho, P. A. Hooper, C. M. Davies, "Ductile damage assessment using continuum damage mechanics and methodology for high strain-rate damage analysis", in *PVP2017, ASME 2017 Pressure Vessels and Piping Conference*, PVP2017-65097, pp. V005T11A001, 2017. (`https://doi.org/10.1115/PVP2017-65097`)

# Acronyms and Abbreviations

| | |
|---|---|
| ASTM | American Society for Testing and Materials |
| CDM | Continuum Damage Mechanics |
| CFD | Computerised Fluid Dynamics |
| CT | Computerised Tomography |
| CT | Compact Tension |
| DCPD | Direct Current Potential Drop |
| DIC | Digital Image Correlation |
| DSLR | Digital Single-Lens Reflex |
| ETP | Electrolytic Tough Pitch |
| FCC | Face Centered Cube |
| FE | Finite Elements |
| FEM | Finite Elements Method |
| GNT | Gurson-Needleman-Tvergaard |
| HGF | Hourglass Flat |
| HGR | Hourglass Round |
| HR | High Rate |
| IR | Intermediate Rate |
| ISO | International Organization for Standardization |
| MTS | Mechanical Threshold Stress |
| PD | Potential Drop |
| QS | Quasi-Static |
| RAM | Random Access Memory |
| RB | Round Bar |
| RNB | Round Notched Bar |
| RVE | Reference Volume Element |
| SEM | Scanning Electron Microscopy |
| SHPB | Split Hopkinson Pressure Bar |
| s/s | Stainless Steel |
| UMAT | User Material Subroutine |
| UNS | Unified Numbering System |

| | |
|---|---|
| UTS | Ultimate Tensile Strength |
| VHS | Very High Speed |
| VUMAT | Vectorial User Material Subroutine |

# Notation

| | |
|---|---|
| $\alpha$ | damage exponent in Bonora model |
| $\gamma_i$ | strain-rate effect parameters of the proposed ductile fracture model ($i = 1, 2$) |
| $\Delta\bar{\varepsilon}_f$ | ductility change |
| $\Delta\bar{\varepsilon}_{pl}$ | equivalent plastic strain increment |
| $\Delta l$ | elongation |
| $\Delta T$ | temperature change |
| $\varepsilon$ | strain |
| $\bar{\varepsilon}$ | equivalent strain |
| $\boldsymbol{\varepsilon}$ | strain tensor |
| $\bar{\varepsilon}_{\bar{\sigma}_{MAX}}$ | equivalent strain at maximum equivalent stress point |
| $\varepsilon_e$ | engineering strain |
| $(\varepsilon_e)_{extens.}$ | extensometer engineering strain |
| $\varepsilon_{el}$ | elastic strain |
| $\boldsymbol{\varepsilon_{el}}$ | elastic strain tensor |
| $\varepsilon_f$ | uniaxial fracture strain |
| $\bar{\varepsilon}_f$ | equivalent fracture strain |
| $(\bar{\varepsilon})_{imaging}$ | true strain obtained from Bridgman approach |
| $\varepsilon_{onset}$ | neck onset strain |
| $\varepsilon_{pl}$ | plastic strain |
| $\bar{\varepsilon}_{pl}$ | equivalent plastic strain |
| $\boldsymbol{\varepsilon_{pl}}$ | plastic strain tensor |
| $\bar{\varepsilon}_{pl,f}$ | fracture equivalent plastic strain |
| $\varepsilon_T$ | true strain |
| $\varepsilon_{th}$ | uniaxial threshold strain |
| $\bar{\varepsilon}_{th}$ | equivalent threshold strain |
| $\varepsilon_{zz,av}$ | cross-sectional average strain in axial direction |
| $\dot{\varepsilon}$ | strain-rate |
| $\dot{\varepsilon}^*$ | nondimensional strain-rate |
| $\dot{\bar{\varepsilon}}_0$ | reference equivalent strain-rate |
| $\dot{\varepsilon}_{av}$ | average strain-rate |

| | |
|---|---|
| $\dot{\varepsilon}_{max}$ | maximum strain-rate |
| $\dot{\varepsilon}_{min}$ | minimum strain-rate |
| $\dot{\varepsilon}_{pl}$ | plastic strain-rate |
| $\dot{\bar{\varepsilon}}_{pl}$ | equivalent plastic strain-rate |
| $\dot{\boldsymbol{\varepsilon}}_{\boldsymbol{pl}}$ | plastic strain-rate tensor |
| $\eta$ | stress triaxiality |
| $\eta_0$ | initial stress triaxiality |
| $\eta_{av}$ | average stress triaxiality |
| $\eta_f$ | fracture stress triaxiality |
| $\eta_{max}$ | maximum stress triaxiality |
| $\eta_{min}$ | minimum stress triaxiality |
| $\eta_{th}$ | theoretical stress triaxiality |
| $\theta$ | Lode angle |
| $\bar{\theta}$ | normalised Lode angle |
| $\lambda$ | Lamé's elasticity constant |
| $\dot{\lambda}$ | plastic multiplier |
| $\mu$ | Lamé's elasticity constant |
| $\nu$ | Poisson's ratio |
| $\nu_i$ | damage accum. parameters of the proposed ductile damage model ($i = 1, 2$) |
| $\nu_{1j}$ | parameters of the proposed $\nu_1(\dot{\varepsilon}, T)$ expression ($j = 1, 2, 3$) |
| $\nu_{2j}$ | parameters of the proposed $\nu_2(\dot{\varepsilon}, T)$ expression ($j = 1, ..., 4$) |
| $\xi$ | parameter related to Lode angle in Xue-Wierzbicki model |
| $\xi_i$ | base parameters of the proposed ductile fracture model ($i = 1, 2, 3$) |
| $\mu$ | fraction of plastic energy transformed into heat |
| $\rho$ | neck/notch radius of curvature |
| $\rho$ | density |
| $\tilde{\rho}$ | effective density |
| $\rho_f$ | final neck/notch radius of curvature |
| $\sigma$ | stress |
| $\bar{\sigma}$ | equivalent stress |
| $\tilde{\sigma}$ | uniaxial effective stress |
| $\underset{\sim}{\boldsymbol{\sigma}}$ | stress tensor |
| $\underset{\sim}{\tilde{\boldsymbol{\sigma}}}$ | effective stress tensor |
| $\sigma_0$ | flow stress |
| $\sigma_e$ | engineering stress |
| $\sigma_H$ | hydrostatic stress |
| $(\bar{\sigma})_{imaging}$ | true stress obtained from Bridgman approach |
| $\sigma_{new}$ | stress of current increment |
| $\sigma_{old}$ | stress of previous increment |

$\sigma_T$ true stress

$\sigma_{YP}$ yield stress

$\sigma_{zz}$ stress in axial direction

$\sigma_{zz,av}$ cross-sectional average stress in axial direction

$\sigma_{zz,MAX}$ cross-sectional maximum stress in axial direction

$\Phi$ yield function

$\varphi$ porosity

$\varphi_{av}$ average porosity

$\varphi_{av,f}$ fracture average porosity

$\varphi_c$ porosity in the centre

$\phi_i$ parameters of the proposed critical damage expression ($i = 1, ..., 4$)

$\chi_i$ parameters of the proposed threshold strain expression ($i = 1, ..., 4$)

$\psi_i$ temperature effect parameters of the proposed ductile fracture model ($i = 1, 2, 3$)

$A$ Johnson-Cook model yield parameter

$\tilde{A}$ isotropic net cross-sectional area

$\tilde{A}_{(\vec{n})}$ net cross-sectional area in the direction of vector $\vec{n}$

$A_0$ isotropic initial cross-sectional area

$A_{0(\vec{n})}$ initial cross-sectional area in the direction of vector $\vec{n}$

$A_{voids}$ isotropic cross-sectional area occupied by voids

$A_{voids(\vec{n})}$ cross-sectional area occupied by voids in the direction of vector $\vec{n}$

$a$ sample/neck/notch cross-sectional radius

$a_0$ sample/neck/notch initial cross-sectional radius

$a_f$ sample/neck/notch final cross-sectional radius

$B$ Johnson-Cook model hardening parameter

$C$ Johnson-Cook model strain-rate parameter

$\underset{\approx}{\mathbf{C}}$ fourth order tensor of elastic components

$C_i$ Xue-Wierzbicki model parameters ($i = 1, ..., 4$)

$C_p$ specific heat

$D$ ductile damage

$D_i$ Johnson-Cook fracture model parameters ($i = 1, ..., 5$)

$D_0$ initial damage

$D_{cont}$ damage from continuous methodology

$D_{cr}$ critical damage

$D_{interr}$ damage from interrupted methodology

$D_{(\vec{n})}$ ductile damage in the direction of vector $\vec{n}$

$E$ elastic modulus

$\tilde{E}$ effective elastic modulus

$E_{cont}$ elastic modulus from continuous methodology

| | |
|---|---|
| $E_{interr}$ | elastic modulus from interrupted methodology |
| $f$ | void volume fraction |
| $f^*$ | effective void volume fraction |
| $f_c$ | critical void volume fraction |
| $f_f$ | void volume fraction at fracture |
| $f_u^*$ | $f^*$ at fracture |
| $\dot{f}$ | void volume fraction rate |
| $\dot{f}_{growth}$ | void volume fraction growth rate |
| $\dot{f}_{nucleation}$ | void volume fraction nucleation rate |
| $h$ | indentation depth |
| $h_f$ | final indentation depth |
| $h_{max}$ | indentation depth at $P_{max}$ |
| $J_3$ | third invariant of the deviatoric stress tensor |
| $l$ | longitudinal distance |
| $m$ | Johnson-Cook model temperature parameter |
| $N$ | fatigue life |
| $n$ | hardening exponent |
| $n$ | number of fatigue cycles |
| $\vec{n}$ | normal to the plane where damage is quantified in the RVE |
| $P$ | load |
| $P_f$ | fracture load |
| $P_{max}$ | maximum indentation load |
| $q_i$ | Gurson model material parameters ($i = 1, 2, 3$) |
| $R$ | electric resistance |
| $\tilde{R}$ | effective electric resistance |
| $R^2$ | coefficient of determination |
| $r$ | radial distance from the axis |
| $r$ | resistivity |
| r | residual |
| $\tilde{r}$ | effective resistivity |
| $r_0$ | spherical void initial radius |
| $\dot{r}$ | void growth rate |
| $S$ | initial unloading stiffness |
| $SS_{res}$ | sum of squares of residuals |
| $SS_{tot}$ | total sum of squares |
| $T$ | temperature |
| $T^*$ | nondimensional temperature |
| $T_m$ | melting temperature |
| $T_{ref}$ | reference temperature |

| | |
|---|---|
| $t$ | time |
| $t_{necking}$ | length of necking process |
| $V$ | voltage |
| $\tilde{V}$ | effective voltage |
| $v$ | velocity |
| $v_L$ | longitudinal wave velocity |
| $\tilde{v}_L$ | effective longitudinal wave velocity |
| $Y_i$ | values predicted by the model ($i = 1, ..., n$) |
| $y_i$ | experimentally measured data points ($i = 1, ..., n$) |
| $\bar{y}$ | mean of all measured data points |

# Chapter 1

# Introduction

Ductile damage is a form of material degradation that appears in ductile metals when sufficient tensile load is applied within their plastic regime. The degradation of the material is a matter of concern for any engineering application, and avoiding its ultimate manifestation, i.e. the fracture of the component, is usually a main consideration of a successful engineering design. While the characterisation of many mechanical properties is well understood, the accumulation of ductile damage and the ductile fracture of metals is still being researched due to the experimental and modelling challenges involved. Aeronautic, defense, automotive and metal forming are examples of industries for which the quantification of ductile damage is relevant. High plastic deformation can appear in some of the components, either during their manufacturing process or their operation. Apart from the high plastic deformation, these products are usually subjected to extreme conditions such as high strain-rate deformation, low or high temperatures, which have a great influence on the damage and fracture behaviours [1, 2]. Therefore, to accurately model fracture in complex designs that operate in extreme conditions, the effect of strain-rate and temperature on plasticity, ductile damage and ductile fracture should be considered.

Contemporary materials research not only intends to provide an accurate representation of the behaviour of materials, but also to reduce the environmental impact of components manufacturing and operation. This is achieved through the development of detailed material models that produce accurate estimations, reducing the need for the conservative safety factors that were employed in conjunction with early simpler models. Experimental characterisation and modelling of materials has become more rigorous over the years, with the aim of extending operative limits of materials and extending lifetime of components without compromising their safe operation. Meticulous designs also lead to cost reductions through the limitation of material waste and the avoidance of components replacement (e.g. Figure 1.1). The detailed characterisation



**(a)** Rocket launch **(b)** Booster landing

**Figure 1.1:** Falcon 9 rocket launch and Falcon Heavy rocket boosters landing for their reuse (Space X, Cape Canaveral, 2018); this is just an example of the current needs for life and operative limits extension, costs reduction and safety of materials operating even in the most extreme conditions (images from [3, 4]).

of high plastic deformation, ductile damage accumulation and ultimate ductile fracture at varying conditions plays a key role in the correct use of materials that meet the demanding requirements of the modern world.

## 1.1 Ductile Damage and Fracture of Metals

Ductile damage is the consequence of the appearance of microscopical voids and micro-cracks when sufficiently high plastic strain is applied to ductile alloys. The macroscopic effect is a reduction or degradation of some mechanical properties of the material, such as stiffness. If a critical value of damage is achieved, the material loses completely its load carrying capacity and it undergoes a macroscopic ductile fracture. In order to characterise these behaviours, adequate experiments are firstly designed. These tests are used to quantify material properties that are relevant for the modelling. The experimental results are then used to calibrate existing material models that represent damage and fracture, or alternatively, to design new models that include additional features. Ultimately, the equations and parameters of these models are implemented in engineering analysis codes that can be used to study the performance of real components.

### Materials Testing

Since ductile damage appears at high levels of plastic deformation, an accurate representation of plasticity is required. Tensile tests are traditionally used to characterise plasticity, however, the deformation of ductile metals near fracture is generally

non-uniform, and realistic results cannot be obtained from the classical tensile test in that case. Specific experiments based on imaging or supplementary finite elements simulations are required to characterise the neck that appears during non-uniform deformation, allowing the calculation of the real plastic strains and stresses involved in damage.

The quantification of the actual ductile damage can be performed following two different approaches: a micromechanical approach, consisting on the measurement of the evolution of individual voids; or a macromechanical approach, that aims to calculate damage form the degradation that it produces on a mechanical property of the material. In both cases, progressive measurements of damage are obtained along the plastic region of the material, from the damage initiation point to the final fracture condition.

The ductile fracture point corresponds to the last operating point of the material on its plasticity and ductile damage curves. Historically, stress triaxiality has been considered to affect significantly this property [5, 6]. The effect of stress triaxiality on ductile fracture is generally studied by means of tensile tests on notched specimens whose different geometries produce different stress states. More recently, the loading conditions (tensile, compression, shear or a combination of them) have also been found to have an effect on ductile fracture, and a variety of sample geometries and tests are used to quantify it.

To study the effects of strain-rate and temperature on material properties, experiments to measure plasticity, fracture and ductile damage are conducted at different conditions. In order to obtain accurate results from these tests, some modifications imposed by the non-standard nature of the experiment are required. Generally, the tests at varying temperature are performed inside an environmental chamber, which provides temperatures lower or higher than the room temperature on the material. The experiments at varying strain-rate impose more limitations. Usually, a non-contact method such as digital image correlation (DIC) has to be used for strain measurement, and high-speed cameras are used for that purpose. The type of equipment required also changes depending on the strain-rate range that is aimed to be studied: from servo-hydraulic tensile machines ($\dot{\varepsilon} = 1 \sim 10^3$ s$^{-1}$), to split Hopkinson pressure bars (SHPB) ($\dot{\varepsilon} = 10^3 \sim 10^5$ s$^{-1}$), and gas guns or ballistic tests for even higher rates.

**Materials Modelling**

Different types of models exist to estimate ductile damage and ductile fracture of metals: micromechanical models based on the dynamics of voids, continuum damage mechanics (CDM) models focused on the macroscopic effects produced on the material and phenomenological models purely based on experimental results. Some models aim to integrate different features of the material behaviour (plasticity, damage accumula-

tion and fracture) into a unified formulation, while others deal only with one of the phenomena. The data collected from the tests at different temperatures and strain-rates can be used to calibrate the mathematical equations of the models. This process consists of fitting the experimental data points to the equations by determining the value of some tunable parameters that appear in the model.

The equations and parameters of the models can be implemented in different engineering analysis codes, such as finite elements (FEM) for structural analysis or computerised fluid dynamics (CFD) for material-fluid interactions. Only a few well established models are available in the libraries of commercial software packages; however, it is generally possible to manually implement other models by means of subroutines developed by the user.

The aim of the modelling process is to extrapolate the few particular cases analysed experimentally to any general combination of conditions that could appear in the real world. A real component designed for an engineering application may present a complex geometry and will operate under varying strains, stress states, strain-rates and temperatures. Accurate experimental measurements, taken from specimens tested under different conditions, lead to improved models that are able to represent more precisely the complex conditions that engineering components undergo.

## 1.2 Aim and Objectives

The aim of this thesis is to investigate and develop experimental methods that can be used to characterise plasticity, ductile damage and ductile fracture of alloys at different strain-rate and temperature conditions; and use the results obtained to develop and calibrate material models able to accurately represent these behaviours at varying strain-rate and temperature. Therefore, the thesis encompasses three different phases: the development and calibration of the experimental methodology, the use of the methodology for experimental results collection and the creation and fitting of the material models.

In order to accomplish the above stated aim, a series of key objectives have been defined:

- Investigate the experimental methods available to characterise plasticity and damage of ductile materials. Find the limitations of these methods and explore improvements to overcome them.
- As part of the experimental methods improvement, develop a technique to measure the true stress - true strain behaviour of an alloy up to fracture, taking into account the variations in specimen geometry through imaging of its profile. This

is required to have a realistic representation once the material stops deforming uniformly and starts necking.

- Analyse the modifications required to the experiments so that they can be applied to obtain accurate results in non-standard conditions, i.e. high strain-rate, low and high temperature.
- As part of the modifications at high speed, explore an in-situ shadowgraph method and a sub-pixel accuracy post-processing algorithm that can be used to obtain accurate stress - strain measurements at high speed.
- As part of the modifications at high speed, design, manufacture and calibrate an experimental rig able to perform interrupted high-speed tensile tests that are required for ductile damage quantification at different levels of plastic strain.
- Apply the proposed experimental methodology to two ductile metallic materials in order to verify the feasibility of the tests and collect data of those materials.
- Explore the material models available in literature which are able to represent plasticity, ductile damage and ductile fracture behaviours, focusing on the models that incorporate the effects of strain-rate and temperature in their formulation. Modify features of the existing models or develop new ones when the available models are not successful representing the material behaviour.
- Calibrate the parameters of the selected models for the materials studied and code user defined subroutines of the models, so that they can be easily implemented in finite elements calculations.

## 1.3 Thesis Outline

This thesis consists of nine chapters. The research topic, aim and objectives are described here. Chapter 2 provides a review of the literature relevant to the research topic under study. The main body of the thesis is divided into six chapters; two on methodology, three on experimental results and one on modelling.

Chapter 3 describes the methodology that has been followed for the characterisation of plasticity, ductile fracture and damage accumulation of isotropic ductile metals. The experiments that have been performed later are explained in this Chapter, including an imaging technique used to monitor the geometry of the specimen and the elastic modulus measurements to estimate ductile damage.

Chapter 4 provides an extension of the previous methodology, in which the modifications required in order to perform equivalent experiments at high strain-rate and different temperatures are explained. An in-situ high-speed shadowgraph method has been devised to extend the applicability of the specimen geometry monitoring technique

to high strain-rate. An experimental rig capable of performing interrupted high-speed tests has been designed, with the aim of studying intermediate stages of damage development. Regarding the post-processing, a sub-pixel edge detection algorithm has been implemented to improve the quality of low resolution images processing. All these developments are covered in this Chapter, and the results obtained using them along with the general methodology are shown in Chapters 6 and 7, considering the effects of strain-rate and temperature respectively.

Chapter 5 investigates the experimental results of the proposed methodology in quasi-static strain-rate ($\dot{\varepsilon} \sim 10^{-3}$ s$^{-1}$) and room temperature ($T \sim 20$°C) conditions on stainless steel 304L and copper C110. The effects of necking on plasticity are studied, as well as the changes produced by stress triaxiality on ductile fracture. Ductile damage accumulation is studied through elastic modulus degradation measurements, and also by means of a void density analysis performed on metallographic micrographs of the specimens.

Chapter 6 describes the results of the same experiments conducted at different strain-rates. Three rates have been investigated, from the quasi-static regime ($\dot{\varepsilon} \sim 10^{-3}$ s$^{-1}$) to relatively high strain-rate ($\dot{\varepsilon} \sim 10^{4}$ s$^{-1}$). A similar investigation is explained in Chapter 7, analysing in this case the effects of temperature on the experimental results. Three temperatures have also been considered: low temperature ($T = -80$°C), room temperature ($T = 20$°C) and high temperature ($T = 180$°C).

The experimental results obtained have been used to calibrate models that represent plastic hardening, ductile fracture and damage accumulation. The classic Johnson-Cook model [1] has been used to represent plasticity, while new models have been created to represent fracture and ductile damage behaviours. In Chapter 8 the models development and fitting process is described. Conclusions of the whole project are presented in Chapter 9 along with some topics for further study.

# Chapter 2

# Literature Review

The technical work developed throughout this thesis is based on a number of concepts, techniques and models which have been developed by many scientists over recent years. As discussed before, the aim is to develop a framework for experimental measurement and modelling of ductile damage at a wide range of strain-rate and temperature conditions. In this Chapter, a summary of the key topics reviewed in literature is presented, including plasticity, damage, the experimental methods available for their measurement and the models to represent them. Firstly, basic plasticity background and some models to represent it which are relevant to this research are commented in Section 2.1. The theory, studies and modelling approaches to represent ductile damage and ductile fracture are explained and compared in Section 2.2. Finally, the most relevant experimental techniques proposed over the years for plasticity, damage and fracture measurement are reviewed in Section 2.3, including considerations for high speed testing.

## 2.1 Metal Plasticity

Plasticity and ductile damage are two phenomena that generally appear together in metals, and a satisfactory study of ductile damage should be accompanied by an accurate characterisation of plastic behaviour. Macroscopically, plastic deformation, unlike elastic deformation, implies that shape changes produced by loads remain when the loads are removed. The first studies on plasticity were performed by Tresca in 1864 [7] from a continuum macroscopic perspective. A similar approach was followed by von Mises [8] to propose his well known yield criterion in 1913. Micromechanical studies of plasticity started around the year 1900 proving that plasticity is caused by the slip of planes of atoms which slide over one another [9]. These slips occur on certain slip planes and in certain slip directions, which are characteristic of the crystal

structure of the material. The dislocation theory was formulated in 1934 [10–12] and explained the crystal planes slip. Dislocations are disruptions in the crystal lattice structure whose propagation results in the slide of a block of crystal structure over another [13]. Therefore, the inelastic flow occurs because of the movement of dislocations through the crystal structure of the material, and the observable macroscopic effects are the consequence of these microscopic phenomena. For example, the intersection of dislocations on different slip planes is a cause of the strain hardening effect.

### 2.1.1 Plasticity Modelling

Plasticity is considered on a continuum level in this research. The aim is to obtain a constitutive equation of the material that provides the relationship between stresses and strains. This is the most basic information required to characterise a material and to perform structural calculations. Metallic materials generally present two clearly defined phases when load is applied. Firstly, a linear elastic deformation phase occurs, followed by a highly non-linear inelastic or plastic deformation phase. The total strain tensor ($\underset{\sim}{\boldsymbol{\varepsilon}}$) can be divided into its elastic ($\underset{\sim}{\boldsymbol{\varepsilon}}_{\boldsymbol{el}}$) and plastic contributions ($\underset{\sim}{\boldsymbol{\varepsilon}}_{\boldsymbol{pl}}$), as presented in Equation 2.1. The elastic part corresponds to the recoverable deformation when stress below the yield condition is applied. It is defined by Hooke's Law of linear elasticity [14], which states the linear relationship between elastic stress ($\underset{\sim}{\boldsymbol{\sigma}}$) and strain through the fourth order tensor of elastic components ($\underset{\approx}{\mathbf{C}}$), as shown in Equation 2.2. For isotropic materials, all the terms of the elastic tensor depend only on two parameters, being Lamé's constants ($\lambda$ and $\mu$) the most extensively used [13].

$$\underset{\sim}{\boldsymbol{\varepsilon}} = \underset{\sim}{\boldsymbol{\varepsilon}}_{\boldsymbol{el}} + \underset{\sim}{\boldsymbol{\varepsilon}}_{\boldsymbol{pl}} \tag{2.1}$$

$$\underset{\sim}{\boldsymbol{\sigma}} = \underset{\approx}{\mathbf{C}} : (\underset{\sim}{\boldsymbol{\varepsilon}} - \underset{\sim}{\boldsymbol{\varepsilon}}_{\boldsymbol{pl}}) \tag{2.2}$$

In order to represent plasticity, three characteristics have to be defined: the yield surface, the flow rule and the hardening law. The yield surface defines when yielding occurs and separates the elastic from the plastic region. Equation 2.3 represents a generic form of the yield function, with a dependency on the stress tensor, plastic strain tensor, temperature and hardening parameters [13]. The flow rule determines the direction of the plastic deformation by means of the calculation of the direction of the plastic strain (Equation 2.4). Finally, in a general case in which hardening appears when the material is plastically deformed, a hardening law is defined to determine the evolution of the yield surface. This hardening can be isotropic (the yield surface expands), kinematic (the yield surface translates) or combined (expansion and translation of the yield surface).

$$f(\underset{\sim}{\boldsymbol{\sigma}}, \underset{\sim}{\boldsymbol{\varepsilon}}_{\boldsymbol{pl}}, T, n) \leq 0 \tag{2.3}$$

$$\dot{\underline{\boldsymbol{\varepsilon}}}_{\boldsymbol{pl}} = \dot{\lambda}\frac{\partial f}{\partial \underline{\boldsymbol{\sigma}}} \tag{2.4}$$

In this work, a special interest is placed on the plasticity models designed to include the effects of temperature and high strain-rate. As previously mentioned, the aim is to obtain a constitutive equation that relates the flow stress with the plastic strain, and in this case, also with the temperature and strain-rate:

$$\bar{\sigma} = f(\bar{\varepsilon}_{pl}, T, \dot{\varepsilon}_{pl}) \tag{2.5}$$

For a deeper understanding of plasticity modelling, some more detailed references can be consulted [15–17].

**Johnson-Cook Model**

One of the most extensivelly used models accounting for temperature and strain-rate is that proposed by Johnson and Cook in 1985 [1], following their experimental studies of plasticity on copper, iron and steel at different temperatures and strain-rates. The model is empirically based, and considers an isotropic hardening law. The flow rule is defined by Equation 2.6, where the first term represents the isotropic plastic strain hardening, the second term the strain-rate hardening effect and the third term the temperature softening effect:

$$\bar{\sigma} = [A + B(\bar{\varepsilon}_{pl})^n]\left[1 + C\ln\left(\frac{\dot{\bar{\varepsilon}}_{pl}}{\dot{\bar{\varepsilon}}_0}\right)\right]\left[1 - \left(\frac{T - T_{ref}}{T_m - T_{ref}}\right)^m\right] \tag{2.6}$$

where $\bar{\sigma}$ represents the von Mises equivalent stress, $\bar{\varepsilon}_{pl}$ the equivalent plastic strain, $\dot{\bar{\varepsilon}}_{pl}$ the equivalent plastic strain-rate, $\dot{\bar{\varepsilon}}_0$ the reference strain-rate, $T$ the temperature, $T_m$ the melting temperature, $T_{ref}$ the reference temperature and $A$, $B$, $n$, $C$ and $m$ the parameters of the model.

The second and third terms of Equation 2.6 modify the flow stress according to the effects of strain-rate and temperature, by means of the nondimensional strain-rate and temperature defined in Equations 2.7 and 2.8. Strain-rate is nondimensionalised by using the lowest rate studied as reference ($\dot{\bar{\varepsilon}}_0$), while temperature is transformed to the parameter $T^*$ that varies between 0 for $T = T_{ref}$ and 1 for $T = T_m$. Some authors use the room temperature as $T_{ref}$ and others use the lowest temperature studied, hence care must be taken to keep consistent its definition.

$$\dot{\varepsilon}^* = \frac{\dot{\bar{\varepsilon}}_{pl}}{\dot{\bar{\varepsilon}}_0} \tag{2.7}$$

$$T^* = \frac{T - T_{ref}}{T_m - T_{ref}} \tag{2.8}$$

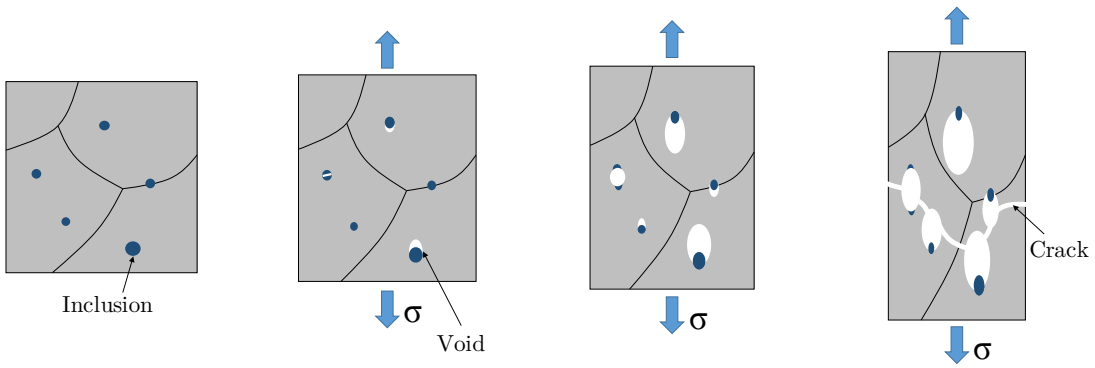
Although Johnson-Cook can be regarded as the most extended plasticity model including dynamic effects, other models have been proposed for this purpose. Some examples include the models developed by Zerilli and Armstrong [18] or the MTS (Mechanical Threshold Stress) model [19], both based on dislocations mechanics.

## 2.2 Ductile Damage and Ductile Fracture

Ductility is the capability that some materials present of undergoing a certain amount of plastic deformation without presenting a macroscopic fracture. However, a form of degradation known as ductile damage generally appears in the material at some point during that process. This type of damage is produced by two different phenomena depending on the stress triaxiality value, which is defined as the ratio of hydrostatic stress and equivalent stress (Equation 2.9). Ductile damage consists of the formation of voids and micro-cracks within the material for moderate and high stress triaxiality values, and on the appearance of shear bands for low triaxialities. The consequence is in both cases a macroscopic degradation of the mechanical properties of the material, however, the present study is focused on the damage caused by voids at high stress triaxiality ($\eta \geq 1/3$).

$$\eta = \frac{\sigma_H}{\bar{\sigma}} \tag{2.9}$$

The evolution of voids during the loading process can be divided into three different phases: nucleation, growth and coalescence, as observed in Figure 2.1. When tensile load is applied to the undamaged material exceeding a certain threshold plastic deformation, microdefects start to nucleate in the surrounding of discontinuities. This nucleation of voids generally occurs in grain boundaries or near inclusions, either by debonding from the metal matrix or by cracking of the particle. These two types of microdefect nucleation are exemplified in Figure 2.2. If further plastic deformation is applied, the voids grow in size increasing the degradation of the material. Finally, when voids reach a certain size they start interacting with their neighbours generating clusters of bigger voids that eventually produce macroscopic cracks. In Figure 2.3 the coalescence of two defects following two different modes of interaction is shown. When the coalescence of voids occurs, the net resisting section of material reduces significantly, as well as the load carrying capacity, leading to the eventual failure of the material known as ductile fracture. Some images of the typical fracture surface produced by ductile fracture are presented in Figure 2.4, where the network of dimples has been produced by the individual voids that have grown plastically to fracture the material.




**(a)** Raw material **(b)** Nucleation **(c)** Growth **(d)** Coalescence

**Figure 2.1:** Phases of ductile damage.

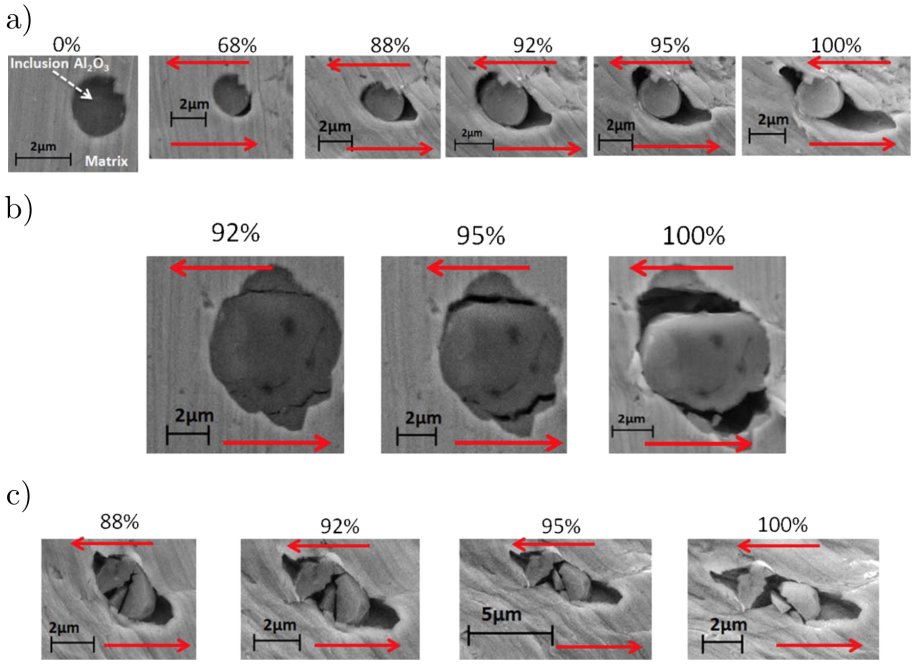



**Figure 2.2:** SEM observations of the different types of void nucleation: a) by debonding of an inclusion from the matrix, b) by cracking of the inclusion or c) a combination of the previous two (image from [20]).

### 2.2.1 From the Early Studies to the Modern Developments on Ductile Damage

The early models proposed to represent ductile damage were quite simple, nonetheless, the interest was not to develop a thorough model but to create a starting point that other researchers could later use and develop. McClintock (1968) [5] developed one of

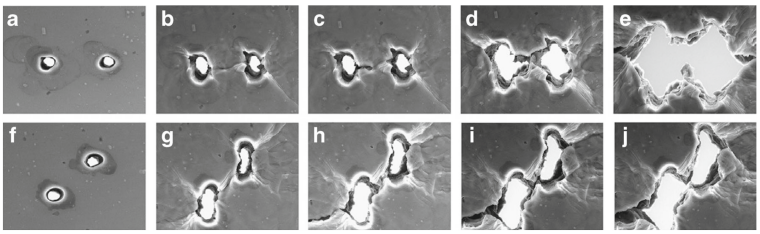
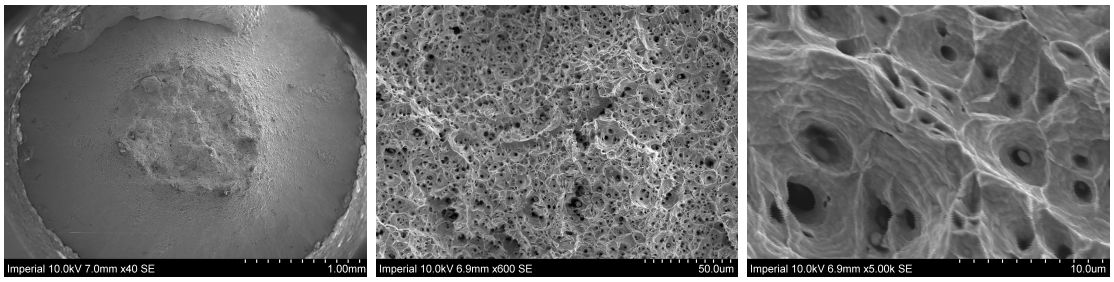



**Figure 2.3:** Coalescence of two voids following two different mechanisms: a)-e) plastic necking between voids and f)-j) shear localisation (image from [21]).




**(a)** 40x magnification **(b)** 600x magnification **(c)** 5000x magnification

**Figure 2.4:** Typical fracture surface produced by ductile fracture.

the pioneering ductile damage investigations, based on the experimental observations of the growth of cylindrical holes in a material subjected to a tensile force perpendicular to the direction of the holes' axis. The failure criterion in this early model considered just the hole growth, assuming failure when the holes grew to a certain threshold size; therefore, void nucleation or interaction was not considered. McClintock observed a strong inverse dependence of fracture strain on hydrostatic stress, and an exponential increase of relative void expansion when transverse stress was increased. These discoveries revealed from the very beginning the key role that stress triaxiality plays in ductile damage development and fracture.

The model developed by Rice and Tracey in 1969 [6] was also rather simple, considering the slightly more realistic case of spherical voids within an infinite uniform medium of perfectly plastic material. A remotely applied tensile field and hydrostatic stresses were superimposed in order to study the effect of stress triaxiality, and include it into the model to modify the void growth rate. The model considered isolated voids, and nucleation and interaction phenomena were not represented. Some conclusions can be obtained from Rice and Tracey study, being a very important one that the trends observed by McClintock [5] were validated. When hydrostatic stress was superimposed, void growth rate increased and fracture strain decreased. It was also observed that the shape changing effect was negligible when compared to the volume change.

After Rice and Tracey model was developed, some other studies were performed considering the same principles and attempting to improve its predictions. Tracey [22] introduced a strain hardened material instead of an elastic-perfectly-plastic material, and also considered a finite instead of an infinite traverse medium. The material hardening showed a void growth deceleration directly related to the hardening rate and stress triaxiality. Needleman [23] introduced the concept of voids interaction using finite elements analyses of arrays of cylindrical holes in elastic-plastic materials. The development of plastic zones around voids was firstly observed, and the voids coalescence led to much lower failure strains. In 1977 Gurson [24] combined the discoveries available to develop his theory of a continuum porous material, composed of an agregate of voids and the ductile matrix. His modelling considered the importance of stress triaxiality and included a yield criterion and a flow rule for porous materials that included a porosity fraction parameter to represent ductile damage. Tvergaard and Needleman [25–28] studied the interactions between voids once they coalesce, and introduced these effects in Gurson's model to develop the widely used model known as GNT (Gurson-Needleman-Tvergaard).

Many other authors have contributed over the years studying other effects on ductile damage. Some of them are: the interaction between particles and matrix to create voids [29] and the nucleation of voids [30–32]; the micro-necking produced between two voids [33] and further studies on the interactions between voids [34–37]; the effect of non-spherical voids [38] and other studies on the void shape effects [39,40]. As observed, from the early experimental studies that McClintock, Rice and Tracey performed in the late 60s and early 70s, to the modern experimental techniques and powerful finite elements simulations that are now available, many complex features involved in ductile damage have been studied. Once these phenomena were understood, different approaches to represent them with mathematical models started to develop.

### 2.2.2 Damage Modelling

Many different models have been proposed over the years to represent ductile damage incorporating the increasing number of discoveries available on the topic. If an elastic-plastic model is coupled with a damage model, a thorough prediction of the progressive degradation of the material properties, as well as of the eventual failure of a structure, can be performed. Several approaches have been proposed in an attempt to represent the problem, and this has led to the development of a wide number of damage models of different nature. It must be noted that there is no universal ductile damage model to date and none of them consider all the effects that affect damage, such as the type of material, strain-rate, temperature, stress state or loading conditions. The

three main approaches for ductile damage modelling are presented below, along with the most representative models of each methodology.

#### 2.2.2.1 Micromechanical Models

Modelling damage from a micromechanical point of view could be regarded as the most precise manner of representing material degradation, since the causes of ductile damage are the micro-defects, such as voids or micro-cracks, generated at a microscopic level. These models represent the natural evolution of the early works developed by McClintock, Rice and Tracey among others, described in the previous section.

**Rice-Tracey model**

The Rice and Tracey model [6] is one of the most basic representations of ductile damage, however, it is still widely used because of its simplicity. For the particular case of a void in a remote uniaxial tension strain-rate field, the void growth is represented in this model by:

$$\frac{\dot{r}}{r_0} = 0.558 \sinh\left(\frac{3}{2}\eta\right) \dot{\bar{\varepsilon}}_{pl} \tag{2.10}$$

where $r_0$ is the spherical void initial radius, $\dot{r}$ the void growth rate in the loading direction, $\eta$ the stress triaxiality and $\dot{\bar{\varepsilon}}_{pl}$ the equivalent plastic strain-rate. This equation provides the growth of voids caused by an applied strain-rate and stress triaxiality condition. Fracture strain can be calculated integrating the previous equation:

$$\frac{\bar{\varepsilon}_f}{\varepsilon_f} = \frac{0.521}{\sinh\left(1.5\eta\right)} \tag{2.11}$$

This expression relates the fracture strain under triaxial stress conditions ($\bar{\varepsilon}_f$), with the uniaxial fracture strain ($\varepsilon_f$) and the stress triaxiality ($\eta$). Finally, a linear accumulation of damage is assumed, providing an easy estimation of damage from the integration of the plastic strain over the multiaxial fracture strain:

$$D = \int \frac{d\varepsilon_{pl}}{\bar{\varepsilon}_f} \tag{2.12}$$

Rice and Tracey model is a very simple representation of ductile damage, however, it already incorporates important ideas like the effect of stress triaxiality on void growth.

**Gurson-type models**

The model proposed by Gurson [24] represents the same phenomena from a slightly different point of view. Instead of studying discrete voids and their interaction, the model modifies the material properties through a void density parameter ($f$). Gurson developed the material equations of a simplified continuum porous model, which un-

dergoes a density reduction when ductile damage is accumulated, due to the higher density of voids within the material. The flow law takes the form of a hardening power law and the yield criterion considers the effect that hydrostatic stress has on void grow. The modification proposed by Needleman and Tvergaard [28] to include void coalescence resulted in the well known GNT (Gurson-Needleman-Tvergaard) model, which presents the following yield function:

$$\Phi = \left(\frac{\bar{\sigma}}{\sigma_0}\right)^2 + 2q_1 f^* \cosh\left(\frac{3}{2}q_2\frac{\sigma_H}{\sigma_0}\right) - [1 + q_3 f^{*2}] = 0 \tag{2.13}$$

where $\Phi$ is the yield function, $\bar{\sigma}$ the equivalent stress, $\sigma_0$ the flow stress, $\sigma_H$ the hydrostatic stress, $f^*$ the effective void volume fraction and $q_1$, $q_2$ and $q_3$ material parameters of the model. According to classical plasticity, plastic deformation does not present a dependence on mean stress, however, Gurson includes in his model a strain softening term which makes the yield function weakly dependent on hydrostatic stress. Since ductile damage is highly dependent on hydrostatic stress, this strain softening term introduces its effects on the model. The GNT model modifies the original Gurson model by replacing the void volume fraction $f$ by the effective void volume fraction $f^*$ to consider void coalescence, which takes the following values:

$$f^* = \begin{cases} f & \text{for} \quad f \leq f_c \\ f_c + \frac{f_u^* - f_c}{f_f - f_c}(f - f_c) & \text{for} \quad f > f_c \end{cases} \tag{2.14}$$

where $f_c$ is the critical void volume fraction at which coalescence starts, $f_f$ the void volume fraction at fracture and $f_u^* = \frac{q_1 \pm \sqrt{{q_1}^2 - q_3}}{q_3}$ the value of $f^*$ at fracture. The evolution of void volume fraction can be represented as the sum of a term for nucleation and a term for growth:

$$\dot{f} = \dot{f}_{nucleation} + \dot{f}_{growth} \tag{2.15}$$

where the nucleation term is usually represented by a Gaussian curve such as that defined in [30], and the growth term is obtained from the integration of the void volume fraction.

Since the appearance of the porous continuum material approach developed by Gurson [24], many of the micromechanical models proposed have followed the same direction by implementing modifications to the original Gurson model to incorporate additional features. A few examples are the works that incorporate voids nucleation [30,32,33], voids size effects [41,42], voids shape effects [43,44], strain hardening [45,46], strain-rate dependency [47], shear effects [48, 49], plastic anisotropy [50, 51] or void-particle interaction [29].

The main difficulty associated to the development and calibration of micromechanical models is the experimental measurement of the microscopical parameters involved

in damage. These include the micro stresses and strains around voids, the changes in void density and even the size and shape evolution of individual voids. The most accurate models include a considerable number of parameters whose measurement can be complicated, making the use of this type of models less attractive, especially for real life industrial applications. This is one of the factors that has led to the development of alternative damage modelling approaches.

#### 2.2.2.2 Phenomenological Models

The phenomenological approach to model damage considers models that have been developed based on experimental observations. Generally, an expression for the fracture strain ($\bar{\varepsilon}_f$) is proposed, which depends on the properties that are known to affect fracture, such as stress triaxiality, strain-rate or temperature. A linear evolution of damage is assumed in most cases, considering the accumulation of damage through an integral like that of Equation 2.12, where the proposed expression for fracture strain is introduced. Progressively applied plastic strain increases the estimation of damage until it reaches the fracture strain given by the model ($\bar{\varepsilon}_{pl} = \bar{\varepsilon}_f$) and fracture occurs. The use of this type of models is extended in modern commercial finite elements codes, since they can be more easily used for industrial applications due to their easier calibration and the parameters libraries that are already available in literature for many materials.

The models are generally calibrated using fracture point information. The early ductile damage studies proved the effect that stress triaxiality ($\eta$) has on ductile damage and ductile fracture [5, 6], and this is usually the key parameter that this type of models include. Experimentally, different stress triaxialities are studied by testing notched samples with different notch geometries that produce various stress states [52, 53]. More recently, the dependency on the loading conditions has also been proved [54, 55]. This is often represented by means of a normalised Lode angle parameter ($\bar{\theta}$), which is related to the second and third invariants of the deviatoric stress tensor (Equation 2.16). This parameter represents the type of loading that the material is undergoing (tension, compression, shear, or a combination of them). A wide variety of specimen geometries and experimental configurations have been proposed in order to study different combinations of $\eta$ and $\bar{\theta}$. In Figure 2.5, the map of possible stress triaxiality and Lode angle combinations, and the loading conditions that appear in each case is presented.

$$\bar{\theta} = 1 - \frac{6\theta}{\pi} = 1 - \frac{2}{\pi} \arccos\left[\frac{27}{2}\frac{J_3}{\bar{\sigma}^3}\right] \tag{2.16}$$

Some of the most relevant empirical fracture models are the constant equivalent fracture strain, maximum shear stress, Johnson-Cook [1], Xue-Wierzbicki [54], Wilkins et al. [56] and Cockcroft-Latham [57]. A comparison of the calibration of these models

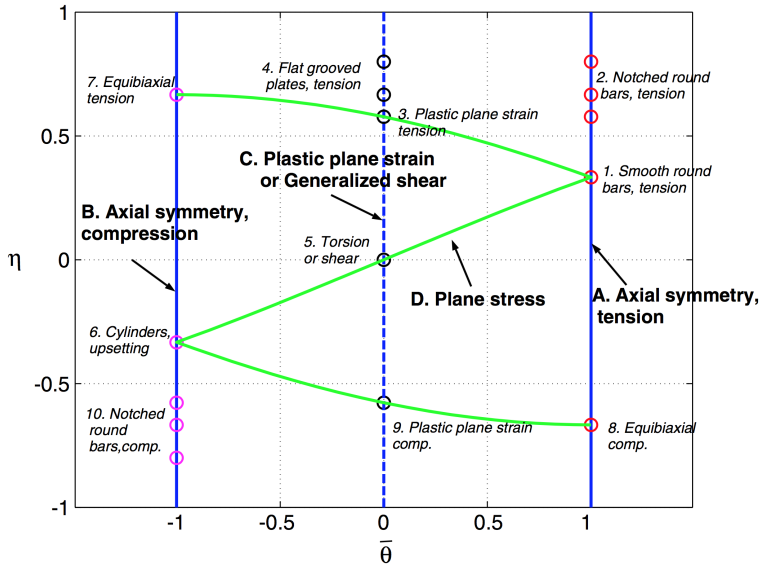



**Figure 2.5:** Stress triaxiality ($\eta$) vs. normalised Lode angle ($\bar{\theta}$) map representing the different stress states and loading conditions that the material can undergo [55].

was performed by Wierzbicki et al. [58], and the simulation of their performance in high velocity events was studied by Teng and Wierzbicki [59]. As said before, most of these models assume a linear accumulation of damage, integrated using Equation 2.12. Other models such as that derived by Cortese et al. [60], proposed an analogy between ductile damage accumulation and the high cycle fatigue damage law used by Palmgrem [61], in which the number of fatigue cycles ($n$) is replaced by the accumulated plastic strain ($\bar{\varepsilon}_{pl}$) and the fatigue life ($N$) by the fracture strain ($\bar{\varepsilon}_f$), as observed in Equation 2.17. Sebek et al. [62] proposed a similar accumulation of damage for Lode dependent plasticity and fracture modelling.

$$\sum \left( \frac{n}{N} \right) \longleftrightarrow \int \frac{\bar{\varepsilon}_{pl}}{\bar{\varepsilon}_f} \tag{2.17}$$

Johnson-Cook model [1] is described below, as it includes the effects of strain-rate and temperature; and Xue-Wierzbicki model [54], since it considers the effects of triaxiality and also of Lode angle.

### Johnson-Cook Model

Johnson and Cook [1] proposed an expression for the equivalent fracture strain, which presents an exponentially decreasing shape with stress triaxiality. In the model, the effects of strain-rate and temperature are also included through two terms that

multiply the base triaxiality dependent term:

$$\bar{\varepsilon}_f = [D_1 + D_2 \exp(D_3 \eta)] \left[1 + D_4 \log\left(\frac{\dot{\bar{\varepsilon}}_{pl}}{\dot{\bar{\varepsilon}}_0}\right)\right] \left[1 + D_5 \left(\frac{T - T_{ref}}{T_m - T_{ref}}\right)\right] \tag{2.18}$$

where $\bar{\varepsilon}_f$ is the equivalent fracture strain, $\eta$ the stress triaxiality, $\dot{\bar{\varepsilon}}_{pl}$ the equivalent plastic strain-rate, $\dot{\bar{\varepsilon}}_0$ the reference strain-rate, $T$ the temperature, $T_{ref}$ the reference temperature, $T_m$ the melting temperature and $D_1$, $D_2$, $D_3$, $D_4$ and $D_5$ the parameters of the model. The material parameters $D_1$, $D_2$ and $D_3$ are calibrated from experimental tests by fitting the model equation to ($\eta$, $\bar{\varepsilon}_f$) pairs of fracture values obtained from at least three different geometries. The parameter $D_4$ controls the effect of strain-rate and $D_5$ the effect of temperature. $T_m$, $T_{ref}$ and $\dot{\bar{\varepsilon}}_0$ are defined as for the plasticity model described in Section 2.1.1.

Johnson and Cook proposed a linear accumulation of damage using Equation 2.12, and fracture occurs when the accumulated damage reaches a critical value of 1, i.e. when $\bar{\varepsilon}_{pl} = \bar{\varepsilon}_f$. The effects of the loading conditions are not included in this model, and neither the fracture by shear bands formation at low triaxiality. However, it is reasonably popular as it includes strain-rate and temperature effects, and it is implemented in most commercial FEM codes.

**Xue-Wierzbicki Model**

Xue and Wierzbicki [54] presented an equivalent fracture strain function that, apart from depending on stress triaxiality ($\eta$), also includes a deviatoric state dependence through the parameter $\xi$, which is related to Lode angle parameter ( $\xi = \frac{27}{2}\frac{J_3}{\bar{\sigma}^3}$ ). Thus, the intention is to reproduce in a more detailed manner the different triaxial stress states that the material can present under different loading conditions.

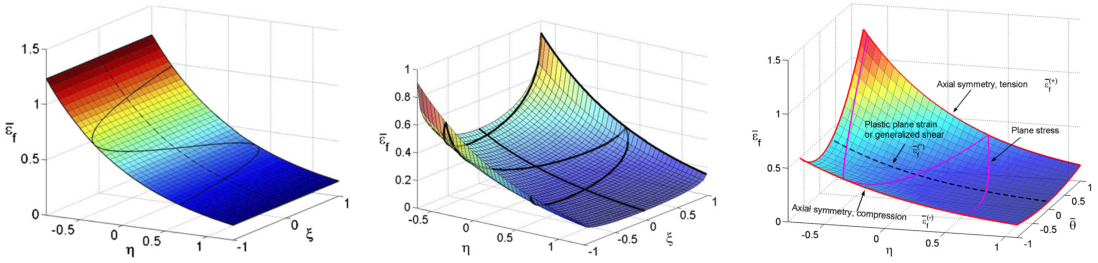
The model proposes that fracture strain as a function of stress triaxiality is bounded between an upper bound, which corresponds to the axsisymmetrical case ($\xi = 1$), and a lower bound, which matches the plane strain case ($\xi = 0$), as shown in Figure 2.5. Both bounds are proposed as exponential curves, each of them introducing two constants to the model. A function of elliptic form governs the difference in ductility between the upper bound and the real intermediate case ($\Delta\bar{\varepsilon}_f$), produced by the deviatoric parameter changing between 1 and 0. Solving that equation, and combining it with the upper and lower bound exponentials, Equation 2.19 is obtained for fracture strain:

$$\bar{\varepsilon}_f = f(\eta, \xi) = C_1 e^{-C_2 \eta} - (C_1 e^{-C_2 \eta} - C_3 e^{-C_4 \eta})(1 - \xi^{1/n})^n \tag{2.19}$$

where $n$ is the hardening exponent and $C_1$, $C_2$, $C_3$ and $C_4$ the four model parameters which have to be calibrated using a curve fitting process similar to that required for Johnson-Cook model.

Xue-Wierzbicki model is able to represent the fracture of different geometries under a wide range of stress triaxialities (from negative to positive values). Nevertheless, it also assumes a linear accumulation of damage (Equation 2.12), and therefore, the intermediate stages of damage are generally inaccurately predicted. The model proposed by Bai and Wierzbicki [55] uses a similar formulation but proposes an asymmetric 3D fracture locus in the space of fracture strain, stress triaxiality and Lode angle. The asymmetry in the Lode angle axis results in a different representation for tensile and compressive cases, as observed in the comparison of fracture loci of Figure 2.6.

As with the micromechanical damage modelling approach, many other models of increasing complexity have been proposed over the years. Some comparisons of fracture criteria have been performed in order to assess their relative accuracy [58,63,64]. Some other relevant phenomenological models are the modified Mohr-Coulomb fracture model proposed by Bai and Wierzbicki [65] or the fracture criterion designed for fracture forming limit diagrams proposed by Lou et al. [66].




**(a)** Johnson-Cook model **(b)** Xue-Wierzbicki model **(c)** Bai-Wierzbibki model

**Figure 2.6:** Comparison of the fracture locus predicted by three phenomenological fracture models in the space of stress triaxiality, Lode angle parameter and equivalent fracture strain ($\eta$, $\bar{\theta}$, $\bar{\varepsilon}_f$) [55].

#### 2.2.2.3 Continuum Damage Mechanics Models

The continuum approach to model damage is an alternative to micromechanical models in which the defects that appear within the metal matrix are not studied individually. Alternatively, damage is quantified throughout an internal constitutive variable of the material that measures the effects of irreversible processes within the microstructure. This modelling strategy lies between the micromechanics void models and the macromechanics phenomenological fracture criteria, since it is based on macroscopic considerations while it still calculates damage from internal variables. Continuum damage mechanics (CDM) foundations were defined for creep damage by Kachanov in 1958 [67,68], and extended afterwards to ductile damage by authors like Chaboche [69,70], Lemaitre [71,72] and Lemaitre and Desmorat [73].

CDM theory considers that load carrying capacity is reduced when internal damage appears, due to the volume occupied by voids and micro-cracks that produces a net reduction in material cross-section. The general anisotropic definition of damage is given by Equation 2.20:

$$D_{(\vec{n})} = 1 - \frac{\tilde{A}_{(\vec{n})}}{A_{0(\vec{n})}} = \frac{A_{voids(\vec{n})}}{A_{0(\vec{n})}} \tag{2.20}$$

where damage in the direction of vector $\vec{n}$ ($D_{(\vec{n})}$) is the ratio of cross-sectional area of a representative volume element (RVE) that is occupied by voids ($A_{voids(\vec{n})}$) and the total cross-sectional area ($A_{0(\vec{n})}$), as shown in Figure 2.7. If isotropic damage is assumed, the damage tensor is transformed into a scalar $D$ value (Equation 2.21).

$$D = 1 - \frac{\tilde{A}}{A_0} = \frac{A_{voids}}{A_0} \tag{2.21}$$

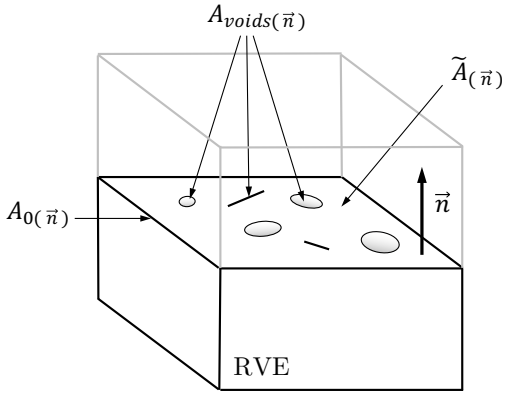



**Figure 2.7:** CDM definition of ductile damage on a representative volume element (RVE).

### Lemaitre model

The ductile damage model proposed by Lemaitre [74] is derived from the thermodynamics framework of irreversible processes of continuum damage mechanics. The state variables are firstly defined, being in this case damage the most important one, which represents the current status of the physical property. Then, the state potential is defined, from which the state laws can be obtained. Finally, the dissipation potential is defined, from which the evolution laws of the state variables related to the dissipation mechanisms can be derived. The isotropic definition of damage of Equation 2.21 is used in this model. In the constitutive equations, the effective stress tensor is used instead of the Cauchy stress tensor, in order to account for the macroscopic effect of damage

(Equation 2.22). The strain equivalence principle determines that this effective stress applied to the undamaged material would produce the same effects that the actual stress produces on the damaged material.

$$\tilde{\boldsymbol{\sigma}} = \frac{\boldsymbol{\sigma}}{(1-D)} \tag{2.22}$$

The integrated expression obtained for ductile damage under proportional loading conditions is the following:

$$D = D_{cr} \left[ \frac{\bar{\varepsilon}_{pl} \left[ \frac{2}{3}(1-\nu) + 3(1-2\nu)\eta^2 \right] - \varepsilon_{th}}{\varepsilon_f - \varepsilon_{th}} \right] \tag{2.23}$$

where $D_{cr}$ is the critical value of damage at fracture, $\bar{\varepsilon}_{pl}$ the equivalent plastic strain, $\nu$ the Poisson's ratio, $\eta$ the stress triaxiality, $\varepsilon_{th}$ the uniaxial damage threshold strain and $\varepsilon_f$ the uniaxial fracture strain. The model predicts no damage before the threshold strain is reached, and a linear accumulation afterwards until the fracture strain is reached.

Lemaitre model includes the effect of stress triaxiality, however, it has been proved that the cases of low triaxiality and shear are not properly represented by the original model [75], and modified models including a dependency on Lode parameter [75–77] and compressive damage [78] have been proposed. Other models follow the same methodology to represent exponential instead of linear damage accumulation, in order to achieve a better fit of the experimental measurents [79–83]. Models that consider the anisotropic definition of damage of Equation 2.20 have also been proposed [84].

**Bonora model**

Bonora (1997) [83] proposed a development of the Lemaitre CDM model described above. The procedure followed was analogous, however, the damage dissipation potential was modified, so that a damage exponent characteristic of each material ($\alpha$) was introduced in the formulation. The main objective of the model was to introduce a non-linear damage accumulation. The expression obtained for damage evolution in the case of proportional loading is the following:

$$D = D_0 + (D_{cr} - D_0) \left\{ 1 - \left[ 1 - \frac{ln(\bar{\varepsilon}_{pl}/\varepsilon_{th})}{ln(\varepsilon_f/\varepsilon_{th})} f(\eta) \right]^{\alpha} \right\} \tag{2.24}$$

where all the parameters and variables have the same meaning as in Lemaitre model [74] and additionally $D_0$ is the initial damage on the raw material and $\alpha$ the exponent of damage accumulation. If the equations of the model for the cases of uniaxial and proportional loading are compared, the following expression is obtained, which provides

the fracture plastic strain for varying stress triaxiality:

$$\bar{\varepsilon}_{pl,f} = \varepsilon_{th} \left[ \frac{\varepsilon_f}{\varepsilon_{th}} \right]^{1/f(\eta)} \tag{2.25}$$

This relationship was used in [85] to perform an analysis of the effects of stress triaxiality on fracture using the model.

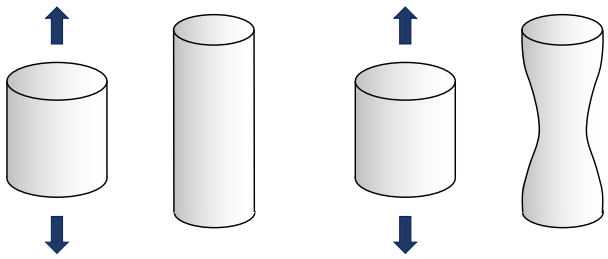
As in the Lemaitre model, the original Bonora model does not consider states of low stress triaxiality. A modification of the model has been proposed by Testa et al. to account for shear-controlled states introducing a dependency on Lode parameter [86].

## 2.3 Experimental Techniques

The conduction of laboratory experiments on specifically designed specimens is necessary throughout the whole process of materials characterisation. Firstly, for the understanding of the plastic and damage phenomena occurring within the material; secondly, to develop material models that take into account the findings about the material behaviour; and finally, to calibrate those models for a wide variety of materials. In this section, some of the techniques proposed for plasticity (Section 2.3.1) and ductile damage (Section 2.3.2) measurement are reviewed. Some of the experiments and techniques specifically developed for their application at high-speed conditions are also summarised in Section 2.3.3.

### 2.3.1 Tensile Testing

One of the first experiments that was developed to study the mechanical properties of engineering materials was the tensile test. A tensile load is applied to the material on a screw or servo-hydraulic driven machine, and the engineering stress and strain history is calculated dividing the load by the initial cross-section and the elongation by the initial gauge length. Plain round specimens are generally used for tensile tests, although flat specimens can also be used depending on the material an its application. Generally, a load cell is used to measure the load applied to the specimen, while the strain can be calculated using different techniques. The displacement of the machine cross-head can be used for an estimation of elongation, however, it is not very appropriate since the measurement includes the deformation of all the connected components of the load chain, and not only that of the gauge length of the sample. Generally, an extensometer attached to the sample is used for elongation measurement. Non-contact methods such as video extensometers and digital image correlation (DIC) techniques are also extensively used nowadays as an alternative to traditional extensometers.



**(a)** Uniform deformation **(b)** Real necking behaviour

**Figure 2.8:** Comparison of the uniform deformation assumption and the real behaviour used to calculate true stress - true strain.

Engineering values of stress and strain are obtained using the initial geometry of the sample, nonetheless, these are not representative when the specimen undergoes large plastic deformation. The traditional approach followed to consider geometrical changes estimates true values of stress and strain from the assumption of material uniform and uniaxial deformation ($\eta = 1/3$). This considers that a cylindrical specimen becomes longer and thinner with the applied load, as observed in Figure 2.8a, and allows for the calculation of true strain and true stress using Equations 2.26 and 2.27 respectively.

$$\varepsilon_T = \ln(1 + \varepsilon_e) \tag{2.26}$$

$$\sigma_T = \sigma_e(1 + \varepsilon_e) \tag{2.27}$$

where $\sigma_T$ and $\varepsilon_T$ are the true stress and strain, and $\sigma_e$ and $\varepsilon_e$ the engineering stress and strain. For most ductile metals though, the uniform deformation assumption is only valid up to a certain level of plastic deformation. At that point, plastic instability occurs and it triggers the formation of a neck on the specimen (Figure 2.8b). The assumption of uniform deformation is no longer valid, and the neck produces a multiaxial stress state, in which stress triaxiality increases as the neck becomes sharper ($\eta \geq 1/3$). For an accurate representation of stresses and strains from neck onset to fracture, the neck geometry has to be monitored and its effect accounted for.

The theory derived by Bridgman [87] can be used to obtain the true stress - true strain behaviour of the specimen up to fracture. From the minimum radius of the sample cross-section the average axial strain in the neck can be obtained using Equation 2.28, and the average stress with Equation 2.29:

$$\varepsilon_{zz,av} = 2\ln\left(\frac{a_0}{a}\right) \tag{2.28}$$

$$\sigma_{zz,av} = \frac{Load}{\pi a^2} \tag{2.29}$$

where $\varepsilon_{zz,av}$ and $\sigma_{zz,av}$ represent the average strain and stress accross the cross-section in the specimen axial direction, $a_0$ the initial cross-sectional radius and $a$ the current cross-sectional radius. Bridgman demonstrated that strain varies very little accross the neck even beyond necking [87]. Whilst strain remains uniform across the neck, stress presents a radial variation that has to be taken into account. The material deforms uniformly before necking, and therefore, stress is also uniform. However, when necking starts the stress distribution has to be corrected and the axial stress at any radial position of the cross-section can be obtained using Equation 2.30:

$$\sigma_{zz}(r) = \frac{\sigma_{zz,av}}{\left(1+\frac{2\rho}{a}\right)\ln\left(1+\frac{a}{2\rho}\right)}\left(1+\ln\left(\frac{a^2+2a\rho+r^2}{2a\rho}\right)\right) \tag{2.30}$$

where $\sigma_{zz}$ is the axial stress, $r$ the radial distance from the axis of the specimen, $\sigma_{zz,av}$ the average axial stress, $a$ the neck cross-sectional radius and $\rho$ the neck radius of curvature. If the radial position studied is exactly the centre of the cross-section, the maximum axial stress is obtained as shown in Equation 2.31:

$$\sigma_{zz,MAX} = \frac{\sigma_{zz,av}}{\left(1+\frac{2\rho}{a}\right)\ln\left(1+\frac{a}{2\rho}\right)}\left(1+\ln\left(1+\frac{a}{2\rho}\right)\right) \tag{2.31}$$

The expression obtained for the equivalent stress in the neck ($\bar{\sigma}$) following Bridgman approach is presented in Equation 2.32:

$$\bar{\sigma} = \frac{\sigma_{zz,av}}{\left(1+\frac{2\rho}{a}\right)\ln\left(1+\frac{a}{2\rho}\right)} \tag{2.32}$$

Maximum axial stress (2.31) and equivalent stress (2.32) expressions only depend on the geometry of the neck ($a$ and $\rho$) and the average axial stress.

### 2.3.2 Ductile Damage Quantification

The quantification of ductile damage is rather complicated since the degradation of the material is an internal phenomenon that cannot be directly measured using conventional sensors the same way stresses and strains are monitored. A number of damage measurement techniques have been proposed, generally implying the assessment of a physical property that is affected by damage, and from which damage evolution can later be derived. Lemaitre and Dufailly presented some of these methods in 1987 [88], and other authors have developed them since then. The most relevant experimental techniques are described below.

**Elastic Modulus Reduction**

This technique consists on the measurement of ductile damage evolution from the degradation that the elastic modulus undergoes due to the accumulation of voids. This method was firstly discussed by Lemaitre and Dufailly [88] and has afterwards been used by Bonora et al. [89–92] and Alves et al. [93, 94], among others.

Following the CDM methodology, the concept of strain equivalence states that the constitutive equations of the undamaged material are still valid for the damaged material if the stresses ($\boldsymbol{\sigma}$) are replaced by the effective stresses ($\tilde{\boldsymbol{\sigma}}$) of Equation 2.22. If this effective stress is introduced in the linear elasticity law of the material (Equation 2.2), the following expression is obtained for the uniaxial case:

$$\varepsilon_{el} = \frac{\tilde{\sigma}}{E} = \frac{\sigma}{E(1-D)} = \frac{\sigma}{\tilde{E}} \tag{2.33}$$

and the following relationship between damaged and undamaged elastic moduli can be derived:

$$D = 1 - \frac{\tilde{E}}{E} \tag{2.34}$$

where $\varepsilon_{el}$ is the elastic strain, $E$ is the undamaged elastic modulus and $\tilde{E}$ the damaged or effective elastic modulus.

From Equation 2.34, damage evolution can be obtained if the initial elastic modulus and its consecutively degraded values are known. To measure each of the damaged modulus values, the sample is initially loaded in tension until a certain value of plastic strain is reached. At that point, the specimen is partially unloaded and re-loaded, and the process is repeated with as many plastic strains as experimental points are desired. Hourglass shaped specimens are usually employed to concentrate damage in a small gauge region, where strain is measured using an extensometer or a small strain gauge. $\tilde{E}$ is obtained from the slope of the stress-strain curve for each of the unloadings. To avoid the non-linearities at both ends of the unloading-loading cycle, only the central region is considered for slope calculation and approximately 10% of the curve is removed at the top and bottom [88, 90, 95]. If strain gauges are utilized, they have to be replaced before they surpass their plastic strain limit. Up to 10 sets of strain gauges may be required when the tested material is very ductile, since their plastic strain limit is rarely higher than 10% [93]. Alternatively, if an extensometer is used, the test can be run without interruptions [92].

Care must be taken when using this method, since the changes in geometry of the specimen during the test have to be considered when calculating damage. If the cross-section reduction and the plastic necking of the specimen are not considered in the calculations, misleadingly high values of damage are obtained. The real damage is just a

small proportion of the value obtained, corresponding the rest to the stiffness loss caused by geometrical changes. Alves et al. performed some finite elements studies to quantify this effect [93], and Bonora et al. proposed a coupled experimental-FE methodology to remove the geometrical effects from the ductile damage calculation [92].

**Metallography Evaluation**

The study of micrographic pictures was mentioned by Lemaitre and Dufailly [88] as a method to measure damage by comparison of the area occupied by voids and micro-cracks and the total area observed. The area that corresponds to voids can be detected on the images by defining a greyscale threshold value. An estimation of damage can then be made using the CDM definition of damage (Equation 2.21). If pictures of the microstructure are taken systematically in a region of material, damage distribution maps can be obtained. The repetition of this procedure for different specimens deformed to increasing levels of plastic strain provides an estimation of the damage accumulation characteristic of the material.

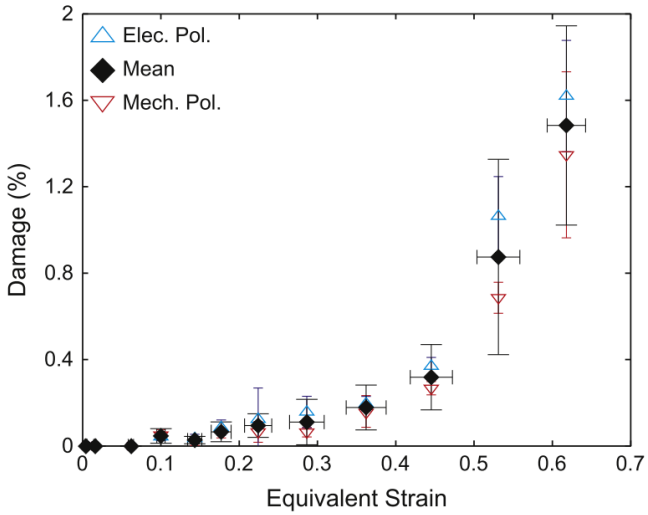



**Figure 2.9:** Damage vs. local equivalent strain results obtained by metallographic evaluation of mechanically polished and electropolished samples of a dual-phase 600 steel (figure from [96]).

The measurements can be taken using an optical or scanning electron microscope (SEM). The samples need to be cut and prepared for observation by mechanical polishing or electropolishing. Tasan et al. [96] considered the mean value in the cross-section as a measure of actual damage. As said before, this technique is quite easy to perform, however, it can be tedious and time consuming. It is reasonably adequate to characterise ductile materials [88] and, unlike most of the described techniques, it considers the micro-mechanical phenomena in the definition of damage. Nevertheless, its stat-

istical error can be high as the measurement region size decreases [96] (see results of Figure 2.9).

**Indentation Measurements**

Hardness evaluation by means of microindentation as a method to obtain damage has the same theoretical principles as elastic modulus reduction technique. The applied load and indentation depth are recorded throughout the test and from the unloading slope elastic modulus, and therefore, ductile damage can be obtained. The post-processing technique proposed by Oliver and Pharr [97, 98] is generally used to perform the calculations. The parameters involved in the indentation test are presented in Figure 2.10, where $S$ represents the initial unloading stiffness from which damage can be calculated using Equation 2.34.

The method was mentioned by Lemaitre and Dufailly [88], Guelorget et al. [99] used it to evaluate elastic modulus reduction and damage, Alves [94] and Tasan et al. [96] compared it with other damage measurement techniques and Zhang et al. [100] compared it with DCPD measurements. The method can be very accurate locally, making it powerful when localisation starts and other techniques lack of accuracy; nonetheless, it is quite tedious to perform due to sample preparation requirements and it is a destructive, and therefore, more expensive test.

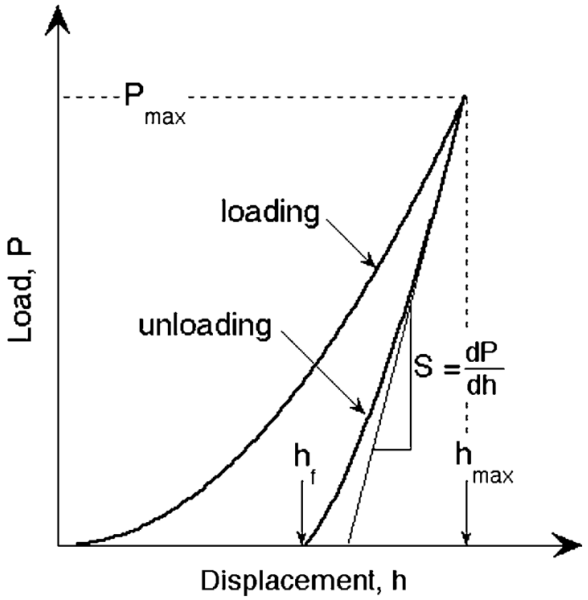



**Figure 2.10:** Load vs. indentation depth measurement in a hardness test and calcualtion of elastic modulus from the slope of the curve (figure from [98]).

**Ultrasonic Response Analysis**

The response of a material to input ultrasonic pulses can be used to investigate the density of voids and internal defects by the measurement of ultrasonic phase velocity or pulse attenuation. The elastic modulus of the material can be obtained from the values of longitudinal and shear wave velocity, which can be experimentally measured using longitudinal and shear ultrasonic transducers respectively, as exposed by Boccaccini and Boccaccini [101]. The longitudinal wave velocity in an isotropic linear elastic cylindrical medium can be expressed as:

$$v_L^2 = \frac{E}{\rho} \frac{1-\nu}{(1+\nu)(1-2\nu)} \tag{2.35}$$

Applying the previous equation to a damaged and undamaged material and substituting in Equation 2.34, the following expression for damage is obtained:

$$D = 1 - \frac{\tilde{\rho}\,\tilde{v}_L^2}{\rho\, v_L^2} \tag{2.36}$$

This method is mentioned by Lemaitre and Dufailly [88], but has not been largely applied to damage characterisation, although it could be promising specially because it is a non-destructive method. However, according to Jhang [102] the linear ultrasonic wave technology is able to detect big defects and cracks, nevertheless, it is not accurate enough to study evenly distributed damage in the form of small voids. While linear techniques measure damage using a propagating signal of constant frequency, in the non-linear case the input and output frequencies vary, being the difference caused by the interaction of waves with voids and other defects.

**CT X-Ray Evaluation**

X-ray micro-tomography technique can be used to obtain the internal volume of voids of a sample which has undergone a certain level of plastic deformation. The technique consists in taking 2D X-Ray scans of the sample from different circumferential positions, and through post-processing, reconstructing the internal 3D features of the sample to measure void density, average diameter or shape. Some practical recommendations about the use of CT technique can be found in [103].

Several studies have been performed using tomography, focused on measuring the evolution of void density and size. Generally, the results have been used to obtain void nucleation and growth laws, which are then used to calibrate micromechanical damage models [104–106]. A small volume located in the central region of the minimum cross-section of the sample is analysed, as it is the location with higher plastic strain and stress triaxiality. The size of the volume scanned is a trade-off between small enough

to obtain almost uniform strain and stress triaxiality conditions, and big enough to be representative of the phenomena taking place (the cubic volume of $\sim 400\mu m^3$ shown in Figure 2.11 has been used in [104, 105]).

A resolution of $1.6\mu m^3$ voxel size was achieved by Landron et al. [105], which is good to characterise relatively big voids. However, the resolution might not be high enough to capture the sub-micron voids that appear during the nucleation phase, considering that the feature should cover at least $2 \sim 3$ voxels in order to be detected. The technique is generally expensive and destructive, since the material has to be cut to a size small enough for the rays to penetrate through it. Nevertheless, it has great potential for the analysis of voids shape and size and for anisotropic damage characterisation.

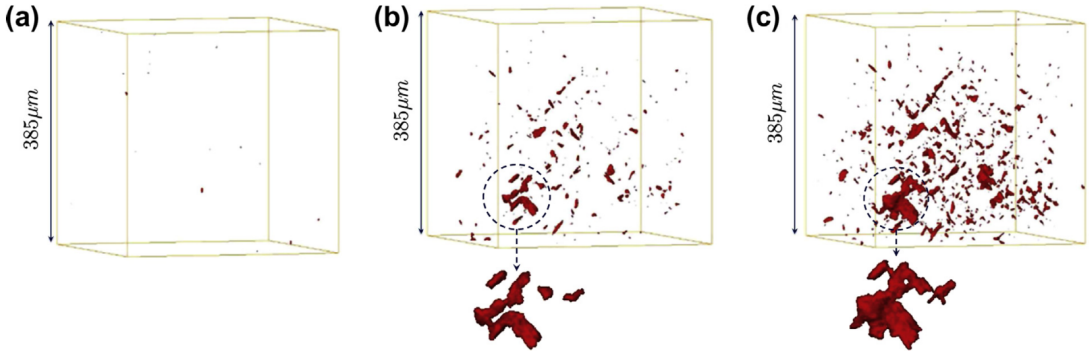



**Figure 2.11:** 3D void volumes of a high carbon steel grade obtained using CT X-Ray in-situ measurements at three different strain levels: (a) $\varepsilon = 0.02$, (b) $\varepsilon = 0.25$ and (c) $\varepsilon = 0.32$ (just before fracture), (figure from [104]).

### Potential Drop (PD)

The decrease of net cross-section generated by the appearance of voids produces an increase of the electrical resistance of the material. When a certain constant current is passed through the material, the increase of resistance (or decrease of voltage) can be monitored and ductile damage derived (Figure 2.12). The technique has been extensively used for crack detection and crack growth measurement in creep and fatigue [107]. It was presented by Lemaitre and Dufailly [88] as a method for ductile damage quantification. However, the area reduction produced by ductile damage is much smaller than that caused by macroscopic cracks, and it is difficult to obtain enough resolution to detect such small variations. The method has been used by different researchers [108–110]. Zhang et al. [100] combined the technique with DIC to derive the damage distribution along the whole sample gauge length.

Making use of the definition of electric resistance and Ohm's law for the undamaged and damaged material the following relationship can be obtained:

$$D = 1 - \frac{V}{\tilde{V}}\frac{\tilde{r}}{r} \approx 1 - \frac{V}{\tilde{V}} = 1 - \frac{R}{\tilde{R}} \tag{2.37}$$

where $V$ and $\tilde{V}$ are the original and damaged material voltage, $r$ and $\tilde{r}$ the original and damaged material resistivity and $R$ and $\tilde{R}$ the original and damaged resistance. The change in resistivity depends on the density variation of the sample, which is generally very small and whose effect can be neglected for small values of damage.

It is important to remark that the decrease of resistance is not entirely caused by ductile damage, in fact, most of the contribution comes from cross-section decrease and necking of the specimen. The geometrical changes have to be measured, their effect on resistance quantified and subtracted from the overall resistance decrease in order to obtain the actual ductile damage measurement. Some authors obtain the geometrical damage by interpolation [100], others from geometrical measurements or FE simulation [110] and others neglect this effect [109], yielding erroneous damage measurements.

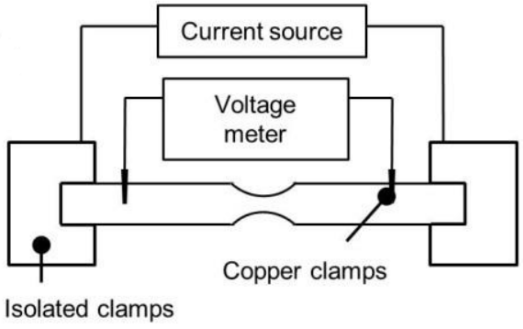



**Figure 2.12:** Diagram of the potential drop test arrangement (figure from [110]).

### Volume Variations

Some authors mention the measurement of volume or density changes as a theoretical option [88], but just a few have actually tried it to quantify damage. Tasan et al. compared this technique with other methods [96], concluding that the results present a very high scatter caused by small sample size and roughness differences. Variations of density have traditionally been measured using Archimedean principle based machines. Farris [111] considered a gas dilatometer to measure volume changes caused by internal porosity on elastomer materials. Other techniques based on a similar principle have also been tried, such as that used by Wu et al. [95], who considered full-3D DIC measurements to obtain the density decrease and ductile damage based on external geometry changes.

### 2.3.3 Temperature and High Strain-Rate Testing

Materials present different mechanical behaviour depending on their temperature of operation and the velocity of the applied deformation. Since properties such as yield condition, strain hardening, ductility or material degradation are affected by temperature and strain-rate, various conditions must be tested and accounted for when the material models are developed [112].

The temperature of the material during an experiment can be modified by running the test within an environmental chamber, or by heating or cooling the material externally (e.g. in an external oven or freezer). In the first case, the material is heated by convection from the surrounding air that at the same time has been heated, generally using electric resistors, or cooled, using nitrogen. If the external heating method is used, the test should be performed immediately after the sample is removed from the oven, otherwise the sample recovers quickly to room temperature by convection with the air and conduction with the holding tool. Therefore, this method is not valid for long tests, being only acceptable for very high speed automated tests. On the other hand, it allows to perform tests without the limitations that the use of an environmental chamber impose, such as restricted view for recording with cameras and lack of space to install additional equipment.

Different experimental techniques have been designed to cover the whole strain-rate range (Figure 2.13). For quasi-static tests a simple screw-driven universal testing machine is generally used, and strain-rates up to $10^{-1}$ $s^{-1}$ can be tested. Higher strain-rates in the dynamic range (up to $10^{3}$ $s^{-1}$) can be tested using the same machine technology but with servo-hydraulic power to deal with the faster response required. The tensile tests performed using these machines follow the theory already described in

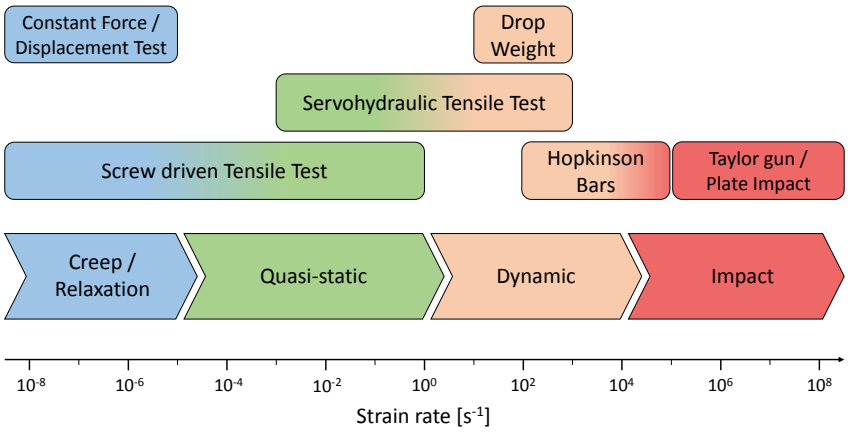



**Figure 2.13:** Experimental techniques used to test different strain-rate ranges.

Section 2.3.1. The Split Hopkinson Pressure Bar (SHPB) is another common technique used to characterise dynamic behaviour (strain-rates in the range $10^2$ $s^{-1}$ to $10^5$ $s^{-1}$) [113–115]. If even higher strain-rates need to be tested, gas gun experiments such as Taylor gun are required [116], with which strain-rates up to $10^6$ $s^{-1}$ can be obtained. Other experiments that fall in the ballistic tests region, such as flying plate, are able to produce even higher strain-rates. However, Taylor and the other tests that produce such high strain-rates are generally validation instead of calibration experiments, and the results are normally obtained from a few high-speed images or from the post-test analysis of specimens (geometry, hardness or SEM measurements).

Many difficulties appear when high-speed tests are performed, even if these are the most typical tensile tests. When a tensile load is suddenly applied at high speed it produces a stress wave that travels through the load chain of the machine and the specimen at the speed of sound. This wave can produce a stress spike in the material when the load is first applied, and subsequent oscillations when the wave travels back and forth in the specimen, causing an oscillation in the stress measurement known as system ringing. To counteract this phenomenon, loss motion devices are applied in order to accelerate the ram of the machine before applying the load to the sample; and also damping elements are introduced in the connections to avoid excessive ringing [117]. High-speed imaging is also an essential technology for high strain-rate testing, since strain measurements generally have to be taken using non-contact methods. Digital image correlation (DIC) and high-speed cameras technology developments have played a key role in the improvement of high strain-rate tests data acquisition and post-processing.

Additional information about these and other techniques for high strain-rate materials characterisation can be found in the review written by Field et al. [118]. It must be noted that most of the tests developed for high-speed conditions are focused on characterising the plastic response of the material, while not so many have been developed for damage quantification. The reason for that knowledge gap is the technical challenges that both investigations impose independently, and not many authors have attempted to combine them.

## 2.4 Summary

In this chapter a summary of the available literature relevant to the present work has been presented. Background on plasticity and ductile damage of metallic materials has briefly been introduced, addressing the main mechanisms of deformation and degradation, as well as the classic studies that deal with these phenomena. The fundamental modelling approaches have also been presented, and some key models have been

described and commented. Finally, the different experiments and techniques proposed to quantify the plastic and damage accumulation behaviours have been reviewed. The interest has been placed in giving an overall view of the modelling and testing approaches available, and focus on the cases that include strain-rate and temperature effects, which is the interest of this work.

The popular Johnson-Cook model [1] has been described for plasticity modelling, and three different approaches have been presented for damage modelling: micromechanics based, phenomenological and continuum damage mechanics. Johnson-Cook plasticity model includes the effects of strain-rate and temperature and its formulation is simple. Since the present work is focused on damage, this model has been considered adequate enough to represent plasticity without adding unnecessary complexity. Regarding damage, most of the models found in literature do not include strain-rate and temperature effects, Johnson-Cook fracture criterion being an exception [1]. Another limitation of most ductile damage models is that a linear accumulation of damage from yield to fracture is assumed, although it has been proved that the real case can be highly non-linear [83].

The experimental techniques to measure plastic strain and stress based on a tensile test are well understood, however, the region of material necking near fracture is very rarely studied, and inaccurate results are obtained if local measurements are not taken. For damage accumulation measurement many techniques based on monitoring the degradation of a physical property have been proposed. The application of some of them presents more difficulties than others, however, all of them are very sensitive and can easily lead to significant scatter in the results. The elastic modulus reduction technique is the most popular in literature, and produces accurate results if the changes in material geometry are accounted for [92]. No experimental study of ductile damage accumulation at high strain-rate conditions has been found in literature. The following chapters explain experimental methodologies and material models that have been developed to address the gaps in the understanding of ductile damage at high strain-rate and different temperatures.

# Chapter 3

# Methodology

## 3.1 Introduction

In this chapter, the baselines of the material characterisation procedure are explained. Firstly, the materials employed for the experimental tests are described (Section 3.2). A methodology for the experimental characterisation and modelling of isotropic ductile metals has been developed, in which three main aspects have been considered:

- The response in the plastic region has been taken into account through experimental measurements collected beyond the point of instability or necking.
- The effect of stress state has been considered when modelling ductile fracture under different stress triaxiality conditions.
- Finally, damage accumulation has also been included in the models, since the linear accumulation typically assumed in many models does not correspond to the experimental measurements observed.

In Sections 3.3-3.5 of this chapter a description of the experiments devised to characterise each of these three aspects is included, as well as the requirements and objectives of the tests. The aim of the project is also to apply the methodology presented in this chapter to different strain-rates and temperatures, in order to include these effects in the models. Although the tests performed are the same, a few variations have been necessary to obtain reliable results in challenging conditions such as high speed. The difficulties found and modifications required will be described in Chapter 4.

Finally, constitutive material models have been calibrated making use of the plasticity, ductility and damage accumulation results obtained experimentally at different conditions of strain-rate and temperature. Some of these models have already been

described in the Literature Review, and others have been developed as part of this research. The general methodology followed for the calibration of these models and their implementation in finite elements codes is depicted in Section 3.6.

## 3.2 Materials

The behaviour of two different materials has been investigated in the present work, one an austenitic 304L stainless steel and the other an electrolytic oxygen-free C110 copper. Both materials were supplied as drawn round bars with known composition and production processes. These materials were chosen since they are of interest to AWE Plc., but also because some of their properties are well documented in the literature and due to their high ductility, which makes them suitable for the development of plasticity and ductile damage models.

### 3.2.1 Austenitic Stainless Steel

Stainless steel 304L is an austenitic steel with very low carbon and high chromium and nickel contents with the S30403 UNS number. It is suitable for welding and has a very good corrosion resistance, making it appropriate for applications such as pressure vessels. Its chemical composition is summarised in Table 3.1 and has been obtained from ASTM A240/A240M standard [119], where it is specified along with its expected mechanical properties. The material was supplied by West Yorkshire Steel Ltd. in the forms of 16.2 mm diameter drawn bar and 4 mm rolled thick flat sheet. Some of the specimens were machined in the research workshop of the Department of Mechanical Engineering of Imperial College London and others in North Wales Aero Forms Ltd. Tensile tests have been carried out on the raw material to check its properties, providing a 0.2% yield strength of 514 MPa. The measured values are higher than those provided by the standard, since these are specified for the annealed condition, and the tested material has undergone a drawing process. Stainless steel 304L presents a FCC crystal structure. The material is well documented in literature and its typical properties can be easily compared and validated before moving to the more novel and complex experiments proposed in this work.

| Element | C | Mn | P | S | Si | Cr | Ni | N |
|---|---|---|---|---|---|---|---|---|
| Composition (%) | 0.030 | 2.00 | 0.045 | 0.030 | 0.75 | $17.5 - 19.5$ | $8.0 - 12.0$ | 0.10 |

**Table 3.1:** Stainless steel 304L chemical composition.

### 3.2.2 Electrolytic Tough Pitch Copper

Copper C110, with the C11000 UNS number and also designated as ETP (Electrolytic Tough Pitch) copper, is a high purity alloy with $> 99.90\%$ copper content and oxygen generally below 0.04%. It is one of the copper alloys most commonly used, mainly in electrical and electronic applications, due to its excellent conductive properties. Its chemical composition and mechanical properties are specified in ASTM B152/B152M standard [120]. The material was provided by Smiths Metal Centres in drawn condition in the form of 14 mm diameter bar. Some of the specimens were machined in the research workshop of the Department of Mechanical Engineering of Imperial College London and others in North Wales Aero Forms Ltd. Tensile tests have been carried out on the raw material to check its properties, and a 0.2% yield strength of 355 MPa has been measured. This material also presents a FCC crystal structure and has been widely studied in plasticity researches because of its softness and ductility.

## 3.3 Experimental Procedure for Plasticity Modelling

A conventional tensile test is usually performed to determine the elasto-plastic behaviour of materials, using an extensometer to measure elongation and a load cell to obtain load. The true stress - true strain performance of the material can then be derived from these measurements, assuming uniform deformation, using Equations 2.26 and 2.27 presented in Section 2.3.1 of the Literature Review. The values obtained following this procedure are generally accepted by the engineering community, nevertheless, they are only valid while the material deforms uniformly, which occurs only before localisation starts. As in this research the whole plastic region up to fracture is to be characterised, a method for the extraction of true stress - true strain in the whole plastic region, which is based on the monitoring of the neck geometry, has been developed. The aim is to measure the tensile and hardening behaviour of the material and use it for plasticity models calibration and to correct the geometrical effects when calculating damage. Figure 3.1 shows an example of the desired results compared to those calculated using the traditional Equations 2.26 and 2.27.

### 3.3.1 Test Description

True stress and true strain can be calculated from images of the sillouhete of a specimen during a tensile test. The pictures are taken throughout the test and used to measure geometrical parameters such as specimen cross-section and neck curvature, which are then used to calculate stress and strain applying the theory derived by

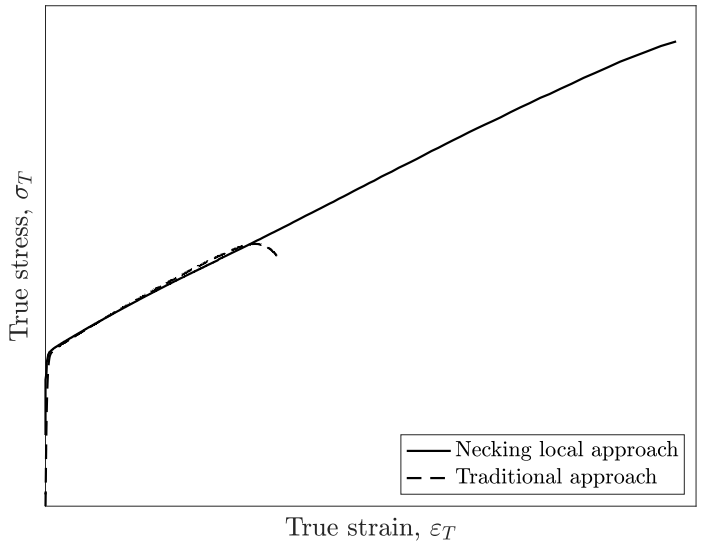



**Figure 3.1:** True stress - true strain ($\sigma_T$ - $\varepsilon_T$) measured using different methods.

Bridgman [87] that was introduced in Section 2.3.1. It must be noted that this method is only valid for materials with isotropic properties, since it assumes a radially uniform cross-section reduction and neck formation, and it extracts the geometrical parameters from pictures taken from just one direction.

The experimental arrangement required for the test can be observed in Figure 3.2 and consists of a camera recording the gauge region of the sample, and a source of light on each side of it. The camera is carefully focused using a flat sheet that is located where the specimen will later be placed, ensuring that the camera will be focused at the mid-plane of the specimen. By using a relatively large aperture (f/2), low exposure time (1/1000), low ISO (100), a focal length of 200 mm and an approximate distance to the sample of 600 mm the depth of field obtained is of 0.5 mm, which is very narrow but assures that a sharp representation of the specimen's profile is obtained. The camera setup must not be moved after it has been calibrated, since with the narrow depth of field used small changes in the distance to the sample would lead to unacceptably blurry specimen edges in the images.

The lamps are required since the settings of the camera used are meant to optimise the sharpness of the image sacrificing its brightness. They also increase the contrast between the specimen and the background, making it easier to extract accurately the external profiles when the images are post-processed. The specimen should be painted white to improve contrast, as well as to avoid reflections from its metallic surface. For

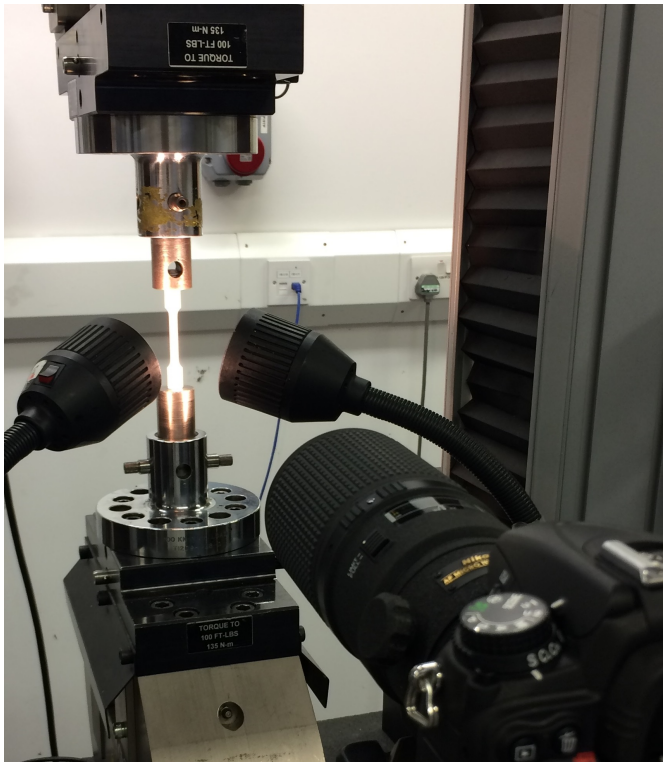



**Figure 3.2:** Experimental arrangement used for the specimen's neck geometry monitoring.

the profile extraction, an image thresholding method has been used (details about the image processing algorithms are available in Section 4.2.4).

With this set-up, the transition between the dark background of the image and the bright region of the sample presents only $2 \sim 3$ pixels of thickness with varying shades of grey, as observed in Figure 3.3. The equivalent size of each pixel can be obtained by comparison of the actual diameter of the sample with the number of pixels across the specimen before the test. In the case represented in Figure 3.3, which corresponds to one of the tests run in quasi-static room temperature conditions, the side of each pixel measures 7.8 μm. If 3 pixels of dimensional uncertainty are considered for the thresholding method, the error of the profile measurement would be $\leq 23.4$ μm, which can also be taken as the accuracy of the method if the camera has been properly focused.

An automated script has been created to extract the external profiles of the specimen in each picture after having applied the threshold to the image. From the profiles the minimum cross-sectional radius ($a$) and the fitted osculating circles' radii ($\rho$) can be determined, as observed in Figure 3.4. These parameters are also calculated automatically by the script for each image after fitting the profile points to the equation of a circle. The true strains are calculated with Equation 2.28, which makes use of

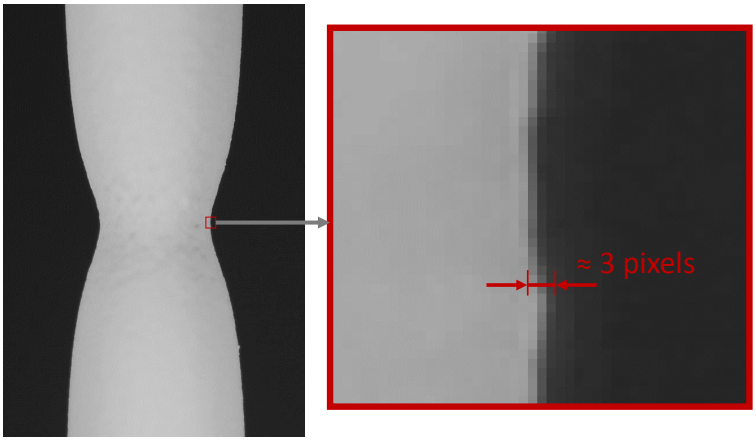



**Figure 3.3:** Accuracy of the neck monitoring technique, thickness of the grey transition between dark and bright pixels of the image.

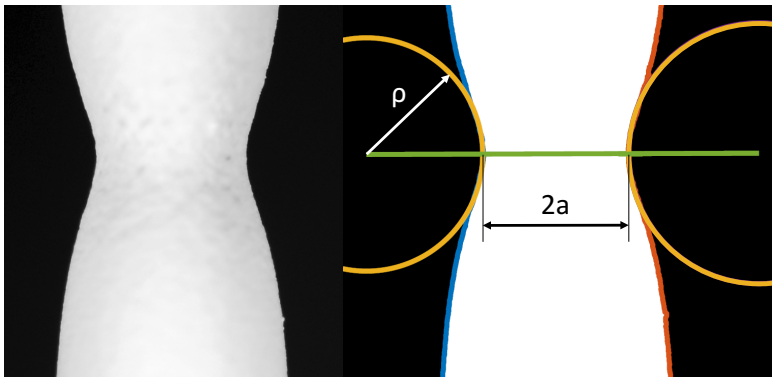



**Figure 3.4:** Necked specimen before and after applying the thresholding filter; the neck shape, minimum radius and osculating circles have been represented.

the monitored cross-section reduction. The stress parameter of interest for the present work is the equivalent stress in the neck, derived following Bridgman's approach [87] to obtain Equation 2.32.

### 3.3.2 Specimens Design

Round bar (RB) specimens (Figure 3.5) have been used to obtain the true stress - true strain behaviour of the materials by using the neck monitoring method. Additional tensile tests have been performed on hourglass round (HGR) specimens (Figure 3.6). The region of interest of these specimens is a central domain of uniform diameter where damage is concentrated when the sample is strained. The section then increases in a very smooth manner in order to minimise changes to the stress and strain fields, and

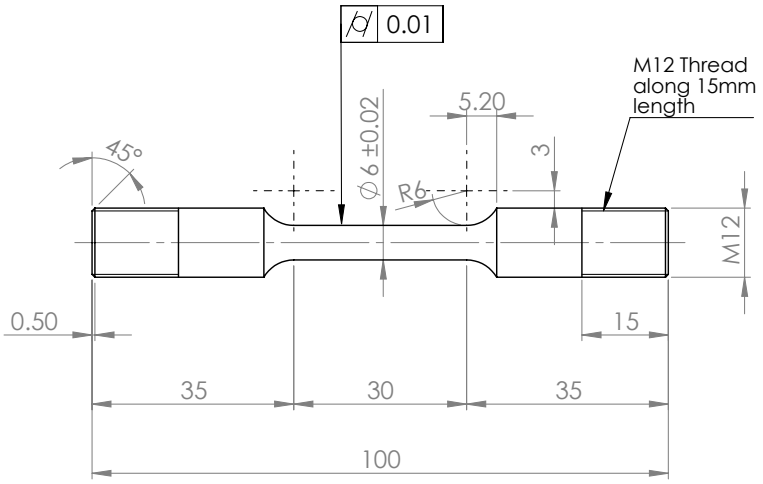



**Figure 3.5:** Round RB6 specimen geometry.

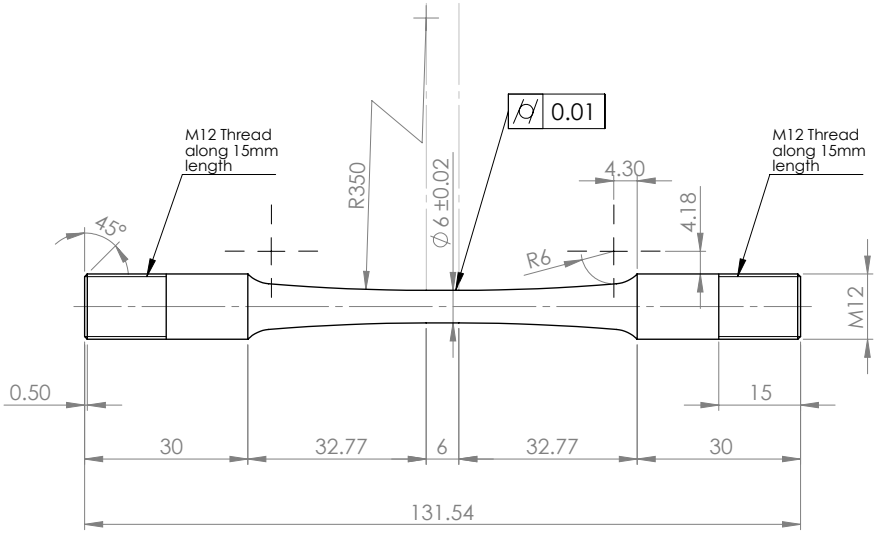
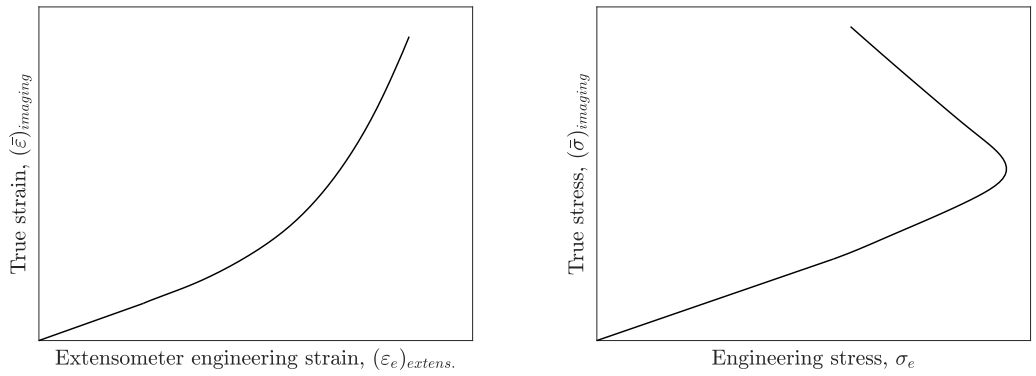



**Figure 3.6:** Hourglass round HGR6 specimen geometry.

keep them as similar as possible to the uniaxial case, but at the same time ensuring that necking, maximum damage and ductile fracture occur in the monitored section.

Strain has been measured in the central region using at the same time the proposed imaging technique and the conventional method with a clip gauge extensometer and Equations 2.26 and 2.27. By doing this, calibration curves for the necking effect correction, such as those of Figure 3.7, have been produced. Using these, the measurements of engineering stress and strain obtained from the extensometer and load cell can be corrected to calculate the true values of stress and strain. It can be observed in Figure 3.7b that the stress correction curve goes backwards in the abscissa axis. This




**(a)** Strain correction ($(\bar{\varepsilon})_{imaging}$ - $(\varepsilon_e)_{extens.}$). **(b)** Stress correction ($(\bar{\sigma})_{imaging}$ - $\sigma_e$).

**Figure 3.7:** Example of necking correction curves obtained from traditional and imaging methods.

occurs because the load measured by the load cell drops when necking occurs, and since Equation 2.27 considers only uniform deformation, a drop in engineering stress takes place. Nevertheless, the real local true stress increases further, since the neck produces a local cross-section reduction larger than the load drop, and therefore, the true equivalent stress calculated following Bridgman approach increases after necking. The point of the curve with highest abscissa corresponds to the UTS location and necking onset; after that point, increasing values of Bridgman equivalent stress are associated to decreasing values of traditional engineering stress. These curves will be used to account for the necking effects in the damage monitoring experiments described in Section 3.5.

## 3.4 Experimental Procedure for Ductile Fracture Modelling

Once the plasticity behaviour of the material is determined it remains the question of the conditions at which it fractures. A plasticity model represents mathematically the flow curve, such as that of Figure 3.1. Nevertheless, that equation can represent infinitely high values of strain, while the real material fractures when a certain level of plastic strain is achieved. A ductile fracture model is required so that when used in conjunction with a plasticity model it provides the operating limits of the material.

As described in Section 2.2 of the Literature Review, previous experimental studies confirm that the equivalent plastic strain at which the material fractures depends on the stress triaxiality ($\eta$) [1, 5, 6, 52, 53, 121] and on the Lode angle ($\theta$) [48, 55, 56, 63, 64, 122] (Equation 3.1).

$$\bar{\varepsilon}_{pl,f} = f(\eta, \theta) \tag{3.1}$$

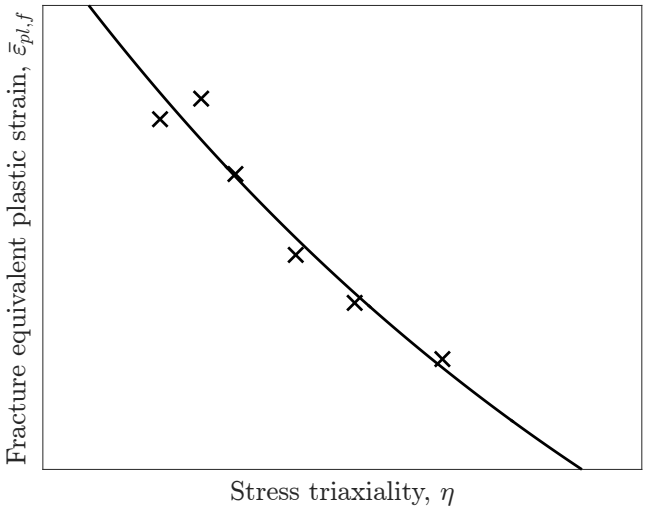



**Figure 3.8:** Fracture equivalent plastic strain - stress triaxiality ($\bar{\varepsilon}_{pl,f}$ - $\eta$) analysis of RNB specimens.

Since the characterisation of the effects of these two parameters on the fracture equivalent plastic strain requires an enormous number of tests, only the effect of stress triaxiality has been considered in this research. The implications of different loading conditions through the Lode parameter should be studied experimentally in the future and included in the models. The aim of the experiments described in this Section is to study the effect of stress triaxiality on fracture equivalent plastic strain, which has been achieved by running tensile tests to fracture on notched specimens. Different notch geometries have been tested to produce different states of stress triaxiality and obtain the desired results of fracture equivalent plastic strain versus stress triaxiality, similar to those of Figure 3.8. These data can later be used to calibrate models of the form of Equation 3.2.

$$\bar{\varepsilon}_{pl,f} = f(\eta) \tag{3.2}$$

### 3.4.1 Test Description

Tensile tests are run on round notched specimens with samples presenting different notch geometries. This type of experiment has widely been used in the past for the measurement of fracture equivalent plastic strain of materials [1, 58, 123–125], nonetheless, its combination with the imaging technique described in Section 3.3.1 gives additional information that generally is not available. The experimental procedure followed for these tests is the same as the one previously described for plasticity modelling.

The evolution of the specimen's external geometry is monitored using the imaging technique and measuring, in this case, the progression of the notch instead of the development of the neck. In the traditional fracture experiments, only the final plastic strain is obtained by measuring the diameter of the fractured specimen after the test and using Equation 3.3:

$$\bar{\varepsilon}_{pl,f} = 2\ln\left(\frac{a_f}{a_0}\right) \tag{3.3}$$

where $\bar{\varepsilon}_{pl,f}$ is the fracture equivalent plastic strain and $a_0$ and $a_f$ the initial and final notch cross-sectional radii, respectively. With the proposed arrangement the geometry of the notch can be measured throughout the test and this allows for two improvements to the experiment:

- **The evolution of strain is calculated as well as the final fracture strain.** Plastic strain can be calculated at any point using the notch geometry and Equation 2.28, while the fracture strain can be obtained from Equation 3.3 using the geometry from the last picture of the specimen before fracture. This provides a measurement of $\bar{\varepsilon}_{pl,f}$ that can be used on its own or for validation of the traditional ex-situ measurement.
- **The evolution of stress triaxiality is calculated.** Different notch geometry designs produce different stress triaxialites, nevertheless, this value varies through the test, generally increasing as the notch plastifies and becomes sharper. For the models calibration, single values of stress triaxiality have to be associated to each fracture equivalent plastic strain (Equation 3.2 and Figure 3.8). In some cases a constant stress triaxiality for the test equal to its initial theoretical value is assumed ($\eta = \eta_0$); other authors use a constant final value obtained from geometrical measurements of the fractured specimen ($\eta = \eta_f$) [1]; and others consider the average value of triaxiality throughout the test (Equation 3.4) [58]. This last case is considered to be the most accurate representation, since it takes into account all the different stress states of the material in a weighted manner instead of just a single condition. In literature, the evolution of stress triaxiality has been estimated with finite elements models calibrated using the initial and final states of the test [58]; the present research obtains the same information directly from experimental measurements, calculating the evolution of stress triaxiality ($\eta(\bar{\varepsilon})$) from the evolution of the neck geometry using Bridgman theory.

$$\eta_{av} = \frac{1}{\bar{\varepsilon}_f}\int_0^{\bar{\varepsilon}_f} \eta(\bar{\varepsilon})d\bar{\varepsilon} \tag{3.4}$$

Apart from using the described imaging method, in this work the fracture equivalent plastic strain has been measured following the traditional technique. A Starret HE400 optical comparator or shadowgraph has been used to measure the geometry of the

fractured specimens, as observed in Figure 3.9. This equipment uses a dual mirror design for high precision correction of the shadow produced by the specimen from which the diameter is being measured. A few diameters have been measured for each specimen in order to check the isotropy of the material, and their average value has been used for the fracture strain calculation.

### 3.4.2 Specimens Design

Round notched bar (RNB) specimens have been used for this analysis. Equation 3.5 can be derived from Bridgman's theory [87] and provides the initial value of stress triaxiality in the minimum cross section of the sample as a function of the geometry of the notch:

$$\eta_{th} = \frac{\sigma_H}{\bar{\sigma}} = \frac{1}{3} + \ln\left(1 + \frac{a}{\rho}\right) \tag{3.5}$$

where $\eta_{th}$ is the initial or theoretical stress triaxiality, $\sigma_H$ the hydrostatic or mean stress, $\bar{\sigma}$ the equivalent von Mises stress, $a$ the cross-sectional radius in the notch and $\rho$ the radius of curvature of the notch.

Different notch geometries have been tested to represent various states of stress triaxiality. Figure 3.10 represents the specimen with a notch of 5 mm minimum diameter and 3 mm notch radius of curvature as an example, while drawings of the rest of RNB specimens can be found in Appendix A.1. Table 3.2 summarises the geometry of all the specimens considered for the ductility analysis, as well as the theoretical stress triaxiality produced in each case, calculated from Equation 3.5. The uniaxial case of the round bar (RB) specimen presented in Section 3.3.2 has also been included in the table, as it can be studied as the extreme case of a RNB specimen with a notch of infinite radius of curvature. This geometry produces an initially uniaxial stress state ($\eta_{th} = 1/3$) that increases when the neck appears.

| Specimen geometry | Notch acuity, $a/\rho$ [-] | Curvature, $\rho$ [mm] | Diameter, $2a$ [mm] | Theoretical triaxiality, $\eta_{th}$ [-] |
|---|---|---|---|---|
| RB6 | 0 | $\infty$ | 6 | 0.333 |
| RNB6-1 | 0.25 | 8 | 4 | 0.557 |
| RNB6-2 | 0.313 | 8 | 5 | 0.605 |
| RNB6-3 | 0.417 | 6 | 5 | 0.682 |
| RNB6-4 | 0.833 | 3 | 5 | 0.940 |
| RNB6-5 | 1.25 | 2 | 5 | 1.144 |
| RNB6-6 | 2.5 | 1 | 5 | 1.586 |

**Table 3.2:** Geometry and stress triaxiality of the specimens used for plastic fracture analysis.



**(a)** Optical comparator with fractured specimen mounted.



**(b)** Detail of the specimen being measured.

**Figure 3.9:** Shadowgraph equipment used for post-fracture neck geometry measurement.

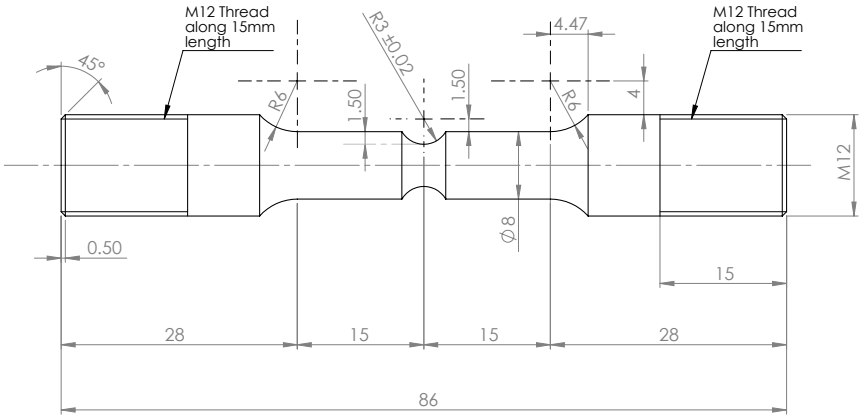



**Figure 3.10:** RNB6-4 specimen geometry ($2a = 5$ mm, $\rho = 3$ mm).

## 3.5 Experimental Procedure for Ductile Damage Modelling

After the plasticity and ductility behaviours are determined the stress - strain performance is known, as well as the moment when the material fractures. Nevertheless, as it has been explained in Section 2.2, ductile materials develop damage in the plastic region before the actual fracture occurs. This is caused by the voids and microcracks that affect the strength of the material. Many models ignore the material degradation

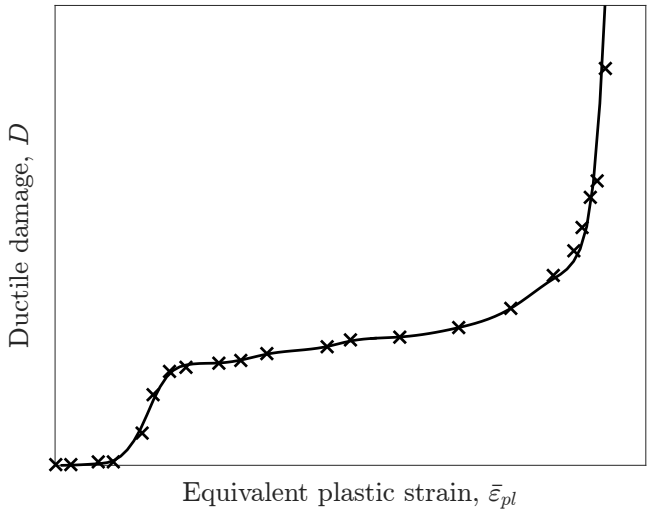



**Figure 3.11:** Ductile damage accumulation - equivalent plastic strain ($D$ - $\bar{\varepsilon}_{pl}$).

prior to fracture, while others assume a linear accumulation of damage, which are not adequate manners of modelling damage, especially for very ductile materials.

In the proposed methodology, damage is measured at different levels of plastic deformation of the material, and that information is used to construct a curve of damage accumulation from onset until final fracture, as observed in Figure 3.11. The purpose is to use this information to incorporate a realistic representation of damage accumulation and material degradation in the constitutive models.

### 3.5.1 Test Description

In order to measure damage accumulation, the elastic modulus reduction method has been used. The technique was already introduced in Section 2.3.2 and consists of a tensile test which, instead of running continuously up to fracture, is stopped at different plastic strain stages, where a partial unloading and reloading cycle is performed. This process is exemplified in Figure 3.12. From the slope of each of the unloading cycles the damaged or effective elastic modulus ($\tilde{E}$) can be obtained, and from this parameter the value of ductile damage can be calculated following the continuum damage mechanics definition (Equation 2.34).

In this case, there is a considerable difference between the tests performed at quasi-static strain-rate and the high-speed tests. While for the slow tests all the loading-unloading cycles are conducted in a continuous test, for the the high-speed case interrupted tests are performed, and the damage measurements are taken separately.

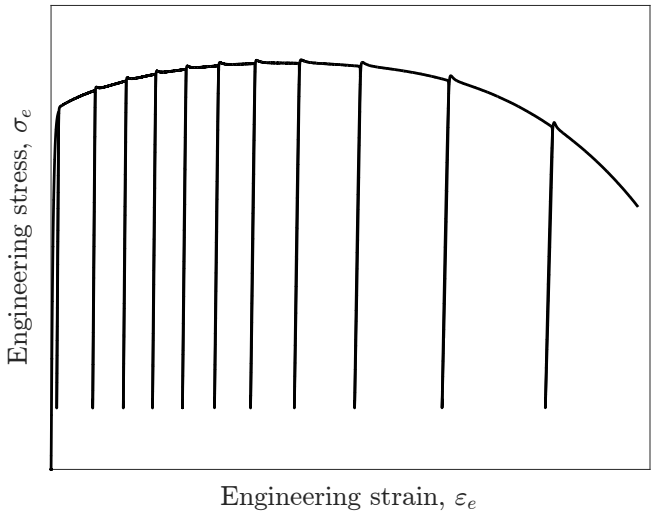



**Figure 3.12:** Engineering stress - engineering strain ($\sigma_e$ - $\varepsilon_e$) of a tensile test for elastic modulus monitoring.

Details about both methods and the reason for this difference can be found in Section 4.2: Strain-Rate Considerations.

No matter if damage is measured in a continuous test or externally, an extensometer of 6 mm gauge length and 100% tensile travel has been used to measure strain in the gauge region (Figure 3.13). As described in Section 2.3.2, in the past the use of strain gauges was the most extended approach to monitor strain for the purpose of elastic modulus calculation [83, 88, 93]. Nevertheless, these are rarely able to measure more than 10% plastic strain before failing and, therefore, several test interruptions and gauge replacements are required if a continuous test is desired, losing the origin of strain measurement and introducing possible inaccuracies to the process. The proposed alternative method can be performed in a continuous manner and reduces considerably the test duration, the specimens preparation complexity and the potential imprecision of strain gauges replacement.

The local strain measurements obtained with the clip gauge extensometer have been used to create curves like that of Figure 3.14, which shows an unloading and reloading cycle. As observed, the cycle presents a small amount of hysteresis produced by the energy dissipated in the unloading-reloading process. This elastic process should imply no energy dissipation, however, a small quantity is lost probably due to anelastic behaviour, generated heat and slight reverse cycling at the bottom of the cycle. For the modulus calculation the unloading measurements have been used, as suggested in [15], but the difference if the reloading data would have been employed would be minor.

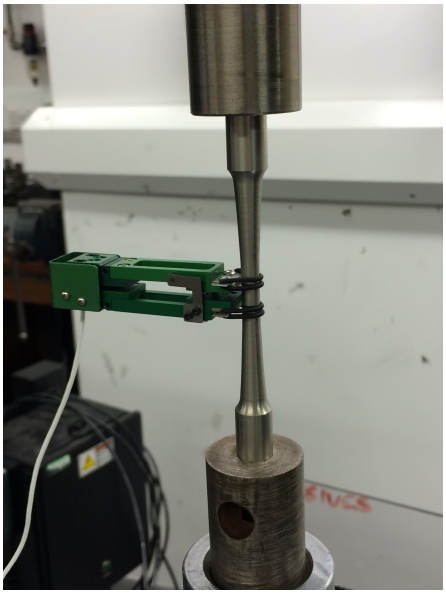


**Figure 3.13:** Experimental setup used for damage monitoring on a HGR6 specimen.

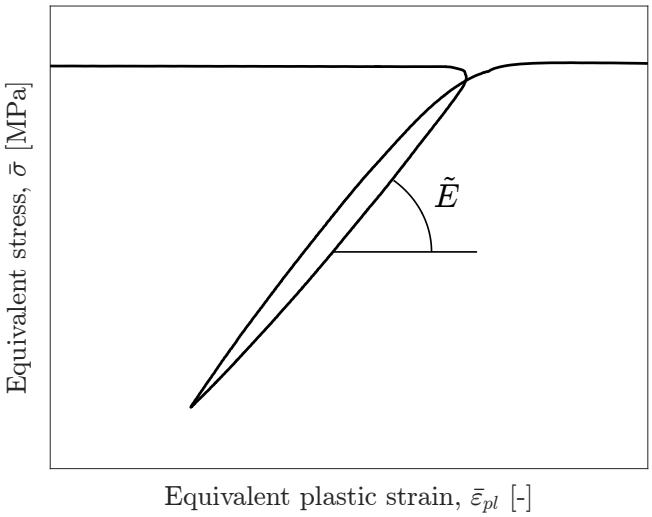



**Figure 3.14:** Equivalent stress - equivalent plastic strain ($\bar{\sigma}$ - $\bar{\varepsilon}_{pl}$) of one unloading-reloading cycle.

The top and bottom 20% data of each unload cycle have been omitted due to the non-linearities in the extremes. The central data has been fitted to straight lines to extract elastic modulus values from their slope. By comparing this effective modulus with the initial value, ductile damage can be calculated from Equation 2.34.

A script has been written to automatically extract the unloading cycles and calculate elastic modulus and damage at each plastic strain step. The effects of cross-section

reduction and necking have been taken into account by correcting the raw engineering stress - strain data measured in this test. For that purpose, the calibration curves obtained from the plasticity analysis have been used (Figure 3.7).

### 3.5.2 Specimens Design

Hourglass shaped specimens have been used for the damage monitoring experiments. These were already introduced in Section 3.3.2 for plasticity measurement (Figure 3.6). As explained in that section, their purpose is to concentrate the maximum damage in the central smooth region of the specimen, without affecting the stress and strain fields. The length of the gauge region has been fixed at 6 mm to match the size of the gauge length of the clip gauge extensometer used. The rest of the geometry has been designed considering suggestions from previous investigations [90, 92, 94].

A flat hourglass specimen has also been designed with exactly the same dimensions in the gauge region (6 mm width x 6 mm length), but with 3 mm thickness (Figure 3.15). This geometry was initially explored for alternative damage measuring techniques, such as using DIC instead of an extensometer for strain measurement. The majority of this research has been conducted using round hourglass specimens, however, some results on flat specimens have also been included in Section 5.4.2 for comparison purposes.

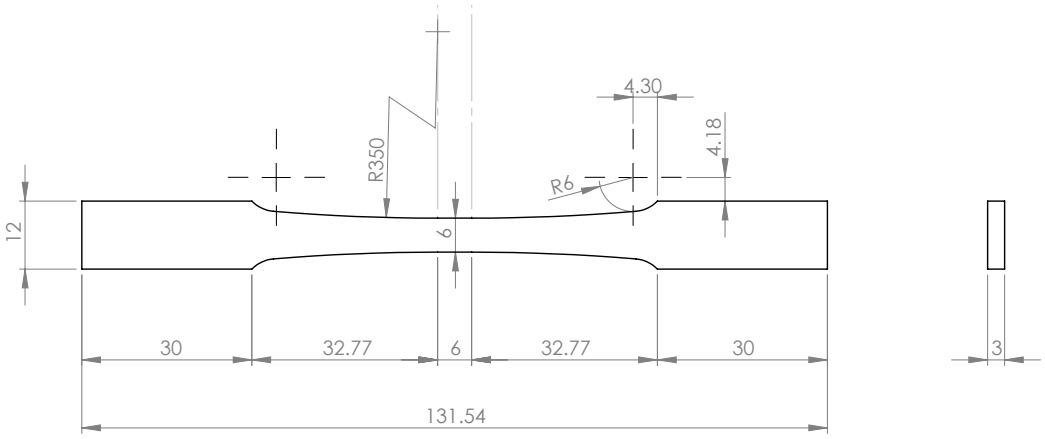



**Figure 3.15:** HGF6 specimen geometry.

## 3.6 Material Modelling and Implementation in Finite Elements

The experimental results obtained with the previously described techniques have been used to calibrate plasticity, ductile fracture and ductile damage accumulation models. The analysis of the models' calibration process and the development of new models when necessary is explained in Chapter 8. In this section, the methodology followed to calibrate the models is explained, as well as to assess the quality of the fit and to implement the models in finite elements codes using user material subroutines.

### 3.6.1 Model Parameters Calibration

The calibration of the models has been performed by means of least-square fit algorithm scripts that have been programmed in Matlab. For the calibration, results from various tests in different conditions have been used at the same time, each of them presenting dissimilar data sampling rate. The results have been processed and the sampling rate normalised, so that all the tests at different conditions have the same weight when the model is calibrated. The outcome after the calibration has been in all cases the numerical values of the model parameters. In some cases, the model parameters have been obtained directly using at the same time the data collected from all the tests at different strain-rate and temperature conditions. For other models, a separate fit of the standard conditions, the effects of strain-rate and the effects of temperature has been required, in order to achieve a better fit.

If different equation fit methods have been used, or if different models have been compared, values of coefficient of determination ($R^2$) have been obtained for model fit quality comparison. Statistically, this parameter represents the proportion of the variance in the independent variable that is predictable from the independent variables. It is calculated using Equation 3.6, which represents the ratio between the sum of squares of residuals and the total sum of squares. In practice, a value of $R^2 = 1$ means a perfect model fit, and the lower the $R^2$ value the worse the fit.

$$R^2 = 1 - \frac{SS_{res}}{SS_{tot}} = 1 - \frac{\sum_i^n (y_i - Y_i)^2}{\sum_i^n (y_i - \bar{y})^2} \tag{3.6}$$

where $SS_{res}$ is the sum of squares of residuals, $SS_{tot}$ the total sum of squares, $y_i$ the measured data points, $Y_i$ the values predicted by the model in the same abscissa locations and $\bar{y}$ the mean of all the measured data points, where $i = 1, ..., n$.

### 3.6.2 Finite Elements Material Subroutines

Although a thorough finite elements study has not been performed, the models developed in this work have been coded and tested in user subroutines so that they can be applied in the future. The software considered are Abaqus/Standard and Abaqus/Explicit for the quasi-static and high strain-rate cases, respectively. The number of plastic and damage models available in the libraries of Abaqus is limited, nevertheless, it includes the possibility of user models implementation by means of user material subroutines (UMAT for Abaqus/Standard and VUMAT for Abaqus/Explicit), in which the material constitutive equations can be coded. In a simulation these equations are solved iteratively to obtain the increments of flow stress, equivalent plastic strain and other state variables for each calculation point of the mesh at each time step, making use of the total strain increments in the integration points solved by the FE code. Apart from stresses and strains, user defined state variables can be implemented in the material subroutine, e.g. to represent damage accumulation. It must be noted that the implementation of a coupled damage model using a UMAT/VUMAT requires unavoidably that the elasto-plastic calculations are also solved using the subroutine. When Abaqus reads a UMAT/VUMAT it understands that the constitutive equations have to be solved using the subroutine, and it jumps the in-built material calculations. The material model subroutines of the models discussed in Chapter 8 have been coded in Fortran and are available in Appendix C.

Although Johnson-Cook plasticity model is available in the library of Abaqus in-built models, UMAT and VUMAT subroutines with the same formulation and also including the proposed damage models have been written. In Figure 3.16 the plasticity performance of both the in-built and the subroutine Johnson-Cook models are compared. As it can be observed, the results are coincident, validating the plasticity calculations of the subroutine.

From a formulation point of view, the elastic and plastic strain-rates have been considered to be additive (Equation 2.1). The equivalent plastic strain increments have been calculated using elastic predictor - radial return algorithm with Newton numerical method for non-linear equations solving [126]. The material temperature change is calculated within the UMAT/VUMAT by assuming adiabatic conditions. This implies no heat transfer between elements and is the same approach followed in the formulation of the in-built Johnson-Cook model in Abaqus. Adiabatic heating is used with Johnson-Cook model since it is generally used for high-speed events, where there is no time for heat conduction to the surrounding material. The temperature rise is calculated using Equation 3.7 and updated for the flow stress calculation:

$$\Delta T = \frac{\mu \Delta \bar{\varepsilon}_{pl}}{2\rho C_p}(\sigma_{old} + \sigma_{new}) \tag{3.7}$$

where $\Delta T$ represents the temperature increment, $\Delta\bar{\varepsilon}_{pl}$ the equivalent plastic strain increment, $\mu = 0.9$ the fraction of plastic energy transformed into heat, $\rho$ the density, $C_p$ the specific heat and $\sigma_{old}$ and $\sigma_{new}$ the stresses of the previous and current steps.

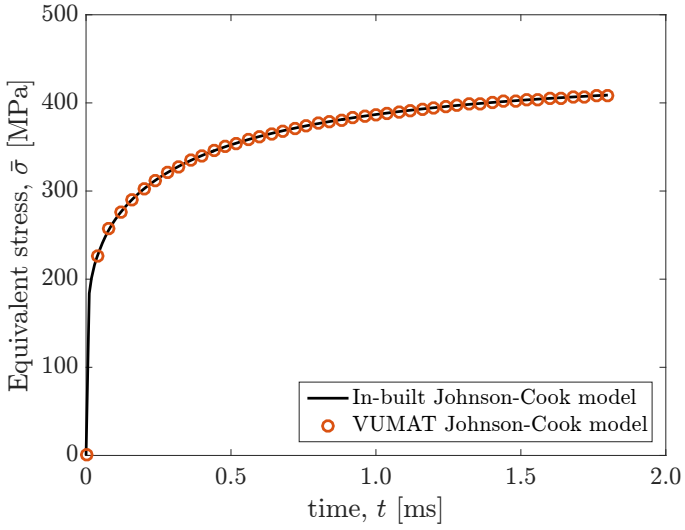



**Figure 3.16:** Equivalent stress - time ($\bar{\sigma}$ - $t$) obtained using in-built and VUMAT Johnson-Cook plasticity models [1].

The damage increment is calculated in each step using the damage model equations and added to the accumulated damage of the calculation point, which is stored in a state variable. The elastic modulus of the material is updated with the new effective modulus ($\tilde{E}$) that has been updated following the continuum damage definition (Equation 2.34). This effective modulus is then used for the stress and strain calculation in the following time step. The state variable containing the accumulated damage is checked at the end of every step, and if its value surpasses the critical damage, it is considered that the calculation point has failed, and the element is removed from the simulation to represent the complete loss of load carrying capacity.

# Chapter 4

# Strain-Rate and Temperature Considerations

## 4.1 Introduction

The methodology based on three experiments (plasticity, fracture and damage) described in the previous chapter has been developed for standard conditions of room temperature and quasi-static strain-rate. However, one of the interests of this research is to apply that methodology to different test speeds, in order to study the effect of strain-rate and include it in the modelling. For most of the experiments, three strain-rates have been analysed: the standard quasi-static conditions ($\dot{\varepsilon} \sim 10^{-3}$ s$^{-1}$), intermediate strain-rate ($\dot{\varepsilon} \sim 10^{2}$ s$^{-1}$) and high strain-rate ($\dot{\varepsilon} \sim 10^{3}$ s$^{-1}$). Although the experiments and their purpose is the same for the three velocities, some modifications have been required to obtain useful results, especially at the highest speeds. The specific requirements of the high strain-rate tests, the equipment used for the different experiments, as well as the methods designed to overcome the challenges are described in Section 4.2.

The effects of varying the temperature of the tests from the standard room temperature ($T \sim 20$°C) to relatively high temperature ($T \sim 180$°C) and considerably low temperature ($T \sim -80$°C) have also been experimentally assessed. The modifications required to apply the proposed methodology to different temperatures are outlined in Section 4.3.

## 4.2 Strain-Rate Considerations

Material characterisation experiments are generally performed in quasi-static conditions, i.e. at speed slow enough that each time instant can be approximated to a static loading case. The reason for testing in those conditions is to remove the dynamic effects that arise when the material is deformed faster. Nevertheless, the static case is not representative of many engineering applications, and for the design of some components those dynamic effects have to be considered. The most typical dynamic loading case is vibrations analysis, which produces fatigue in the materials and generally appears in machines with moving parts. The other dynamic loading case is the deformation at very high speeds, generally caused by impact or blast loading, which is the deformation and failure case analysed in this research. The experimental results obtained from the strain-rate analysis described in this section will be presented in Chapter 6.

### 4.2.1 High-Speed Tests Considerations

While quasi-static tests are well understood and standardised, high-speed tests imply overcoming some challenges if measurements of a similar quality are desired, involving generally particular modifications for each test. The following are the main challenges that have been faced when applying the methodology described in Chapter 3 to high-speed conditions:

- **System ringing.** Stress waves travelling through the material at speed of sound usually produce dynamic ringing in the load measurements [117]. This ringing or oscillation phenomenon occurs when the load is initially applied at high speed, producing a high amplitude stress wave when the elements enter into contact. This complicates the extraction of smooth results and makes it necessary to apply filtering to the raw data, although some properties might be difficult to estimate depending on the degree of oscillation of the load trace (see Figure 4.1). The oscillation is highly dependent on the load chain arrangement; it is more pronounced when the load cell is located far from the specimen and accentuated by threaded connections, therefore, the specimen has been located as close as possible to the load cell and damping has been introduced in the joints. This has been attained by placing rubber washers to decrease the ringing without affecting the measurement of material properties.
- **Stress spikes.** Stress spikes of very high magnitude and short duration may appear at the beginning of the test. These are caused by the sudden acceleration of the machine to very high speeds and the subsequent stress wave produced. If these unusually high values of stress are not taken into account samples may fail prematurely in an apparently brittle manner or equipment may be damaged. This

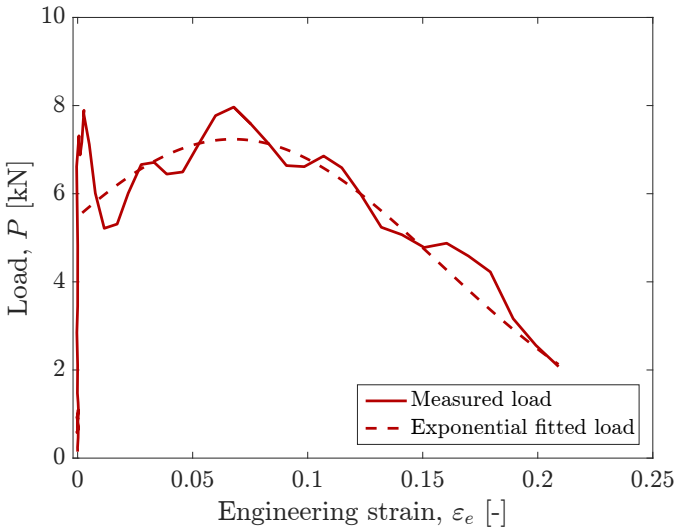



**Figure 4.1:** Load - engineering strain ($P$ - $\varepsilon_e$) measured in a high-speed tensile test ($v \approx 17$ m/s).

phenomenon can be observed at the beginning of the plastic region in Figure 4.1. To limit the stress spikes, an acceleration ramp has been introduced in the high-speed experiments instead of applying the desired value instantaneously.

- **Load capacity.** The tensile machines and load cells used for high-speed testing have lower load capacity than the quasi-static equipment. In this research, the limiting load in quasi-static conditions is around 250 kN, while for high speed this value is around 12 kN. This lower limit has required the samples to be scaled down, the dimensions of the round specimens used are summarised in Table 4.1 and drawings can be found in Appendix A.1. It must be noted that the notches of RNB specimens have been scaled down maintaining the same theoretical stress triaxiality.
- **Strain measurement.** While in low-speed tests strain is generally measured using extensometers or strain gauges, non-contact methods are required at high speed. These methods involve the use of high-speed cameras, which work with a limited fixed internal memory that is constantly filled with images until the camera is triggered and the information stored in that moment is saved. The fixed memory can be used to record a substantial number of pictures of low resolution, or alternatively, a lower number of pictures of higher resolution. Normally, the resolution is lowered to obtain the highest possible frame rate while recording a reasonable time interval at the same time. However, when the resolution of images is too low, it becomes difficult to extract geometrical features from them and the quality of the results diminishes. To counteract this effect, a sub-pixel

| | Quasi-static | | High speed | |
|---|---|---|---|---|
| Specimen geometry | Diameter, $2a$ [mm] | Notch radius, $\rho$ [mm] | Diameter, $2a$ [mm] | Notch radius, $\rho$ [mm] |
| RB | 6 | $\infty$ | 3.5 | $\infty$ |
| HGR | 6 | $\infty$ | 3.5 | $\infty$ |
| RNB | 4 | 8 | - | - |
| | 5 | 8 | 2.5 | 4 |
| | 5 | 6 | - | - |
| | 5 | 3 | 2.5 | 1.5 |
| | 5 | 2 | 2.5 | 1 |
| | 5 | 1 | 2.5 | 0.5 |

**Table 4.1:** Dimensions of the specimens used at low and high speed.

accuracy edge detection algorithm has been used in the post-processing. The implementation of this method is covered in Section 4.2.4.2.

- **Specimens painting.** When pictures of the specimens are taken, these are generally painted beforehand in order to improve their contrast against the background, or speckled to track some features of their surface. At high speed the paint shatters and detaches from the specimen, making it very difficult to interpret the images. For this purpose, an in-situ high-speed shadowgraph method has been proposed, which removes the need of painting the specimens and allows for the extraction of the geometrical information required. This procedure is explained in detail in Section 4.2.3.3.
- **Interrupted tests.** The interruption of tests at controlled levels of deformation is generally not possible with high-speed equipment. The servo-hydraulic system used in this research requires a finite time and distance to slow down and stop, which would not be acceptable for the damage experiments. An experimental rig has been designed in order to interrupt the tests at the desired level of load or displacement. The design of this experimental rig is explained in Section 4.2.5.

### 4.2.2 Tests and Equipment Set-up

The quasi-static tests have been conducted in a conventional 250 kN tensile Instron machine. A 16 megapixels DSLR camera with a 200 mm lens and one source of light on each side of the sample have been used to record images of the sample geometry in plasticity and ductile fracture experiments (as observed in Figure 3.2). A crosshead displacement speed of 1.2 mm/min has been used, which has produced average strain-rates of $\dot{\varepsilon} = 10^{-3} \sim 10^{-2}\ \mathrm{s}^{-1}$. The images have been recorded at a rate of 0.5 Hz, i.e. one picture every two seconds. For the damage accumulation tests, the successive loading

and unloading programme has been specified in the Instron control software (Bluehill 3), so that the test has run in a continuous manner in quasi-static conditions. The engineering strain in the gauge region of HGR specimens has been measured using an extensometer of 6 mm gauge length and 100% tensile travel (as observed in Figure 3.13).

The high-speed tests have been run in a VHS Instron servo-hydraulic test machine capable of performing tests up to a velocity of 20 m/s. A schematic and a picture of the set-up used for the plasticity and ductile fracture tests are presented in Figure 4.2. A lost-motion device has been used in order to apply load on the specimen only when the desired constant velocity has been achieved. The actuator of the machine requires some distance to reach constant velocity and this system, consisting of a slack rod inside the actuator piston, allows for the acceleration of the actuator along that distance without load application. As an impact between the lost-motion slack rod and the bottom surface of the ram occurs, rubber washers have been used to minimise the dynamic effects, such as stress waves propagating through the specimen. A piezoelectric PCB 222B load cell with a limit dynamic tensile load of 11.12 kN and a maximum operating frequency of 120 kHz has been used to measure the load applied to the specimen. The strain measurement in high-speed conditions requires the use of a non-contact device,

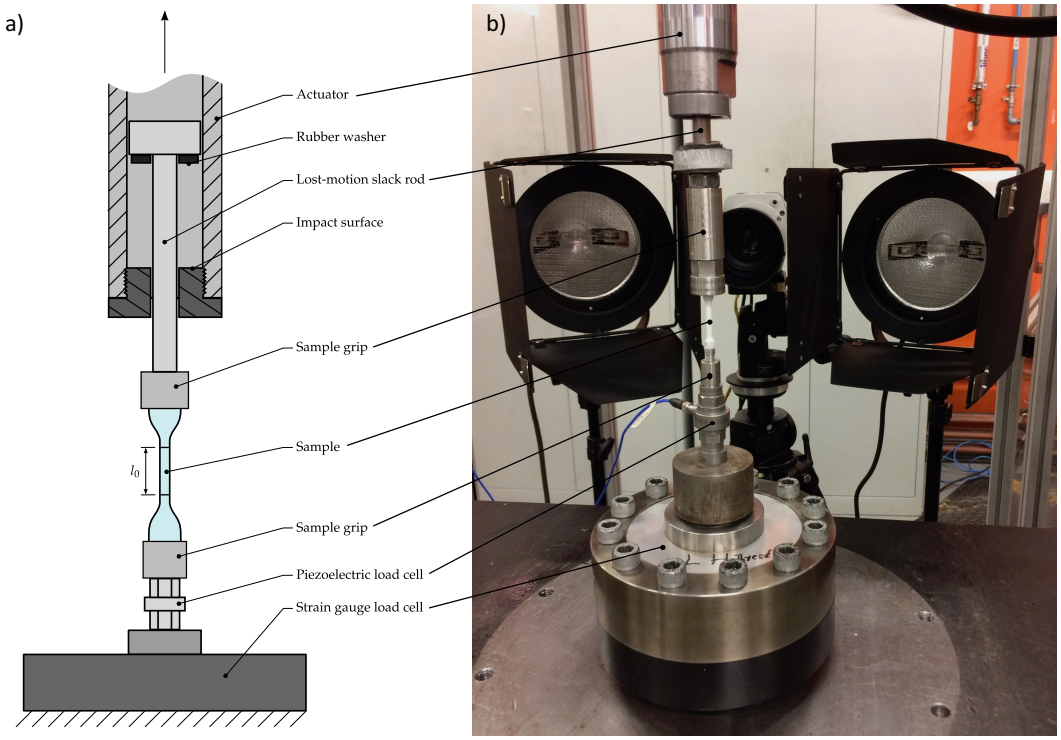



**Figure 4.2:** High strain-rate tensile tests set-up; a) load chain schematic and b) picture of the actual test set-up.

due to the difficulty of data acquisition using mechanically attached equipment. In this case, a Phantom V1610 high-speed camera with a 100 mm lens has been used to record images of the deformation throughout the test. This camera provides a maximum resolution of 1 megapixel (1280x800) and a minimum exposure of 500 ns. Additionally, two high power halogen lights have been employed to provide the amount of light required in order to obtain images of sufficient quality at the high frame rate used. This system has been used to perform tests at room temperature and velocities of approximately 1 m/s and 12 m/s, that produce in the specimens average strain-rates of $\dot{\varepsilon} = 10^2 \sim 10^4$ s$^{-1}$. For the intermediate-speed tests ($v \sim 1$ m/s) images have been recorded at a rate of $20,000 \sim 28,000$ Hz, and for the high-speed tests ($v \sim 12$ m/s) a rate of $37,500 \sim 120,000$ Hz has been used.

### 4.2.3 Strain Measurement

The measurement of stress and strain at high strain-rate is always challenging, moreover, it is even more complicated when the properties during the development of the neck need to be monitored. The designed experiment uses the shadowgraph concept to measure the geometry of the specimen during the test. Other techniques such as a video-extensometer and DIC have been considered as alternatives, and in the end used for validation of the selected in-situ high-speed shadowgraph method. The three techniques (video-extensometer, DIC and in-situ shadowgraph) are presented bellow and their outputs compared.

#### 4.2.3.1 Video-extensometer

Traditional clip gauge extensometers cannot be used in high-speed applications, therefore, video-extensometers are sometimes used as an alternative. The measurement taken is the same in both cases, recording the relative displacement of two points along the longitudinal axis of the specimen. Engineering strain can be calculated using this measurement and engineering stress from the load cell reading. True stress and true strain can then be obtained applying the equations for uniform deformation

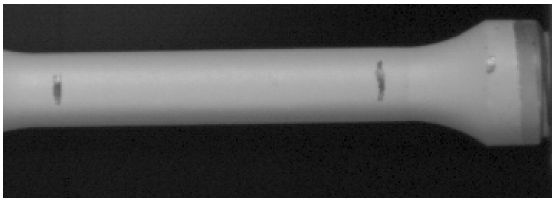


**Figure 4.3:** Specimen preparation for video-extensometer technique.

(Equations 2.26 and 2.27). It has to be noted that this method does not take into account the localised deformation of the specimen, and consequently, the true stress - true strain values obtained are representative only up to the necking onset point.

For the current research, two horizontal black lines separated by the initial gauge length have been painted on the specimen and pictures have been taken throughout the test. The samples have been previously painted in white to improve the contrast of the images and avoid reflections, as observed in Figure 4.3. The test set-up used is that presented in Figure 4.2b, with the high speed camera located in front of the specimen and two lights placed on its sides. The distance between lines has been obtained for each picture applying a thresholding algorithm to the images and the results used to calculate strain.

#### 4.2.3.2 2D DIC

The use of 2D DIC technique allows for the measurement of full field deformation of a surface instead of just point-to-point 1D strain. The specimen is painted with a white background and a black speckle pattern is applied on top, as shown in Figure 4.4, making it possible to track the local displacement of each location of the specimen surface. With this technique local values of strain concentration can be measured as long as they are located on the surface and the paint quality is adequate. The test set-up used for this technique is also the one presented in Figure 4.2b.

In this work, ARAMIS software from GOM GmbH has been used to solve the strains on the specimens and obtain strain field maps. Nevertheless, the focus of this research is not on the full strain contours analysis, but on the comparison of axial strain with the value obtained from other techniques. Thus, the displacement of a few points located at the initial gauge length has been tracked and used in the same manner as a video-extensometer to calculate longitudinal strain and compare it to the rest of techniques.

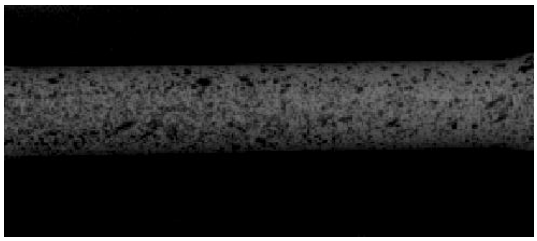


**Figure 4.4:** Specimen preparation for DIC technique.

#### 4.2.3.3 Shadowgraph

Apart from the lighting, in order to obtain images with the best contrast possible the specimens are generally painted in white colour, which also helps to eliminate reflections on metallic materials. Nevertheless, at high speed the paint cannot follow the fast deformation of the surface of the specimen and it generally detaches and shatters independently of the wetness of the paint. This problem is especially severe when the neck is developing, which is the region of highest interest for this research.

An alternative test set-up in which painting the specimen is not necessary has been developed. In this case only one light located exactly behind the specimen has been used and the high-speed camera has been placed in front of the specimen, as observed in Figure 4.5. A white diffusion lighting gel sheet has been used to cover the halogen light and produce evenly distributed lighting conditions without reflections. The work-

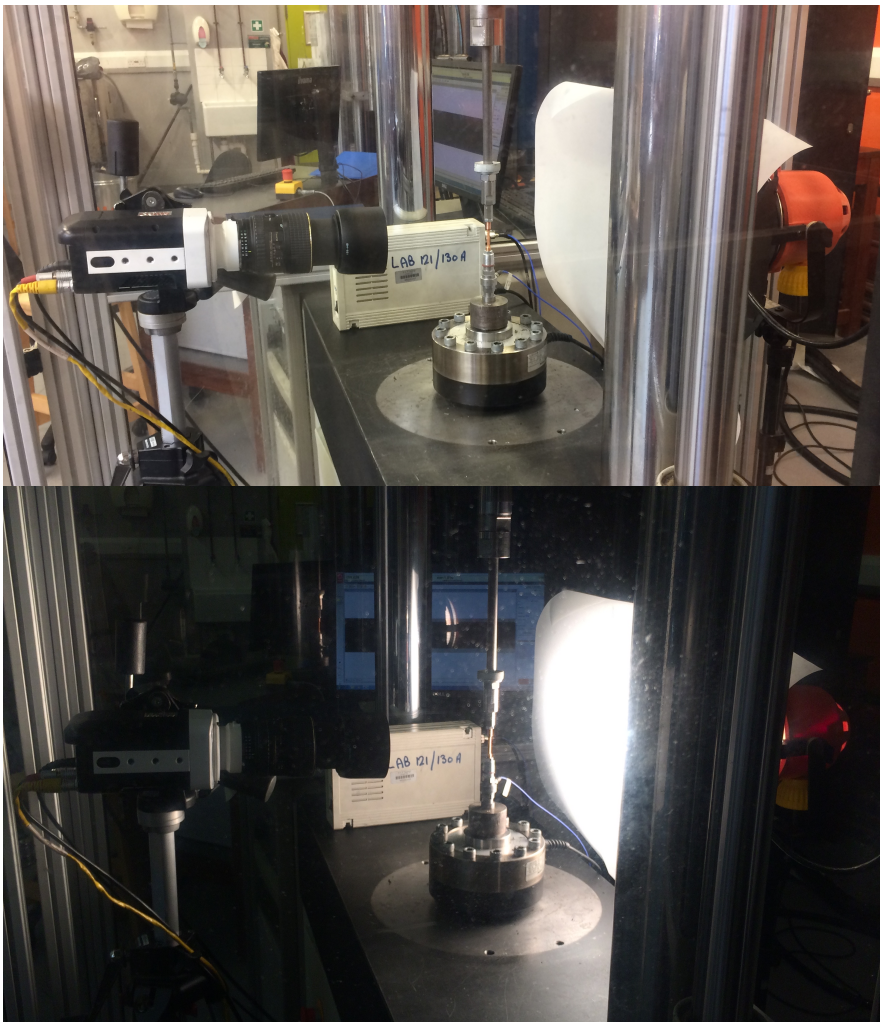


**Figure 4.5:** In-situ shadowgraph for high strain-rate tensile tests.

ing principle is the same as that of a shadowgraph but applied during a tensile test in high-speed conditions. As images of the shadow produced by the specimen instead of pictures of the specimen surface are taken, paint is not required and, at the same time, reflections are avoided. Figure 4.6 shows an image taken using this method compared to one of a painted specimen recording its surface instead of its shadow. The high quality of the shadow image can be appreciated, as well as the improvement derived from removing the paint from the specimen. This experimental technique can be combined with a sub-pixel edge detection processing algorithm (Section 4.2.4.2) for the highest accuracy in the calculation of stress and strain using the Bridgman relationships described in Section 2.3.1.

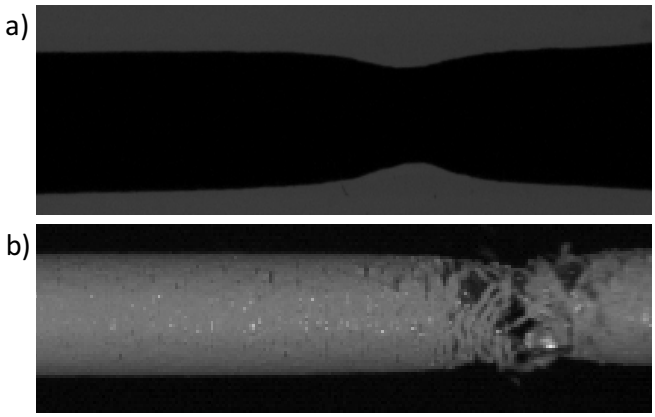



**Figure 4.6:** Necking images a) using the in-situ shadowgraph method and b) taking pictures of painted specimen.

The three strain measurement techniques (video-extensometer, DIC and shadowgraph) have been assessed at a test velocity of 1 m/s and their results compared. Table 4.2 shows a summary of the tested specimens and the techniques used in each case; all the specimens used are made of stainless steel 304L and have the round RB3.5 geometry described in Section 3.3.2. The in-situ shadowgraph method has been selected for the rest of the research because the neck measurements have provided the most accurate results. Figure 4.7 presents the stress - strain results obtained for all the specimens tested, the strain-rate evolution along the tests is also presented. The results obtained with the three experimental techniques are consistent, presenting virtually equal results in the early stages of plastic deformation where the deformation is still uniform. The stress - strain curves obtained using the video-extensometer and DIC techniques can only be applied before necking starts ($\varepsilon = 0.25 \sim 0.30$ for this material). After this point the results stop being representative since Equations 2.26 and 2.27 do not consider localisation. In this sense, both the video-extensometer and DIC techniques present comparable results, as would be expected, since the underly-

| Specimen | Velocity, $v$ [m/s] | Strain measurement method | | |
|---|---|---|---|---|
| | | Video-extens. | 2D DIC | Neck geometry |
| RB #1 | 1 | x | | x |
| RB #2 | 1 | x | | x |
| RB #3 | 1 | | x | |

**Table 4.2:** Specimens analysed for high-speed strain measurement methods comparison and validation.

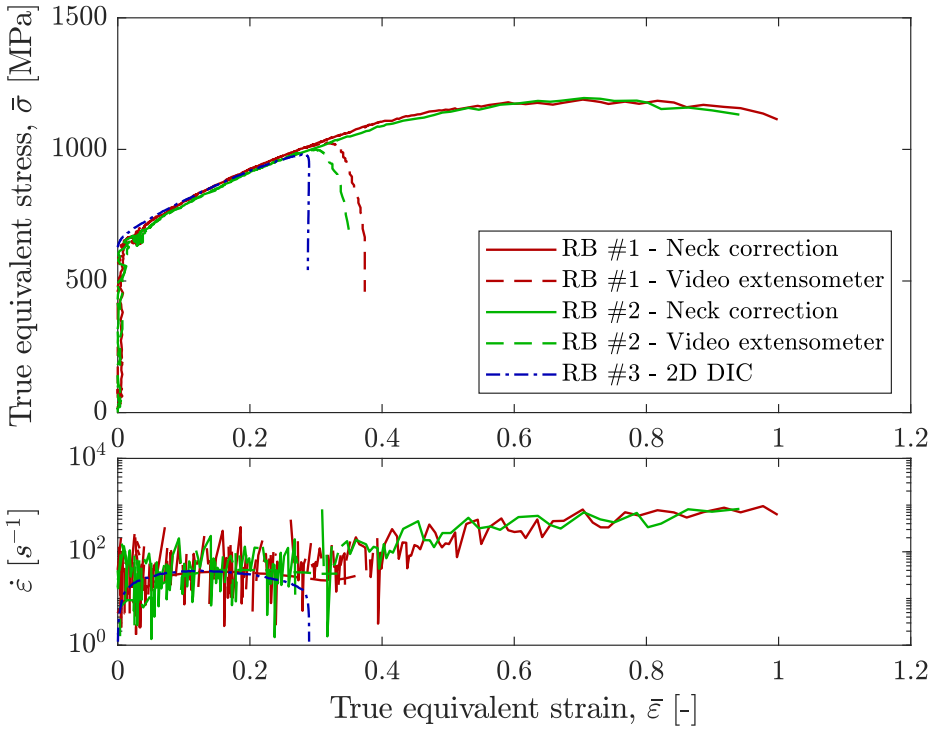



**Figure 4.7:** Comparison of true equivalent stress - true equivalent strain curves ($\bar{\sigma}$ - $\bar{\varepsilon}$) obtained using different strain measurement methods. Strain-rate - true equivalent strain curves ($\dot{\varepsilon}$ - $\bar{\varepsilon}$) are also represented.

ing processing method is the same. The results from the specimen shape monitoring technique also coincide with the other two methods at the beginning, which serves as validation of the method. Nevertheless, stress and strain grows further in this case, since the local neck behaviour is measured with this method, giving real values of local equivalent stress and strain in the necked section. The robustness and repeatability of the shadowgraph method can also be observed if the results of the two specimens processed using this method are compared, being the yield stress, hardening rate and fracture strain values consistent.

### 4.2.4 Post-processing Algorithm

One of the challenges of high-speed conditions is the difficulty of obtaining an image with sufficient resolution to capture the shape of the specimen accurately. Two different image processing algorithms have been investigated and are described below:

#### 4.2.4.1 Thresholding Algorithm

If sufficiently high-resolution images of the specimen can be taken, a simple thresholding algorithm can be used to extract the external edges of the sample. As observed in Figure 4.8, this method consists in defining a threshold grey scale value to delimit two areas with different contrast or intensity values, and therefore, to obtain the edge between them. Different threshold values are initially used and the raw images are compared with the predicted edges; the value that provides a better approximation to the real geometry is selected. This manually calibrated threshold can then be used for all the images that present the same brightness properties.

The method is accurate enough for tests where high-resolution and good contrast images can be obtained. Those conditions are very difficult to achieve in high-speed tests, where generally the resolution and brightness of the images are quite low due to the extremely high frame rate required. The images presented in Figure 4.8 correspond to one of the high-speed tests conducted as part of this research, and it can be observed that they are quite dark around the edges and present a relatively poor resolution. As a consequence, the edge extracted with the thresholding algorithm has a stepped shape, and its quality is not good enough to extract properly the geometrical parameters of the neck, especially the neck radius of curvature.

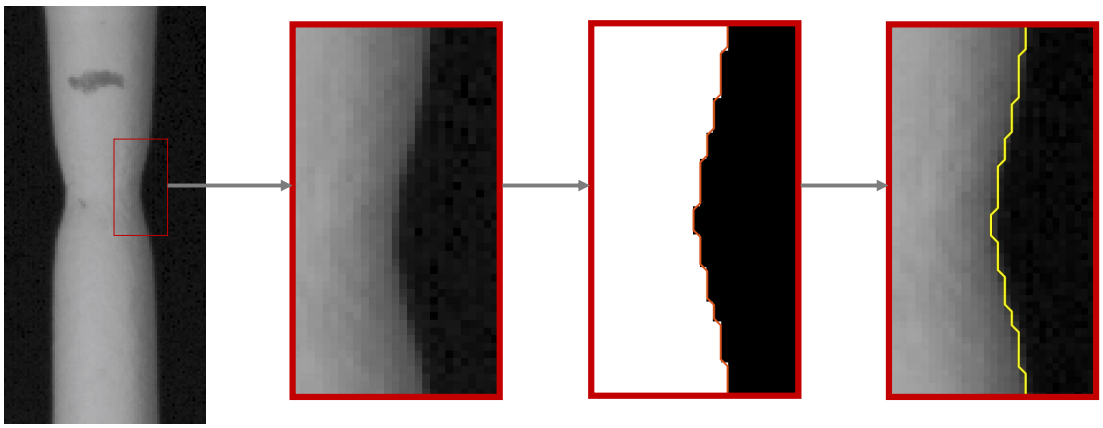


**Figure 4.8:** Specimen contour measurement using a thresholding algorithm.

#### 4.2.4.2 Sub-pixel Edge Detection Algorithm

In order to extract smooth edges from relatively low quality images a sub-pixel edge detection algorithm has been implemented. It eliminates the stepped shape extracted using a thresholding algorithm, since it is able to locate edges within pixels and not only on their boundaries. This algorithm was proposed by Trujillo-Pino et al. [127] and applied to high-precision edge detection in medical images. In this case, a bigger window covering the analysed pixel and its neighbours is considered to locate the edge (5 x 3 pixels window centred in the analysed pixel), instead of using just the individual grey-scale value of each pixel. The method is based on the partial area effect which treats the edge within the pixel as a discontinuity in the intensity value (grey-scale value) of the image. It uses the intensity value of neighbouring pixels to calculate the position, orientation and curvature of the edge inside the pixel. This algorithm was chosen for this research due to its accuracy in noisy, blurred or low-contrast images, as proven by Trujillo-Pino et al. [127]. Figure 4.9 shows the edge extraction process for the same image previously analysed with the thresholding algorithm. The sub-pixel accuracy allows for a much more accurate edge detection leading to a smooth edge whose location, normal and curvature is calculated within each pixel, as can be appreciated in the zoomed in image of Figure 4.9.

Focusing the analysis on the specimen shape monitoring technique, the two image processing algorithms have been compared to evaluate the improvement of results when sub-pixel edge detection instead of thresholding is used. Figure 4.10 shows the evolution of the neck geometrical parameters for the same specimen processed using both techniques. The improvement on radius of cross-section ($a$) is not noticeable, since its decrease with plastic strain is fairly regular. An upgrade does appear in the radius

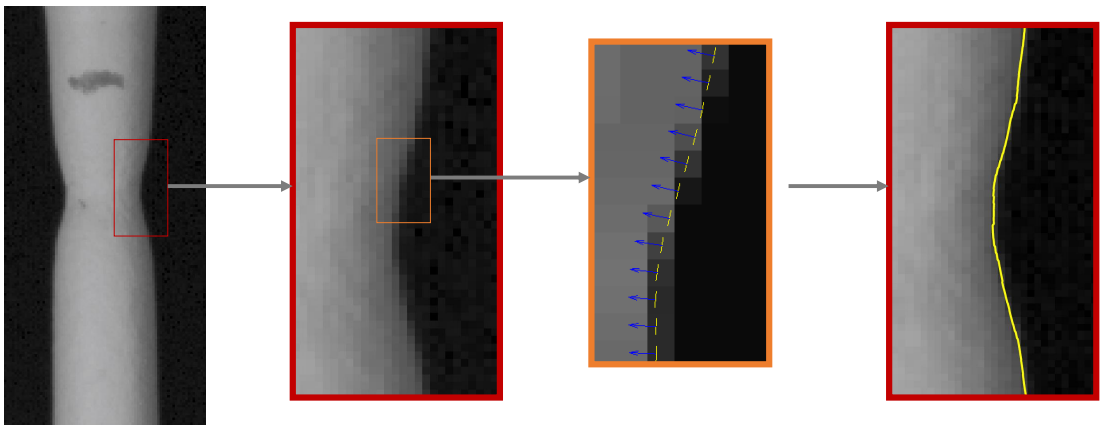


**Figure 4.9:** Specimen contour measurement using a sub-pixel edge detection algorithm.

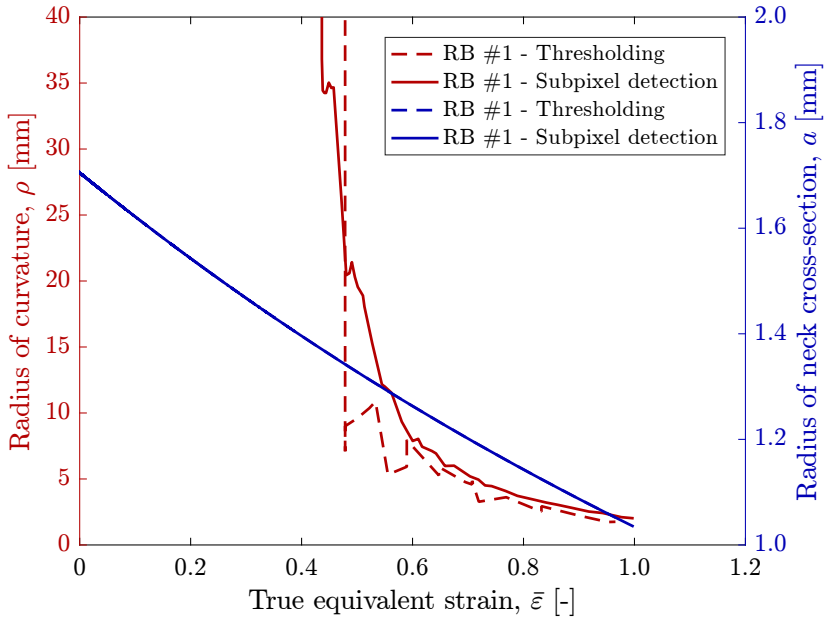



**Figure 4.10:** Comparison of the neck geometry obtained using thresholding and sub-pixel edge detection algorithms.

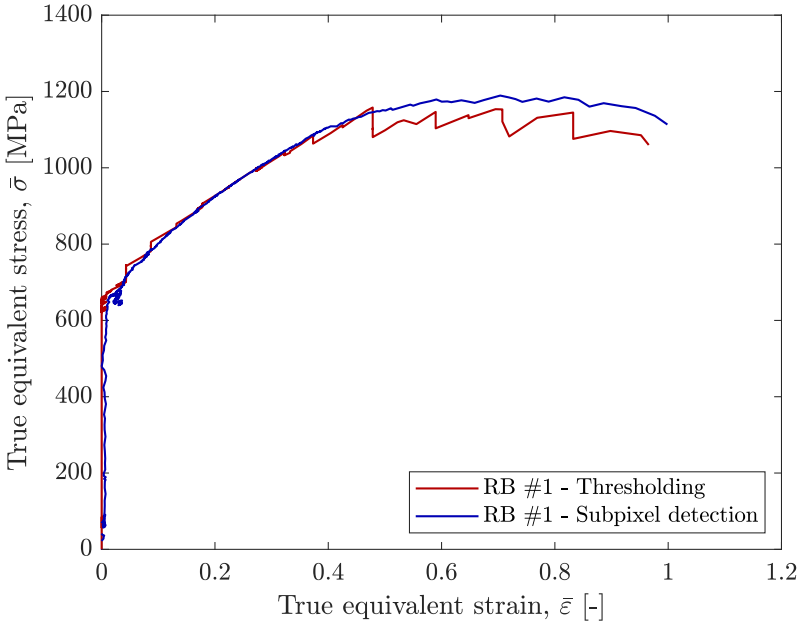



**Figure 4.11:** Comparison of the true equivalent stress - true equivalent strain curve ($\bar{\sigma}$ - $\bar{\varepsilon}$) obtained using thresholding and sub-pixel edge detection algorithms.

of curvature ($\rho$), which is calculated by fitting circles to the edges of the neck, and is much more affected by the irregular edges of the neck obtained using the thresholding algorithm. The effects can be observed in Figure 4.11, where the true equivalent stress - true equivalent strain curves of the same specimen are presented post-processed using both algorithms. Visibly both curves follow the same trend, but that corresponding to the sub-pixel edge detection method is much smoother than that obtained by thresholding, eliminating the stepped shape of the curve.

The shape monitoring technique with in-situ shadowgraph and sub-pixel edge detection algorithm is, therefore, the method that has been used to obtain equivalent stresses and strains in high-speed tensile conditions. A noteworthy aspect is that the method maintains its robustness at the highest speeds tested, being the maximum frame rate achievable with the high-speed camera the only limitation.

### 4.2.5 Interrupted High-Speed Test

For damage accumulation measurement at high speed, a continuous test with integrated loading and unloading cycles cannot be performed due to the practical restrictions mentioned at the beginning of the chapter. Therefore, an interrupted methodology has been devised in which the plastic deformation is applied at high strain-rate and the damage measurement is performed separately in quasi-static conditions. An experimental rig has been developed aimed at interrupting high-speed tensile tests at strain-rates around $10^3$ $s^{-1}$. Details on the design, calibration and experimental use of the rig for damage assessment are discussed here.

#### 4.2.5.1 Damage Measurement

To overcome the obstacles derived from high-speed tests a hybrid method has been developed which consists of separating the plastic loading of the specimen from the elastic modulus measurement. The test is interrupted at different levels of plastic deformation using a self-designed experimental rig, which allows to stop the high-speed test varying the amount of deformation applied to the sample. The modulus measurement is then performed separately at lower speed following the same measurement procedure explained for quasi-static conditions, and also validated taking porosity measurements.

The whole process is illustrated in Figure 4.12. Firstly, a plastic deformation ($\varepsilon_{pl,1}$) is applied to the specimen at high strain-rate, the actual amount of strain undertaken by the sample is measured through its geometrical changes using the shadowgraph

method (Section 4.2.3.3). Then, several quasi-static loading and unloading cycles in the elastic region are applied to the specimen, with the 6 mm gauge length extensometer placed on its gauge region to determine the slope of the unloadings, and therefore, the effective modulus ($\tilde{E}_1$) and damage ($D_1$) values for $\varepsilon_{pl,1}$. Further plastic deformation is then applied ($\varepsilon_{pl,2}$), and again the values of $\tilde{E}_2$ and $D_2$ for $\varepsilon_{pl,2}$ are determined by loading and unloading the specimen in quasi-static conditions and recording the elastic strain changes. This process can be repeated as many times as desired, providing each cycle a pair of $D - \varepsilon_{pl}$ values to construct the damage accumulation curve. Either the same or different samples can be used to take the measurements, by running multiple shots on the same specimen, or by straining each specimen to a certain value of plastic strain. Since the test is discontinuous, it allows for material analysis along the plastic deformation process using other ex-situ techniques, such as X-Ray CT, microhardness or microstructure analysis.

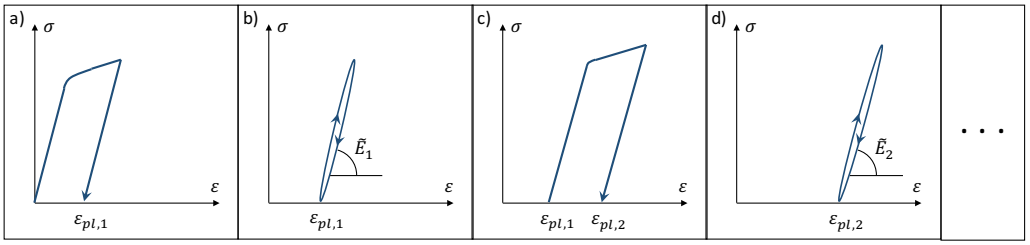



**Figure 4.12:** Hybrid method for ductile damage measurement at high strain-rates: a) first plastic deformation, b) first load-unload cycle, c) second plastic deformation, d) second load-unload cycle.

#### 4.2.5.2 Method Validation in Quasi-Static Conditions

The method has been validated in fully quasi-static conditions before having been applied to high strain-rate. This has consisted of following the described methodology, applying the plastic strain in quasi-static instead of dynamic conditions. The validation test is, therefore, the same as that used in the quasi-static assessment but including interruptions and re-zeroing the extensometer for each elastic modulus measurement cycle. This test fulfils a double validation purpose, since it has also served to compare the stress - strain response of the damage hourglass specimens (HGR) with that of the round bar specimens (RB). For that reason the whole test has been monitored with a DSLR camera and post-processed as shown in Section 3.3.

The true equivalent stress - true equivalent strain values obtained for the validation test are represented in Figure 4.13. Seven loading steps have been performed, interrupting the test after each of them. Loading-unloading cycles have then been separately

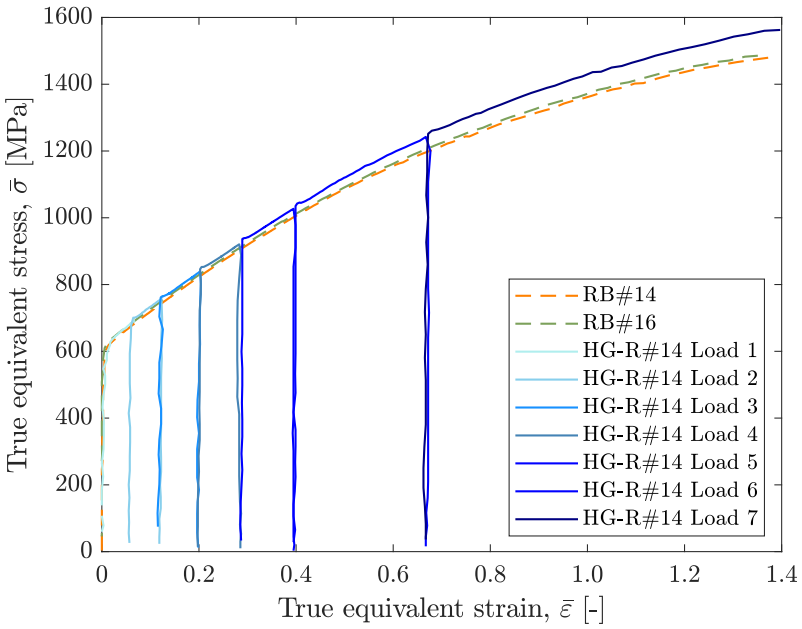



**Figure 4.13:** True equivalent stress - true equivalent strain ($\bar{\sigma}$ - $\bar{\varepsilon}$) measurements of hybrid test with plastic load applied in quasi-static conditions and comparison with continuous tests.

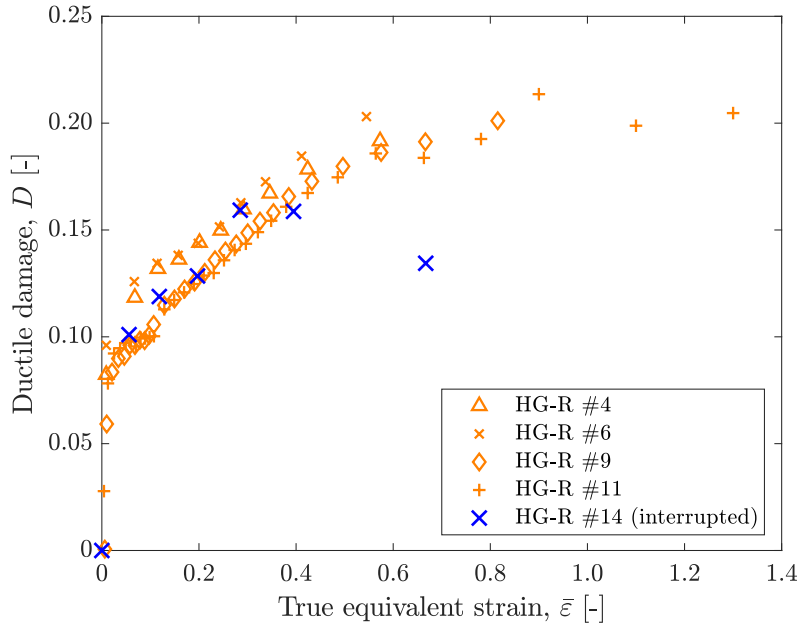



**Figure 4.14:** Ductile damage - true equivalent strain ($D$ - $\bar{\varepsilon}$) measurements of hybrid test with plastic load applied in quasi-static conditions and comparison with continuous tests.

| $\bar{\varepsilon}_{pl}$ [-] | $E_{interr}$ [GPa] | $E_{cont}$ [GPa] | $D_{interr}$ [-] | $D_{cont}$ [-] |
|---|---|---|---|---|
| 0 | 181.5 | 178.0 | 0 | 0 |
| 0.06 | 163.2 | 158.4 | 0.10 | 0.11 |
| 0.12 | 159.9 | 156.6 | 0.12 | 0.12 |
| 0.20 | 158.2 | 154.9 | 0.13 | 0.13 |
| 0.29 | 152.6 | 151.3 | 0.16 | 0.15 |
| 0.39 | 152.7 | 147.7 | 0.16 | 0.17 |
| 0.67 | 157.1 | 144.2 | 0.13 | 0.19 |

**Table 4.3:** Comparison of elastic modulus and damage values obtained with the continuous and interrupted techniques.

completed in order to measure elastic modulus, as previously described. The elastic modulus and damage results for the loading-unloading cycles, as well as a check of the initial modulus of the material, are presented in Table 4.3 and in Figure 4.14. The results of this interrupted methodology ($E_{interr}$ and $D_{interr}$) are compared with those obtained with the continuous procedure ($E_{cont}$ and $D_{cont}$). As observed in the table, the trend followed by the elastic modulus and damage measurements is similar using both techniques. Small variations are observed, which should be treated carefully since the magnitude of damage undergone by the material is also small. Only the last plastic strain analysed presents a considerable difference, however, this can be attributed to the imperfect re-attachment of the extensometer to the already necked specimen when the interrupted method is used. Therefore, it can be concluded that both techniques yield similar results, but only within the region of uniform deformation.

#### 4.2.5.3 Experimental Rig Design

As previously mentioned, the main difficulty lies on the interruption of high-speed tests at controlled levels of deformation, so that damage can be measured externally in slower conditions. For that purpose a new experimental rig has been designed and built.

The operating principle of the rig is based on placing two specimens in series, the actual specimen and a shear pin, and applying tensile load to the whole system. Since both parts have different geometries and are made of different materials they present dissimilar fracture loads, and when one of them breaks the other one has only consumed part of its plastic deformation capabilities. For the current experiment, the fracture load of the pin is required to be higher than that of the specimen. By doing that, the specimen is initially plastically deformed, and at some point this deformation is mechanically stopped allowing the load on the pin to increase further. When the tensile load reaches the fracture load of the pin this one breaks but the specimen

only keeps the allowed plastic deformation. A design of this type was proposed by Fitoussi et al. [128], in which the deformation of the specimen was controlled by the cross-section of a notched tensile pin. In order to subject the specimen to higher plastic strains bigger notch cross-sections, and therefore, higher fracture loads were used. This approach is valid for materials with considerable strain hardening, for which the use of different pin fracture loads can be used to tune the amount of plastic strain in the specimen. However, if the material tested presents limited strain hardening, closer to a flat perfectly plastic material, or if a fine adjustment of the amount of deformation is required, a displacement controlled experiment would be more desirable. Dongfang et al. [129] and Yang et al. [130] explored approaches for displacement controlled interrupted tests in Hopkinson bar experiments. In both cases, a fixed element attached around the specimen was used to limit the displacement of the gauge region after some deformation had been applied. After that point, the load concentrated in a weak region of the specimen that acted as a mechanical fuse, playing the same role as the shear pin in the load controlled experiment.

The experimental rig designed for this work combines the benefits of load and displacement controlled interrupted test arrangements, since it is possible to control the specimen deformation by using any of the two techniques or a combination of both. A model of the rig design is presented in Figure 4.15 and a picture of the actual experimental set-up is shown in Figure 4.16. The rig consists of a rigid frame which is fastened to the base of the VHS Instron tensile machine described in Section 4.2.2. On the loading axis of the machine, the specimen (located under the frame) is connected in series with a cylindrical shear pin (over the frame) by means of a conical-cylindrical part. As observed in Figure 4.15, after a certain level of deformation has been applied to the specimen, the conical part contacts with the top plate of the frame, which also has a conical shape. From that point of the test onwards all the elements under the frame behave rigidly and the tensile load increases further in the shear pin, which eventually fractures releasing the ram of the machine and allowing it to complete the high-speed stroke. A 100 kN load cell has been placed at the bottom of the rig and a more accurate 12 kN piezoelectric load cell has been connected directly behind the specimen to record the applied load. The actual strain of the specimen has been calculated using the high-speed shadowgraph imaging method described in Section 4.2.3.3. Two threaded elements connect both load cells at the bottom of the rig. These act as a length selector device, which allows to control the distance between the cone and the frame. The thread pitch of this element is 2 mm, which allows for an easy and fine adjustment of the amount of deformation applied to the specimen during each test. A lost motion device has also been placed on top of the rig, connecting the shear pin holder with the ram of the machine. This element is used to get rid of the acceleration

time that the machine requires, ensuring a constant velocity of the ram by the time the load is applied to the specimen.

Different materials have been selected for the components of the rig based on their function during the experiment. The main structure of the frame is made of structural steel EN24T and presents a thick section since it is expected to behave rigidly under the impacts of the conical part that it receives in operation. Four brackets also made out of EN24T have been bolted at the top of the frame to further improve its stiffness. In order to ensure that the conical part slides smoothly in vertical direction, a linear plain bearing has been installed in a bearing housing on top of the frame. A precipitation hardened steel 17-4PH has been selected for the threaded elements used to control the displacement. These parts located at the base of the rig have to withstand high tensile loads, including high-speed stress waves and their geometry cannot be deformed, since they are the elements used to finely adjust the level of plastic deformation of the sample. Finally, the conical part and the two shear pin holder elements have been machined out of Ti-6Al-4V, as these parts have to be strong and durable to resist the impact against

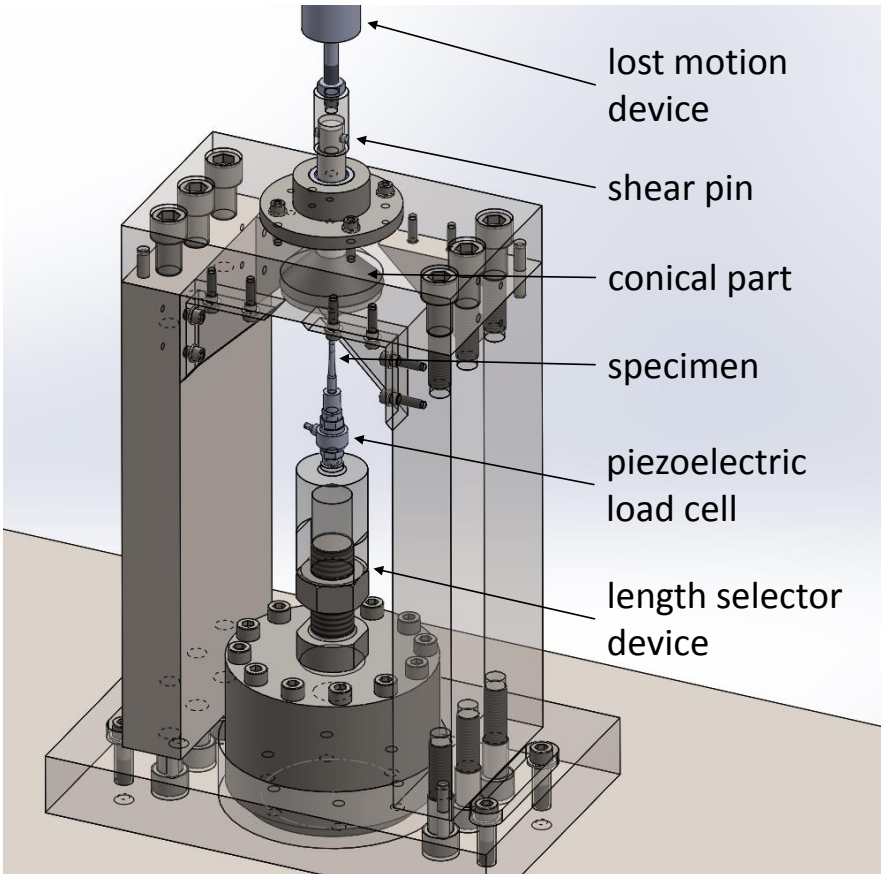



**Figure 4.15:** Design model of the experimental rig for adjustable interrupted high strain-rate tensile tests.

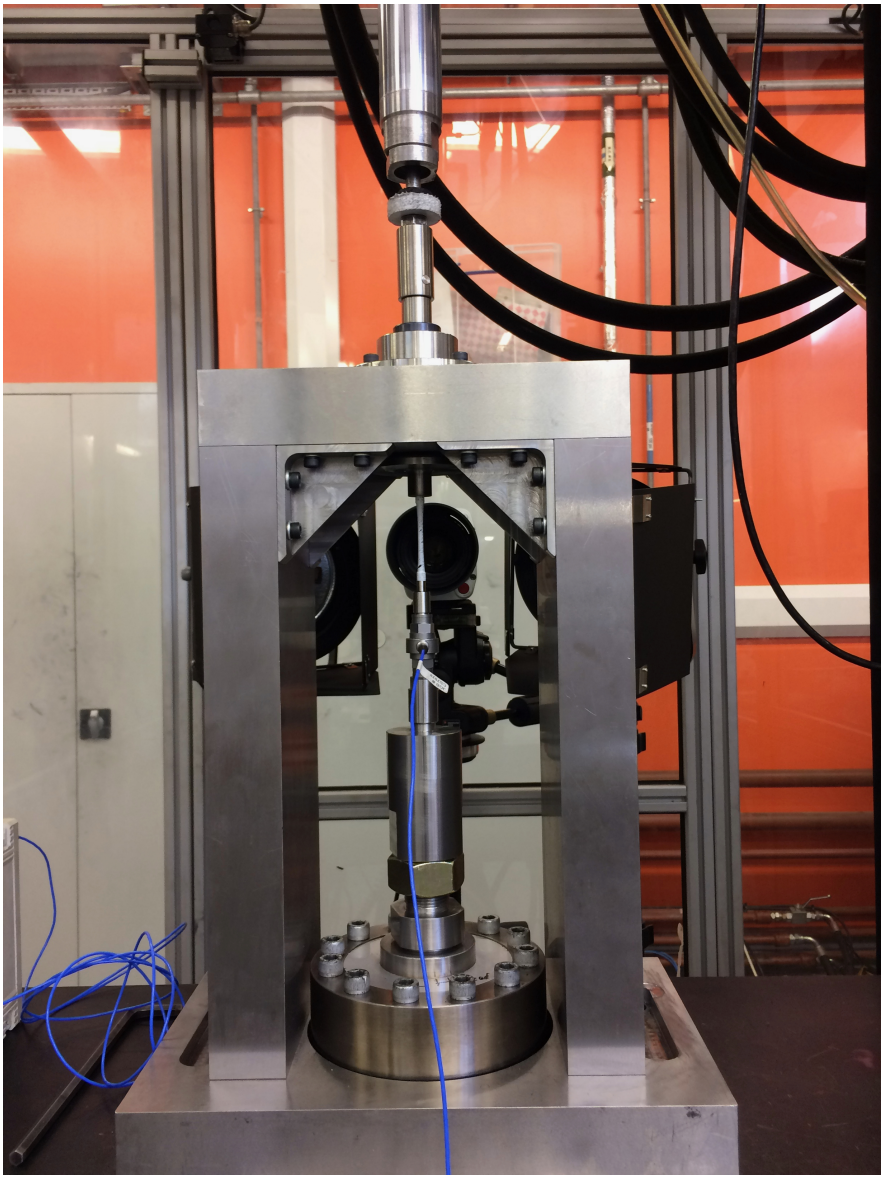


**Figure 4.16:** Experimental set-up for adjustable interrupted high strain-rate tensile tests.

the frame and the wear against the shear pin without major deformation or damage. At the same time, it is required that these moving components are relatively light to limit the weight of the load chain, which directly affects the magnitude of the stress waves generated when the high-speed load is applied. Detailed drawings of the assembly and the different components of the experimental rig can be found in Appendix A.2.

The material used for the pin has to be strong enough to withstand the deformation of the specimen, and quite brittle to suddenly shear when its fracture load is achieved, ideally without presenting much plastic deformation inside the pin holder.

An investigation of possible materials that fulfil those conditions has been conducted, and specimens of aluminium 6082-T6 and 7075 with groove diameters ranging from 4.4 mm to 5.1 mm have been tested. Figure 4.17 shows a comparison of the load response of all these pins at a test velocity of 1 m/s. Shear pins of aluminium 7075 with 5 mm groove diameter have been selected for the current research because of their limited ductility ($\varepsilon_{pl,f} \sim 10\%$) and the high yield stress ($\sigma_{YP} \sim 500$ MPa), which leads to a fracture load of $P_f \sim 10$ kN. This fulfils the requirement of a shear pin load higher than that of the specimen and lower than the limit withstood by the load cell and machine.

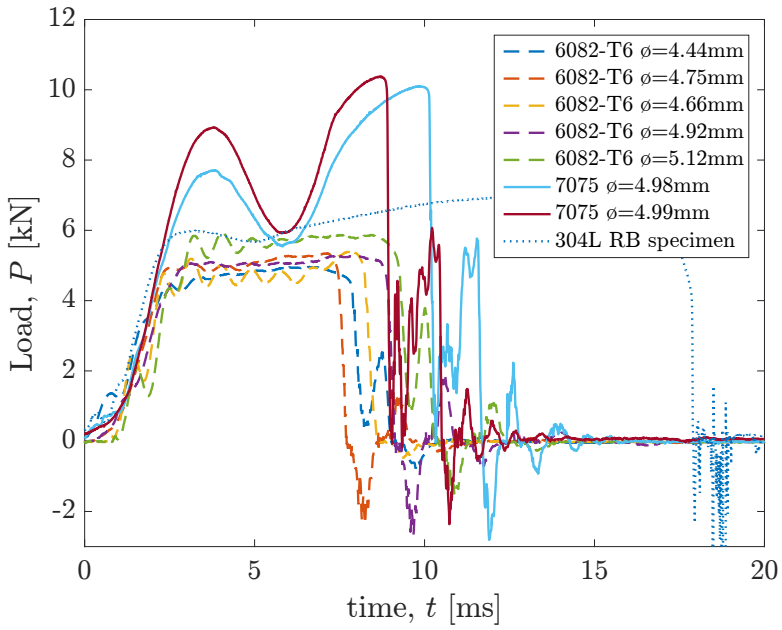



**Figure 4.17:** Load - time ($P$ - $t$) response of different shear pin designs.

#### 4.2.5.4 Rig Modelling and Validation

A finite elements model of the rig has been created and analysed in Abaqus/Explicit in order to estimate the performance of the rig. The appearance of the model is shown in Figure 4.18 and details of the mesh in the pin and specimen are presented in Figure 4.19. Only the top plate of the frame has been modelled, being the rest of the frame considered perfectly rigid. The length adjustment device behind the sample has also been modelled as perfectly rigid in order to simplify the model. The pin and the specimen are the parts of interest of the model and have been meshed with continuum eight-node linear brick elements with reduced integration (C3D8R). The shear pin holders have been modelled with a high density of continuum 10-node quadratic tetrahedral elements (C3D10M), which present reasonably good contact properties.

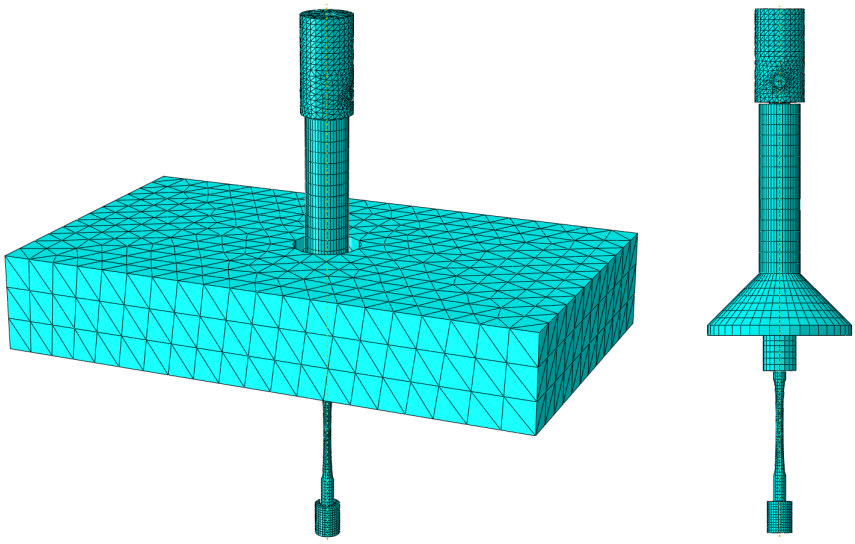


**Figure 4.18:** Finite elements model of the main components of the experimental rig.

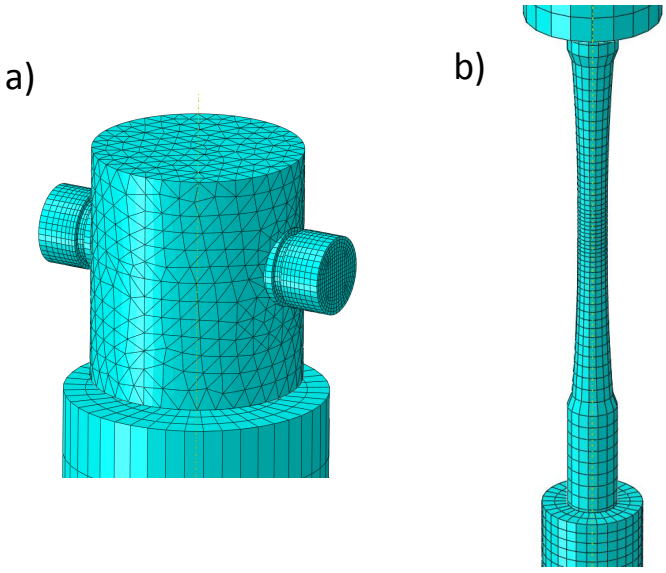



**Figure 4.19:** Finite elements model detail of: a) shear pin and b) specimen.

All the parts have been modelled as elastic, except the pin and the specimen for which typical plastic properties for aluminium 7075 and stainless steel 304L have also been used, respectively. The general contact algorithm of Abaqus/Explicit with no friction has been used to model the contact between the pin and its holders. The ductile fracture option has also been included in the shear pin in order to represent its failure. No damage accumulation option has been selected since the material is quite brittle, and a sudden failure of the elements has been specified at a ductility of

$\varepsilon_f = 0.10$. The elements are removed from the mesh when this plastic strain is reached, to model the pin fracture.

Different velocity and deformation conditions have been analysed. The velocity is applied at the top surface of the pin holder and the amount of deformation in the specimen is modified by modulating the distance between cone and impact plate. The predicted behaviour of the pin when a velocity of 1 m/s and a deformation step of 2 mm are applied is represented in Figure 4.20 in terms of von Mises equivalent stress ($\bar{\sigma}$). The

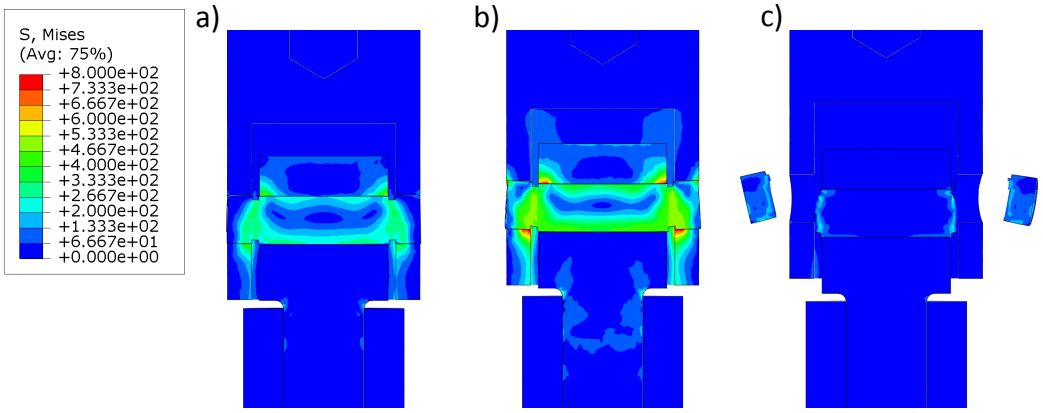



**Figure 4.20:** Von Mises stress ($\bar{\sigma}$) in section through the pin, a) during the deformation of the specimen, b) before fracture, c) after fracture.

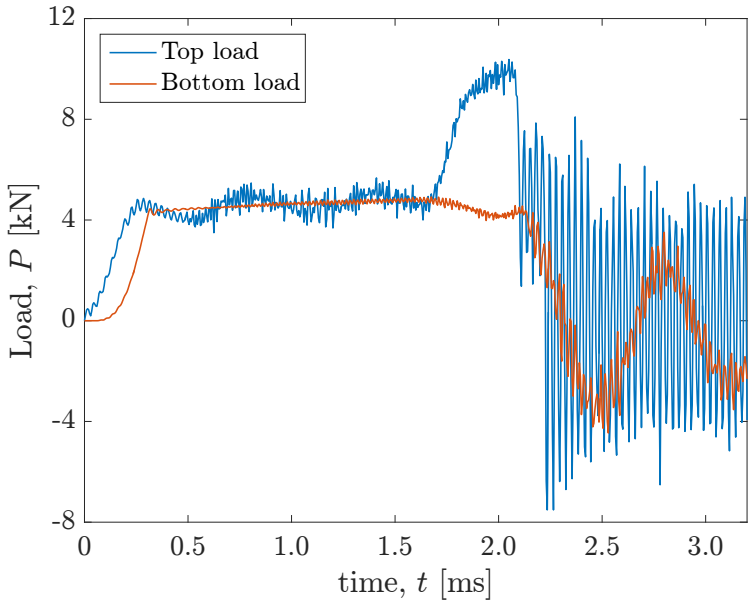



**Figure 4.21:** Load carried by the specimen and the shear pin ($P$ - $t$).

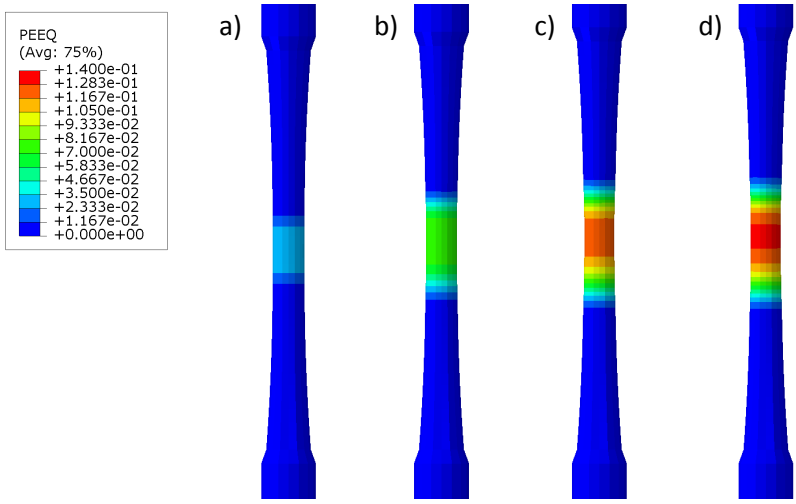



**Figure 4.22:** Equivalent plastic strain ($\bar{\varepsilon}_{pl}$) in the specimen after elongation of a) 0.5 mm, b) 1 mm, c) 1.5 mm and d) 2 mm.

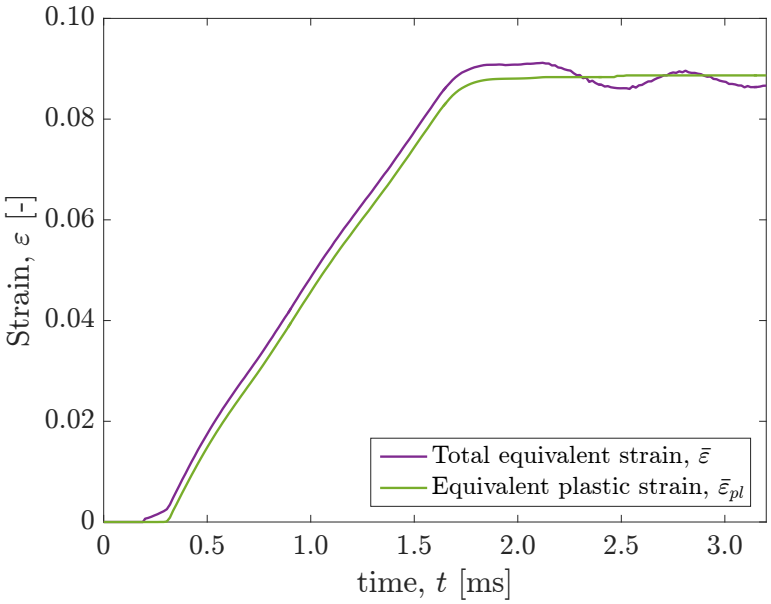



**Figure 4.23:** Total equivalent strain and equivalent plastic strain on the centre of the specimen axis ($\bar{\varepsilon}$ - $t$ and $\bar{\varepsilon}_{pl}$ - $t$).

estimated loads in the specimen-pin system measured at the top (lost motion device) and bottom (piezoelectric load cell) of the dynamic system are shown in Figure 4.21. The bottom load presents the same measurement that would be obtained with the piezoelectric load cell, which is the load that the specimen withstands. On the other hand, the top load represents the conditions on the shear pin. Initially, both loads

record the same values since all the elements are connected in series, with the values at the top slightly ahead of those at the bottom due to the time required for the stress waves to propagate within the material. When the conical element contacts the frame of the rig ($t \sim 1.6$ ms), the bottom load remains constant because the specimen undergoes no further deformation, while the top load starts rising again representing the load increase on the pin. When the pin shears ($t \sim 2.1$ ms), the top load suddenly drops, since the ram of the machine is not loaded any more and the load just fluctuates around zero until it is damped. The same happens on the specimen but with a lower frequency vibration.

The behaviour of the specimen in the $v = 1$ m/s and $\Delta l = 2$ mm conditions is shown in Figure 4.22 in terms of its equivalent plastic strain ($\bar{\varepsilon}_{pl}$) contours for increasing elongation. The evolution of total equivalent strain ($\bar{\varepsilon}$) and equivalent plastic strain ($\bar{\varepsilon}_{pl}$) on the central element of the specimen axis is presented in Figure 4.23. It can be observed how both strains accumulate fairly linearly up to the point of contact ($t \sim 1.6$ ms), remain constant until the pin breaks ($t \sim 2.1$ ms), and the plastic strain stays constant afterwards, while the total strain fluctuates with the same frequency as the load in Figure 4.21 until the oscillation disappears. As the plastic strain remains constant, no further permanent deformation is applied on the specimen due to the oscillation after the pin breaks, and the fluctuation in total strain can be attributed entirely to the elastic strain.

The geometry of the shear pin has been iteratively modified in this finite elements model in order to obtain the appropriate pin fracture load. With the final design of 5 mm diameter pin (to which Figures 4.20-4.23 correspond), a fracture load value of 10 kN has been obtained, as observed in Figure 4.21, which validates the experimental measurements of Figure 4.17. This value is higher than the maximum load expected on the specimen ($\sim$ 8 kN) and lower than the maximum load that the load cell can measure ($\sim$ 12 kN), and therefore, fulfils the requirements for the experiment.

## 4.3 Temperature Considerations

Basic material characterisation tests are run at room temperature ($T \sim 20$°C) and quasi-static strain-rate ($\dot{\varepsilon} \sim 10^{-3}$ s$^{-1}$). These conditions allow for the heat generated by the plastic deformation process to dissipate both by convection in the surrounding air and by conduction within the material itself, producing an isothermal state. However, as it occurs with the strain-rate analysis, many real life applications require the operation of material at temperatures far from 20°C. Heat engines for automotive industry, gas turbines for aerospace or metal forming and forging processes are only a few examples of applications that require high temperature materials characterisation.

Low temperature modelling is also an issue when designing arctic vessels, aircraft or space components such as satellites.

The experimental methodology described in Chapter 3 has been applied to different temperatures in order to analyse the effect it produces on plasticity, ductile fracture and damage accumulation, and include it in the models. The procedure used for these tests has only required minor modifications compared to the experiments described for room temperature and quasi-static conditions, and those are described below. The experimental results obtained from the temperature analysis will be presented in Chapter 7.

### 4.3.1 Temperature Tests Challenges

Some challenges have been faced when performing the temperature experiments in comparison with the standard room temperature conditions:

- **Chamber lighting.** The tests at high and low temperature have been run inside an environmental chamber limiting the amount of light available, which is required to obtain high quality images. The chamber only has a small window and lamps have been fitted outside, introducing some light through it.
- **Specimens painting.** In order to improve the contrast of images specimens have been painted in white, however, while high temperature paint is easy to find and performs well at 180°C, no conventional paint has been found for the low temperature tests. At −80°C paint cracks and detaches from the surface of the samples.
- **Ice formation.** Moisture present in the air condenses and forms ice and snow if the temperature is low enough. This phenomenon has been very problematic in the low temperature tests, affecting the quality of the images taken. Particularly troubling for images acquisition is the ice that forms on the surface of the specimen and on the inner surface of the window, as well as the mist that appears in the air within the chamber. This problem becomes worse the longer the door of the chamber remains opened, since this allows for warmer and more humid air to enter the cold and dry atmosphere inside the chamber. Therefore, the operations that required opening the door of the chamber have been performed as rapidly as possible in order to limit this effect.

### 4.3.2 Tests and Equipment Set-up

The tests have been performed in a 150 kN Instron test machine, very similar to the one used in standard conditions, but in this case the sample and surrounding fittings have been placed inside an environmental chamber, as shown in Figure 4.24.

The furnace is capable of raising temperature up to 200°C using a series of resistance coils located on its walls. Very low temperatures can also be achieved by introducing nitrogen into the chamber from an external vessel of liquid nitrogen. The internal temperature on the chamber is monitored using a thermocouple and the specimens are kept inside for sufficient time before the experiment so that they reach the desired uniform temperature.

Images of the specimens have been taken during the tests to account for changes in geometry and the necking process, and from that information, calculate local stress and strain values. In this case, the images have been taken from the outside of the chamber and through the small window located on its front door, as shown in Figure 4.24. The same DSLR camera and lens used at room temperature have been used in these tests. Lighting of the specimen has been a challenge, since the lights have to be placed outside the chamber. The same lamps have been used and their location has been changed until a good compromise of light, reflections from the glass of the window and shadows from the extensometer has been achieved.




**Figure 4.24:** Experimental set-up for high and low temperature tensile tests with damage accumulation measurements.

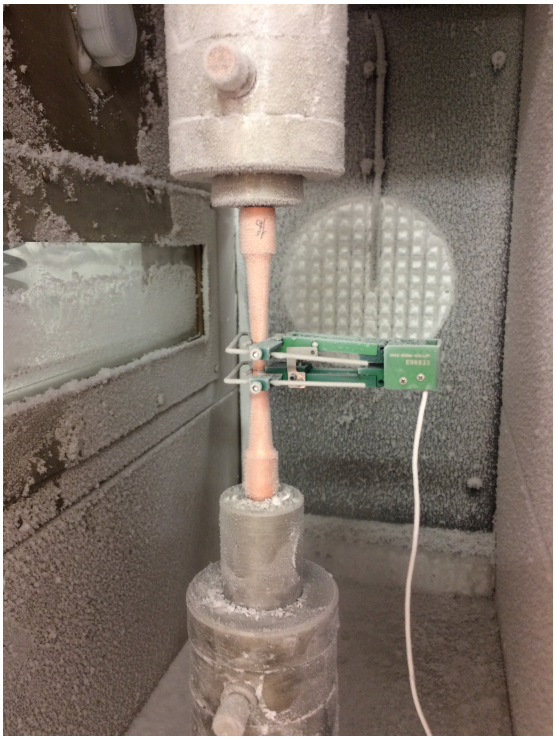


**Figure 4.25:** Ice formation on the surface of the specimen in a low temperature damage accumulation test.

For the high temperature tests, special white paint capable of resisting the severe conditions without cracking or detaching has been applied on the surface of the specimens. Since no appropriate paint has been found to resist the low temperature tests without cracking, these experiments have been conducted on unpainted specimens and a white plastic background has been placed behind the specimen. In this case the opposite contrast has been pursued, dark specimen surface and bright background, although the ice formation on the surface of the specimen (Figure 4.25) and its metallic colour have complicated the extraction of high quality pictures.

The damage measurement procedure used in the temperature tests has been the same as that described for standard conditions, making use of the same 6 mm gauge length extensometer, as shown in Figure 4.25 for a low temperature test. A program of continuous unloading-loading cycles has been run using Bluehill 3 software with the objective of obtaining the effective elastic moduli.

# Chapter 5

# Experimental Results in Quasi-Static and Room Temperature Conditions

## 5.1 Introduction

The proposed methodology for the characterisation of ductile materials consists of three experiments aimed at measuring plasticity, ductile fracture and damage accumulation. The experimental results obtained for the two analysed materials following that methodology are presented in this chapter. All the results commented here correspond to tests performed in the baseline conditions of quasi-static strain-rate ($\dot{\varepsilon} \sim 10^{-3}$ s$^{-1}$) and room temperature ($T \sim 20$°C). The results of plasticity tests are presented and discussed in Section 5.2, those of ductile fracture in Section 5.3 and of damage accumulation in Section 5.4. Apart from the three main experiments described in Chapter 3, a microstructure analysis has been conducted on some of the specimens in order to validate the results. This additional method for damage analysis and the results obtained are covered in Section 5.5. Finally, some conclusions are commented in Section 5.6.

## 5.2 Plasticity Tests

The true stress - true plastic strain behaviour of the material has been determined by applying the neck monitoring technique described in Section 3.3. The results presented here correspond to tensile tests on round RB6 specimens. Hourglass HGR6 specimens have also been tested to obtain the necking effect correction curves, which are also included in this section and will be used in the damage accumulation analysis. A

summary of all the specimens tested and the post-processing techniques employed for each of them is presented in Table 5.1.

| Material | Geometry | Specimen | $\sigma$-$\varepsilon$ measurement | |
|---|---|---|---|---|
| | | | Imaging | Extensometer |
| s/s 304L | RB6 | #14 | x | |
| | | #16 | x | |
| | | #12 | | x |
| | | #13 | | x |
| | HGR6 | #21 | x | x |
| copper C110 | RB6 | #1 | x | |
| | | #2 | x | x |
| | HGR6 | #8 | x | x |

**Table 5.1:** Specimens studied in the quasi-static room temperature plasticity analysis.

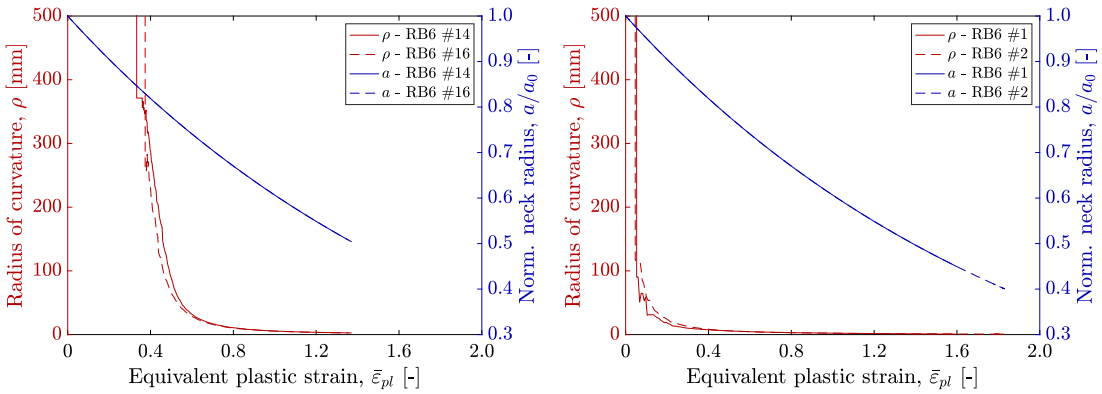
### 5.2.1 Neck Geometry

From the images post-processing, the history of specimen minimum radius ($a$) and neck radius of curvature ($\rho$) has been measured. The evolution of these geometrical parameters is represented in Figure 5.1a for stainless steel 304L and in Figure 5.1b for copper C110. Some key numerical results are also summarised in Table 5.2. Two RB6 samples of each material have been analysed.

As observed, the cross-sectional radius reduces approximately uniformly with applied strain for both materials. The other geometrical parameter of interest is the neck radius of curvature, which presents an infinite value before necking due to the initially cylindrical geometry of the specimen. At the onset of necking this value decreases more or less quickly depending on how rapid the neck development is. Apart from the higher ductility and cross-section reduction of copper compared to stainless steel, the onset of

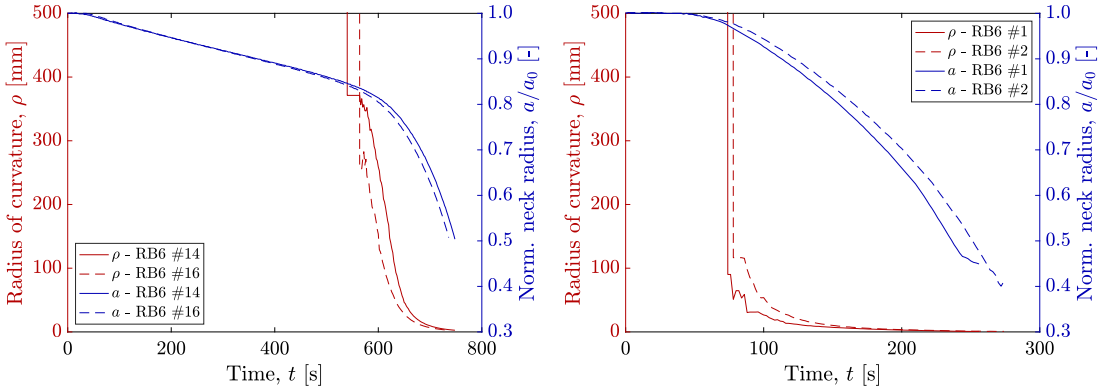
| Material | Geometry | Specimen | Imaging | | | Shadowgraph |
|---|---|---|---|---|---|---|
| | | | $\varepsilon_{onset}$ [-] | $\rho_f$ [mm] | $a_f$ [mm] | $a_f$ [mm] |
| s/s 304L | RB6 | #14 | 0.35 | 2.62 | 1.50 | 1.49 |
| | | #16 | 0.38 | 2.58 | 1.51 | 1.53 |
| copper C110 | RB6 | #1 | 0.04 | 0.94 | 1.29 | 1.27 |
| | | #2 | 0.05 | 0.88 | 1.22 | 1.22 |

**Table 5.2:** Neck onset strain ($\varepsilon_{onset}$), final neck radius of curvature ($\rho_f$) and final cross-sectional radius ($a_f$) measured with imaging method; final cross-sectional radius ($a_f$) measured with shadowgraph.




**(a)** stainless steel 304L **(b)** copper C110

**Figure 5.1:** Evolution of the neck geometry (radius of curvature of the osculating circle and normalised minimum cross-sectional radius vs. equivalent plastic strain ($\rho$ - $\bar{\varepsilon}_{pl}$ and $a/a_0$ - $\bar{\varepsilon}_{pl}$)).




**(a)** stainless steel 304L **(b)** copper C110

**Figure 5.2:** Evolution of the neck geometry (radius of curvature of the osculating circle and normalised minimum cross-sectional radius vs. time ($\rho$ - $t$ and $a/a_0$ - $t$)).

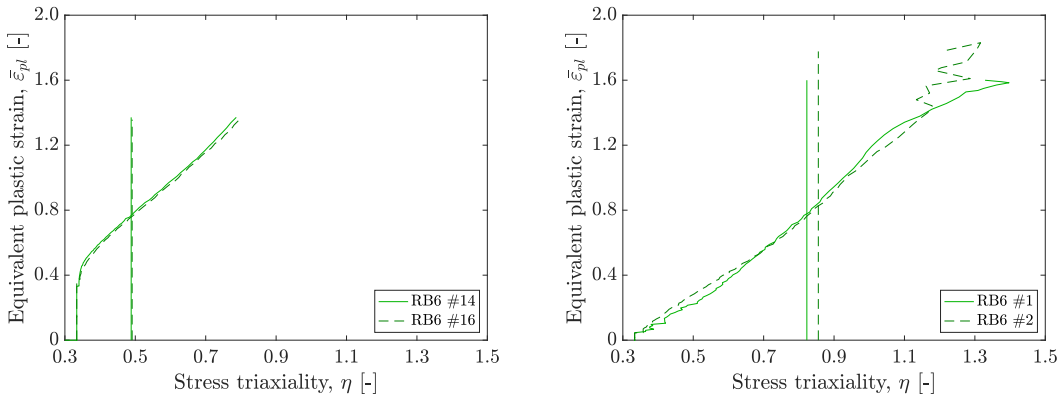
necking location of both materials can be compared in Figure 5.1 and Table 5.2. While stainless steel presents a clear region of uniform plastic deformation up to $\bar{\varepsilon}_{pl} \sim 0.35$, copper necks almost from the beginning of the plastic region allowing only $\sim 0.04$ strain before the instability starts. The values of final specimen cross-section measured with a shadowgraph are also included in Table 5.2, and as observed, they are very similar to those obtained with imaging, validating the method.

Although the neck cross-section decreases approximately linearly with plastic strain, it has to be noted that plastic strain accumulates much quicker towards the end of the test, when the neck is already developed. This effect can be observed in Figure 5.2

where the same parameters previously analysed are represented as a function of test time, instead of strain. In this case, the difference between the linear cross-section reduction of uniform deformation and the sudden drop after necking can be observed. This drop is quite sudden for stainless steel 304L (Figure 5.2a) compared to copper C110 (Figure 5.2b) if the whole test is considered; nevertheless, the necking process up to fracture takes a similar time for both materials ($t_{necking} \sim 200$ s).

### 5.2.2 Stress Triaxiality

Making use of the imaging method, the evolution of stress triaxiality throughout the test can be measured, which will be of particular interest for ductile fracture analysis. Here, the change in triaxiality of the tested uniaxial specimens is presented in Figure 5.3a for stainless steel and Figure 5.3b for copper. It is quite clear from the results that, although round specimens are generally used for uniaxial conditions analysis ($\eta = 1/3$), the stress state changes considerably once the specimen starts to neck. For copper, the neck appears from the beginning of the test, leaving an almost nonexistent region of uniaxial behaviour. During necking, the change in stress triaxiality with equivalent plastic strain is approximately linear for both materials and determined by the geometrical changes of the neck through Equation 3.5. The average stress triaxiality of each test is represented by a vertical line in Figure 5.3, and it highlights the difference between the theoretical uniaxial case ($\eta = 1/3$), and the real case for stainless steel ($\eta_{av} \sim 0.5$) and especially copper ($\eta_{av} \sim 0.85$).

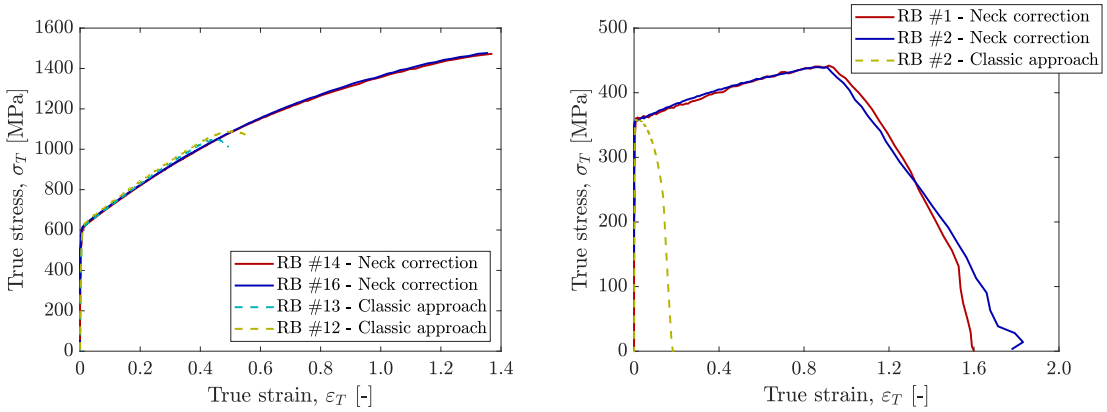



**(a)** stainless steel 304L **(b)** copper C110

**Figure 5.3:** Variation of equivalent plastic strain - stress triaxiality throughout the tensile tests ($\bar{\varepsilon}_{pl}$ - $\eta$), vertical lines represent the average triaxiality of the test.

### 5.2.3 Equivalent Stress - Strain

Making use of the geometrical parameters presented above, and using Equations 2.28-2.32, the curve of equivalent true stress - equivalent true strain in the centre of the neck can be obtained. Figure 5.4a shows the results for stainless steel 304L, where results of two additional conventional tensile tests have also been presented. For these last two tests, strain has been measured using a clip gauge extensometer, and Equations 2.26-2.27 have been used to post-process the results. As expected, the outcome of both methods coincides before the specimen necks and the traditional approach lacks accuracy after necking, where real stress and strain increases much more than what is predicted by Equations 2.26-2.27. The same results are presented for copper C110 in Figure 5.4b, where a conventional tensile test has also been plotted. The outcome is the same as that of stainless steel, being in this case even more pronounced due to the early necking of copper. The plastic stress - strain obtained for this material using Equations 2.26-2.27 is incorrect, since it necks almost from the beginning of the test. The fracture mode is also different in both materials, while the stainless steel fails suddenly in a relatively brittle manner presenting a typical 45° cup and cone shape when it reaches its failure strain, the copper fails progressively in a more ductile manner, hence the gradual stress decrease observed in Figure 5.4b. The fracture behaviour of these materials is further studied in Section 5.3.

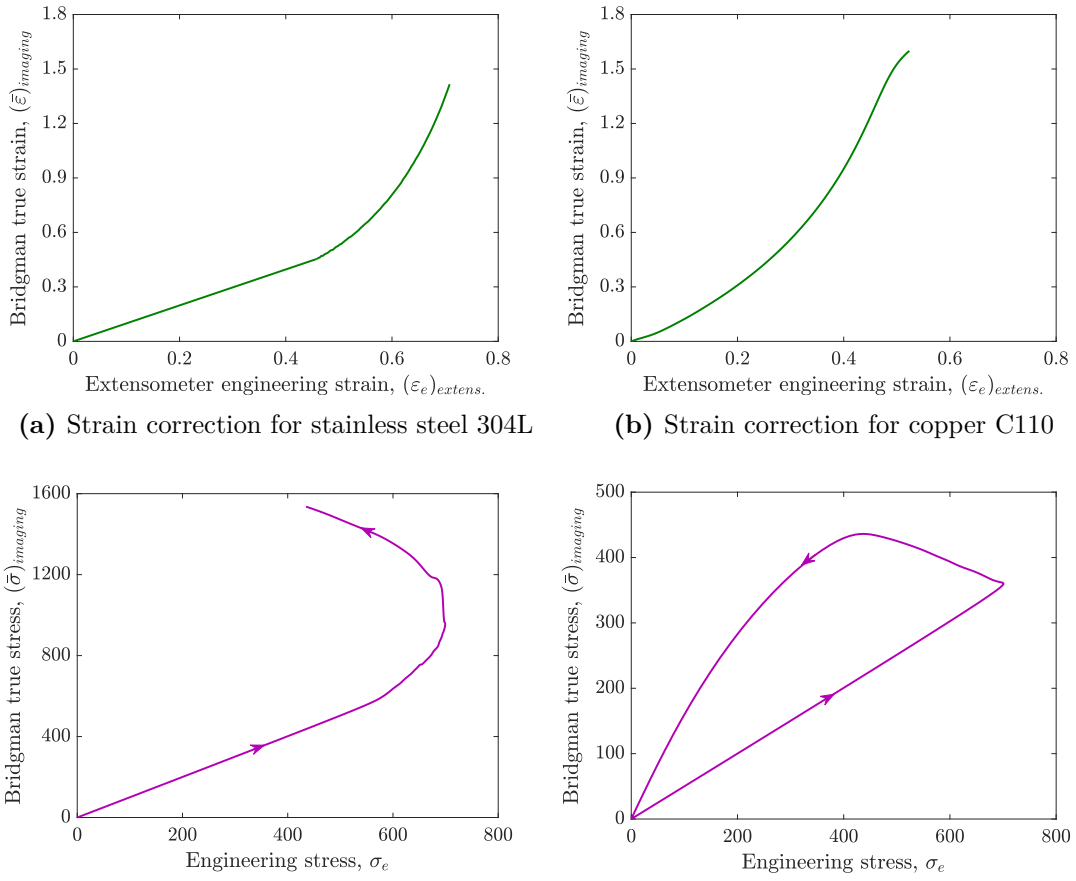



**(a)** stainless steel 304L **(b)** copper C110

**Figure 5.4:** True equivalent stress - true equivalent strain ($\bar{\sigma}$ - $\bar{\varepsilon}$) obtained with the imaging method and "true" stress - "true" strain ($\sigma_T$ - $\varepsilon_T$) obtained with the traditional method.

### 5.2.4 Stress - Strain Neck Correction

The same methodology used to characterise plastic hardening with RB6 specimens has been applied to a HGR6 hourglass specimen of each material. In these tests, apart from using the imaging and Bridgman [87] approach to calculate stress and strain, a 6 mm clip gauge extensometer has been used to measure engineering strain. The outcome of the tests is shown in Figure 5.5 in the form of curves that can be used for the correction of necking effects. The corrected true equivalent strain ($(\bar{\varepsilon})_{imaging}$) obtained with the imaging method is plotted against the extensometer engineering strain ($(\varepsilon_e)_{extens.}$) obtained with the traditional clip gauge method. The same calibration curves are represented for the stresses correction ($(\bar{\sigma})_{imaging}$ - $\sigma_e$). These curves are used to correct the engineering values obtained from traditional tests to true values by scaling the measured values applying the scaling factors provided by the curves. As expected, the correction curves are lines of slope value $\sim 1$ before necking, since both




**(a)** Strain correction for stainless steel 304L

**(b)** Strain correction for copper C110

**(c)** Stress correction for stainless steel 304L

**(d)** Stress correction for copper C110

**Figure 5.5:** Necking effect correction curves: strain correction ($(\bar{\varepsilon})_{imaging}$ - $(\varepsilon_e)_{extens.}$) and stress correction ($(\bar{\sigma})_{imaging}$ - $(\sigma_e)$).

methods yield the same results. When the neck develops, the slope increases in all the curves due to the localisation of stress and strain that is not captured by the traditional approach.

While the increasing slope is easily observed for strains, a backwards or boomerang effect appears in the stress curves. Engineering stress starts decreasing passed the UTS, however, the real true stress keeps increasing. The point of highest abscissa of these curves corresponds to the UTS point, after which localisation occurs with either local true stress increasing further up to failure (stainless steel, Figure 5.5c), or increasing and then decreasing back to zero, due to the material degradation (copper, Figure 5.5d). The calibration curves have later been used to correct the extensometer measured stress - strain values of damage accumulation tests on the HGR6 samples studied in Section 5.4.

## 5.3 Ductile Fracture Tests

The second experiment contemplated in the methodology consists of the study of the effect of stress triaxiality on ductility by testing round notched bar specimens with different notch geometries. The results correspond to specimens of RNB6 geometry with different notch sizes, however, results of round RB6 specimens are also included here, since they represent the extreme case of a notch with an infinite notch radius. A

| Material | Geometry | Notch acuity $a/\rho$ | Specimen | $\sigma$-$\varepsilon$ measurement | $\bar{\varepsilon}_{pl,f}$ measurement | |
|---|---|---|---|---|---|---|
| | | | | Imaging | Imaging | Shadowgr. |
| s/s 304L | RB6 | 0 | #14 | x | x | x |
| | | | #16 | x | x | x |
| | RNB6-1 | 0.25 | #19 | x | x | x |
| | RNB6-3 | 0.417 | #15 | x | x | x |
| | RNB6-4 | 0.833 | #11 | x | x | x |
| | RNB6-5 | 1.25 | #7 | x | x | x |
| | RNB6-6 | 2.5 | #3 | x | x | x |
| copper C110 | RB6 | 0 | #1 | x | x | x |
| | | | #2 | x | x | x |
| | RNB6-2 | 0.313 | #11 | x | x | x |
| | RNB6-4 | 0.833 | #8 | x | x | x |
| | RNB6-5 | 1.25 | #5 | x | x | x |
| | RNB6-6 | 2.5 | #2 | x | x | x |

**Table 5.3:** Specimens studied in the quasi-static room temperature ductile fracture analysis.

summary of all the specimens tested and the post-processing techniques employed for each of them is presented in Table 5.3.

### 5.3.1 Fracture Surface

Images of the fracture surface of a stainless steel 304L and a copper C110 specimens have been taken at different magnifications ranging from 40x to 2000x using a scanning electron microscope (SEM). These are presented in Figure 5.6 and significant differences can be appreciated between both materials. The voids distribution is approximately

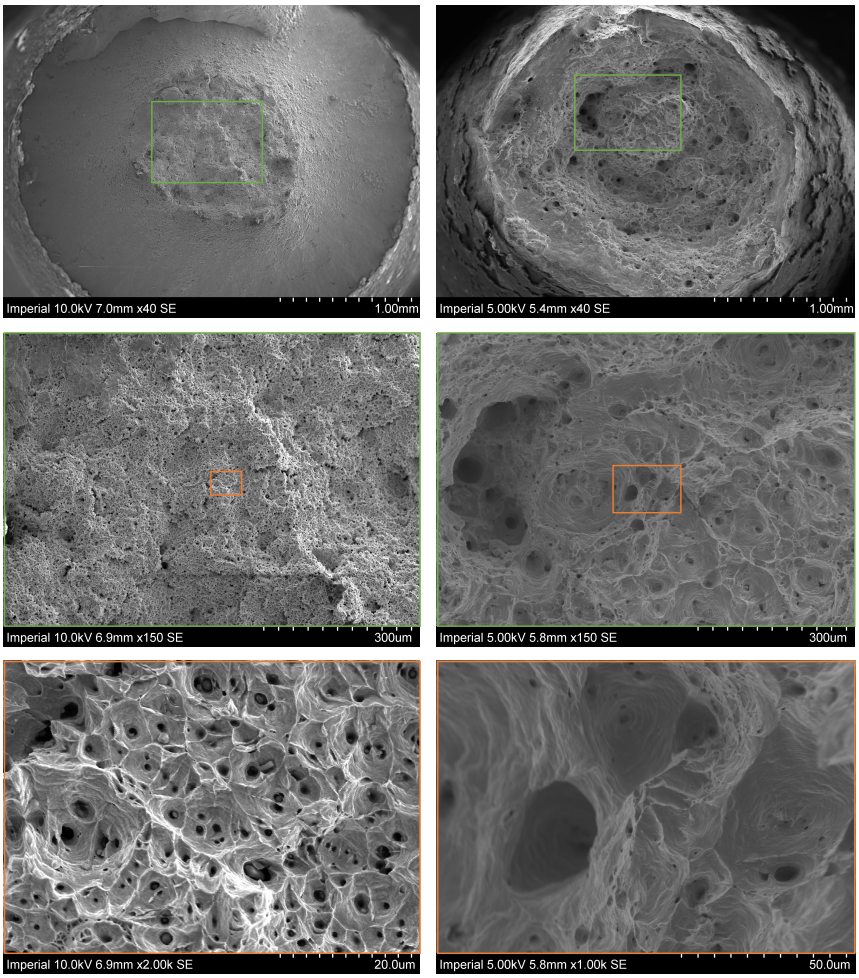



**Figure 5.6:** Fracture surface of tensile specimens in quasi-static and room temperature conditions: stainless steel 304L at (a) 40x, (b) 150x and (c) 2000x magnification; copper C110 at (d) 40x, (e) 150x and (f) 1000x magnification.

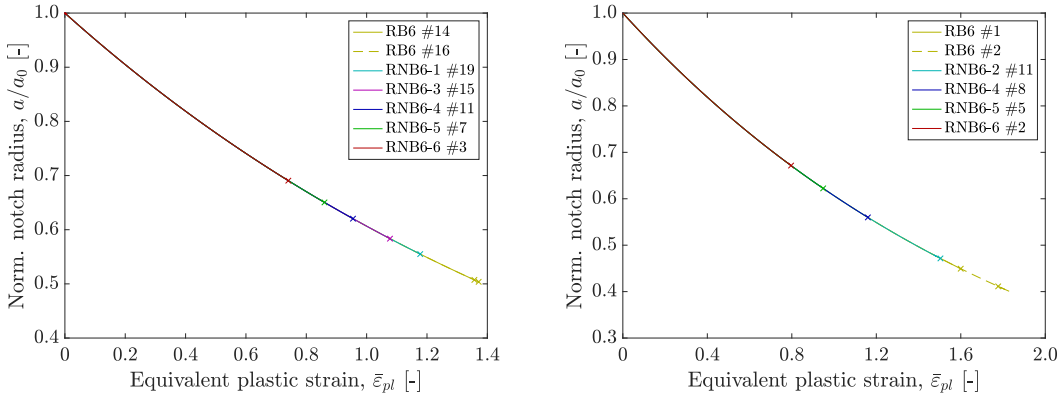
uniform in stainless steel, as observed in the 150x image, while greater concentration of defects can be found in certain areas of the copper sample. The size distribution is also fairly regular in stainless steel, even in the 2000x image, in which most voids range in size from 1-2 μm. The copper sample shows voids of much bigger size, some of them being clearly observable even in the 40x image. The size distribution is also much wider, measuring the voids 1-30 μm, and being possible to find even bigger voids in other regions (up to around 100 μm).

If the 150x images of both materials are compared, the regular distribution of very small defects in stainless steel contrasts with the irregular distribution of a lower number of bigger voids in copper. The uniformity of stainless steel has probably enhanced an abrupt fracture when the cross-section could no longer stand the load. The large voids of copper have grown degrading significantly the material, with evidence of this ductile growth observed in the beach-like shapes present surrounding the defects. However, the lower number of voids has meant that relatively undamaged areas able to withstand load have been preserved until very high deformation, avoiding a rapid fracture. These observations confirm the behaviour observed near fracture in the round specimens analysed in Section 5.2.3.

### 5.3.2 Notch Geometry

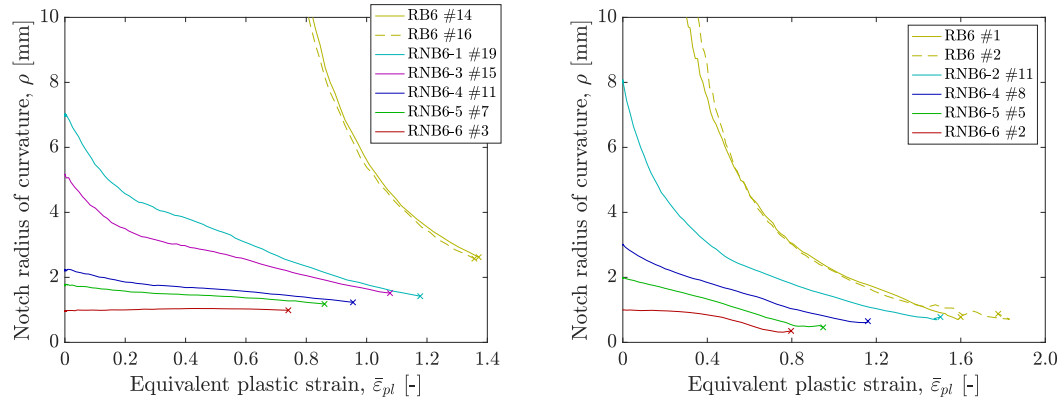
The same imaging methodology previously presented for tensile tests has been employed here for the analysis of notched specimens. Tracking the curvature of the neck, present from the beginning in these specimens, the evolution of the geometrical parameters $a$ (cross-sectional radius) and $\rho$ (notch radius of curvature) has been obtained. The progression of neck radius of all the tested specimens is shown in Figure 5.7a for stainless steel 304L and Figure 5.7b for copper C110. It is observed that the neck reduction as a function of equivalent plastic strain is independent of the stress triaxiality since all the curves corresponding to different triaxialities lie on top of each other. This is the expected response, as in the definition of logarithmic strain (Equation 2.28) the sample cross-section and the equivalent strain are directly related and there is no stress triaxiality dependency. The curves only differ on the fracture strain point, represented in the plots by crosses, which becomes smaller for higher triaxialities and is related to the void growth mechanisms described in Section 2.2.1.

The evolution of the other parameter, the notch radius of curvature, is presented in Figure 5.8a for the stainless steel and Figure 5.8b for the copper. Both materials follow similar trends, presenting a small curvature variation the sharper notches (almost no variation for stainless steel), and a considerable radius decrease the smoother geometries. The curvature at fracture is slightly smaller for the copper compared to




**(a)** stainless steel 304L **(b)** copper C110

**Figure 5.7:** Evolution of the minimum radius of the notch cross-section with applied equivalent plastic strain for the different RNB tensile tests; the results are normalised with the initial radius of each sample ($a/a_0$ - $\bar{\varepsilon}_{pl}$).



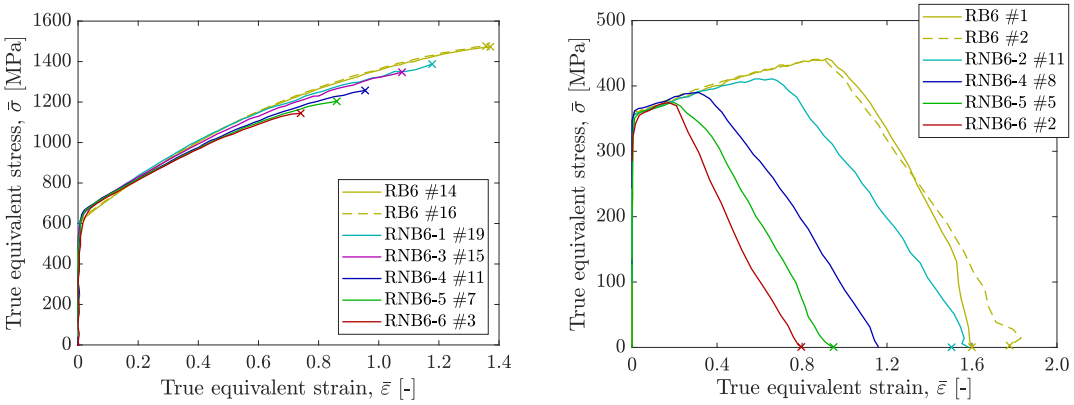

**(a)** stainless steel 304L **(b)** copper C110

**Figure 5.8:** Evolution of the radius of curvature of the notch with applied equivalent plastic strain for the different RNB tensile tests ($\rho$ - $\bar{\varepsilon}_{pl}$).

the stainless steel. For each of the materials all the specimens fail at similar values of curvature, with a slight ascending trend for decreasing triaxialities.

### 5.3.3 Equivalent Stress - Strain

The true stress - true strain curves of all the tests conducted and obtained using the imaging method are presented in Figure 5.9a for stainless steel 304L and Figure 5.9b for copper C110. In Figures 5.7-5.9 the yellow curves correspond to the round bar tensile test and have been previously presented in Figure 5.1 for radius of neck cross-section and radius of curvature, and in Figure 5.4 for stress - strain. The rest of curves




**(a)** stainless steel 304L **(b)** copper C110

**Figure 5.9:** True equivalent stress - true equivalent strain of the RNB tensile tests ($\bar{\sigma}$ - $\bar{\varepsilon}$).

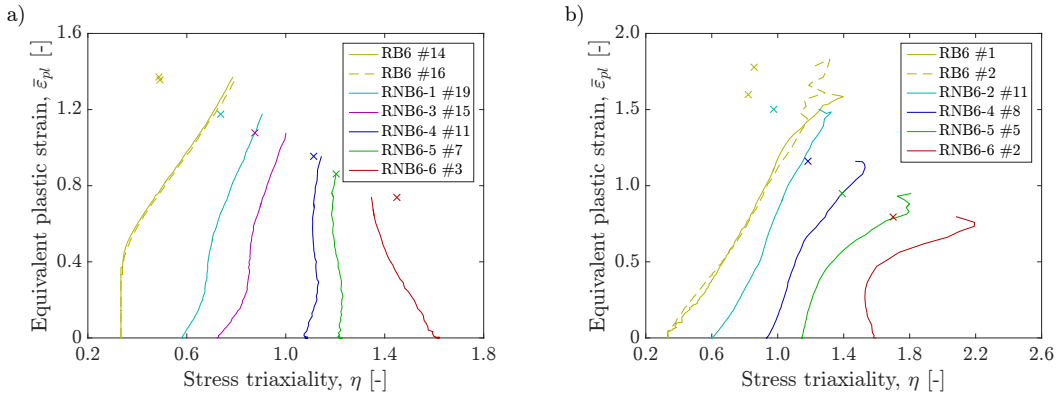
depict the different notch geometries tested, presenting these the expected trend of decreasing fracture equivalent strain for increasing triaxiality already observed in the $a$ and $\rho$ plots. The effective yield stress and the hardening rates are similar for all the specimens regardless of the notch geometry. The failure mode is the same observed in tensile tests and in Figure 5.6, with a brittle and abrupt fracture of stainless steel and a progressive ductile failure of copper.

### 5.3.4 Effect of Stress Triaxiality on Ductility

From a damage modelling point of view, the outcome of highest interest from these experiments is the variation of fracture equivalent strain with stress triaxiality. These results are presented in Figure 5.10, where the stress triaxiality history of each specimen (that has been obtained from the images taken during the experiment) has also been plotted. The crosses represent the fracture strain conditions against the average stress triaxiality throughout the test, which in some cases varies considerably. In many investigations the initial or final stress triaxialities have been used, however, as explained in Section 3.4, this implies a large error for some geometries, and since in this case the triaxiality history is known, the use of an average triaxiality value (Equation 3.4) has been considered the most adequate alternative.

Detailed results with the information presented in Figure 5.10 are also available in Tables 5.4 and 5.5 for stainless steel and copper respectively. For each specimen the theoretical value of stress triaxiality predicted by Equation 3.5 is firstly shown. Since this value changes through the experiment the values of initial, final and average triaxiality calculated with the imaging method are presented. Finally, the fracture

equivalent strain obtained with the imaging technique is shown, and the same value obtained from the post-test shadowgraph measurement is also displayed for comparison and validation.




**(a)** stainless steel 304L **(b)** copper C110

**Figure 5.10:** Variation of stress triaxiality with applied equivalent plastic strain for the different RNB tensile tests, the crosses represent the fracture equivalent plastic strain - average triaxiality ($\bar{\varepsilon}_{pl,f}$ - $\eta_{av}$).

| Geometry | Notch acuity $a/\rho$ | Specimen | Theor. | Imaging | | | | Shadowgr. |
|---|---|---|---|---|---|---|---|---|
| | | | $\eta_0$ | $\eta_0$ | $\eta_f$ | $\eta_{av}$ | $\bar{\varepsilon}_f$ | $\bar{\varepsilon}_f$ |
| RB6 | 0 | #14 | 0.333 | 0.333 | 0.787 | 0.491 | 1.37 | 1.39 |
| | | #16 | 0.333 | 0.333 | 0.796 | 0.494 | 1.36 | 1.34 |
| RNB6-1 | 0.25 | #19 | 0.546 | 0.582 | 0.905 | 0.742 | 1.18 | 1.18 |
| RNB6-3 | 0.417 | #15 | 0.660 | 0.726 | 1.001 | 0.880 | 1.08 | 1.04 |
| RNB6-4 | 0.833 | #11 | 0.892 | 1.084 | 1.144 | 1.117 | 0.96 | 0.96 |
| RNB6-5 | 1.25 | #7 | 1.110 | 1.225 | 1.203 | 1.207 | 0.86 | 0.88 |
| RNB6-6 | 2.5 | #3 | 1.540 | 1.614 | 1.346 | 1.447 | 0.74 | 0.75 |

**Table 5.4:** Stress triaxiality results of stainless steel 304L. Theoretical initial stress triaxiality ($\eta_0$) obtained using Equation 3.5; initial ($\eta_0$), final ($\eta_f$) and average ($\eta_{av}$) stress triaxiality throughout the test obtained using the proposed imaging method; and fracture equivalent strain ($\bar{\varepsilon}_f$) obtained using the proposed imaging technique and the shadowgraph measurements.

| Geometry | Notch acuity $a/\rho$ | Specimen | Theor. | Imaging | | | | Shadowgr. |
|---|---|---|---|---|---|---|---|---|
| | | | $\eta_0$ | $\eta_0$ | $\eta_f$ | $\eta_{av}$ | $\bar{\varepsilon}_f$ | $\bar{\varepsilon}_f$ |
| RB6 | 0 | #1 | 0.333 | 0.333 | 1.397 | 0.823 | 1.60 | 1.69 |
| | | #2 | 0.333 | 0.333 | 1.316 | 0.867 | 1.78 | 1.78 |
| RNB6-2 | 0.313 | #11 | 0.606 | 0.602 | 1.324 | 0.981 | 1.50 | 1.49 |
| RNB6-4 | 0.833 | #8 | 0.958 | 0.936 | 1.530 | 1.198 | 1.16 | 1.19 |
| RNB6-5 | 1.25 | #5 | 1.173 | 1.147 | 1.808 | 1.403 | 0.95 | 0.98 |
| RNB6-6 | 2.5 | #2 | 1.532 | 1.586 | 2.081 | 1.721 | 0.80 | 0.77 |

**Table 5.5:** Stress triaxiality results of copper C110. Theoretical initial stress triaxiality ($\eta_0$) obtained using Equation 3.5; initial ($\eta_0$), final ($\eta_f$) and average ($\eta_{av}$) stress triaxiality throughout the test obtained using the proposed imaging method; and fracture equivalent strain ($\bar{\varepsilon}_f$) obtained using the proposed imaging technique and the shadowgraph measurements.

## 5.4 Damage Accumulation Tests

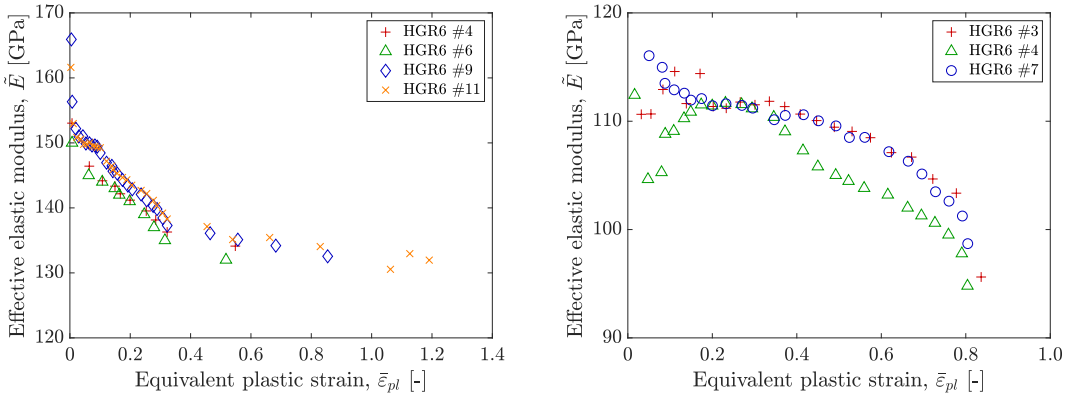
The outcome of this experiment is the evolution of ductile damage, accumulated in the form of voids and microcracks, as the equivalent plastic strain progresses in the uniaxial tensile loading case. These results characterise the degradation process that occurs between damage initiation and final fracture. The hourglass shaped round specimen geometry has been used for this analysis. An alternative method to measure damage has been considered using DIC on hourglass flat samples, and its results have been presented in Section 5.4.2. A summary of all the specimens tested and the post-processing techniques employed for each of them is presented in Table 5.6.

| Material | Geometry | Specimen | $D$-$\bar{\varepsilon}_{pl}$ measurement | |
|---|---|---|---|---|
| | | | Extensom. | DIC |
| s/s 304L | HGR6 | #4 | x | |
| | | #6 | x | |
| | | #9 | x | |
| | | #11 | x | |
| | HGF6 | #13 | | x |
| | | #19 | x | |
| | | #20 | x | |
| copper C110 | HGR6 | #3 | x | |
| | | #4 | x | |
| | | #7 | x | |

**Table 5.6:** Specimens studied in the quasi-static room temperature damage accumulation analysis.

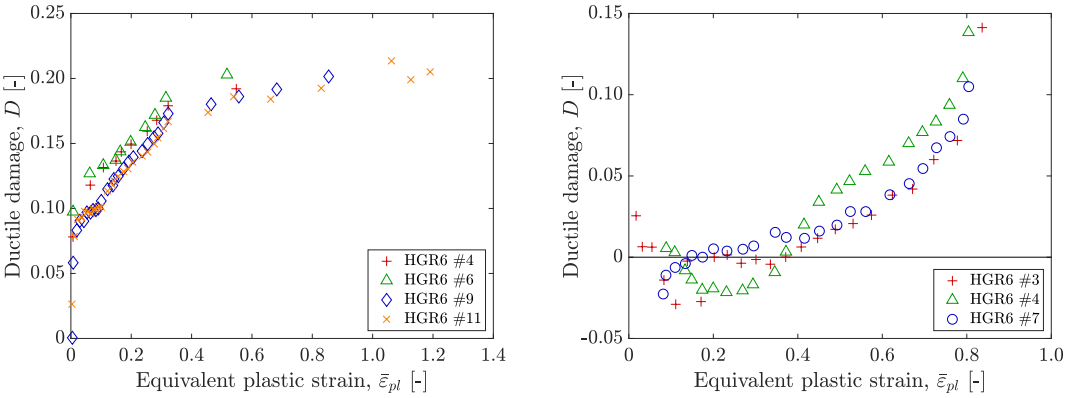
### 5.4.1 Damage Accumulation Measurement Using Extensometer

The continuous testing methodology for the measurement of elastic modulus with a small extensometer that was described in Section 3.5 has been used to obtain these results. Elastic modulus values obtained from the experiments are presented in Figure 5.11, and the associated ductile damage values calculated from them in Figure 5.12. The same damage results are presented in Figure 5.13 in the form of mean and standard deviation results instead of representing every data point, so that the trend of damage evolution can be more easily appreciated. To take into account the effects of strain localisation when post-processing these results, the neck correction curves of Figure 5.5 have been used. As observed, the repeatability of results is quite good in the case of stainless steel and the results display a similar shape to that presented in [92] for an-



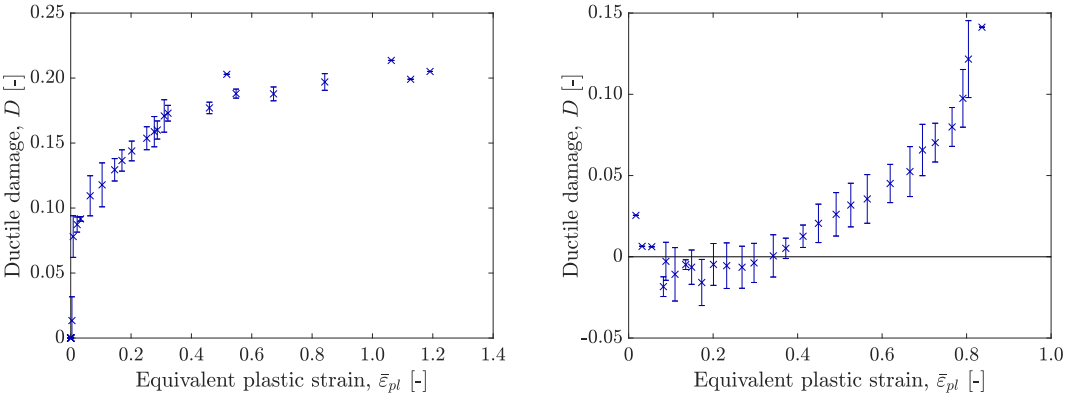

**(a)** stainless steel 304L **(b)** copper C110

**Figure 5.11:** Effective elastic modulus - equivalent plastic strain ($\tilde{E}$ - $\bar{\varepsilon}_{pl}$) experimental results.




**(a)** stainless steel 304L **(b)** copper C110

**Figure 5.12:** Ductile damage - equivalent plastic strain ($D$ - $\bar{\varepsilon}_{pl}$) experimental results.




**(a)** stainless steel 304L **(b)** copper C110

**Figure 5.13:** Ductile damage mean and standard deviation - equivalent plastic strain ($D$ - $\bar{\varepsilon}_{pl}$) experimental results.

other steel. In the case of copper, results show a bigger scatter, and the trend observed is clearly different to that of stainless steel. A very similar material was also studied in [88, 92], and the behaviour reported is in close agreement with that obtained in the present research.

The stainless steel shows a prominent initial increase of damage that progressively stabilises to a quite low critical damage value, while for the copper, damage does not appear at the early stages of deformation and then increases fairly linearly. This exemplifies the different damage accumulation behaviours that diverse materials can present and the requirement of a non-linear damage growth model that allows to modify the shape of the accumulation. The appearance of ductile damage at initial stages of plasticity is generally associated to the nucleation of voids due to the fracture or debonding of particles within the material. The results suggest that these defects appear in stainless steel 304L as soon as plastic deformation is applied, however, some plastic strain has to be applied to copper C110 before damaging the material. These observations have been validated through a metallographic study that is discussed in Section 5.5.

It can be observed in Figure 5.12b that there are no damage measurements beyond an equivalent plastic strain of $\bar{\varepsilon}_{pl} \sim 0.9$. The reason is that from that point onwards the material is so degraded that unloading and reloading cycles cannot be performed without fracturing the specimen. This definite loss of load carrying capacity can be appreciated in Figure 5.4b.

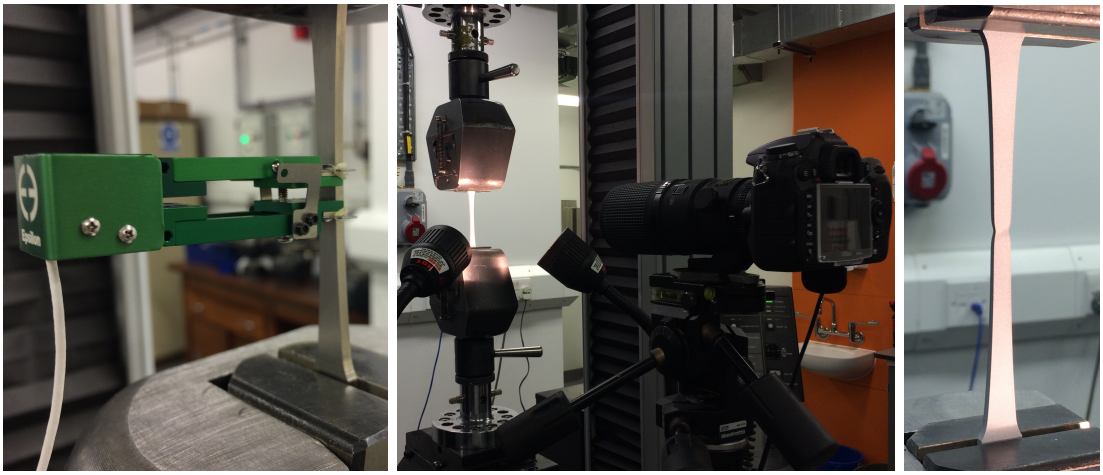
### 5.4.2 Damage Accumulation Measurement Using Digital Image Correlation

Digital image correlation has also been explored as a method for ductile damage accumulation measurement. Damage has also been calculated from the degradation of elastic modulus, however, the strain is obtained using DIC instead of an extensometer. The aim was to investigate a non-contact modulus measurement method that could be applied at high strain-rate. For that purpose, some flat hourglass specimens (HGF6) have been tested using both the extensometer and DIC techniques to measure strain for elastic modulus calculation. Figure 5.14 shows some pictures of the measurement techniques involved in these experiments.

The results obtained are presented in Figure 5.15a in terms of elastic modulus degradation and in Figure 5.15b in damage accumulation. Firstly, it can be observed that the scatter in the results is much higher with flat specimens than with round specimens. When using the extensometer to measure strain, it is attached to the surface of the sample by means of flat knife edges. Nevertheless, the deformation is not uniform in the line of contact between edge and specimen, producing small slips of the extensometer that lead to some noise in the results. However, the trend followed by the damage accumulation results and their order of magnitude has been the same for both round and flat geometries.

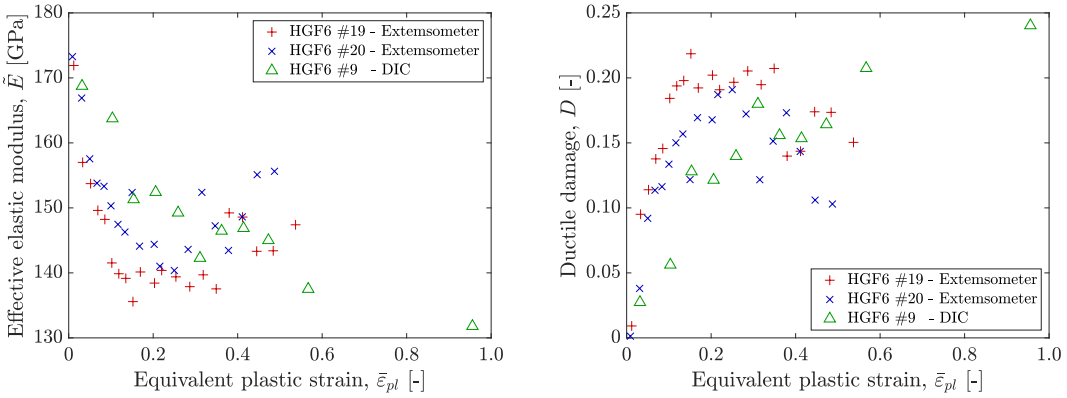
DIC technique has also proven to be relatively inaccurate for the measurement of elastic modulus changes. The variations in elastic strain that have to be detected are of very small magnitude and even the high resolution images used for this experiment provide quite scattered effective modulus results. The aim would have been to apply this method to high strain-rate conditions, however, the resolution of high-speed cameras is lower if pictures are taken at a high frame rate, probably leading to even more scattered results. Also, as it has been discussed in Section 4.2.5, it is impossible to perform continuous tensile tests with loadings and unloadings at very high speed and, therefore, the DIC technique has not been explored further as a method for damage accumulation measurement. Round instead of flat hourglass specimens have been used in the rest of experiments due to their axisymmeteric properties, and to keep the consistency with the specimens used for the other experiments (RB and RNB geometries).

An advantage of this method compared to the use of a clip gauge extensometer is that it is possible to take direct measurements of local strain. This has made possible the calculation of the last data point in Figure 5.15, which corresponds to a plastic strain where necking is already developing. For the damage analysis of round specimens the neck correction curves presented in Figure 5.5 have been required in order to account for this effect, while if DIC is used it is not necessary.



**(a)** Small gauge extensometer arrangement **(b)** 2D digital image correlation arrangement **(c)** Necking process

**Figure 5.14:** Damage accumulation measurement in stainless steel 304L flat samples.




**(a)** Effective elastic modulus - equivalent plastic strain ($\tilde{E}$ - $\bar{\varepsilon}_{pl}$) **(b)** Ductile damage - equivalent plastic strain ($D$ - $\bar{\varepsilon}_{pl}$)

**Figure 5.15:** Ductile damage analysis of stainless steel 304L HGF6 samples.

## 5.5 Damage Validation and Comparison Tests

As explained in Chapter 2, a variety of methods have been proposed to quantify damage accumulation. In this section, an alternative technique to the elastic modulus measurement has been applied, and damage has been measured through porosity estimations obtained from a metallographic study. A summary of the specimens investigated using this method is provided in Table 5.7.

It must be noted that, unlike the elastic modulus technique, this method is destructive, since it requires to cut a slice of the material for its ex-situ analysis. This means

| Material | Geometry | Specimen | Plastic strain, $\varepsilon_{pl}$ [-] |
|---|---|---|---|
| s/s 304L | HGR6 | #34 | 0.110 |
| | | #33 | 0.214 |
| | | #32 | 0.384 |
| | | #36 | 0.673 |
| | | #31 | 0.993 |
| | | #37 | 0.993 |
| | | #6 | 1.292 |

**Table 5.7:** Specimens studied in the quasi-static room temperature damage validation analysis.

that the method is more expensive, as a sample provides information of only one condition. The specimens preparation and measurement is also time consuming, although more information can be extracted, such as spatial damage distribution. For all those reasons and its relative simplicity, the measurement of changes in elastic modulus has been chosen as the main experiment for ductile damage measurement in this research, however, the porosity results discussed in this section have been used for comparison and validation.

### 5.5.1 Specimens Preparation

Round hourglass specimens (HGR6) of stainless steel 304L have been used for the porosity analysis. Several specimens have been plastically deformed to the plastic strain levels specified in Table 5.7 in the same quasi-static and room temperature conditions used to obtain the results of Section 5.4. After being strained, the central region of the specimens was cut using a Struers Accutom-5 high precision cut-off machine. Six specimens have been cut perpendicularly to the tensile loading direction across the central cross-section of the neck, and one has been cut parallely through the central plane containing the specimen axis to check damage distribution in the longitudinal direction.

The specimens have then been mounted in Bakelite using an ATA Opal 410 automatic mounting press. An ATA Saphir 520 semi-automatic metallographic grinder and polisher has been used to prepare the surface of the samples. Since they are quite small and the cut is generally clean, very short initial grinding stages have been required. Samples have been polished down to 0.1 µm using OP-S colloidal silica suspension as final stage. The details of the different grinding and polishing stages are presented in Table 5.8.

| Abrassive | Pressure [N] | Speed - Dir. [rpm] | Time [min] |
|---|---|---|---|
| P360 SiC paper | 5 | 150 - comp. | 0 : 20 |
| P800 SiC paper | 5 | 150 - comp. | 1 : 00 |
| P2400 SiC paper | 5 | 150 - comp. | 1 : 00 |
| 6 µm w.b. diamond | 5 | 150 - comp. | 3 : 30 |
| 3 µm w.b. diamond | 5 | 150 - comp. | 3 : 30 |
| 1 µm w.b. diamond | 5 | 150 - comp. | 3 : 30 |
| 0.1 µm OP-S suspension | 5 | 100 - comp. | 20 : 00 |

**Table 5.8:** Details of the grinding and polishing stages followed to prepare specimens.

### 5.5.2 Post-process Methodology

Once the samples have been polished, a Zeiss compound optical microscope has been used to take pictures of their microstructure. The main objective of the investigation has been to quantify the porosity or void density in the micrographs, defined as percentage of the total area occupied by voids (definition of Equation 2.21 and Figure 2.7). A thresholding algorithm has been programmed in Matlab for that purpose, which has been used to batch process the images from the microscope. Measurements of porosity have been taken in different locations of the specimen's section. Figure 5.16a shows the grid of points analysed in each specimen in order to construct cross-sectional porosity distribution maps. The same information is presented in Figure 5.16b for the analysis in the longitudinal plane. The intention has been to calculate the radial and longitudinal distributions of porosity/damage within the sample. Finally, the results for all the specimens have been represented together against plastic strain ($\varphi$ - $\bar{\varepsilon}_{pl}$) to analyse the evolution of void fraction along the plastic region.

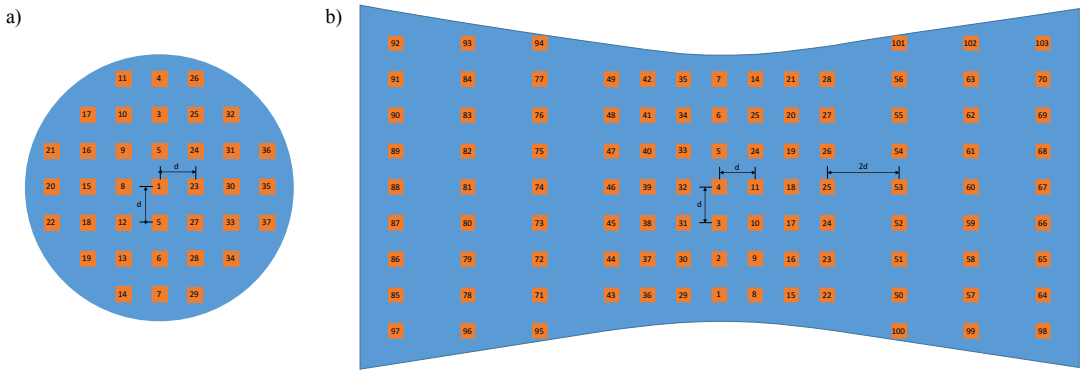
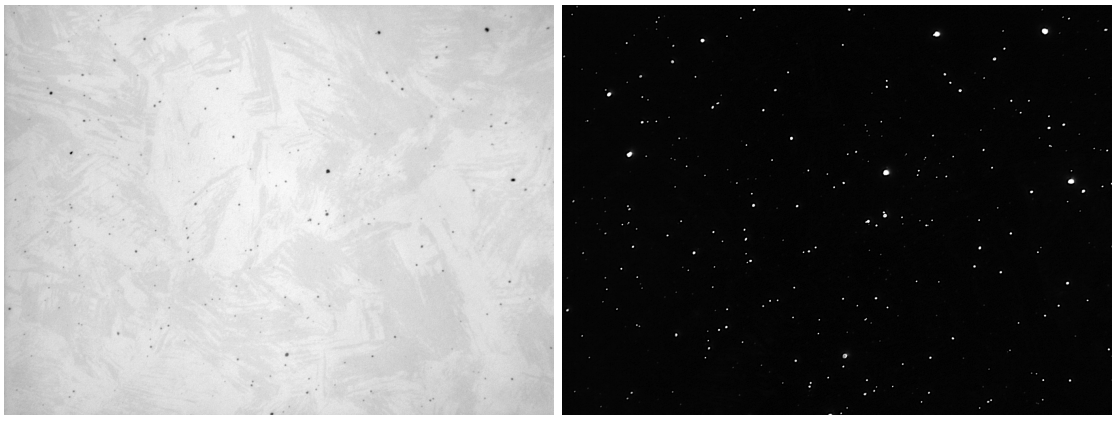



**Figure 5.16:** Grid of locations analysed to obtain porosity maps in the sample (a) cross-section and (b) longitudinal-section.

Dark-field microscopy has been found very useful to detect voids, since the images have provided an improved contrast, making it easier to differentiate the defects from the material during the thresholding process. Figure 5.17 shows a comparison of the same image taken using bright and dark-field microscopy, where it can be observed that other microstructural features of the material disappear in the dark-field image. The thresholding process can be observed in Figure 5.18. A 50x magnification has been selected for the research, since it provides a region of intermediate size, yielding very similar porosity values as the 20x and 100x images, which were considered too big and too small respectively. A square region of size 156 µm x 156 µm in the centre of the picture has been analysed, as observed in Figure 5.18, in order to avoid brightness and contrast peaks from the corners. The threshold value used in the images post-processing has been calibrated by analysing the zoomed-in image of individual voids, both in the original and the thresholded picture. Their size has been compared and the threshold modified until the size of both voids has been reasonably similar, as shown in Figure 5.19.

This methodology has been used to analyse porosity in two specific cases: the cross-section of a fractured specimen (Section 5.5.3) and a longitudinal slice of a necked specimen (Section 5.5.4). The objective in both cases has been to study the void density distribution inside these severely damaged samples. Moreover, a more quantitative porosity analysis has been performed over a series of samples strained to different levels of plastic strain (Section 5.5.5). The aim in this case has been to validate the damage accumulation results obtained from elastic modulus measurements in Section 5.4.



**(a)** Bright-field micrograph ($\varphi = 0.0036$). **(b)** Dark-field micrograph ($\varphi = 0.0038$).

**Figure 5.17:** Comparison of bright and dark field microscopy for porosity calculation of the same stainless steel 304L micrograph with a 50x magnification.

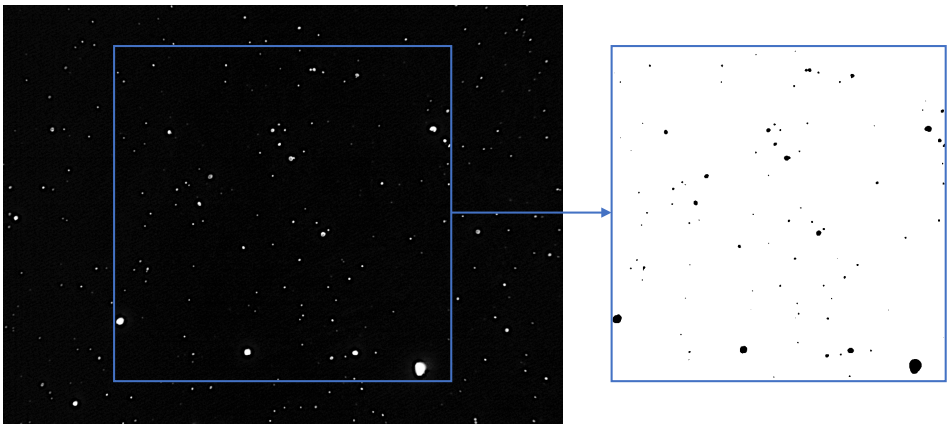


**Figure 5.18:** Thresholding process used to estimate porosity from micropgraphs ($\varphi = 0.0059$).

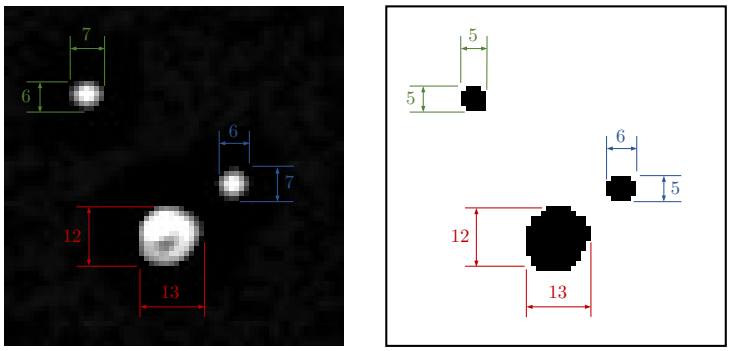



**Figure 5.19:** Size comparison of individual voids in the original and thresholded pictures for the calibration of the intensity threshold value; numbers represent size in pixels.

### 5.5.3 Porosity Study of a Fractured Specimen

A tensile test to fracture has been carried out on a stainless steel 304L specimen (HGR6 #6) in quasi-static and room temperature conditions. A metallographic picture of the sample cross-section just below its fracture section is presented in Figure 5.20. Qualitatively, a higher void concentration in the centre of the specimen than in the external regions can be observed, as shown in the 100x magnification details. The fairly uniform distribution of small voids agrees with the fracture surface studied in Figure 5.6, earlier in this chapter.

By taking pictures across the cross-section, as specified in Figure 5.16a, and analysing the porosity value of each of them following the thresholding procedure, the results presented in Figure 5.21 have been obtained. Figure 5.21a shows the spatial

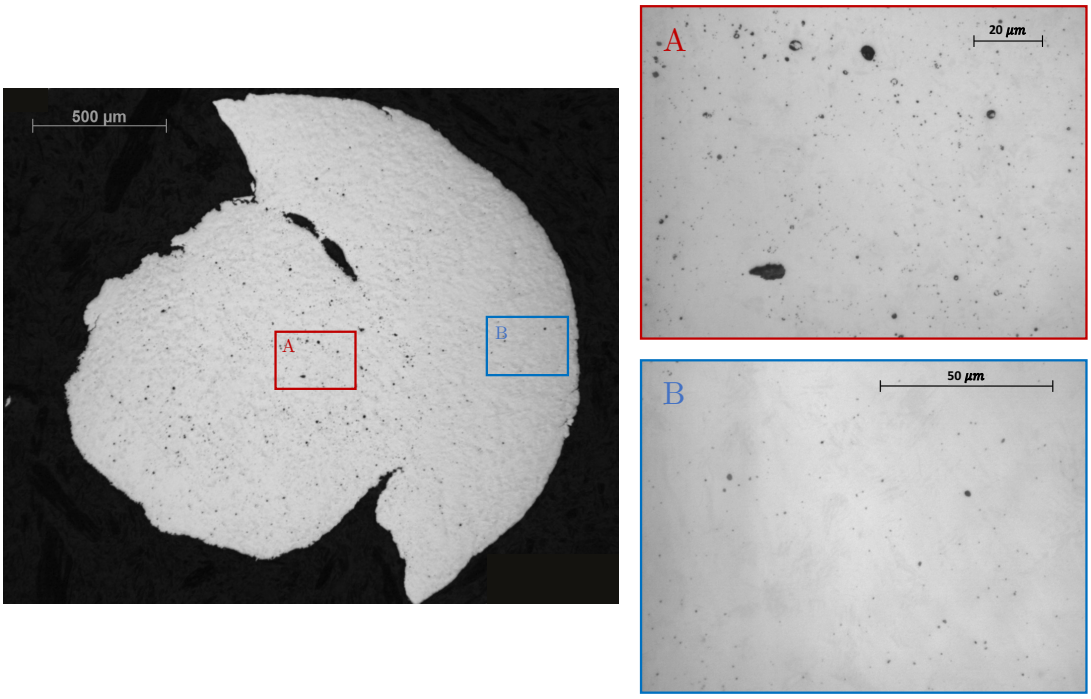
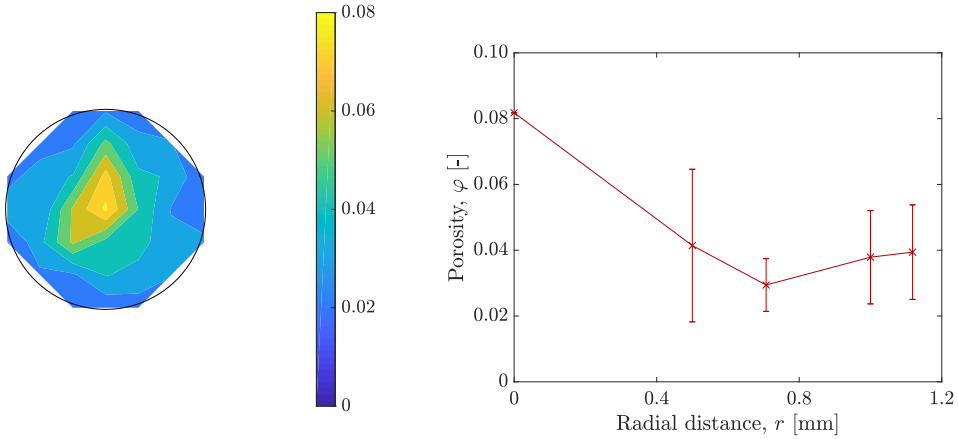



**Figure 5.20:** Porosity below the fracture cross-section of a stainless steel 304L specimen; porosity details in the centre and near the surface of the sample at 100x magnification.




**(a)** Porosity map

**(b)** Porosity radial distribution.

**Figure 5.21:** Porosity analysis of a fractured stainless steel 304L specimen.

void density distribution across the section, and Figure 5.21b the mean and standard deviation values of radial distribution. The highest concentration of voids occurs in the centre, and in this case, it can be quantified around $\varphi \sim 0.08$. Porosity decreases when moving away from the centre; however, the damage level of external regions is considerable ($\varphi \sim 0.04$) when compared to the unstrained specimens, as will be discussed in Section 5.5.5.

### 5.5.4 Porosity Study of a Necked Specimen

An interrupted tensile test has been run on a stainless steel 304L specimen (HGR6 #37) in quasi-static and room temperature conditions. The test has been run as usual, nonetheless, it has been stopped when the neck was sufficiently developed, at an equivalent plastic strain of $\bar{\varepsilon}_{pl} = 0.993$. The sample has then been unloaded, cut and polished as previously explained. A metallographic reconstruction of the longitudinal mid-plane is presented in Figure 5.22. Micrographs have been taken in the locations specified in Figure 5.16b, and after their post-process, the porosity map of Figure 5.23 has been obtained.

Three detail images passing approximately through the sample axis have been included in Figure 5.22 (details A, B and C). By comparison, a higher concentration of voids in the centre of the neck (C) can be observed. While the void density decreases quickly when moving away from the centre, some voids are still observed in A. Those are the voids that appear in the material during its uniform deformation phase, before necking starts, and are uniformly distributed throughout the whole specimen. The same behaviour can be more easily appreciated in the contours of Figure 5.23 and in Figure 5.24a. In the latter, the porosity distribution along the axis is plotted, as well as the mean and standard deviation at each longitudinal position taking into account all the measurements taken across the cross-section. In this last representation, high magnitude and high dispersion appears in the centre of the neck, and low magnitude and low dispersion when moving away from it. This highlights the lower and uniform values of damage away from the neck, in the order of $\varphi \sim 0.005$, and the damage peak in the centre of the neck with decreasing concentration near the edges.

The radial distribution of porosity has been studied in a similar manner, in the details C, D and E of Figure 5.22, the contours of Figure 5.23 and the voids distribution of Figure 5.24b. In the details, a high density of voids is observed in C and D, and almost no voids in E. In Figure 5.24b, the radial porosity through the centre of the neck is plotted and also the mean and standard deviation of all the values taken at the same radial distance from the axis. A very similar behaviour to that analysed in the longitudinal direction is observed in the radial direction, with lower density of voids and lower dispersion near the surface and high concentration in the centre.

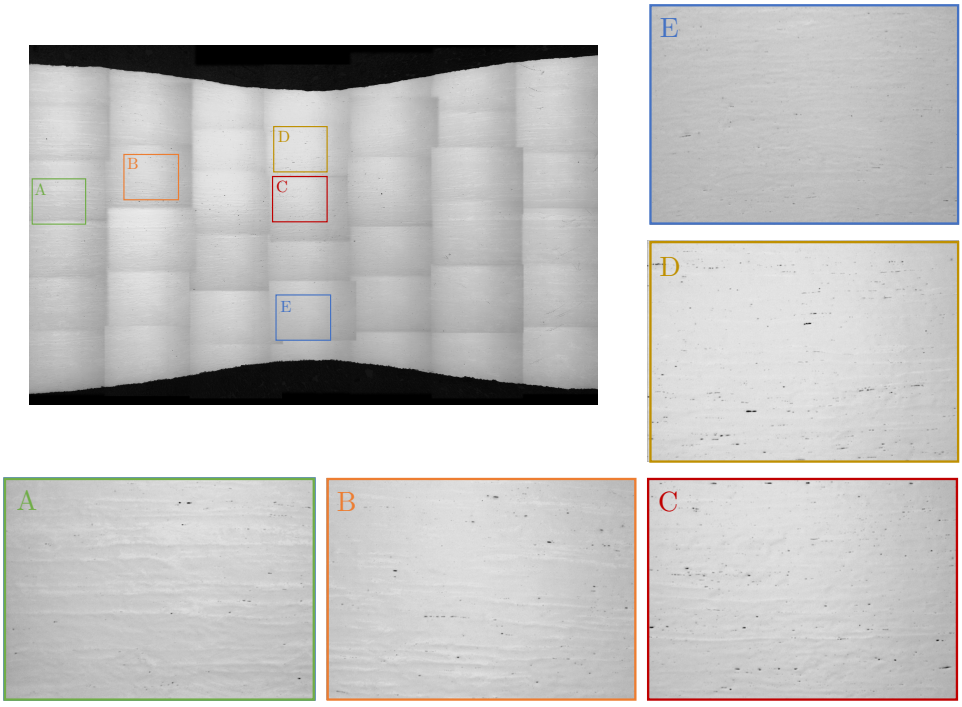



**Figure 5.22:** Porosity in the longitudinal mid-plane of a stainless steel 304L necked specimen ($\bar{\varepsilon}_{pl} = 0.993$); details A,B & C approximately in the specimen axis and details C, D & E in the central cross-section of the neck.

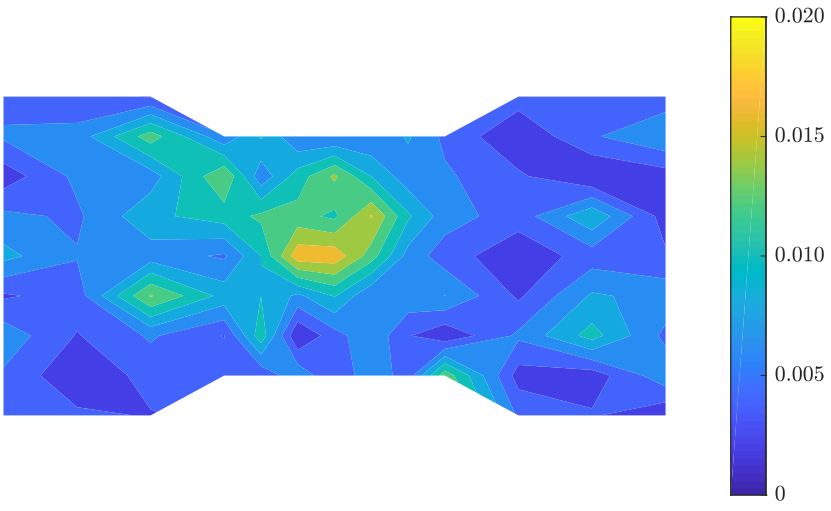
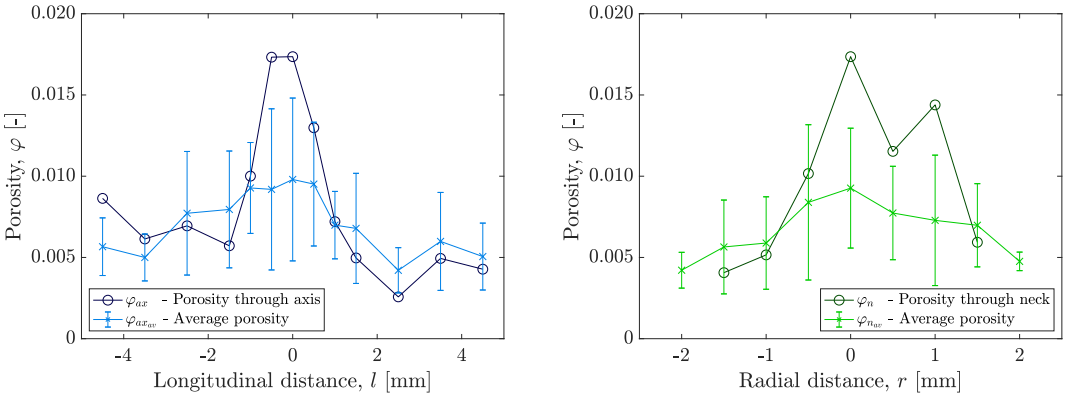



**Figure 5.23:** Contours of porosity in the longitudinal slice of a necked specimen ($\bar{\varepsilon}_{pl} = 0.993$).




**(a)** Longitudinal distribution of porosity.

**(b)** Radial distribution of porosity.

**Figure 5.24:** Distributions of porosity in the longitudinal slice of a necked specimen ($\bar{\varepsilon}_{pl} = 0.993$).

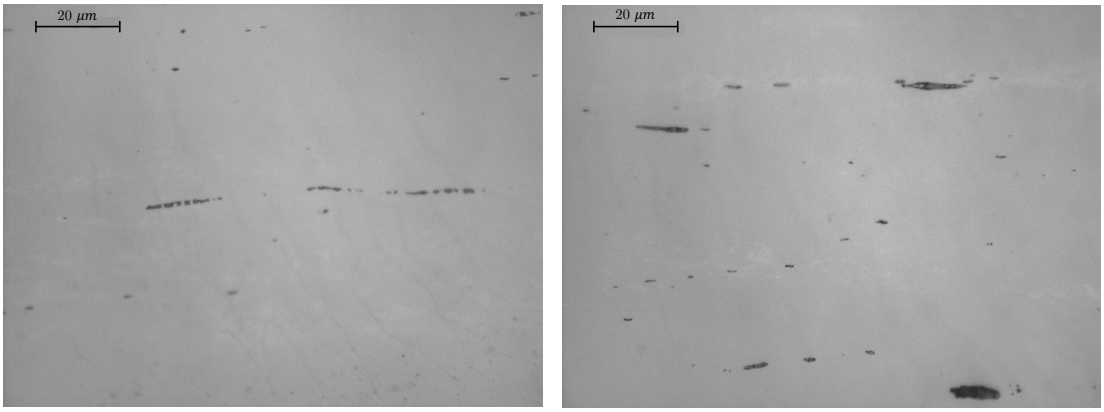



**Figure 5.25:** 100x magnification micrographs of the centre of the neck in a stainless steel 304L specimen strained to $\bar{\varepsilon}_{pl} = 0.993$.

The shape of the voids can also be analysed from Figure 5.22. While the rest of samples have been studied in transversal direction and voids present an almost circular shape, in this longitudinal analysis the elongated shape of voids is appreciated. These features can clearly be seen in details C and D of Figure 5.22 and in the zoomed in images of Figure 5.25, which have been taken in the centre of the sample at a 100x magnification. The elongation of the microstructure of the material due to the tensile load can also be appreciated in Figure 5.22, as well as its directionality following the shape of the neck, leaving grain orientations similar to those obtained in metal forming processes.

### 5.5.5 Porosity Study of Damaged Specimens

Void density has been studied in seven specimens deformed to increasing levels of plastic deformation by carrying out interrupted tensile tests. The first specimen corresponds to the non-deformed raw material, while the last one is the fractured specimen studied in Section 5.5.3; the rest of tests lie in between those extreme cases, as specified in Table 5.7. The post-process of micrographs has provided the porosity contour maps of Figure 5.26. In these plots, the final diameters of all samples are proportional to the real values for an easier comparison. The colour scale is also the same in all of them except in the last one, which presents much higher void density than the rest. The radial distribution of void density of all the samples studied has been plotted in Figure 5.27.

The first specimen corresponds to the raw material, hence its almost perfectly uniform and very low porosity, that can be attributed to the inherent defects in the material resulting from the manufacturing process. As observed in Figure 5.26, porosity is also fairly uniform in the cross-section of the following four specimens. This can also be appreciated in Figure 5.27, where the radial distribution is approximately flat. These specimens have undergone plasticity, and the lighter blue in the porosity contours shows the higher void density. Nevertheless, they lie within the uniform deformation plastic range before localisation occurs, resulting in uniform damage accumulation in the form of voids throughout the material.[1] Finally, the last two specimens were deformed beyond the necking limit, presenting a much higher porosity in general, and a higher concentration in the centre of the specimen than near its surface. This effect is subtle at $\bar{\varepsilon}_{pl} = 0.99$, but becomes significant in the fractured specimen ($\bar{\varepsilon}_{pl} = 1.29$), which was already analysed in Section 5.5.3 and shows a peak void density of 0.08 in its centre. In the analysis of a necked specimen of Section 5.5.4 it was observed that the porosity far from the neck presented a value around $\varphi \sim 0.005$. If the contours of Figure 5.26 are analysed, the porosities measured when uniform deformation is taking place have a very similar value, confirming that the localisation of porosity occurs only in the centre of the neck, which is the region of highest stress triaxiality.

The porosity results discussed so far in this section have been plotted together in Figure 5.28a, where the evolution of void density along the plastic range can be analysed. For each sample, the average and standard deviation of all the measurements in the cross-section, and also the measurement in the centre of the specimen, have been represented. While in the tests with relatively low plasticity the scatter within the

[1] Sample HGR6 #36 does lie within the early stages of necking, according to the results obtained in Section 5.2.1, which estimate the onset of necking around $\varepsilon_{onset} \sim 0.35 - 0.38$ for this material. However, this study suggests that either the concentration of voids only increases in the centre at a later necking stage, or that the resolution of porosity calculation is not high enough to detect such small changes.

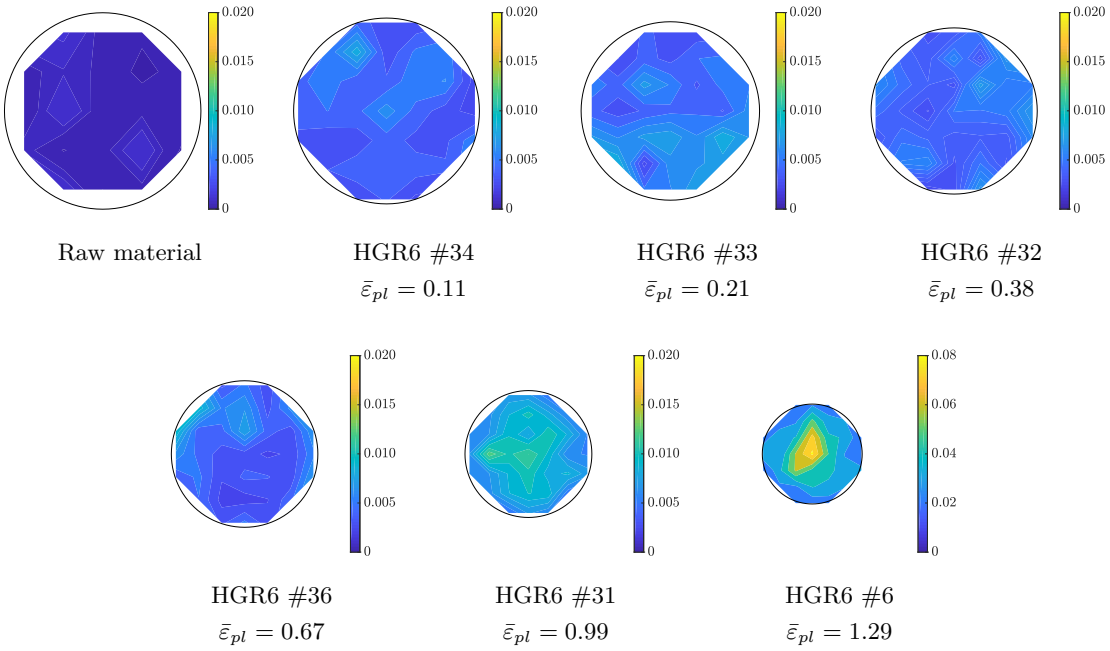



**Figure 5.26:** Contours of porosity in the cross-section of the analysed specimens.

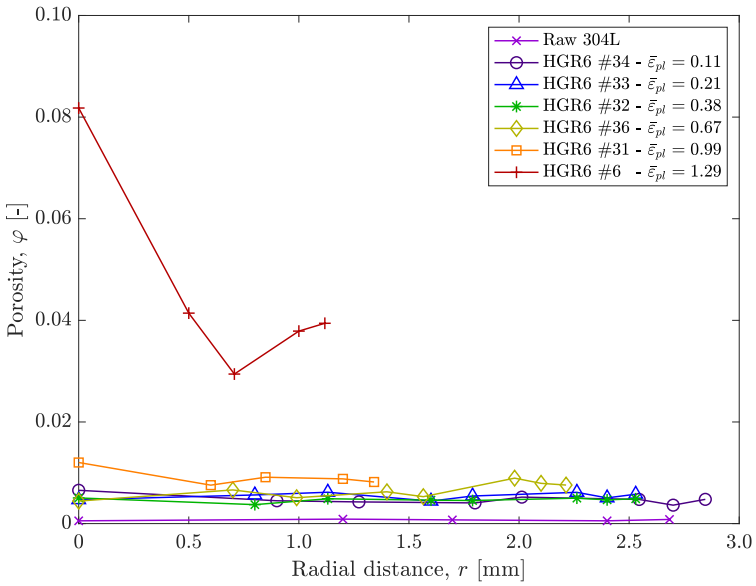
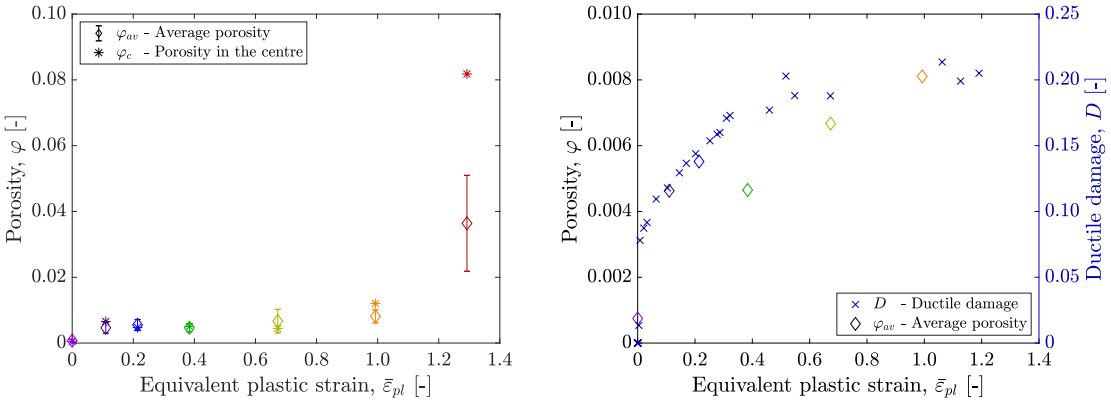



**Figure 5.27:** Radial distribution of porosity in the specimens studied in Figure 5.26.




**(a)** Porosity - equivalent plastic strain ($\varphi$ - $\bar{\varepsilon}_{pl}$) of the different specimens analysed. **(b)** Comparison of the porosity and ductile damage accumulation behaviours.

**Figure 5.28:** Analysis of the porosity and ductile damage evolution with equivalent plastic strain.

cross-section is very low, the higher the plasticity, the higher the concentration of voids in the centre, and hence the higher the deviation from the average and the higher the porosity in the centre compared to that average. It can be observed that void density increases considerably when plasticity is first applied, and it stabilises afterwards in a plateau region, until it increases further near fracture.

In Figure 5.28b the same data is represented zoomed in for porosities lower than $\varphi = 0.01$, i.e. for the analysis of the early plasticity region. In this figure, the ductile damage results obtained in Section 5.4.1 by measuring changes in elastic modulus have also been included. Although the macroscopic ductile damage affecting the mechanical properties of the materials is not of the same order of magnitude of the density of voids, both present the same trend. These results prove that the ductile damage measured from elastic modulus degradation is driven by voids nucleation, growth and coalescence. However, they also suggest that the reduction of mechanical properties does not take exactly the same value as the area reduction that these voids produce in the cross-section, as is generally asserted by continuum damage mechanics formulation through Equation 2.21. Therefore, additional degradation processes linked to the density of voids, but not entirely to the area that they occupy, have to be responsible of the reduction of material properties. From the degradation of elastic modulus, which is an actual macroscopic quantifiable property, a value of ductile damage can be obtained and used in material models to perform useful engineering calculations. The microscopic analysis carried out in this section serves as validation of the trends followed by the ductile damage parameter, but it is considered that the elastic modulus approach can provide a more real representation of the real macroscopic operation of components.

## 5.6 Conclusions

In this chapter, the proposed methodology has been tested on stainless steel 304L and copper C110 in the standard conditions of quasi-static strain-rate ($\dot{\varepsilon} \sim 10^{-2}$ s$^{-1}$) and room temperature ($T \sim 20$°C). Firstly, the plastic behaviour of these materials has been studied in tensile tests including the effects of necking up to fracture. From the images taken during the test more information can be extracted than using the traditional approach, such as the evolution of stress triaxiality and the real true equivalent stress - strain. Some materials, such as the studied stainless steel, present a region of uniform deformation where the traditional method is applicable, however, after the onset of necking, the behaviour differs extremely if neck corrections are not performed. Other materials, such as copper, develop the neck almost as soon as the material begins to deform plastically, being the imaging method even more beneficial for accurate calculations and hardening models calibration.

Once plasticity has been studied in uniaxial tests, the effect of stress triaxiality on plasticity, and especially on ductile fracture, has been analysed through tensile tests on notched specimens. Different notch geometries have produced theoretical triaxialities ranging from 0.33 to 1.5, and thanks to the imaging technique, the evolution of triaxiality during the test has been calculated. This parameter can change considerably when the material is plastically deformed, and the results demonstrate that the assumption that it stays approximately constant is not acceptable. An average value that takes into account the stress state history has been used as a better representation of the ductile fracture conditions. The fracture plastic strain of each test has been obtained using the imaging approach and also post-test measurements have been taken using a shadowgraph. The results obtained are very similar, serving as validation of the imaging method.

Finally, the ductile damage evolution that occurs during plasticity has been studied by measuring changes in the elastic modulus of the material. The great diversity in the shape of this curve for different materials has been proven by the results obtained for stainless steel and for copper, presenting early damage that then stabilises the first one, and no initial damage followed by a linear accumulation the second one. This suggests that voids appear in stainless steel as soon as plastic strain is applied, but their size does not change for most of the plastic region, as confirmed by the observations from microscopic measurements. On the other hand, no voids are initially formed in copper until a certain plastic deformation level is reached, growing progressively afterwards. These behaviours highlight the need of a non-linear adjustable model for ductile damage that can be tuned for diverse materials. The experimental measurements have been validated by means of a metallographic study, which has provided estimations of porosity or void density along the plastic deformation process. From the results obtained,

it can be concluded that the trends followed by the increase in void density and the degradation of elastic modulus are coincident. However, the magnitude of modulus decrease is much higher than that of porosity increase, suggesting that void density does determine the shape of damage accumulation, but additional degradation phenomena proportional to void density occur within the material.

# Chapter 6

# Experimental Results - Strain-Rate Effect

## 6.1 Introduction

In this chapter, the effects of strain-rate on the behaviour of materials are analysed based on the experimental results obtained. The methodology described in Chapter 3 is followed, combined with the modifications discussed in Chapter 4, specific to the high-speed tests. A study of strain-rate effect on plasticity can be found in Section 6.2, the effects on ductile fracture are discussed in Section 6.3 and finally the ductile damage accumulation behaviour is covered in Section 6.4; some conclusions are presented in Section 6.5. Three strain-rate conditions have been tested in most of the experiments, and from now on are referred to as: quasi-static ($\dot{\varepsilon} \sim 10^{-3}$ s$^{-1}$), intermediate rate ($\dot{\varepsilon} \sim 10^{2}$ s$^{-1}$) and high rate conditions ($\dot{\varepsilon} \sim 10^{3}$ s$^{-1}$). It must be noted that the strain-rate value varies along a test and an average value has been used to categorise each test. These values can differ significantly depending on the test, but they have been grouped in one of the above categories, as long as they have the same order of magnitude. All the tests discussed in this chapter have been run in room temperature conditions ($T \sim 20$°C) on stainless steel 304L and copper C110 materials. The experimental results presented in this chapter will later be used in Chapter 8 to include the effect of strain-rate on material models.

## 6.2 Strain-Rate Effect on Plasticity

The imaging methodology outlined in Section 3.3 has been used to quantify the geometry of the neck during the tests. However, unlike in quasi-static conditions, in

intermediate and high rate conditions the in-situ shadowgraph approach explained in Section 4.2.3.3 has been incorporated to improve the quality of the images taken. The quasi-static strain-rate results are those obtained in Section 5.2 using RB6 specimens, while RB3.5 geometry has been used for the higher rates. The tests that have been run for this analysis are presented in Table 6.1, along with the average strain-rate achieved and the processing methods used for each of them. The resolution and frame-rate used to acquire images in the different test conditions are shown in Table 6.2. As explained before, image resolution has been sacrificed in high-speed tests in order to achieve a higher frame rate, hence the processing algorithm explained in Section 4.2.4.2 being required for improved quality.

| Material | Geom. | Spec. | Strain-rate, $\dot{\varepsilon}_{av}$ [$s^{-1}$] | $\sigma$-$\varepsilon$ measurement | | |
|---|---|---|---|---|---|---|
| | | | | Imaging | Video-Extens. | DIC |
| s/s 304L | RB6 | #14 | $6.28x10^{-3}$ | x | | |
| | | #16 | $6.15x10^{-3}$ | x | | |
| | | #12 | $9.21x10^{-4}$ | | x | |
| | | #13 | $7.21x10^{-4}$ | | x | |
| | RB3.5 | #1 | $2.99x10^{1}$ | | | x |
| | | #2 | $3.03x10^{2}$ | x | x | x |
| | | #3 | $2.94x10^{2}$ | x | x | |
| | | #5 | $3.79x10^{3}$ | x | | |
| | | #6 | $4.37x10^{3}$ | x | | |
| copper C110 | RB6 | #1 | $1.05x10^{-2}$ | x | | |
| | | #2 | $1.12x10^{-2}$ | x | x | |
| | RB3.5 | #1 | $4.80x10^{2}$ | x | | |
| | | #2 | $6.34x10^{2}$ | x | | |
| | | #4 | $8.11x10^{3}$ | x | | |
| | | #5 | $7.40x10^{3}$ | x | | |

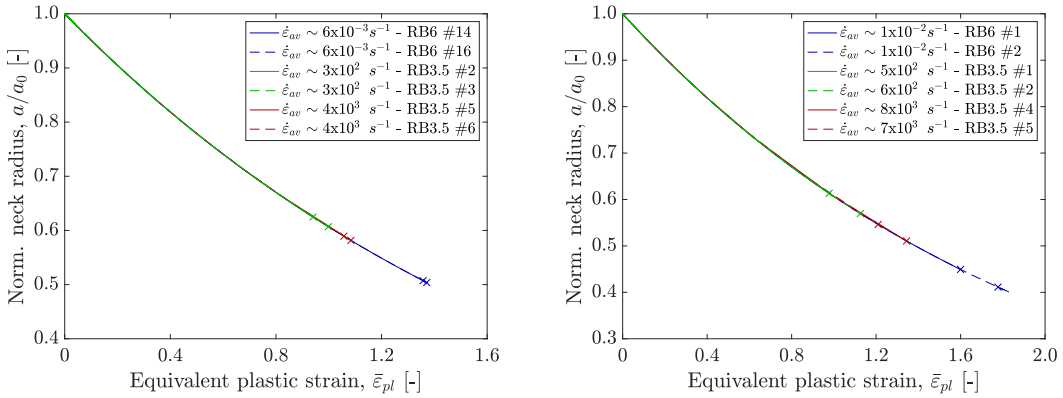
**Table 6.1:** Specimens studied in the analysis of strain-rate effects on plasticity.

| Geometry | Strain-rate, $\dot{\varepsilon}$ [$s^{-1}$] | Image resolution [pixels] | Frame rate [Hz] |
|---|---|---|---|
| RB6 | QS ($\sim 10^{-3}$) | 4928x3264 | 0.5 |
| RB3.5 | IR ($\sim 10^{2}$) | 192x504 | 20,000 |
| | HR ($\sim 10^{3}$) | 128x640 | 37,500 |
| HGR6 | QS ($\sim 10^{-3}$) | 4928x3264 | 0.5 |
| HGR3.5 | IR ($\sim 10^{2}$) | 128x504 | 28,000 |
| | HR ($\sim 10^{3}$) | 128x448 | 50,000 |

**Table 6.2:** Camera set-up for the plasticity analysis at varying strain-rate.

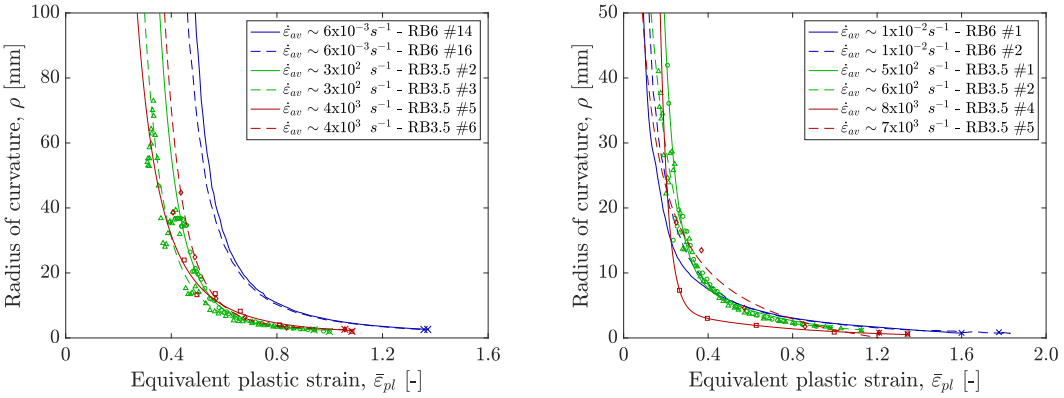
### 6.2.1 Neck Geometry

The effect of strain-rate on the evolution of the neck geometry is presented in Figure 6.1 for the neck cross-section ($a$) and Figure 6.2 for the neck radius of curvature ($\rho$). Firstly, a reduced ductility in the high-speed conditions can be observed for both materials, which could be expected due to the lack of time for the crystalline planes to slip. However, the tests performed at the highest strain-rate ($\dot{\varepsilon} \sim 10^3$ s$^{-1}$) present slightly higher ductility than those run at intermediate rate ($\dot{\varepsilon} \sim 10^2$ s$^{-1}$). The difference in strain-rate is relatively low between those conditions, and it is therefore difficult to determine whether this is a real effect or simply the scatter typical of high-speed tests.




**(a)** stainless steel 304L **(b)** copper C110

**Figure 6.1:** Effect of strain-rate on the normalised minimum cross-sectional radius - equivalent plastic strain ($a/a_0$ - $\bar{\varepsilon}_{pl}$).




**(a)** stainless steel 304L **(b)** copper C110

**Figure 6.2:** Effect of strain-rate on the radius of curvature of the neck - equivalent plastic strain ($\rho$ - $\bar{\varepsilon}_{pl}$).

| Material | Geom. | Spec. | Strain-rate, $\dot{\varepsilon}_{av}$ [$s^{-1}$] | Imaging $\varepsilon_{onset}$ [-] | Imaging $\rho_f$ [mm] | Imaging $a_f$ [mm] | Shadowgr. $a_f$ [mm] |
|---|---|---|---|---|---|---|---|
| s/s 304L | RB6 | #14 | $6.28x10^{-3}$ | 0.35 | 2.62 | 1.50 | 1.49 |
| | | #16 | $6.15x10^{-3}$ | 0.38 | 2.58 | 1.51 | 1.53 |
| | RB3.5 | #2 | $3.03x10^{2}$ | 0.28 | 2.02 | 1.03 | 1.02 |
| | | #3 | $2.94x10^{2}$ | 0.22 | 2.50 | 1.07 | 1.05 |
| | | #5 | $3.79x10^{3}$ | 0.19 | 2.04 | 0.99 | 1.01 |
| | | #6 | $4.37x10^{3}$ | 0.30 | 2.65 | 1.01 | 1.01 |
| copper C110 | RB6 | #1 | $1.05x10^{-2}$ | 0.04 | 0.94 | 1.29 | 1.27 |
| | | #2 | $1.12x10^{-2}$ | 0.05 | 0.88 | 1.22 | 1.22 |
| | RB3.5 | #1 | $4.80x10^{2}$ | 0.11 | 1.58 | 1.06 | 1.05 |
| | | #2 | $6.34x10^{2}$ | 0.05 | 1.15 | 0.98 | 0.96 |
| | | #4 | $8.11x10^{3}$ | 0.12 | 0.61 | 0.88 | 0.89 |
| | | #5 | $7.40x10^{3}$ | 0.04 | 0.81 | 0.94 | 0.98 |

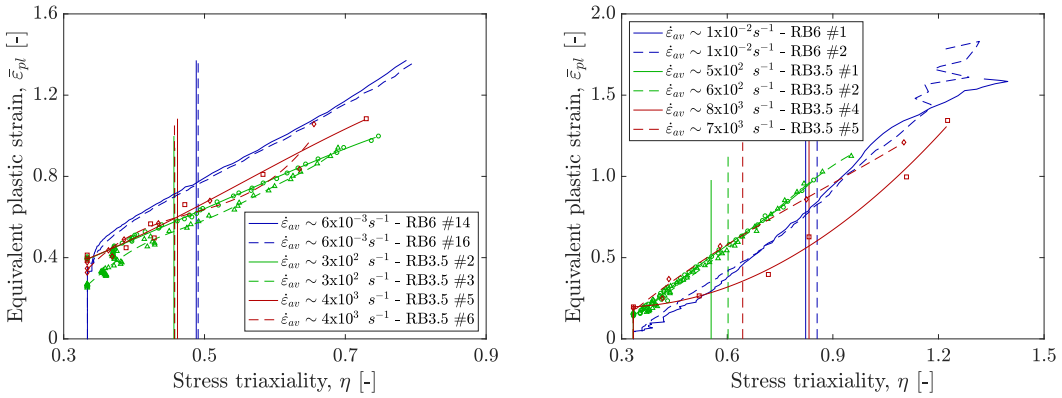
**Table 6.3:** Effect of strain-rate on neck onset strain ($\varepsilon_{onset}$), final neck radius of curvature ($\rho_f$) and final cross-sectional radius ($a_f$) measured with imaging method; and final cross-sectional radius ($a_f$) measured with shadowgraph.

Similar difficulties arise when the effect on curvature is analysed in Figure 6.2. All the conditions seem to follow a similar exponentially decreasing curvature trend, displaced depending on the neck onset and ductile fracture points. For a better interpretation, the intermediate and high rate results have been fitted to exponential curves, which are represented along with the actual data points. For stainless steel, a displacement of the curves towards lower strains is observed when strain-rate is increased, although a clear difference between the intermediate and high strain-rates cannot be appreciated. For copper, most of the high-speed tests present a slightly higher neck onset strain and a steeper decrease of curvature, fracturing at lower strain values, as observed also in the cross-section analysis. The effect is a somewhat longer uniform deformation region before necking starts, a faster neck development once it appears, and a failure at lower strain than in quasi-static conditions. Nevertheless, the number of data points available at the highest strain-rate is very small and limited by the speed of the cameras. Accordingly, the results in those conditions have to be treated carefully and the trends analysed are only illustrative.

Other numerical results extracted from these experiments are presented in Table 6.3, where values of the neck onset strain and final geometry are given. The final neck cross-section of the specimens is also compared with the value measured ex-situ with a shadowgraph, and the similar results obtained serve as validation of the method.

### 6.2.2 Stress Triaxiality

The effect of strain-rate on stress triaxiality is shown in Figure 6.3. The same difficulties faced when analysing the geometry of the neck also appear here: scatter in the high-speed results, reduced number of data points available and similar order of magnitude of the two high-speed conditions studied. The data points at intermediate and high speed have been fitted in this case to polynomial curves, in order to ease their interpretation.




**(a)** stainless steel 304L **(b)** copper C110

**Figure 6.3:** Effect of strain-rate on the equivalent plastic strain - stress triaxiality ($\bar{\varepsilon}_{pl}$ - $\eta$).

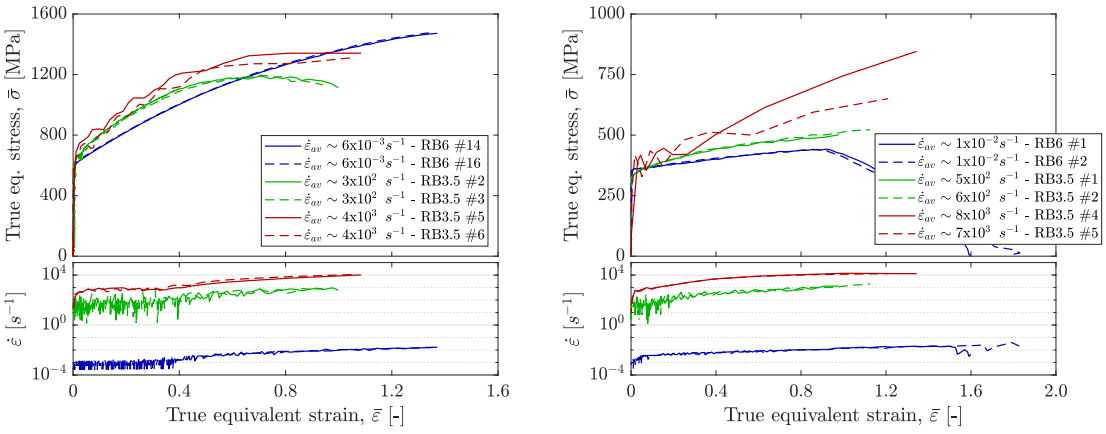
| Material | Geom. | Spec. | Strain-rate, $\dot{\varepsilon}_{av}$ [$s^{-1}$] | Stress triaxiality $\eta_{av}$ [-] | $\eta_{min}$ [-] | $\eta_{max}$ [-] |
|---|---|---|---|---|---|---|
| s/s 304L | RB6 | #14 | $6.28\text{x}10^{-3}$ | 0.488 | 0.333 | 0.787 |
| | | #16 | $6.15\text{x}10^{-3}$ | 0.491 | 0.333 | 0.796 |
| | RB3.5 | #2 | $3.03\text{x}10^{2}$ | 0.457 | 0.333 | 0.747 |
| | | #3 | $2.94\text{x}10^{2}$ | 0.458 | 0.333 | 0.690 |
| | | #5 | $3.79\text{x}10^{3}$ | 0.462 | 0.333 | 0.729 |
| | | #6 | $4.37\text{x}10^{3}$ | 0.457 | 0.333 | 0.655 |
| copper C110 | RB6 | #1 | $1.05\text{x}10^{-2}$ | 0.713 | 0.333 | 0.965 |
| | | #2 | $1.12\text{x}10^{-2}$ | 0.855 | 0.333 | 1.287 |
| | RB3.5 | #1 | $4.80\text{x}10^{2}$ | 0.554 | 0.333 | 0.845 |
| | | #2 | $6.34\text{x}10^{2}$ | 0.602 | 0.333 | 0.952 |
| | | #4 | $8.11\text{x}10^{3}$ | 0.832 | 0.333 | 1.226 |
| | | #5 | $7.40\text{x}10^{3}$ | 0.644 | 0.333 | 1.102 |

**Table 6.4:** Effect of strain-rate on stress triaxiality; the average ($\eta_{av}$), minimum ($\eta_{min}$) and maximum ($\eta_{max}$) values of triaxiality for each test are presented.

It is noticeable that the curves of different strain-rates have a similar slope and triaxiality changes almost linearly with plastic strain, once the neck has started to develop. Only one of the copper specimens tested at high rate (RB3.5 #4) shows a more erratic behaviour, nevertheless, that curve is obtained based on few data points, and therefore, it has been difficult to obtain a clear fit or trend. For stainless steel, the high-speed results are displaced downwards, meaning that triaxiality starts increasing earlier, which is consistent with the earlier neck onset and curvature decrease mentioned in the previous section. The opposite occurs for copper, for which an upwards displacement is observed at high speeds, also in line with the delayed neck development that was observed for this material in the previous section. The average value of triaxiality along the tests is also represented in Figure 6.3 by means of vertical lines. The values obtained for most high-speed tests are lower than the quasi-static cases, being this fundamentally caused by the reduced ductility observed in those conditions. Numerical values of the average, minimum and maximum stress triaxiality of each test are available in Table 6.4.

### 6.2.3 Equivalent Stress - Strain

The local true stress - strain behaviour at different strain-rates has been calculated using the geometrical parameters studied in the previous sections and the methodology described in Section 3.3. The true equivalent stress - strain curves are shown in Figure 6.4, where the evolution of strain-rate throughout the tests is also represented.




**(a)** stainless steel 304L **(b)** copper C110

**Figure 6.4:** Effect of strain-rate on true equivalent stress - true equivalent strain behaviour ($\bar{\sigma}$ - $\bar{\varepsilon}$); the evolution of strain-rate for increasing strain in each experiment is also represented ($\dot{\varepsilon}$ - $\bar{\varepsilon}$).

For the three velocities tested, strain-rate stays approximately constant during the uniform deformation stage and increases considerably throughout the necking process, rising around one order of magnitude towards the end of the test. This effect is easier to observe in the stainless steel, as copper necks from very early stages of plasticity, especially in quasi-static conditions. The minimum, maximum and average strain-rates of each test are available in Table 6.5. Since local stresses and strains occurring in the neck are generally not studied, the values of average strain-rate that are normally presented are much lower than the ones obtained in this work. It is during necking when local strain-rate rises up to one order of magnitude, and this process occupies a great range of the plastic region, resulting in considerably higher average strain-rates.

Both materials increase their strength and reduce their ductility when strain-rate increases. A small increase in yield stress is observed in both high rate conditions studied in stainless steel. The hardening rate is similar to that in quasi-static conditions at the beginning of the plastic region, and it decreases towards the end due to the heating of the sample. Initially, the material is at room temperature and the high strain-rate effects dominate the behaviour, which is hardened and stronger. As the plasticity develops in the material, the sample heats up adiabatically and at some point this effect is not negligible and pushes the material response downwards, towards the effect that high temperature imposes, which is the opposite to that of high strain-rate, as analysed in Section 7.2. Copper, on the other hand, shows no appreciable increase of yield stress at high strain-rates. Quantitatively, the bigger change comes from an increase in hardening rate, which is subtle in the intermediate rate conditions,

| Material | Geom. | Spec. | Strain-rate | | |
|---|---|---|---|---|---|
| | | | $\dot{\varepsilon}_{av}$, [s$^{-1}$] | $\dot{\varepsilon}_{min}$, [s$^{-1}$] | $\dot{\varepsilon}_{max}$, [s$^{-1}$] |
| s/s 304L | RB6 | #14 | $6.28\text{x}10^{-3}$ | $1.06\text{x}10^{-3}$ | $1.70\text{x}10^{-2}$ |
| | | #16 | $6.15\text{x}10^{-3}$ | $1.05\text{x}10^{-3}$ | $1.64\text{x}10^{-2}$ |
| | RB3.5 | #2 | $3.03\text{x}10^{2}$ | 2.38 | $7.71\text{x}10^{2}$ |
| | | #3 | $2.94\text{x}10^{2}$ | 1.32 | $8.30\text{x}10^{2}$ |
| | | #5 | $3.79\text{x}10^{3}$ | $1.14\text{x}10^{2}$ | $1.03\text{x}10^{4}$ |
| | | #6 | $4.37\text{x}10^{3}$ | $1.13\text{x}10^{2}$ | $1.11\text{x}10^{4}$ |
| copper C110 | RB6 | #1 | $1.05\text{x}10^{-2}$ | $1.40\text{x}10^{-3}$ | $1.95\text{x}10^{-2}$ |
| | | #2 | $1.12\text{x}10^{-2}$ | $1.03\text{x}10^{-3}$ | $2.27\text{x}10^{-2}$ |
| | RB3.5 | #1 | $4.80\text{x}10^{2}$ | 1.31 | $1.30\text{x}10^{3}$ |
| | | #2 | $6.34\text{x}10^{2}$ | 5.23 | $1.93\text{x}10^{3}$ |
| | | #4 | $8.11\text{x}10^{3}$ | $7.00\text{x}10^{1}$ | $1.30\text{x}10^{4}$ |
| | | #5 | $7.40\text{x}10^{3}$ | $1.47\text{x}10^{2}$ | $1.32\text{x}10^{4}$ |

**Table 6.5:** Average ($\dot{\varepsilon}_{av}$), minimum ($\dot{\varepsilon}_{min}$) and maximum ($\dot{\varepsilon}_{max}$) values of strain-rate of the tensile tests.

and considerable in the high rate case, allowing it to double its fracture true stress. Qualitatively, a change in the fracture mechanism is observed, with the material losing its progressive degradation behaviour, and failing in a more abrupt and brittle manner at high strain-rates, as will be discussed in the following section.

## 6.3 Strain-Rate Effect on Ductile Fracture

The experimental procedure described in Section 3.4 with the same modifications for high-speed tests applied to the previous section has been employed here to test RNB specimens instead of the smooth RB geometry. The effect of strain-rate on the material behaviour for different stress triaxiality conditions has been analysed by testing different notch geometries. A summary of the specimens tested is presented in Table 6.6, organised by notch acuity ($a/\rho$) and the average strain-rate conditions of the test.

| Material | Notch acuity, $a/\rho$ [-] | Average strain-rate, $\dot{\varepsilon}_{av}$ | | | | | |
|---|---|---|---|---|---|---|---|
| | | $\sim 10^{-2}$ s$^{-1}$ | | $\sim 10^{2}$ s$^{-1}$ | | $\sim 10^{4}$ s$^{-1}$ | |
| s/s 304L | 0 | RB6 | #14 | RB3.5 | #2 | RB3.5 | #5 |
| | | | #16 | | #3 | | |
| | 0.25 | RNB6-1 | #19 | | | | |
| | 0.313 | | | RNB3.5-2 | #16 | RNB3.5-2 | #19 |
| | | | | | #17 | | #20 |
| | 0.417 | RNB6-3 | #15 | | | | |
| | 0.833 | RNB6-4 | #11 | RNB3.5-4 | #12 | RNB3.5-4 | #14 |
| | | | | | #13 | | #15 |
| | 1.25 | RNB6-5 | #7 | RNB3.5-5 | #7 | RNB3.5-5 | #9 |
| | | | | | #8 | | #10 |
| | 2.5 | RNB6-6 | #3 | RNB3.5-6 | #3 | RNB3.5-6 | #4 |
| | | | | | | | #5 |
| copper C110 | 0 | RB6 | #1 | RB3.5 | #1 | RB3.5 | #4 |
| | | | #2 | | #2 | | #5 |
| | 0.313 | RNB6-2 | #11 | RNB3.5-2 | #13 | RNB3.5-2 | #15 |
| | | | | | #14 | | #16 |
| | 0.833 | RNB6-4 | #8 | RNB3.5-4 | #10 | RNB3.5-4 | #12 |
| | 1.25 | RNB6-5 | #5 | RNB3.5-5 | #5 | RNB3.5-5 | #7 |
| | | | | | #6 | | #8 |
| | 2.5 | RNB6-6 | #2 | RNB3.5-6 | #1 | RNB3.5-6 | #3 |
| | | | | | #2 | | #4 |

**Table 6.6:** Specimens studied in the analysis of strain-rate effects on ductile fracture.

### 6.3.1 Fracture Surface

SEM pictures of the fracture surface of stainless steel 304L specimens tested at different velocities are presented in Figure 6.5 at different magnifications, and similar images of copper C110 samples are available in Figure 6.6. The images confirm the reduced ductility and necking capability of the studied materials at high strain-rate because of their limited diameter reduction. It has to be born in mind though, that the initial diameter of quasi-static samples is 6 mm, while that of high-speed samples is 3.5 mm, and therefore, their final diameters cannot be directly compared.

The region of ductile deformation of stainless steel at high speed is reduced to a very small area in the centre of the specimen, surrounded by sharp edges where brittle fracture has occurred. The morphology of voids is not highly affected by strain-rate, however, slightly smaller and less uniform defects can be appreciated in the high strain-rate cases, with some clusters of bigger voids. The main difference is that, while in the quasi-static case the ductile fracture area is approximately flat, at high speed

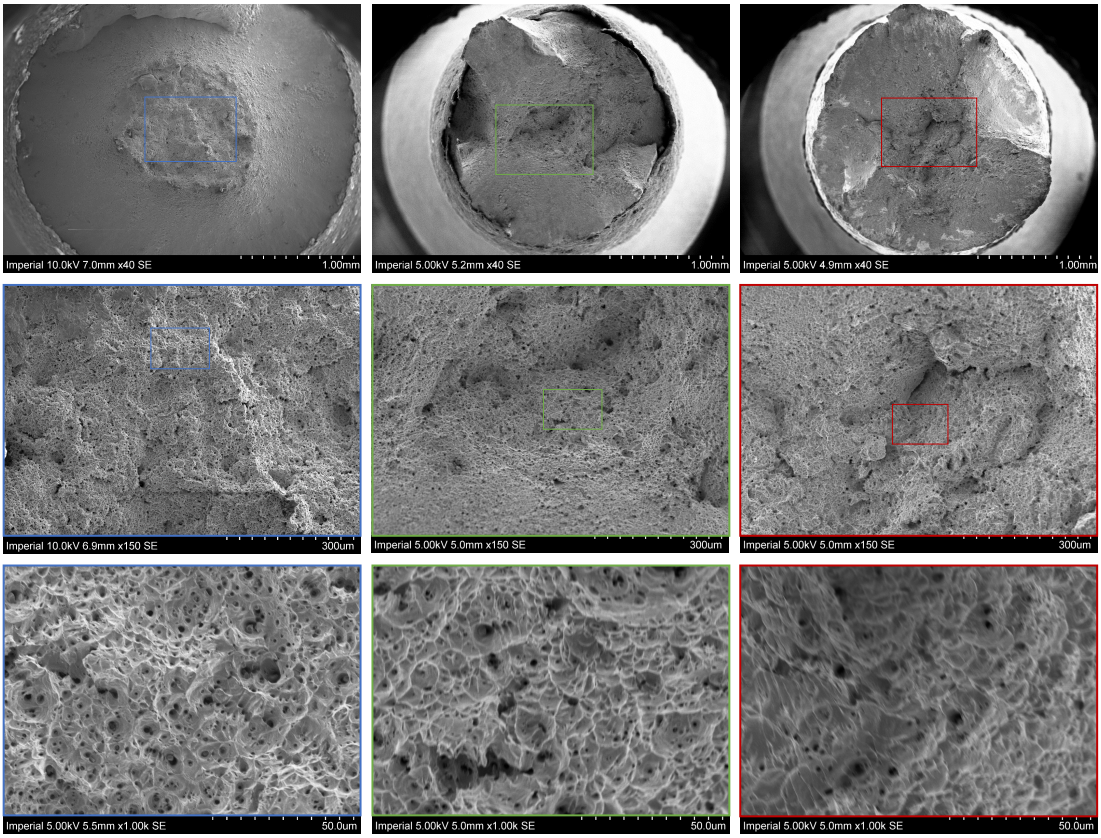



**Figure 6.5:** Effect of strain-rate on the fracture surface of stainless steel 304L (from left to right: $\dot{\varepsilon} \sim 10^{-3}$ s$^{-1}$, $\dot{\varepsilon} \sim 10^{2}$ s$^{-1}$ and $\dot{\varepsilon} \sim 10^{3}$ s$^{-1}$; from top to bottom: 40x, 150x and 1000x magnification.

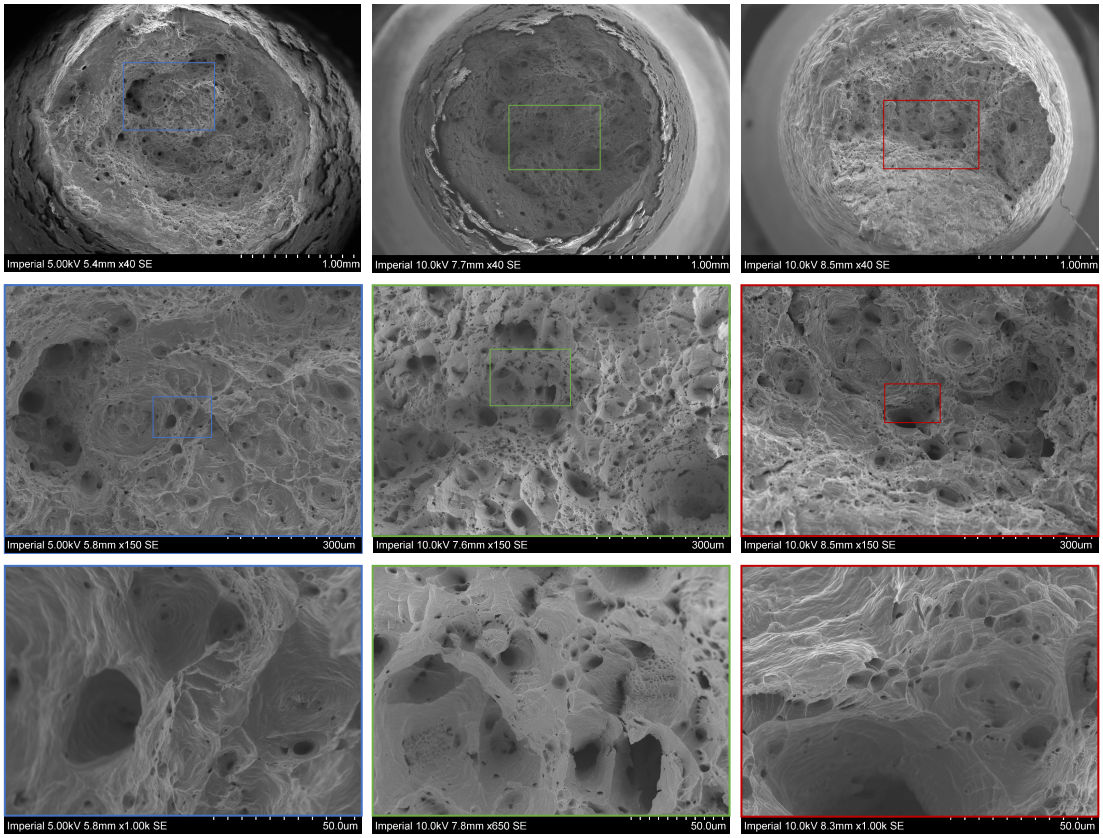



**Figure 6.6:** Effect of strain-rate on the fracture surface of copper C110 (from left to right: $\dot{\varepsilon} \sim 10^{-3}$ s$^{-1}$, $\dot{\varepsilon} \sim 10^{2}$ s$^{-1}$ and $\dot{\varepsilon} \sim 10^{3}$ s$^{-1}$; from top to bottom: 40x, 150x and 1000x magnification.

the surface is sharper presenting peaks and troughs, and showing ductile failure only in a small area of the centre. The similar form and distribution of voids at different rates is reflected in the subtle differences in stress - strain behaviour of Figure 6.4, while the reduced ductile area leads to a limited ductility of the material.

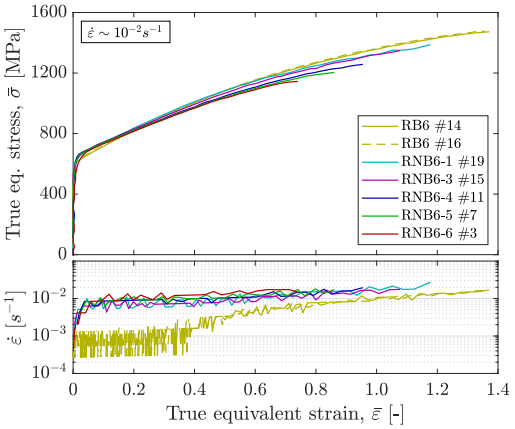
A dramatic change in void size or distribution is not observed in copper either (Figure 6.6), since the size in all conditions is in the range 2-50 μm. Sharper micro-features can be observed, especially in the intermediate rate conditions, that suggest brittle abrupt micro-fracture, as opposed to the progressive ductile degradation in quasi-static conditions.

### 6.3.2 Equivalent Stress - Strain

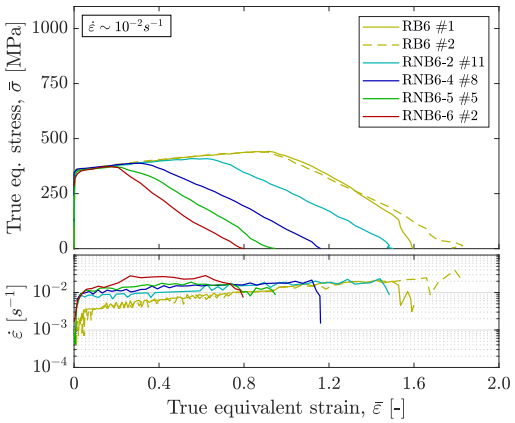
Tensile tests have been performed on the notched samples at different velocities and the evolution of the geometry of the notches has been tracked.[1] From those geometrical parameters the equivalent stress - strain plots of Figure 6.7 have been obtained, where the strain-rate throughout each test has also been represented. The results are divided according to their average strain-rate, being the quasi-static at the top (Figure 6.7a and 6.7b), the intermediate rate in the middle (Figure 6.7c and 6.7d) and the high rate at the bottom (Figure 6.7e and 6.7f). Maximum axial stress results ara also available in Figure 6.8. Different effects can be analysed from the observation of these plots:

- **Effect of notch acuity on the stress - strain behaviour.** This effect was already studied in Section 5.3 for quasi-static conditions (Figure 6.7a and 6.7b). A very similar behaviour can be observed in the other two strain-rates analysed, with the yield stress increasing and an overall upwards movement of the maximum stress curves for higher notch acuities. The effect on hardening rate is not that clear in this case, staying this parameter unchanged in the quasi-static case, there seems to be some variation at intermediate rates (e.g. in Figure 6.7d), although it is difficult to determine it, given the scatter of some of the high strain-rate results (Figure 6.7f).
- **Effect of strain-rate on the stress - strain behaviour.** This phenomenon has been analysed in Section 6.2 on RB specimens (all the yellow curves of Figure 6.7). When compared with the quasi-static case, a small increase of yield stress occurs at $\dot{\varepsilon} \sim 10^2$ s$^{-1}$; nevertheless, it is at the highest strain-rate tested ($\dot{\varepsilon} \sim 10^4$ s$^{-1}$) when a significant increase is observed for all the samples of both materials. A reduction of ductility also takes places in the RNB specimens when the velocity of the test is increased. For stainless steel, the decrease of hardening rate observed at high levels of plastic strain in the intermediate and high rate curves of RB samples also appears in the RNB geometries. For copper, all the samples fracture abruptly at high strain-rate, unlike the progressive degradation observed in quasi-static conditions.
- **Strain-rate evolution through the test.** As explained in Section 6.2, the strain-rate stays approximately constant before the neck appears, and it increases up to an order of magnitude during necking. RNB specimens include a notch, which behaves as a neck present from the beginning of the test. It has been observed that a relatively constant strain-rate takes place for these samples, near the upper bound of the range observed in RB specimens. The strain-rate increase during the test is almost non-existent for RNB samples at quasi-static and

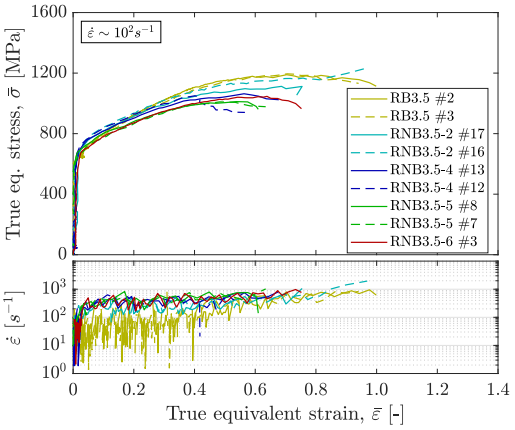
[1] Plots of the evolution of notch geometry used to calculate stress - strain for each sample are available in Figures B.1 and B.4 for $a/a_0$-$\bar{\varepsilon}_{pl}$ and Figures B.2 and B.5 for $\rho$-$\bar{\varepsilon}_{pl}$, both in Appendix B.



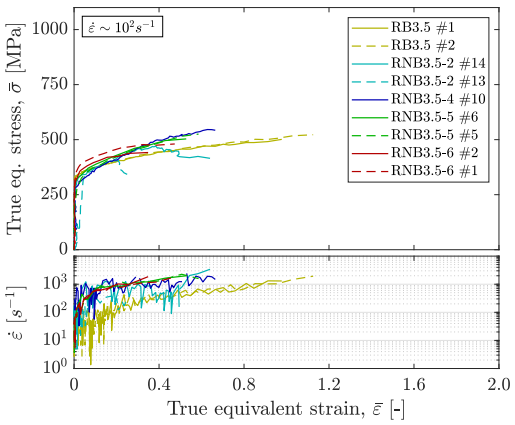

**(a)** stainless steel 304L - $\dot{\varepsilon} \sim 10^{-2}$ s$^{-1}$



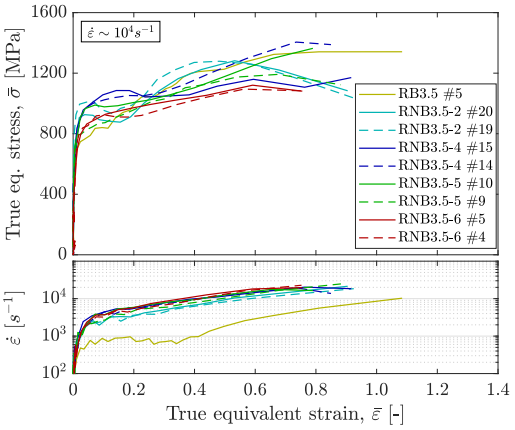

**(b)** copper C110 - $\dot{\varepsilon} \sim 10^{-2}$ s$^{-1}$



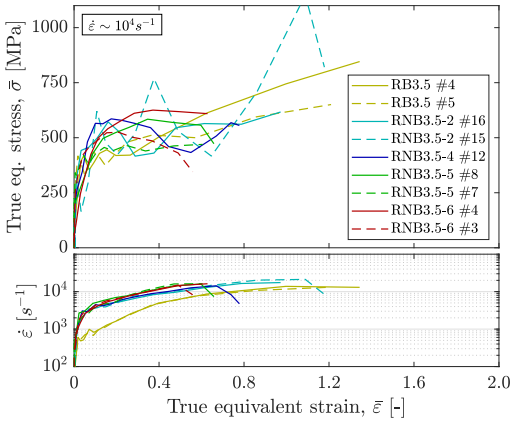

**(c)** stainless steel 304L - $\dot{\varepsilon} \sim 10^{2}$ s$^{-1}$




**(d)** copper C110 - $\dot{\varepsilon} \sim 10^{2}$ s$^{-1}$

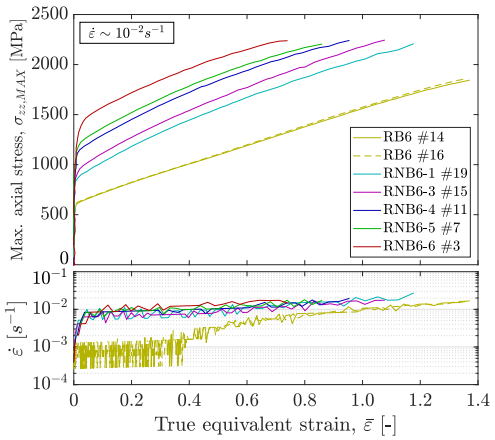



**(e)** stainless steel 304L - $\dot{\varepsilon} \sim 10^{4}$ s$^{-1}$

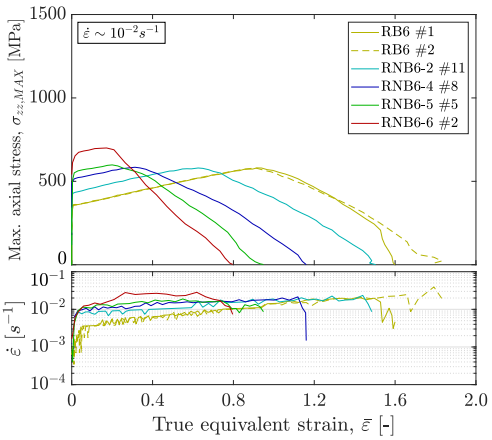



**(f)** copper C110 - $\dot{\varepsilon} \sim 10^{4}$ s$^{-1}$

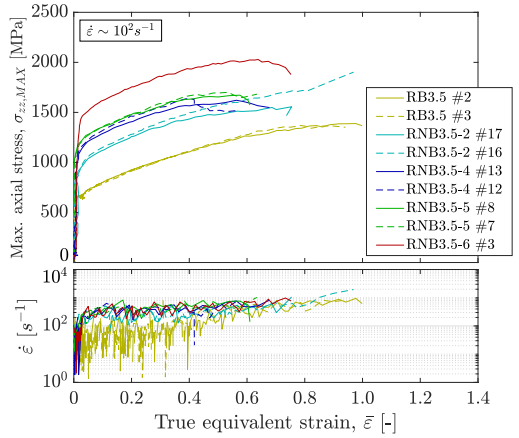
**Figure 6.7:** Effect of strain-rate on true equivalent stress - true equivalent strain ($\bar{\sigma}$ - $\bar{\varepsilon}$) for the notched bar tests; the evolution of strain-rate for each experiment is also represented ($\dot{\varepsilon}$ - $\bar{\varepsilon}$).



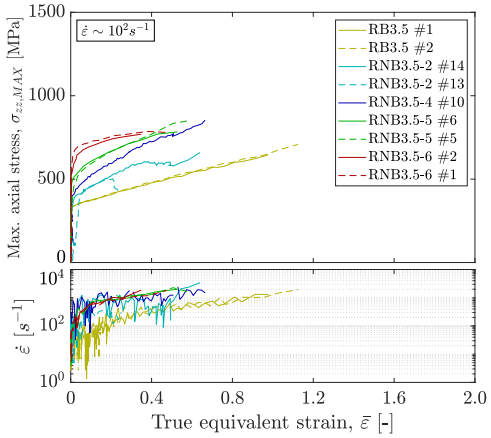

**(a)** stainless steel 304L - $\dot{\varepsilon} \sim 10^{-2}$ s$^{-1}$



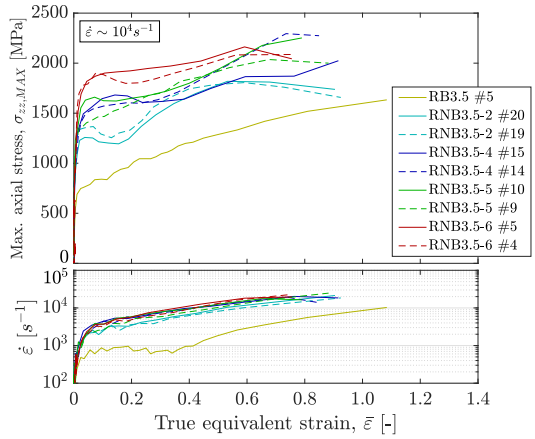

**(b)** copper C110 - $\dot{\varepsilon} \sim 10^{-2}$ s$^{-1}$



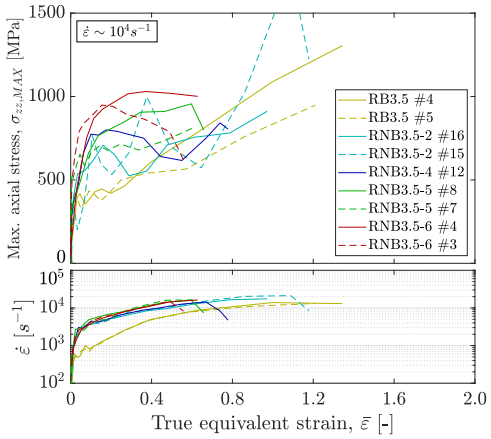

**(c)** stainless steel 304L - $\dot{\varepsilon} \sim 10^{2}$ s$^{-1}$




**(d)** copper C110 - $\dot{\varepsilon} \sim 10^{2}$ s$^{-1}$




**(e)** stainless steel 304L - $\dot{\varepsilon} \sim 10^{4}$ s$^{-1}$




**(f)** copper C110 - $\dot{\varepsilon} \sim 10^{4}$ s$^{-1}$

**Figure 6.8:** Effect of strain-rate on maximum axial stress - true equivalent strain ($\sigma_{zz,MAX}$ - $\bar{\varepsilon}$) for the notched bar tests; the evolution of strain-rate for each experiment is also represented ($\dot{\varepsilon}$ - $\bar{\varepsilon}$).

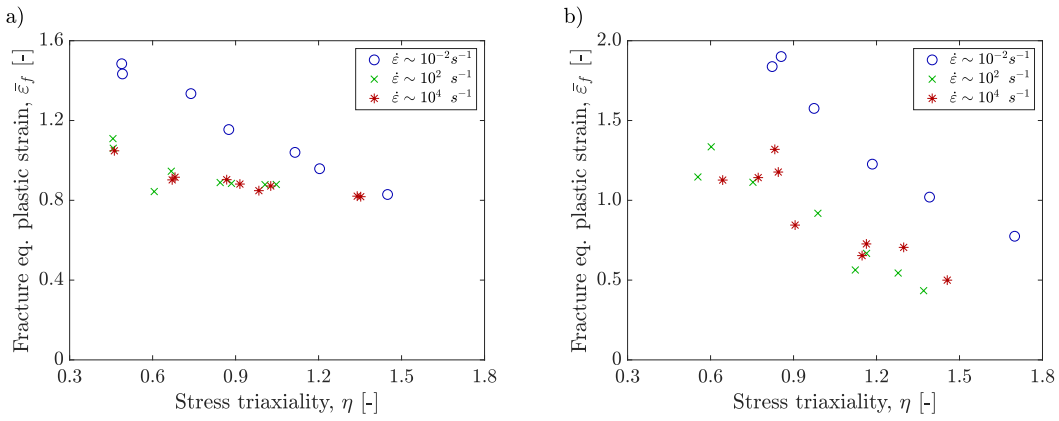
intermediate rates, while a considerable increase takes place at high rate. This generally higher strain-rate produces greater values of average strain-rate if the tests are run at the same crosshead velocity.

### 6.3.3 Effect of Stress Triaxiality on Ductility

The fracture equivalent plastic strain of each test has been plotted against the average stress triaxiality throughout the experiment, giving each test a single point that represents its ductile fracture condition and the effect that stress triaxiality has on it. Those results have been plotted in Figure 6.9 for the different strain-rates analysed and following the methodology explained in Section 3.4.[2]

For both materials, a downwards displacement of the $\bar{\varepsilon}_f - \eta$ curve occurs when the strain-rate increases. This behaviour is linked to the reduced ductility that has been commented in previous sections. Another common observation for both materials is the overlap of results in the intermediate and high strain-rate conditions, suggesting either that there is not enough difference in strain-rate between those conditions or that there is a saturation rate over which ductility stops decreasing.

The stainless steel at high strain-rate shows a considerable decrease in fracture strain at low triaxialities (samples with smooth or no notch), compared to the very small or non-existent decrease at high triaxialities (sharp notch). This results in a flatter shape of the curve, which implies that stress triaxiality has almost no effect on




**(a)** stainless steel 304L **(b)** copper C110

**Figure 6.9:** Effect of strain-rate on fracture equivalent plastic strain - stress triaxiality ($\bar{\varepsilon}_f$ - $\eta$).

[2]The numerical values of stress triaxiality and ductility of the tests are available in Tables B.1 and B.2; and plots of the evolution of stress triaxiality along the test in Figures B.3 and B.6, both in Appendix B.

fracture strain at high strain-rate. The observations show that the necking capability of the material is lower at high strain-rate. States of high stress triaxiality already present a reduced neck in quasi-static conditions; but it seems that the additional plasticity available in the cases of lower triaxiality is lost at high rate due to the limited necking in those conditions. As a consequence, all the stress states fracture at the reduced ductility level normally characteristic of high triaxialities, while the case of high stress triaxiality remains almost unaffected.

The behaviour of copper is slightly different, instead of becoming flatter, the $\bar{\varepsilon}_f - \eta$ curve shifts downwards and leftwards almost parallelly to the quasi-static case, when the strain-rate is increased. The ductility reduction at high speed is accompanied by a decrease in average stress triaxiality of the tests that provokes the shift of the curve towards the left. The amount of fracture strain reduction is significant, for example at an average stress triaxiality of 1 it falls from $\bar{\varepsilon}_f = 1.50$ in quasi-static strain-rate to $\bar{\varepsilon}_f = 0.88$ at high strain-rate.

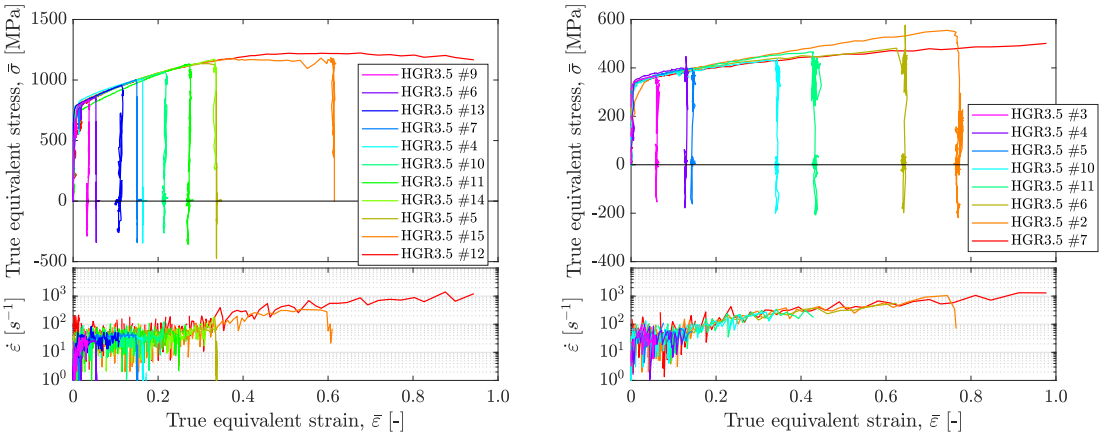
## 6.4 Strain-Rate Effect on Damage Accumulation

For the quantification of ductile damage at high strain-rate the approach described in Section 4.2.5 has been followed. It consists of performing tensile tests interrupted at different plastic strain levels, using the experimental rig developed for that purpose and explained in the same section, and measuring damage ex-situ afterwards. Two different techniques have been used for the damage estimation, the first one based on the elastic modulus measurement at slow rate of the sample that has been damaged at high rate, and the second one based on a metallographic analysis of the void density inside the sample. The results obtained from the modulus analysis are presented in Section 6.4.1 and those of the porosity study in Section 6.4.2. Although both techniques are very different, it has already been proved in Section 5.5.5 that they can provide the same trends of damage evolution.

As said before, interrupted tests have been run to analyse different levels of damage and plastic deformation. Multiple shots on the same specimen have been avoided, and a separate sample has been used to study each condition. Following this approach, the sample tested under each condition has been available for ex-situ analysis, including the destructive preparation required for the porosity measurements. The specimen geometry employed has in all cases been HGR, varying the diameter depending on the target strain-rate. A summary of the samples employed is presented in Table 6.7, and the stress - strain history of all the high-speed tests is presented in Figure 6.10, where the level of plastic deformation achieved for each specimen can be appreciated. In this figure the strain-rate history has also been plotted, and the same increasing tendency

| Material | Average strain-rate, $\dot{\varepsilon}_{av}$ | | | | | |
|---|---|---|---|---|---|---|
| | $\sim 10^{-2}$ s$^{-1}$ | | $\sim 10^{2}$ s$^{-1}$ | | | |
| s/s 304L | HGR6 | #4<br>#6<br>#9<br>#11 | HGR3.5 | #4<br>#5<br>#6<br>#7 | #9<br>#10<br>#11<br>#12 | #13<br>#14<br>#15 |
| copper C110 | HGR6 | #3<br>#4<br>#7 | HGR3.5 | #2<br>#3<br>#4 | #5<br>#6<br>#10 | #11<br>#7 |

**Table 6.7:** Specimens studied in the analysis of strain-rate effects on ductile damage accumulation.



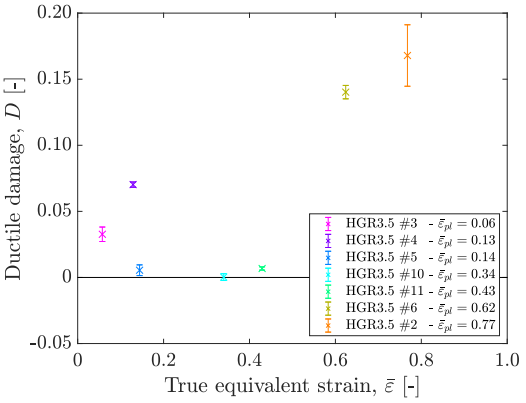

**(a)** Stainless steel 304L **(b)** Copper C110

**Figure 6.10:** True equivalent stress - true equivalent strain ($\bar{\sigma}$ - $\bar{\varepsilon}$) of the interrupted tensile tests used for damage estimation at $\dot{\varepsilon} \sim 10^2$ s$^{-1}$.

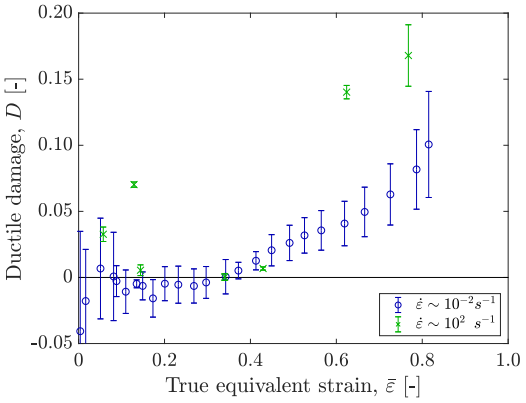
observed in the plasticity analysis can be appreciated. This behaviour results in a higher average strain-rate for the specimens that have undergone higher plasticity.

### 6.4.1 Elastic Modulus Analysis

The procedure followed in this case is the same described in Section 3.5 for the quasi-static case, however, unlike the continuous test performed in those conditions, here elastic modulus is measured in each already damaged specimen using the quasi-static tensile machine. Figure 6.11a shows the damage measurements obtained from all copper interrupted tests that have been described in Figure 6.10b. Six loading-unloading cycles have been performed in each specimen in order to have a few measurements of elastic modulus; the results presented in the plots correspond to the mean and standard deviation of those measurements. Figure 6.11b presents the same information compared

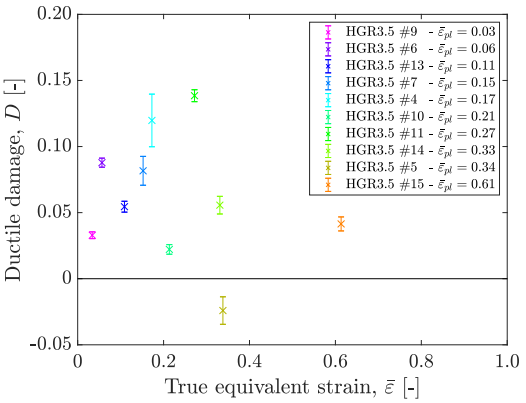



**(a)** Ductile damage evolution at $\dot{\varepsilon} \sim 10^2 s^{-1}$.

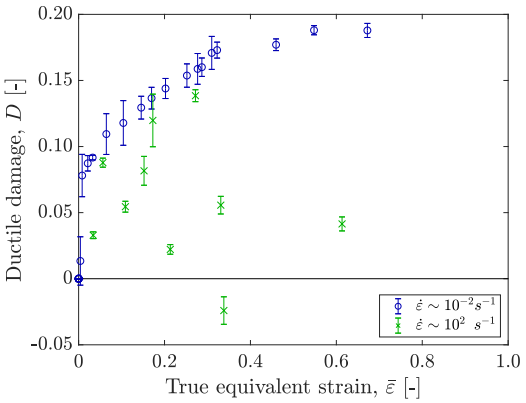



**(b)** Effect of strain-rate on ductile damage.

**Figure 6.11:** Ductile damage accumulation of copper C110 at different strain-rates obtained using the elastic modulus reduction method ($D$ - $\bar{\varepsilon}$); mean and standard deviation values of damage are represented.




**(a)** Ductile damage evolution at $\dot{\varepsilon} \sim 10^2 s^{-1}$.




**(b)** Effect of strain-rate on ductile damage.

**Figure 6.12:** Ductile damage accumulation of stainless steel 304L at different strain-rates obtained using the elastic modulus reduction method ($D$ - $\bar{\varepsilon}$); mean and standard deviation values of damage are represented.

to the results in quasi-static conditions that were obtained in Section 5.4. Analogous results are available for stainless steel 304L in Figure 6.12, which correspond to the tests of Figure 6.10a. From the results some conclusions can be drawn.

- It is clear that the number of data points available is much lower than in the quasi-static analysis, since while in that case many data points can be obtained from a single sample, here each specimen provides only one point that corresponds

to a certain plastic strain. If a higher density of data or repeat conditions are required many more specimens are needed, increasing the cost and time of the experiment.

- The scatter of results is also a difficulty. While in the results for copper only one data point seems to be off its expected location (HGR3.5 #4), no useful conclusion can be drawn for the stainless steel, since it has been impossible to obtain a clear trend for that material. This suggests that the technique cannot directly be used for all types of materials, and results should be treated carefully in any case.
- Apart from the limitations of the results obtained, a trend can be observed in the results for copper, particularly when these are compared to the base quasi-static results in Figure 6.11b. The trend followed is the same that has been previously obtained for copper, with basically no damage for a considerable part of the plastic region, and then a linear increase in damage. The threshold strain seems to be similar to the one measured in quasi-static ($\varepsilon_{th} \sim 0.4$), and the damage measured afterwards also seems to present a linear accumulation, although it is difficult to assess it, as there are only two data points available. The difference compared to the quasi-static case is that the level of damage is higher for a given plastic strain.

Due to the limitations of the method, specially when measuring stainless steel 304L, the use of a second method to measure the accumulated damage on samples has been required. The measurement of porosity to account for void density and ductile damage has been selected as the alternative technique.

### 6.4.2 Porosity Analysis

For the ductile damage estimation using porosity measurements the same procedure used for the validation of stainless steel quasi-static results in Section 5.5 has been followed. The samples deformed at high speed that have been described in the previous section (Figure 6.10) have now been cut, mounted and polished following a process analogous to that of Section 5.5.1. Pictures of the cross-section have then been taken in different locations, porosity has been quantified using an automated thresholding algorithm and the values obtained have been used to obtain porosity maps and radial distributions of porosity.

The porosity contour maps of the stainless steel 304L samples are presented in Figure 6.13, where the final diameter of all specimens is represented at the same scale. All contours also have the same scale, except for the last sample that has much higher porosity. The radial distribution of porosity for each specimen is presented in Fig-

ure 6.14a and the evolution of porosity with increasing plastic strain in Figure 6.14b, represented by the mean and standard deviation in each cross-section and also the value in the centre. The results show a considerable initial increase of porosity at very early stages of plasticity, a fairly constant density of voids for most of the plastic region and a noticeable increase towards the end. The flat radial distribution suggests uniform deformation until high plasticity is reached; at the point when the neck starts developing a clearly higher density of voids is observed in the centre of the last two specimens (#15 and #12). The trends observed coincide with those analysed in Section 5.5.5 for the same material in quasi-static conditions.

In Figure 6.15 the results of average porosity in the cross-section obtained at different strain-rates are compared for stainless steel. A very similar trend can be appreciated for both rates, with the flat region that appears in most of the plastic region at slow speed almost disappearing at high speed, and becoming a continuously increasing porosity of increasing slope towards the end. Another difference is the maximum porosity at fracture, which is much lower at high strain-rate ($\varphi_{av,f} \sim 0.018$ at $\dot{\varepsilon} \sim 10^2$ s$^{-1}$ compared to $\varphi_{av,f} \sim 0.037$ at $\dot{\varepsilon} \sim 10^{-2}$ s$^{-1}$). Similarly to the limited ductility at high speed, voids are unable to grow as much as they would in quasi-static conditions. At slow speed voids have time to grow without dynamic effects affecting the nucleation-growth-coalescence process, while at high speed other dynamic effects overlap with this phenomenon. For the same level of equivalent plastic strain, the higher porosity of the material deformed at high speed may have been caused by higher local stresses around inclusions in those conditions, apart from the conventional damage mechanisms. Since the results obtained using the elastic modulus reduction technique for this material at high speed were not satisfactory, these porosity results have been considered the damage accumulation results of stainless steel 304L.

The results for copper C110 are presented in the same fashion, with the porosity contours of the different specimens shown in Figure 6.16, and again with the same colour scale used for all specimens except the last two, where the differences are noticeable, as explained later. The radial distributions of porosity are shown in Figure 6.17a and, since there is a considerable magnitude difference between the last two specimens and the rest, an image zoomed in in the region $0 < \varphi < 0.006$ has been plotted in Figure 6.17b. The same occurs with the evolution of porosity with plastic strain, which is plotted in Figure 6.18a for the whole porosity range, and in Figure 6.18b for the zoomed in region. In this material very low porosity is observed in the early stages of plasticity. This can be appreciated by comparison of the porosity contours of the first samples with that of the raw material, and also by observation of the radial distributions that appear in Figure 6.17b, all of them bellow $\varphi = 0.005$. Only the last two samples show significant damage, which can be appreciated in all the available results. The scales used for the contour plots of these two samples (#2 and #7) have a much wider range, to represent

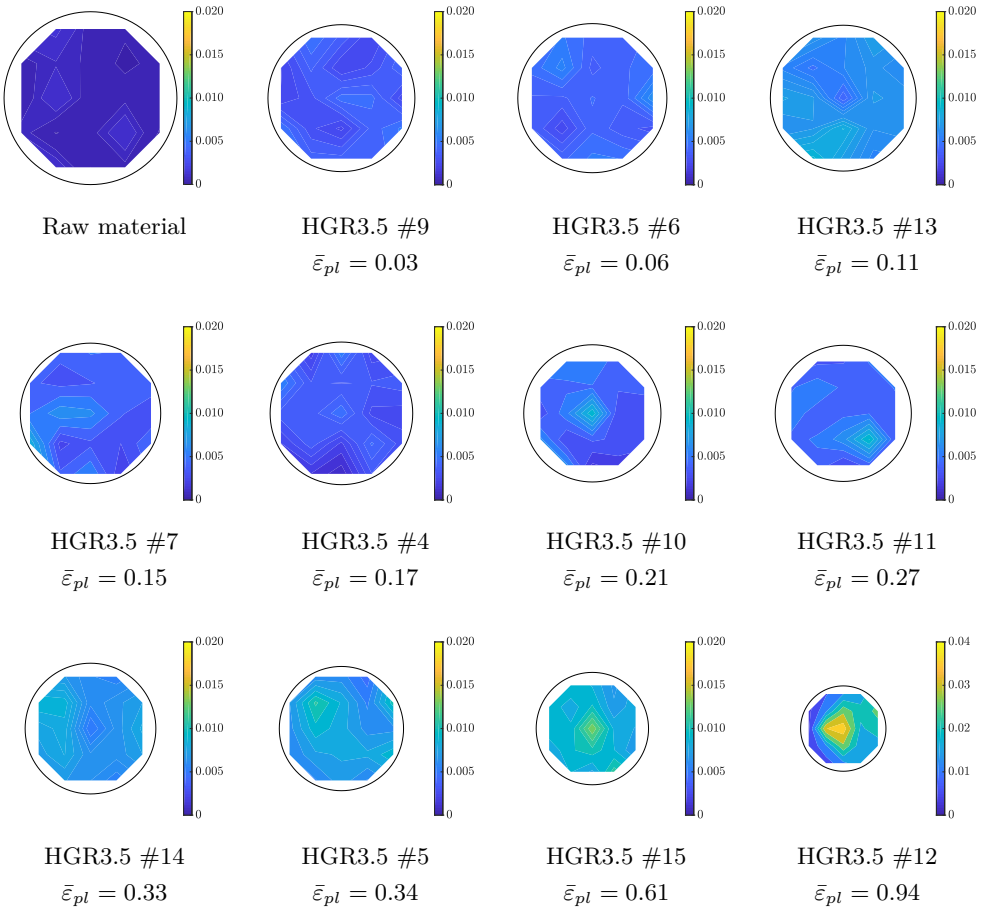
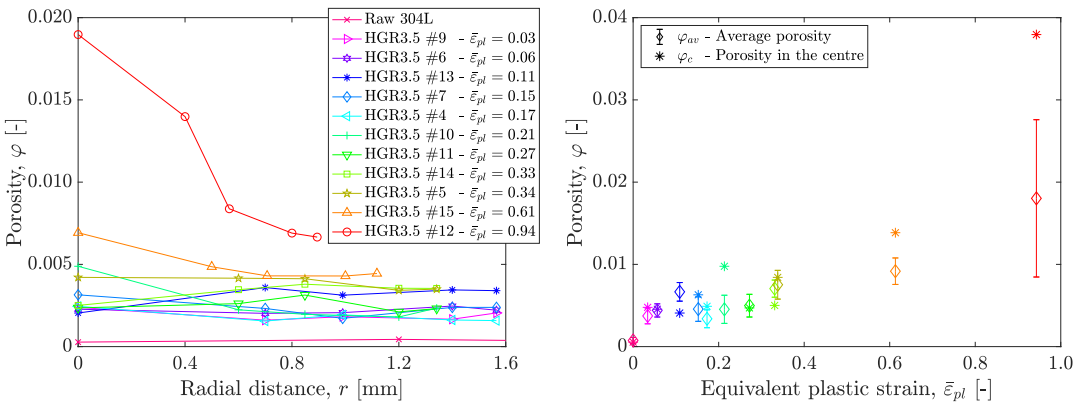



**Figure 6.13:** Contours of porosity in the cross-section of stainless steel 304L specimens deformed at high strain-rate.




**(a)** Radial distributions of porosity. **(b)** Porosity evolution with plastic strain.

**Figure 6.14:** Evolution of the porosity with equivalent plastic strain for stainless-steel 304L specimens deformed at high strain-rate ($\dot{\varepsilon} \sim 10^2$ s$^{-1}$).

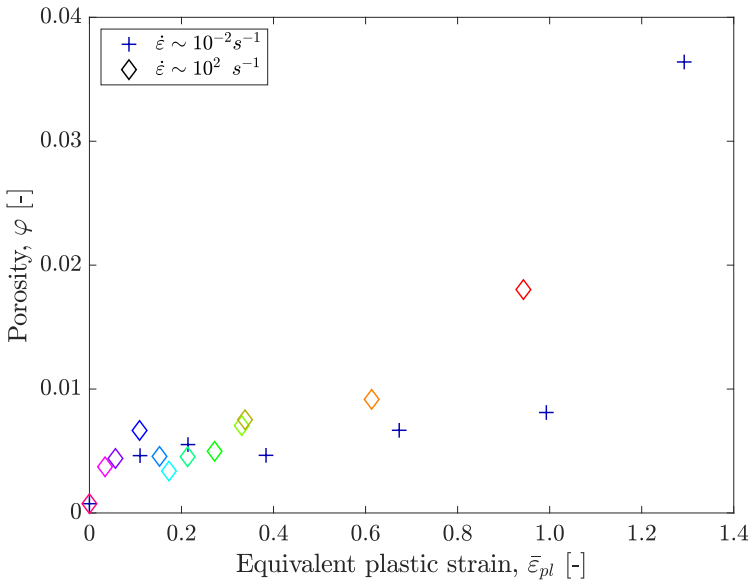



**Figure 6.15:** Effect of strain-rate on the evolution of the porosity vs. equivalent plastic strain ($\varphi$ - $\bar{\varepsilon}_{pl}$) for stainless steel 304L.

the real difference between regions. The fracture of copper at high strain-rate has not been perfectly circular as that of stainless steel, and regions with massive cracks and holes have appeared due to the interactions of voids. As a result, the contour plots of these specimens depict not only the porosity of the material, but also the highly degraded regions where these holes have appeared. For a better understanding, 5x magnification pictures of the cross-section of these specimens have been included in Figure 6.19, where the magnitude of the holes can be observed, and a comparison with the porosity contours can be made.

If the radial distribution of porosity in copper is analysed, it can be observed that a smooth trend as the one observed in stainless steel does not appear. It has already been shown that the degradation is not uniform in the cross-section, and considerable macroscopic defects appear in random locations of higher concentration of voids. Therefore, the clear high concentration in the middle that diminishes towards the edges of the sample is not observed in this material. A random distribution is rather observed, as shown in Figure 6.17, or in the consistently high deviations of Figure 6.18. Finally, if the porosity evolution with plastic strain is studied, the same trend as that obtained in the previous section measuring elastic modulus degradation is observed here. After a relatively long part of the plastic region with virtually no damage, porosity increases for the last two specimens in a linear fashion, if the last three mean porosity data points are observed. In this case, as both methods yield similar trends, the elastic modulus reduction results have been considered for the models calibration, and these porosity observations have been used as validation of those results.

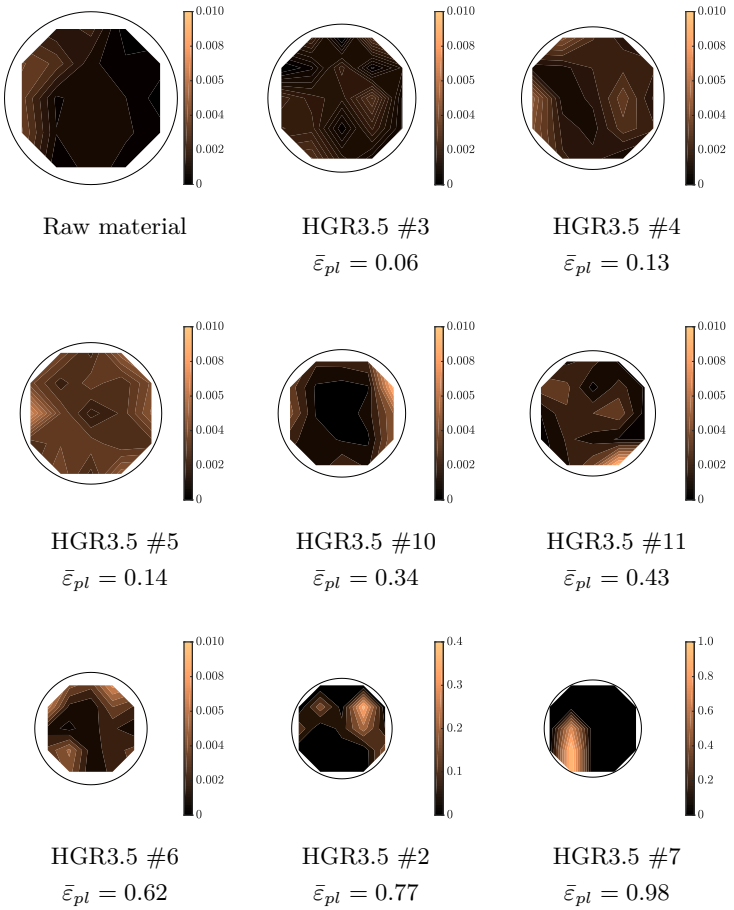
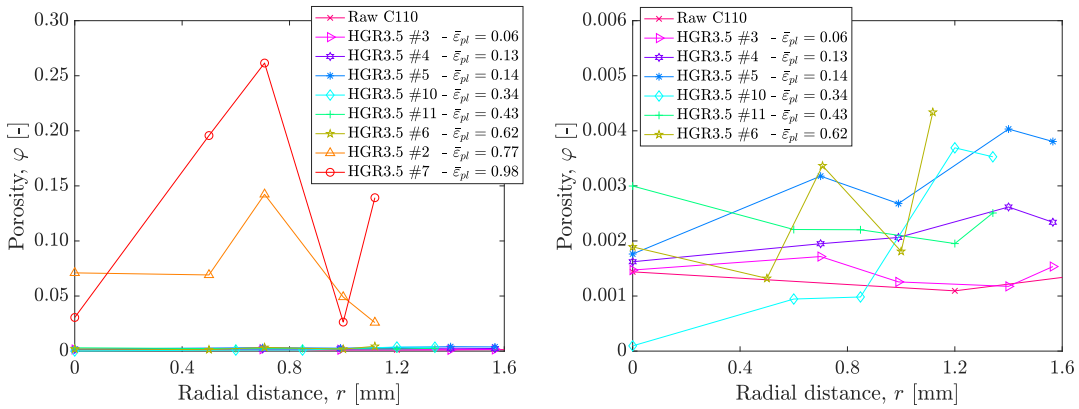
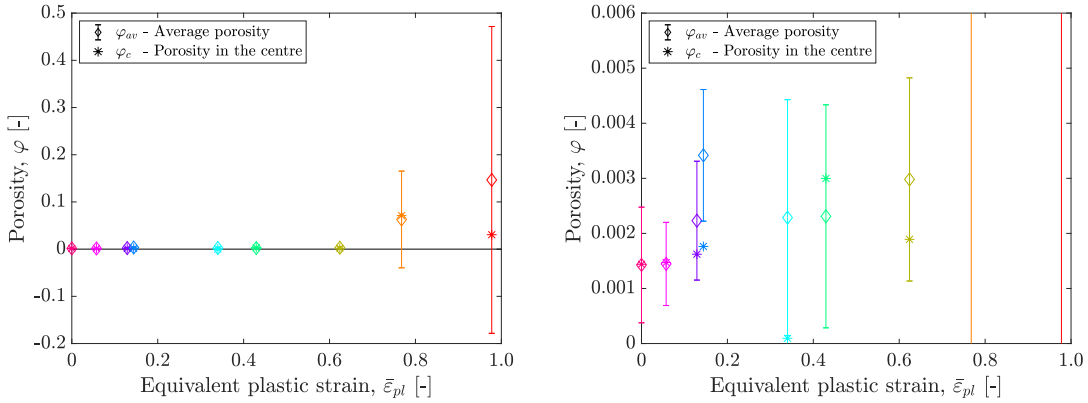



**Figure 6.16:** Contours of porosity in the cross-section of copper C110 specimens deformed at high strain-rate.



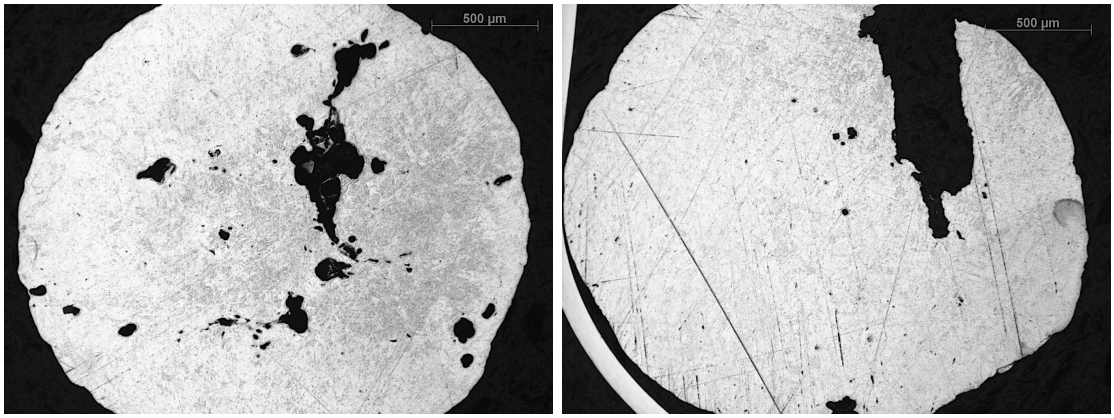

**(a)** Radial distributions of porosity. **(b)** Detail at low porosity.

**Figure 6.17:** Evolution of the porosity radial distribution for copper C110 specimens deformed at high strain-rate ($\dot{\varepsilon} \sim 10^2$ s$^{-1}$).




**(a)** Porosity evolution with plastic strain. **(b)** Detail at low porosity.

**Figure 6.18:** Evolution of the porosity with equivalent plastic strain for copper C110 specimens deformed at high strain-rate ($\dot{\varepsilon} \sim 10^2$ s$^{-1}$).




**(a)** C110 HGR3.5 #2 - $\bar{\varepsilon}_{pl} = 0.77$. **(b)** C110 HGR3.5 #7 - $\bar{\varepsilon}_{pl} = 0.98$.

**Figure 6.19:** Pictures of the cross-section of copper C110 samples at 5x magnification.

## 6.5 Conclusions

In this chapter, the experiments for metal plasticity and damage characterisation have been applied to different strain-rate conditions. Stainless steel 304L and copper C110 have been investigated at quasi-static ($\dot{\varepsilon} \sim 10^{-3}$ s$^{-1}$), intermediate ($\dot{\varepsilon} \sim 10^2$ s$^{-1}$) and high strain-rate ($\dot{\varepsilon} \sim 10^3$ s$^{-1}$), while the temperature has been kept at standard room conditions ($T \sim 20$°C). The specimen monitoring technique with in-situ shadowgraph and the sub-pixel accuracy post-processing algorithm have been used to obtain the results. Firstly, the plastic behaviour has been assessed, and although the scatter is bigger and the number of data points available lower at high strain-rate, some trends have been extracted from the necking process. In general, when the velocity of deformation increases, the materials have shown reduced ductility, causing lower average

stress triaxiality during the tests. The onset of necking seems to be slightly accelerated for stainless steel and delayed for copper. The flow curves move upwards showing the expected increase in strength at high speed, and also increasing the hardening rate, especially for copper at the highest rate studied.

Secondly, the ductile fracture performance has been assessed by means of tests on round notched samples that produce triaxiality conditions equivalent to those studied in the quasi-static case. The geometry of the notches has been tracked using the same technique as in the plasticity analysis. The overall change produced at high strain-rate in ductile fracture is a decrease of the fracture strain. However, while for copper the magnitude of this decrease is almost the same for any given state of stress triaxiality, for stainless steel the decrease is accentuated in the low triaxiality region and almost non-existent at high triaxiality.

The final study corresponds to the ductile damage accumulation in the form of voids. To study the damage at different levels of plastic deformation, the experimental rig for interrupted high-speed tensile tests has been used. After the specimens have been strained, two properties have been measured to estimate damage: the elastic modulus decrease and the void density from micrographs. The scatter of results and the small number of data points have entailed difficulties, however, it has been possible to extract quite clear trends. Copper follows the same damage accumulation tendency at different strain-rates, the part of linear damage rise seems to be steeper though if the material is deformed at high speed. Stainless steel, however, loses at high rate the damage plateau that appears in the intermediate plastic strain region in quasi-static conditions, presenting a sustained damage increase that rises more quickly near fracture. The porosity analysis also shows a more random distribution of damage in the cross-section of copper specimens compared to that of stainless steel, caused by the rapid interaction of clusters of voids that lead to macroscopic holes and cracks within this material.

# Chapter 7

# Experimental Results - Temperature Effect

## 7.1 Introduction

The experimental results obtained with the proposed methodology and applied to different temperature conditions are presented and discussed in this chapter. The techniques introduced in Chapter 3 are applied taking into account the variations considered in Chapter 4, which are specific to temperature tests. The effect that temperature has on plasticity is discussed in Section 7.2, on ductile fracture in Section 7.3 and on damage accumulation in Section 7.4; some conclusions are discussed in Section 7.5. Three temperatures have been analysed as part of this work: low temperature ($T \sim -80°\text{C}$), room temperature ($T \sim 20°\text{C}$) and high temperature ($T \sim 180°\text{C}$). All these tests have been conducted in quasi-static strain-rate conditions ($\dot{\varepsilon} \sim 10^{-3}$ s$^{-1}$) on stainless steel 304L and copper C110. As for the variable strain-rate tests discussed in the previous chapter, the results analysed here will be used to include temperature effects on material models in Chapter 8.

## 7.2 Temperature Effect on Plasticity

A series of tensile tests have been performed on round bar RB6 specimens in an environmental chamber, in order to analyse the effect of temperature on plastic yield and hardening behaviours. The neck monitoring method described in Section 3.3 has been employed to obtain the real values of local true stress and true strain, capturing the strain localisation phenomenon. The considerations suggested for temperature tests in Section 4.3 have been taken into account to improve the quality of results. An

| Material | Geometry | Specimen | Temperature, $T$ [K] | $\sigma$-$\varepsilon$ measurement | |
|---|---|---|---|---|---|
| | | | | Imaging | Extensom. |
| s/s 304L | RB6 | #24 | 193 | x | |
| | | #14 | 294 | x | |
| | | #16 | 294 | x | |
| | | #12 | 294 | | x |
| | | #13 | 294 | | x |
| | | #21 | 453 | x | |
| | | #22 | 453 | x | |
| | HGR6 | #38 | 193 | x | x |
| | | #21 | 295 | x | x |
| | | #30 | 453 | x | x |
| copper C110 | RB6 | #7 | 193 | x | |
| | | #8 | 193 | x | |
| | | #1 | 293 | x | |
| | | #2 | 293 | x | x |
| | | #5 | 453 | x | |
| | | #6 | 453 | x | |
| | HGR6 | #14 | 193 | x | x |
| | | #8 | 294 | x | x |
| | | #10 | 453 | x | x |

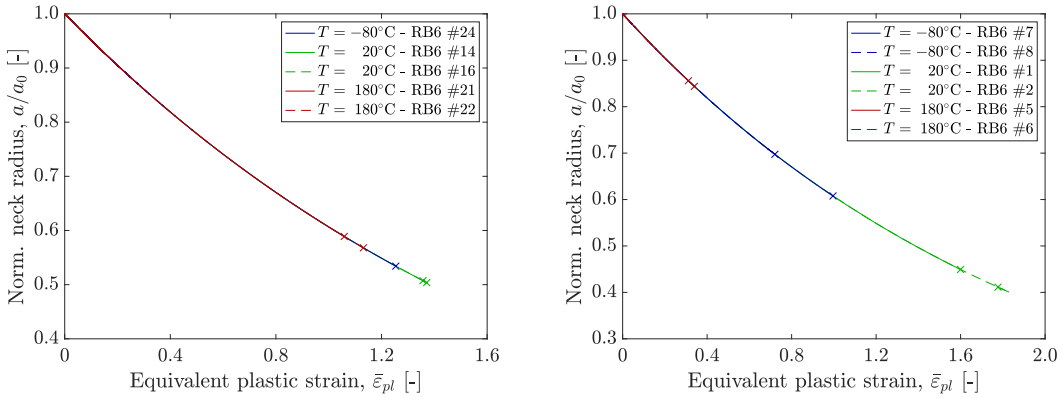
**Table 7.1:** Specimens studied in the analysis of temperature effects on plasticity.

hourglass HGR6 sample has also been tested in each of the conditions in order to obtain the necking correction curves, which have later been used for the damage accumulation analysis. A summary of the tested specimens is shown in Table 7.1.

### 7.2.1 Neck Geometry

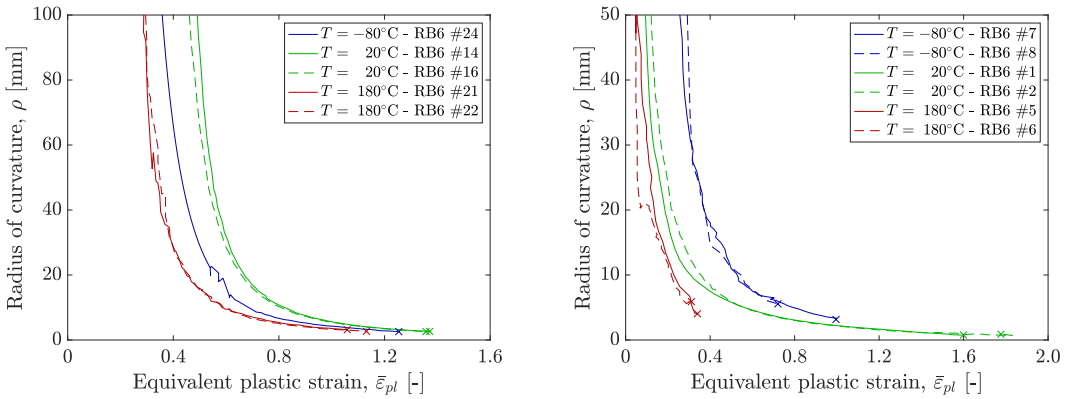
The reduction of specimen cross-section with applied plastic strain is represented in Figure 7.1 for specimens tested at the three temperatures under study. For both materials, neck reduction capability decreases both at high and low temperature conditions compared to room temperature, being the effect more pronounced in hot conditions. Also, while these effects are subtle for stainless steel, they are severe for copper. The diameter reduction capability for copper is 39.0% lower at −80°C than it is at room temperature, and 73.6% lower at 180°C. On the contrary, the necking capacity of stainless steel is just 5.8% lower at the analysed low temperature conditions and 14.7% lower at the high temperature.

Additionally, the radius of curvature of the neck has been measured in this test, and its evolution with plastic strain is represented in Figure 7.2. The noisier results at high




**(a)** stainless steel 304L **(b)** copper C110

**Figure 7.1:** Effect of temperature on normalised minimum cross-sectional radius - equivalent plastic strain ($a/a_0$ - $\bar{\varepsilon}_{pl}$).




**(a)** stainless steel 304L **(b)** copper C110

**Figure 7.2:** Effect of temperature on radius of curvature of the neck - equivalent plastic strain ($\rho$ - $\bar{\varepsilon}_{pl}$).

and low temperature compared to the data at room temperature are a consequence of the difficulties of taking appropriate quality photographs within the environmental chamber. More challenging lighting conditions within the furnace and ice formation at $-80°C$ have been determining issues, which have made complex the capture of a smooth sample shape for the post-processing. Nevertheless, the results are adequate to provide a clear trend followed by curvature at different temperatures. The earlier fracture in low and high temperature conditions can also be observed in these plots. Moreover, the plastic strain at which necking starts can also be estimated from the location where the curves of Figure 7.2 stop being asymptotic and $\rho$ starts decreasing. For stainless steel, the onset of necking shifts towards lower plastic strains for both low and high temperature, following in both cases a similar decrease rate to the one

| Material | Geom. | Spec. | Temp. $T$, [K] | Imaging $\varepsilon_{onset}$ [-] | Imaging $\rho_f$ [mm] | Imaging $a_f$ [mm] | Shadowgr. $a_f$ [mm] |
|---|---|---|---|---|---|---|---|
| s/s 304L | RB6 | #24 | 193 | 0.27 | 2.58 | 1.57 | 1.51 |
| | | #14 | 294 | 0.35 | 2.62 | 1.50 | 1.49 |
| | | #16 | 294 | 0.38 | 2.58 | 1.51 | 1.53 |
| | | #21 | 453 | 0.21 | 3.16 | 1.74 | 1.70 |
| | | #22 | 453 | 0.22 | 2.66 | 1.68 | 1.67 |
| copper C110 | RB6 | #7 | 193 | 0.070 | 3.16 | 1.80 | 1.67 |
| | | #8 | 193 | 0.096 | 5.55 | 2.06 | 2.00 |
| | | #1 | 293 | 0.04 | 0.94 | 1.29 | 1.27 |
| | | #2 | 293 | 0.05 | 0.88 | 1.22 | 1.22 |
| | | #5 | 453 | 0.039 | 4.04 | 2.50 | 2.50 |
| | | #6 | 453 | 0.034 | 5.90 | 2.53 | 2.56 |

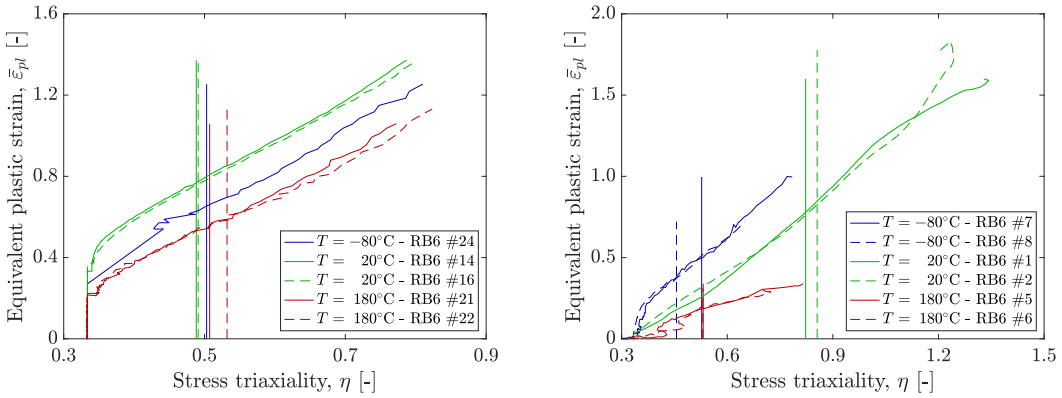
**Table 7.2:** Effect of temperature on neck onset strain ($\varepsilon_{onset}$), final neck radius of curvature ($\rho_f$) and final cross-sectional radius ($a_f$) measured with imaging method; and final cross-sectional radius ($a_f$) measured with shadowgraph.

observed at room temperature (Figure 7.2a). For copper, however, necking appears at a higher plastic strain at $-80$°C than at 20°C, presenting a longer region of uniform deformation (Figure 7.2b). The neck appears almost instantaneously at 180°C, with a sudden decrease in curvature that implies a very quick development of the neck. In this case, unlike the rest of conditions studied, curvature decreases almost linearly without presenting a stabilisation at low values, being this the cause of the very low fracture plastic strain.

Some of the features observed in the figures are also summarised in Table 7.2 in the form of numerical results. The onset of necking strain and the final values of neck curvature and cross-section are presented for each specimen. The final cross-sectional radius has also been measured ex-situ using a shadowgraph. The comparatively small difference between the values obtained using both methods serves as further validation of the neck imaging technique. The only case in which a slight difference is observed is the low temperature tests, where the measured final diameter is fairly smaller than the one recorded during the test. The cause is the ice that forms on the surface of the specimen in those conditions, creating an artificially thicker diameter.

### 7.2.2 Stress Triaxiality

One of the most interesting features of the neck monitoring technique is the capability of tracking stress triaxality in the centre of the neck throughout the test. The effect of temperature on this parameter is represented in Figure 7.3, where the average




**(a)** stainless steel 304L **(b)** copper C110

**Figure 7.3:** Effect of temperature on equivalent plastic strain - stress triaxiality ($\bar{\varepsilon}_{pl}$ - $\eta$).

| Material | Geometry | Specimen | Temp. $T$, [K] | Stress triaxiality $\eta_{av}$ [-] | $\eta_{min}$ [-] | $\eta_{max}$ [-] |
|---|---|---|---|---|---|---|
| s/s 304L | RB | #24 | 193 | 0.503 | 0.333 | 0.810 |
| | | #14 | 294 | 0.488 | 0.333 | 0.787 |
| | | #16 | 294 | 0.491 | 0.333 | 0.796 |
| | | #21 | 453 | 0.507 | 0.333 | 0.772 |
| | | #22 | 453 | 0.532 | 0.333 | 0.823 |
| copper C110 | RB | #7 | 193 | 0.527 | 0.333 | 0.785 |
| | | #8 | 193 | 0.456 | 0.333 | 0.649 |
| | | #1 | 293 | 0.823 | 0.333 | 1.329 |
| | | #2 | 293 | 0.855 | 0.333 | 1.205 |
| | | #5 | 453 | 0.532 | 0.333 | 0.815 |
| | | #6 | 453 | 0.530 | 0.333 | 0.691 |

**Table 7.3:** Effect of temperature on stress triaxiality; the average ($\eta_{av}$), minimum ($\eta_{min}$) and maximum ($\eta_{max}$) values of triaxiality for each test are presented.

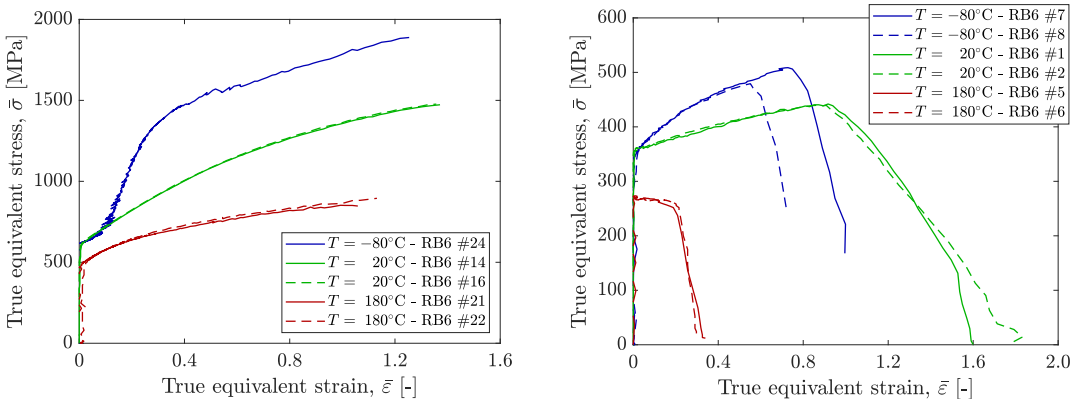
value for each test is also represented as a vertical line. Numerical values of average, minimum and maximum stress triaxiality measured for each test are also shown in Table 7.3.

Temperature does not have a great effect on triaxiality for stainless steel 304L, as observed in Figure 7.3a, where the curves are approximately parallel to each other, shifted downwards in non-room temperature conditions because of the earlier necking onset, but failing at similar stress triaxiality levels and, therefore, producing similar average triaxialities. From these results it can be inferred that the neck development process of stainless steel 304L is very similar at different temperatures, varying only the

plastic strain at which necking starts. However, temperature provokes great changes in copper C110 stress triaxiality. In Figure 7.3b, it can be observed that at $-80°C$ stress triaxiality stays constant during a short region of plastic strain (short vertical region), corresponding to the previously mentioned deferred onset of necking. Triaxiality then increases fairly linearly at a similar rate to that of room temperature, but failing at an earlier neck development, which results in a lower value of average stress triaxiality. On the other hand, it has already been discussed that tests at 180°C have shown a quick and sudden neck development, and that behaviour is also reflected in the flatter triaxiality curves, which represent a considerable stress triaxiality rise for small plastic strain. The level of stress trixiality at fracture is similar to the cold conditions producing a similar average value.

### 7.2.3 Equivalent Stress - Strain

Finally, the equivalent stress - equivalent strain curves obtained from the geometric analysis are plotted in Figure 7.4. In both cases the effect is the expected, an increase in the strength of the material when temperature is reduced. Stainless steel does not present a great effect of temperature on yield stress, however, the hardening rate reduces slightly at high temperatures. An interesting characteristic of 304L at low temperature is the elbow that the stress - strain curve presents at low equivalent strain ($\bar{\varepsilon} \sim 10\%$). This phenomenon was already observed in austenitic steels by authors like DeSisto and Carr [131] and Park et al. [132], and corresponds to the formation of a strain-induced martensitic transformation. Those experimental studies show that the austenite of 304L steel is transformed into martensite at cryogenic temperatures, being the consequence a severe increase in hardening, known as the strong hardening phenomenon. Viscoplastic

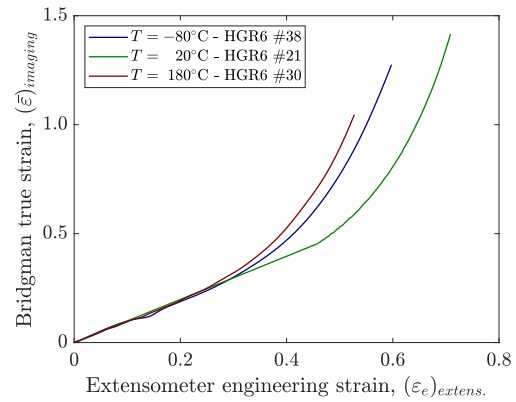



**(a)** stainless steel 304L **(b)** copper C110

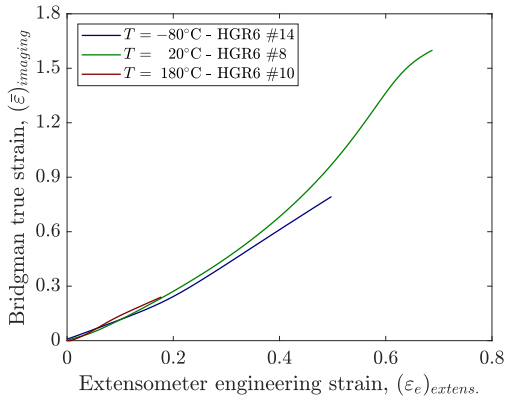
**Figure 7.4:** Effect of temperature on true equivalent stress - true equivalent strain behaviour ($\bar{\sigma}$ - $\bar{\varepsilon}$).

models that include this effect have been developed [133, 134]; nonetheless, they have not been implemented in the models formulation of this thesis, since it is not the main topic of research and it has been considered that they would add unnecessary complexity.

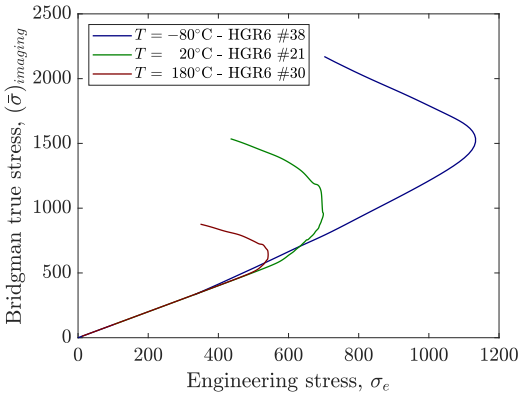
Low temperatures do not affect the yield stress of copper and the only effect is a significant increase in the hardening rate. The material becomes more brittle, although the failure is still ductile and progressive. The effect on fracture strain is considerable, since while at room temperature the degradation process occurs along a sustained range of plastic strain (from $\bar{\varepsilon}_{\bar{\sigma}_{MAX}} \sim 1.10$ at maximum stress point to $\bar{\varepsilon}_f \sim 1.73$ at final fracture), at low temperature it is much more sudden ($\bar{\varepsilon}_{\bar{\sigma}_{MAX}} = 0.75$ and $\bar{\varepsilon}_f = 1.00$). At 180°C the yield point falls considerably and the material behaves perfectly plastically or even presents slight strain softening. Interestingly, instead of flowing to very high plastic strains the material has failed relatively early.



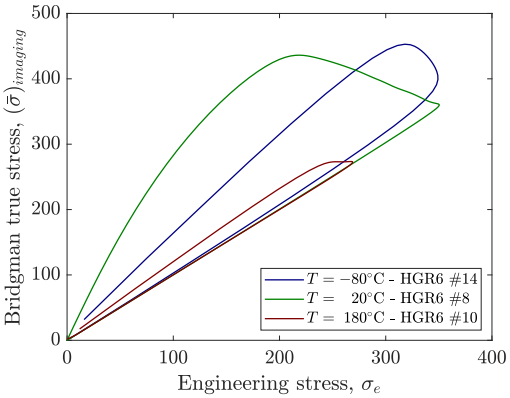

**(a)** Strain correction for stainless steel 304L




**(b)** Strain correction for copper C110




**(c)** Stress correction for stainless steel 304L




**(d)** Stress correction for copper C110

**Figure 7.5:** Effect of temperature on the necking correction curves: strain correction ($(\bar{\varepsilon})_{imaging}$ - $(\varepsilon_e)_{extens.}$) and stress correction ($(\bar{\sigma})_{imaging}$ - $(\sigma_e)$).

### 7.2.4 Stress - Strain Neck Correction

As mentioned before, a HGR6 specimen has been tested in each of the conditions and for both materials, with the aim of obtaining relationships to correct the effects of material necking. By taking measurements with both the imaging methodology and the extensometer, the correction curves of Figure 7.5 have been obtained. The curves at different temperatures present the same shape as those at room temperature that were discussed in Section 5.2.4, nevertheless, they encompass the general temperature effects that have been analysed in the previous figures:

- linear relationship of strains up to the onset of necking;
- lower ductility for low and high temperature;
- "boomerang" shape of stress curves with abrupt failure for stainless steel and progressive failure for copper;
- higher loads at low temperatures.

## 7.3 Temperature Effect on Ductile Fracture

The effects of temperature on ductile fracture at different stress triaxiality conditions have been studied by running tensile tests on notched RNB6 specimens inside an environmental chamber. The imaging methodology has also been used to track stress - strain and stress triaxiality throughout the tests, as explained in Section 3.4. The specimens analysed are summarised in Table 7.4, organised by their notch acuity and the average temperature conditions tested.

### 7.3.1 Fracture Surface

A comparison of the fracture surfaces at low, room and high temperature is shown in Figure 7.6 for stainless steel 304L and in Figure 7.7 for copper C110. All these pictures have been taken using SEM microscopy from the tensile RB6 specimens discussed in the previous section. The lower necking capability at $-80°C$ and $180°C$ described before can be appreciated in the 40x magnification images, which show central sections of bigger diameter. The radial isotropy of the materials is also confirmed since all the 40x images show a circular fracture section.

The higher magnification images allow for a better analysis of the microscopic appearance of fractured voids at different temperatures. In stainless steel 304L at room temperature, a fairly uniform distribution of small voids (1-2 μm) is observed. Some voids of bigger size (10-30 μm) are observed at $180°C$, alongside the smaller ones also

| Material | Geometry | Notch acuity, $a/\rho$ [-] | Temperature, $T$ 193 K | 293 K | 453 K |
|---|---|---|---|---|---|
| s/s 304L | RB6 | 0 | #24 | #14<br>#16 | #21<br>#22 |
| | RNB6-1 | 0.25 | | #19 | |
| | RNB6-2 | 0.313 | #28 | | #27 |
| | RNB6-3 | 0.417 | | #15 | |
| | RNB6-4 | 0.833 | #26 | #11 | #25 |
| | RNB6-5 | 1.25 | #24 | #7 | #23 |
| | RNB6-6 | 2.5 | #22 | #3 | #21 |
| copper C110 | RB6 | 0 | #7<br>#8 | #1<br>#2 | #5<br>#6 |
| | RNB6-2 | 0.313 | #10 | #11 | #12 |
| | RNB6-4 | 0.833 | #7 | #8 | #9 |
| | RNB6-5 | 1.25 | | #5 | #6 |
| | RNB6-6 | 2.5 | #1 | #2 | |

**Table 7.4:** Specimens studied in the analysis of temperature effects on fracture strain.

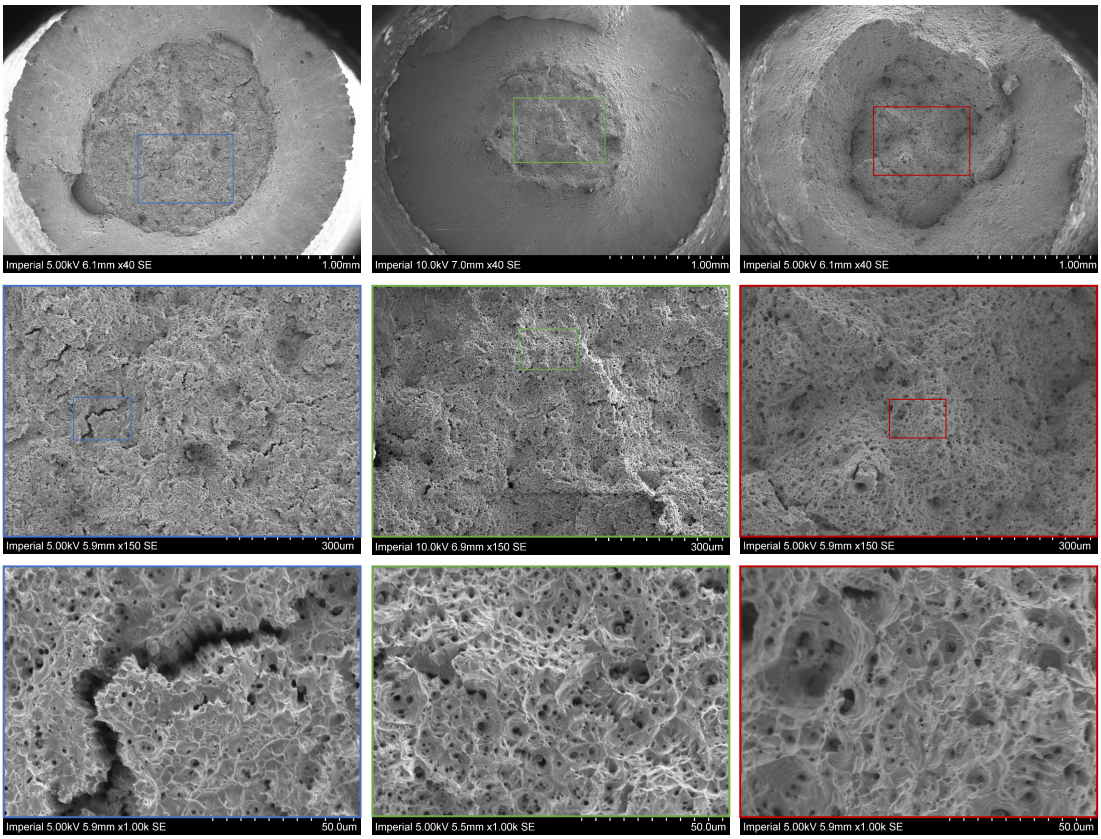



**Figure 7.6:** Effect of temperature on the fracture surface of stainless steel 304L (from left to right: $T \sim -80°C$, $T \sim 20°C$ and $T \sim 180°C$; from top to bottom: 40x, 150x and 1000x magnification.

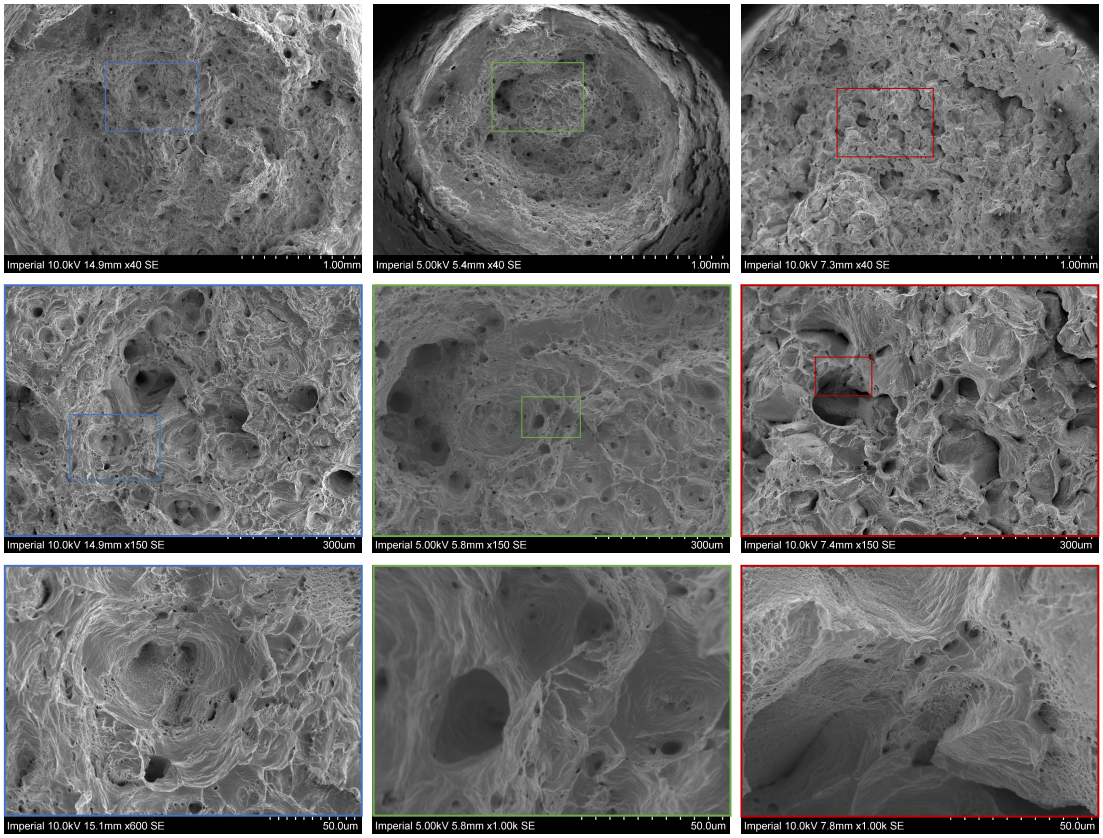



**Figure 7.7:** Effect of temperature on the fracture surface of copper C110 (from left to right: $T \sim -80°C$, $T \sim 20°C$ and $T \sim 180°C$; from top to bottom: 40x, 150x and 1000x magnification.

present at room temperature. At $-80°C$, on the other hand, a lower number of small voids is observed, however, a series of relatively big cracks appear (width of $\sim 10$ µm and variable length up to $\sim 200$ µm). They have potentially been caused by a combination of voids coalesce and material cracking, due to the higher brittleness of the martensite present at cryogenic temperature, which still allows an overall ductile failure mechanism but may have enhanced material micro-cracking.

The voids observed in copper C110 are comparatively bigger than those of stainless steel in all the temperatures analysed. The images of Figure 7.7 show that at high temperature it becomes very difficult to distinguish individual voids, since their size is much bigger and the surface looks rocky and degraded. The main voids observed at low magnification have a size of 50-150 µm, while in the 1000x image much smaller pores (1-3 µm) appear within the bigger voids. The considerable size of some defects may have produced an accelerated degradation of the material that has lead to its very early fracture. The difference between the room and low temperature fractures is not enormous, as it happened with the stress - strain behaviour in these conditions

(Figure 7.4). The average size of voids is very similar and only a slightly lower density of defects can be appreciated at low temperature. In the three temperatures, beach-like marks can be observed around voids. These may have been caused by the progressive ductile failure mechanism that copper has undergone, as opposed to the sudden brittle fracture of stainless steel.

### 7.3.2 Equivalent Stress - Strain

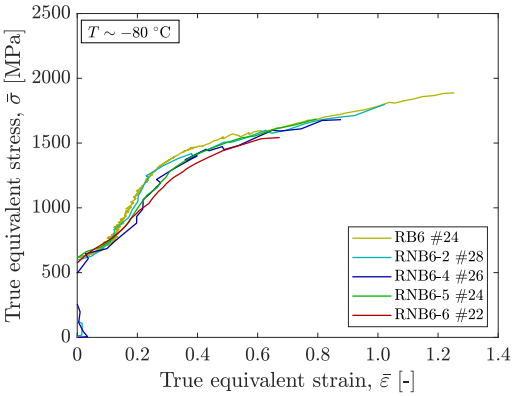
The equivalent stress - strain curves of Figure 7.8 have been obtained using the imaging method.[1] Maximum axial stress - equivalent strain results are also available in Figure 7.9. For an easier interpretation of the results, these have been separated according to their temperature, being the low temperature results at the top, room temperature in the middle and high temperature at the bottom. In these plots the combination of two effects already presented in previous sections can be appreciated:

- **Effect of notch acuity on the stress - strain behaviour.** This was analysed in Section 5.3 for room temperature tests (results of Figure 7.8c and 7.8d). When these plots are compared to the results at $-80°C$ (Figure 7.8a and 7.8b) and at $180°C$ (Figure 7.8e and 7.8f), the same trends can be appreciated. The higher notch acuities reduce the fracture plastic strain. The curves are parallel to each other at a given temperature, suggesting no significant effect of stress triaxiality on the hardening rate. All the samples tested at a given temperature fracture at a similar maximum axial stress level, especially noticeable at low temperature (Figure 7.9a).
- **Effect of temperature on the stress - strain behaviour.** This was analysed in Section 7.2 with the round bar geometry (all the yellow curves of Figure 7.8 and 7.9), and is extended here to different notch geometries. The trend followed by each geometry is equivalent to that observed for round specimens on Figure 7.4 of the previous section. An increase of temperature reduces yield stress and hardening rate in all cases. Ductility has decreased in all the samples tested at $-80°C$ and $180°C$. The strong hardening phenomenon is observed in all the 304L specimens tested at $-80°C$, as observed in Figure 7.8a, appearing the martensitic transformation slightly earlier for high values of notch acuity (sharper notches).

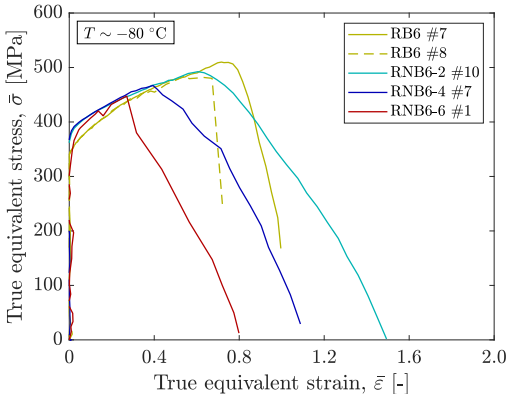
### 7.3.3 Effect of Stress Triaxiality on Ductility

The ultimate aim of analysing samples with different notches has been to study fracture strain under different stress triaxiality conditions. Those results are presented

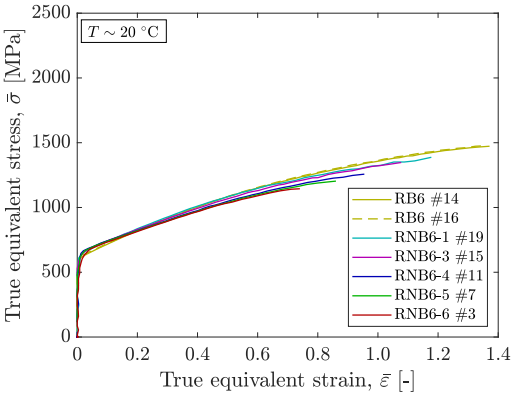
[1] Plots of the evolution of notch geometry used to calculate stress - strain for each sample are available in Figures B.7 and B.10 for $a/a_0$-$\bar{\varepsilon}_{pl}$ and Figures B.8 and B.11 for $\rho$-$\bar{\varepsilon}_{pl}$, both in Appendix B.



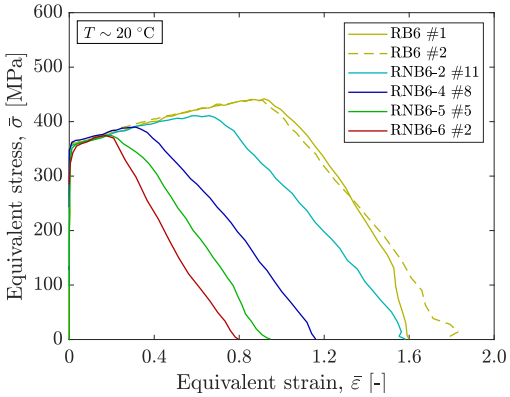

**(a)** stainless steel 304L - $T \sim -80$°C



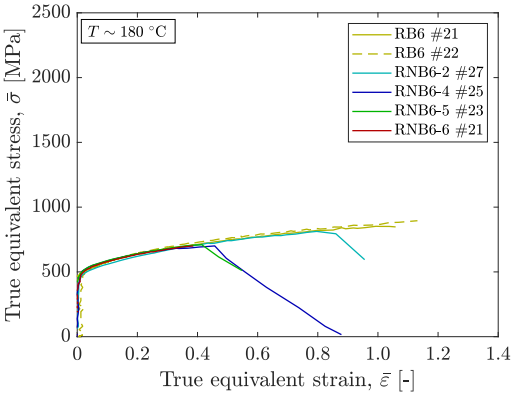

**(b)** copper C110 - $T \sim -80$°C



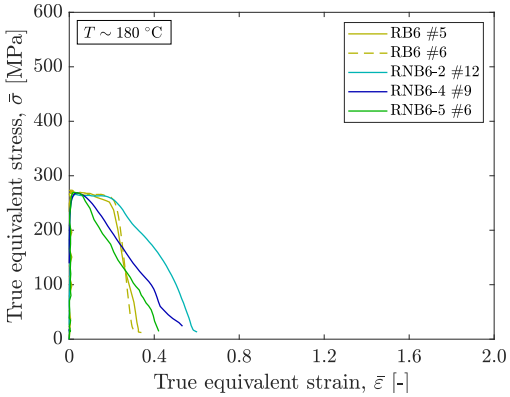

**(c)** stainless steel 304L - $T \sim 20$°C




**(d)** copper C110 - $T \sim 20$°C

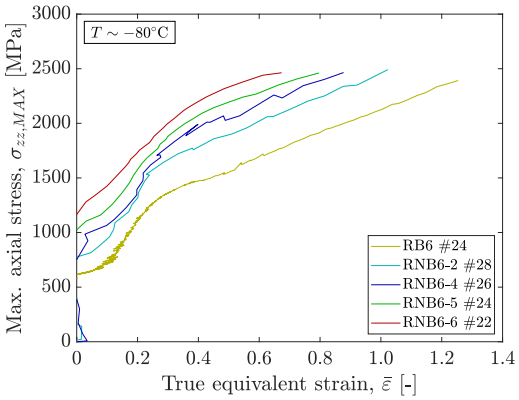



**(e)** stainless steel 304L - $T \sim 180$°C

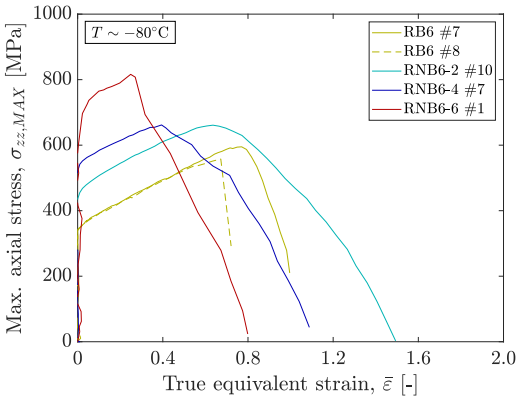



**(f)** copper C110 - $T \sim 180$°C

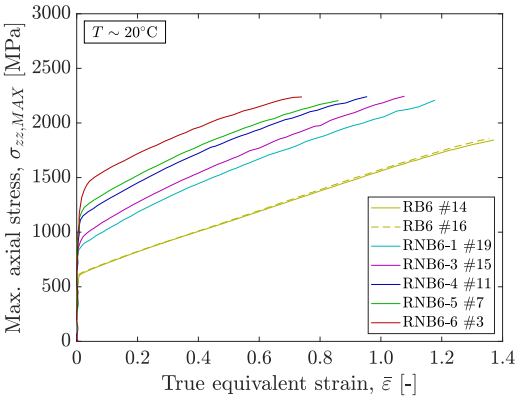
**Figure 7.8:** Effect of temperature on true equivalent stress - true equivalent strain ($\bar{\sigma}$ - $\bar{\varepsilon}$) for the notched bar tests.



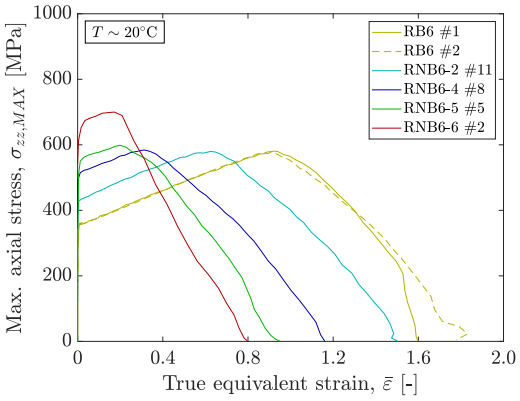

**(a)** stainless steel 304L - $T \sim -80°C$



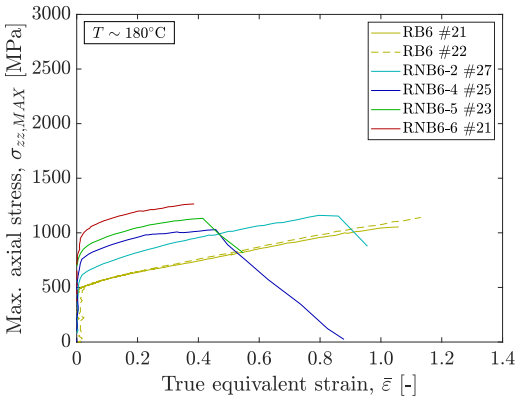

**(b)** copper C110 - $T \sim -80°C$



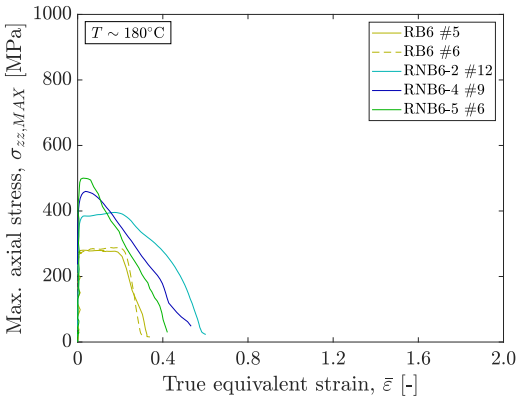

**(c)** stainless steel 304L - $T \sim 20°C$




**(d)** copper C110 - $T \sim 20°C$




**(e)** stainless steel 304L - $T \sim 180°C$




**(f)** copper C110 - $T \sim 180°C$

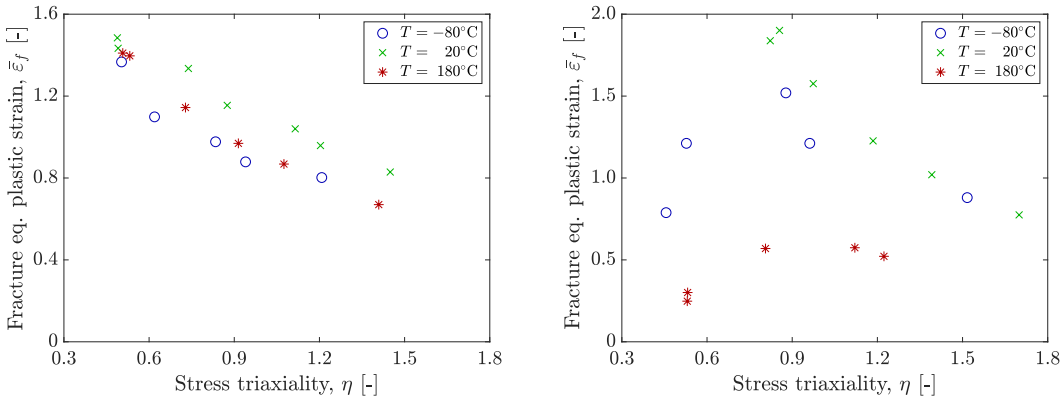
**Figure 7.9:** Effect of temperature on maximum axial stress - true equivalent strain ($\sigma_{zz,MAX}$ - $\bar{\varepsilon}$) for the notched bar tests.

in Figure 7.10 for the three temperatures studied. In these plots, each point corresponds to the final fracture equivalent plastic strain of a test plotted against the average stress triaxiality during the test.[2] As observed, both high and low temperatures have a detrimental effect on ductile fracture, since for a given stress triaxiality state the plastic strain at which the material fails is reduced.

While the effects at $T \sim 180°C$ on stainless steel 304L are subtle, the ductility of copper is seriously compromised at that temperature. The behaviour of the austenitic steel shifts downwards, entailing a slightly reduced ductility under any stress state. For copper, the ductility reduction is massive falling at a stress triaxiality of $\eta \sim 0.8$ from $\bar{\varepsilon}_{pl,f} = 1.82$ at $T = 20°C$ to $\bar{\varepsilon}_{pl,f} = 0.57$ at $T = 180°C$. The results are also almost independent of stress state, presenting an almost horizontal trend instead of the typical exponential decrease.

At low temperature, the behaviour is similar to that at room temperature, but the results are slightly shifted downwards and leftwards. This means that not only the ductility is reduced, but also the average triaxiality decreases. This effect is caused by the lower necking capability available at low temperatures, which also reduces the maximum stress state achievable. The only inconsistent results are those of the copper RB6 specimens which have shown unexpectedly low values of ductile fracture strain.

The results are in accordance with the observations of fracture surfaces of Figure 7.6 and Figure 7.7, which suggested a significantly more damaged austenitic steel at low




**(a)** stainless steel 304L **(b)** copper C110

**Figure 7.10:** Effect of temperature on fracture equivalent plastic strain - stress triaxiality ($\bar{\varepsilon}_f$ - $\eta$).

[2]The numerical values of stress triaxiality and ductility of the tests are available in Table B.3 and Table B.4; and plots of the evolution of stress triaxiality along the test in Figures B.9 and B.12, both in Appendix B.

and high temperatures, slightly bigger voids in copper at cold temperature and much bigger defects in the same material at high temperature.

## 7.4 Temperature Effect on Damage Accumulation

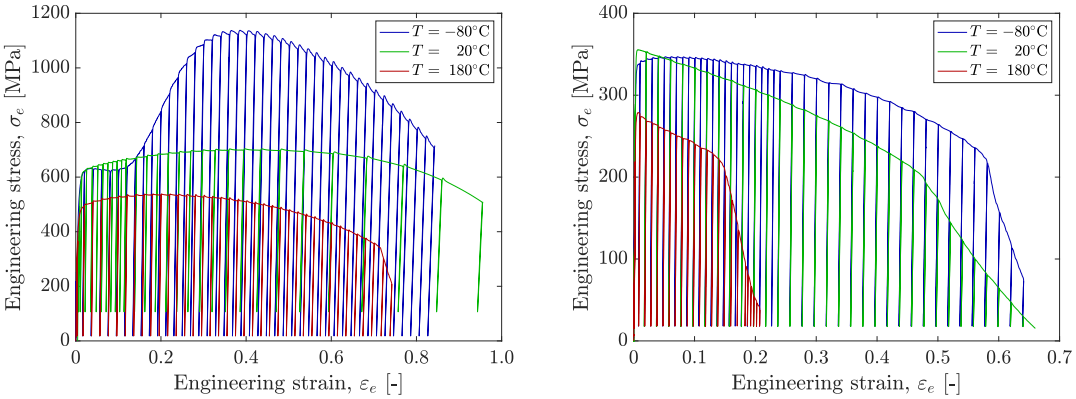
To analyse the effect of temperature on damage accumulation, tests have been run on HGR6 specimens following the methodology described in Section 3.5. Table 7.5 shows a summary of the tests performed, and Figure 7.11 an example of the raw engineering stress - engineering strain history curve obtained in one test of each of the temperatures and materials.

In order to study damage, each of the unloading cycles, such as those of Figure 7.11, has been analysed and the effective elastic modulus has been extracted from its unloading slope. Ductile damage has then been estimated making use of the CDM definition (Equation 2.34). The evolution of elastic modulus with plastic strain for the three temperature conditions studied is presented in Figure 7.12 and the ductile damage accumulation results in Figure 7.13.

Damage accumulation results in room temperature conditions were analysed in Section 5.4 and correspond to the green crosses of Figure 7.12 and Figure 7.13. Stainless steel 304L presents an abnormal behaviour at low temperature caused by the martensitic transformation phase change. During the transformation that occurs in the $\bar{\varepsilon}_{pl} = 0 \sim 0.2$ interval, the elastic modulus decreases from its initial value of $E \sim 190$ GPa to $E \sim 137$ GPa. This rapid modulus decrease cannot be associated to voids formation, in essence because part of that modulus is recovered by the time the transformation has ended around $\bar{\varepsilon}_{pl} = 0.25$. Consequently, the initial region has not been taken into account for the damage analysis, and only the remaining elastic

| Material | Geometry | Temperature, $T$ | | |
|---|---|---|---|---|
| | | 193 K | 293 K | 453 K |
| s/s 304L | HGR6 | #26<br>#27<br>#28 | #4<br>#6<br>#9<br>#11 | #12<br>#22<br>#23<br>#24<br>#25 |
| copper C110 | HGR6 | #15<br>#16<br>#18 | #3<br>#4<br>#7 | #11<br>#12<br>#13 |

**Table 7.5:** Specimens studied in the analysis of temperature effects on ductile damage accumulation.

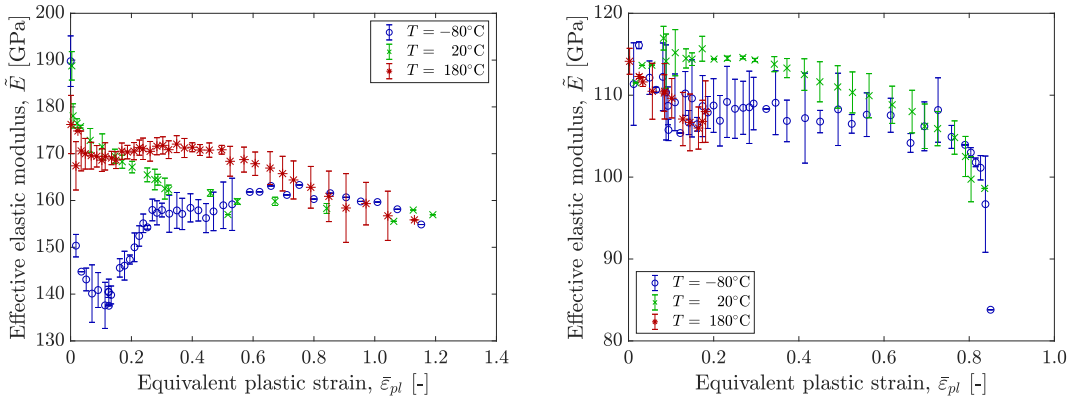



**(a)** stainless steel 304L **(b)** copper C110

**Figure 7.11:** Example of engineering stress - engineering strain ($\sigma_e$ - $\varepsilon_e$) of loading-unloading experiments run at different temperatures.

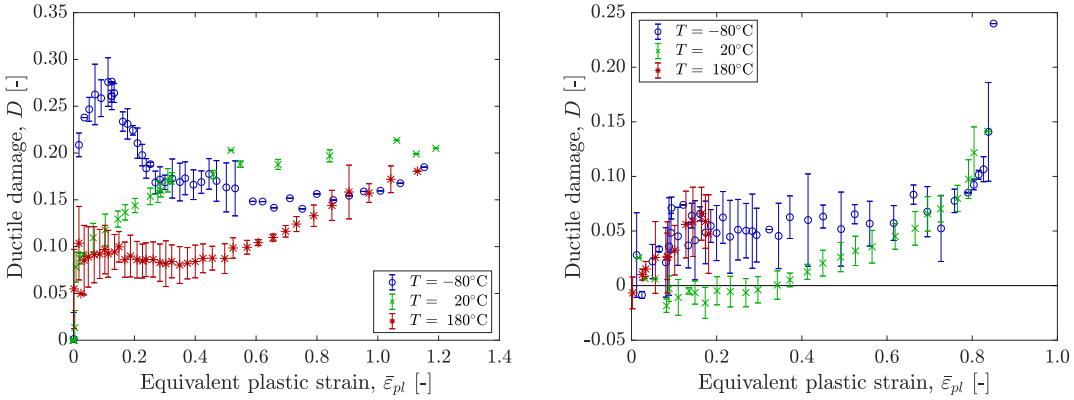
modulus fall has been considered damage. As shown in Figure 7.13a, damage is slightly lower than that measured at room temperature and presents a similar plateau region. Damage increases then lightly towards the end of the plastic region, approaching similar values to the ones measured at room temperature. Regarding the high temperature results, as soon as the material starts yielding, damage rises to a value similar to the one measured at room temperature. Afterwards, while at room temperature damage increases at moderate rate, at high temperature it stabilizes until $\bar{\varepsilon}_{pl} \sim 0.5$ is reached. After this point, it starts increasing again in a fairly linear manner, overlapping with the damage obtained at low temperature and eventually, also with the room temperature value.

Damage does not appear in copper until $\varepsilon_{th} \sim 0.3$ in standard room temperature conditions. In Figure 7.13b, the results at low temperature show the appearance of damage from earlier stages of deformation, and the subsequent rise to a relatively stable value around $D \sim 0.05$ for most of the plastic region. In the region of high plastic deformation, the damage behaviour becomes similar to that at room temperature and damage increases rapidly at a similar rate, with a maximum measured damage value of $D_{cr} \sim 0.24$. The results at high temperature follow almost the same path as those at low temperature, with damage appearing at the beginning of the plastic region and increasing up to around $D \sim 0.05$. The difference in this conditions is the failure point, since these specimens fractured at very low plastic strain ($\bar{\varepsilon}_{pl,f} \sim 0.2$) as already commented in the previous sections of this chapter. Very low maximum damage was recorded, without noticeable damage rise towards the material fracture conditions ($D_{cr} \sim 0.05$).




**(a)** stainless steel 304L **(b)** copper C110

**Figure 7.12:** Effect of temperature on effective elastic modulus - equivalent plastic strain ($\tilde{E}$ - $\bar{\varepsilon}_{pl}$); mean and standard deviation values of elastic modulus represented.




**(a)** stainless steel 304L **(b)** copper C110

**Figure 7.13:** Effect of temperature on ductile damage - equivalent plastic strain ($D$ - $\bar{\varepsilon}_{pl}$); mean and standard deviation values of damage represented.

## 7.5 Conclusions

This chapter has presented the results obtained when the methodology proposed in the thesis is applied to different temperatures. A discussion of the behaviour of stainless steel 304L and copper C110 at low temperature ($T \sim -80°C$), room temperature ($T \sim 20°C$) and high temperature ($T \sim 180°C$) has been included. The techniques used in the tests for stress and strain measurement have been almost the same used in the standard room temperature tests, including only some minor variations at low and high temperature. In general, the plastic flow behaviour shows the expected yield and hardening increase for low temperatures, as well as some interesting features, such as a

martensitic transformation of 304L at low temperature, and the sustained degradation of copper until it completely loses its load carrying capacity at any temperature. Copper is especially affected by high temperature, presenting an almost instantaneous neck that develops and leads to fracture very quickly.

A fracture analysis has validated the previous results, including similar tensile tests on notched specimens that have provided the effect of stress triaxiality on the material behaviour. Both low and high temperatures have produced a decline of fracture strain throughout the whole triaxiality range. Stainless steel presents a small decrease for both temperatures and this drop has a similar magnitude for every triaxiality. Copper shows a similar beahaviour in cold conditions, but a much more pronounced ductility decrease at high temperature, leading to an almost triaxiality independent trend.

Regarding ductile damage accumulation, elastic modulus decrease measurements have been used to study the level of material degradation. For stainless steel, damage increases quickly at the beginning of plastic deformation at the three temperatures studied. Afterwards, it increases slowly at room temperature, stays constant almost until fracture at low temperature and stays in a plateau and then rises at high temperature; reaching in all cases a similar critical damage. For copper, while at room temperature damage does not appear until a threshold strain of 0.3 is reached, at low and high temperature it appears from the beginning. The behaviour near fracture is similar at room and low temperature, while the material fractures very early at high temperature. All these very different and complex behaviours for different materials, and even for the same material operated in different conditions, highlight the need of a flexible non-linear model that is able to represent all these variations.

# Chapter 8

# Material Models Development and Calibration

## 8.1 Introduction

Experimental results of the material behaviour in different conditions have been discussed in Chapters 5-7, including the investigation of the changes that varying the temperature and strain-rate conditions produce in the performance of the material. That information is used in this chapter to develop and calibrate material models that are able to predict the behaviour of metals in a range of conditions wider than the tested cases. Different models have been analysed to represent each of the material characteristics studied in the experiments: the modelling of plastic hardening is assessed in Section 8.2, of ductile fracture in Section 8.3 and of ductile damage in Section 8.4. The implementation of these models in software for structural calculations, such as finite elements method, allows to determine the performance of real complex components in a variety of strain-rate and temperature conditions. A summary of conclusions about the modelling process is presented in Section 8.5.

## 8.2 Plasticity Modelling

From the models discussed in Section 2.1.1 of the Literature Review, Johnson-Cook model [1] has been selected to represent plastic hardening in this research. The reasons for choosing this model are that it incorporates strain-rate and temperature effects in its formulation, the great number of investigations in which it has been used and its simplicity. The fitting of the plastic model to the experimental results that include post-necking behaviour has been analysed. However, the main interest of this research

is not plasticity modelling, therefore, a model that provides a good enough hardening representation was desired, without being the aim to develop a thorough comparison with other alterntives, such as Zerilli-Armstrong [18], MTS [19] or Bai-Wierzbicki [55] models.

### 8.2.1 Johnson-Cook Model Fit

Johnson-Cook plasticity model [1] represents the flow stress of the material as a function of plastic strain, and incorporates two additional terms that include the effects of strain-rate and temperature respectively. The model was described in Section 2.1.1 (Equation 2.6), and includes five parameters that have to be calibrated from experimental data: three are relative to the isotropic hardening ($A$, $B$ and $n$), one to the strain-rate effect ($C$) and another one to the temperature effect ($m$). In order to obtain the best parameters fit possible different approaches have been attempted, either fitting all the experimental data to the whole equation at once, or fitting the hardening, strain-rate and temperature terms separately. Both cases are discussed and compared below.

The experimental equivalent stress ($\bar{\sigma}$) - equivalent plastic strain ($\bar{\varepsilon}_{pl}$) data used for the models fitting are those obtained in previous chapters. From the experiments, the history of plastic strain-rate ($\dot{\bar{\varepsilon}}_{pl}$) is also available and used here for the model calibration. Regarding the temperature ($T$), isothermal conditions are assumed for the quasi-static strain-rate tests, while adiabatic heating is considered for the high strain-rate tests because of the high velocity of the deformation. The temperature rise is estimated using Equation 3.7 and the outcome presented in Figure 8.1 for the two materials analysed at the two high strain-rates considered.

The lowest strain-rate and temperature conditions tested for each material have been taken as reference conditions for the model fit. The reference parameters used in the modelling are shown in Table 8.1. In this table the density and specific heat of the materials has also been included, as these properties have been needed for the high-speed adiabatic heating calculation.

| Material | $\dot{\varepsilon}_0$ [s$^{-1}$] | $T_m$ [K] | $T_{ref}$ [K] | $\rho$ [kg/dm$^3$] | $C_p$ [J/kg.K] |
|---|---|---|---|---|---|
| Stainless steel 304L | 6.11x10$^{-3}$ | 1698 | 193 | 8.03 | 500 |
| Copper C110 | 4.71x10$^{-3}$ | 1338 | 193 | 8.89 | 385 |

**Table 8.1:** Reference parameters for Johnson-Cook model and adiabatic heating calculations.

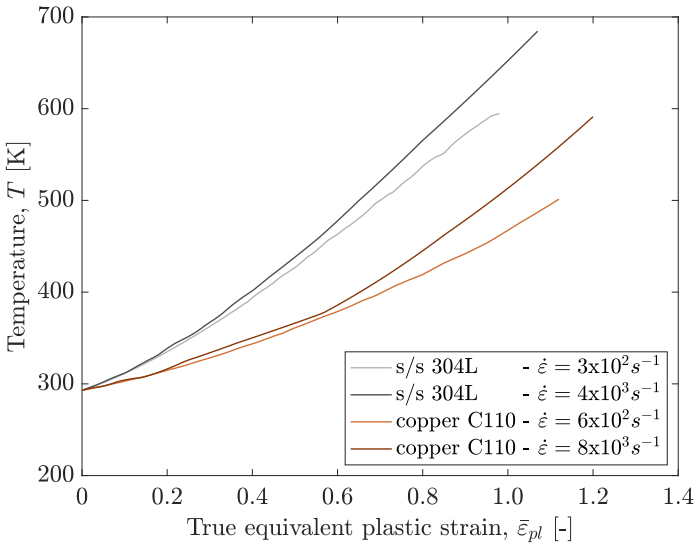
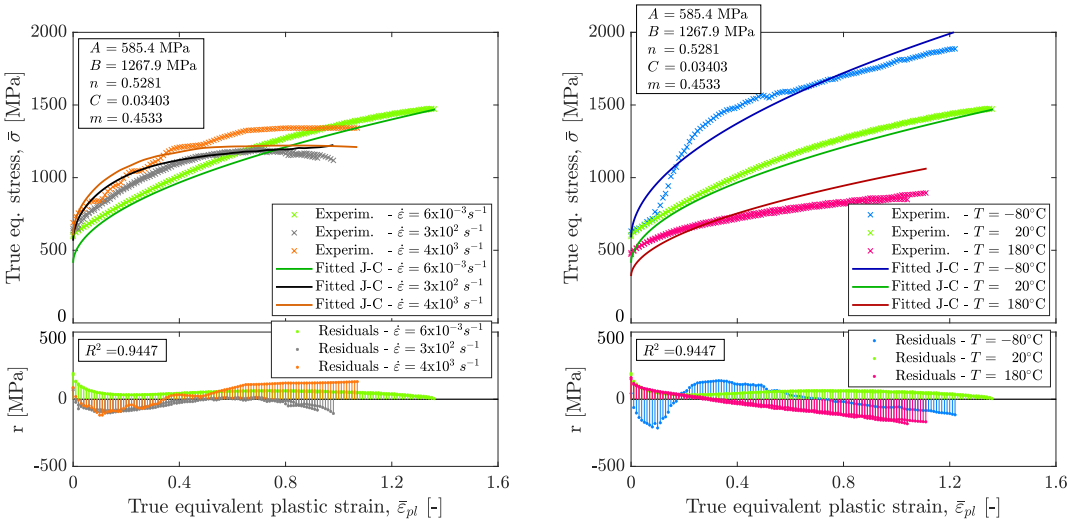



**Figure 8.1:** Estimated temperature along the high-speed tests.

#### 8.2.1.1 Simultaneous Model Fit

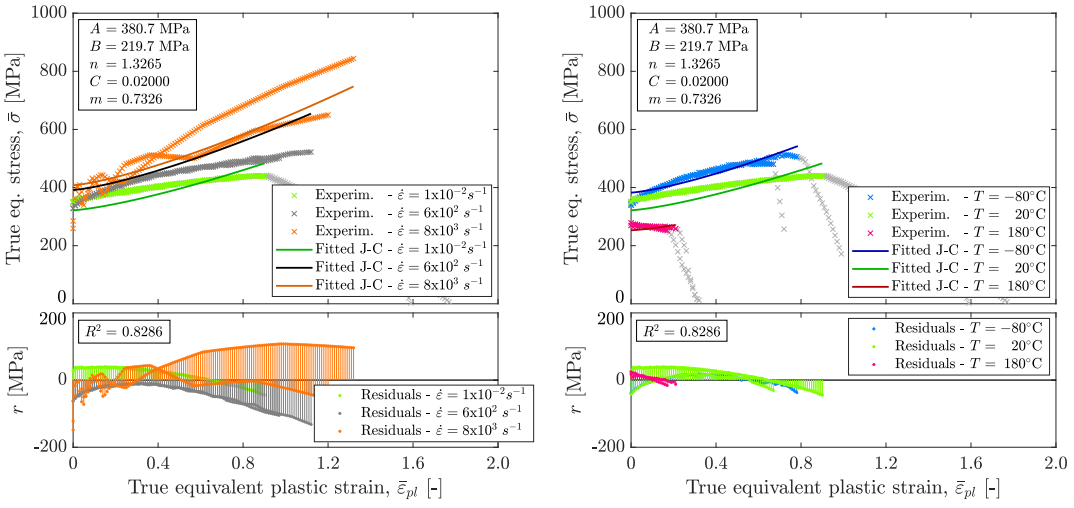
A Matlab script based on a least-squares fitting algorithm has been used as explained in Section 3.6 to obtain the model parameters. In this case, the groups of ($\bar{\sigma}$, $\bar{\varepsilon}_{pl}$, $\dot{\bar{\varepsilon}}_{pl}$, $T$) experimental data of each experiment have been considered together, and a fit of Equation 2.6 has been pursued. The curves obtained with the fitted model are represented in Figure 8.2 for stainless steel 304L, along with the experimental data. Figure 8.2a shows the strain-rate effect and Figure 8.2b the temperature effect predicted by the model. The same results are presented for copper C110 in Figure 8.3. The residuals of the calibration of each experiment are also plotted in each figure.

For stainless steel, the decrease of hardening at intermediate rate caused by the heating of the specimen is captured by the model. However, at high speed the model pushes the curve downwards more than the trend observed in the experimental results. In this case, it is thought that the increase of strain-rate towards the end of the necking process has a greater effect than the heating of the material, causing the behaviour observed in the tests. Nevertheless, the model is not able to capture this stronger hardening and the curve still presents a downwards tendency due to the high temperature achieved. The yield stress is not properly captured, especially in the different temperature conditions. The main cause is probably the elbow shape of the flow curve produced by the martensitic transformation at low plastic strain in low temperature conditions. The characteristics of this phenomenon induce a false downwards tendency around the yield point and early plastic region. In spite of these comments, a good fitting quality is achieved ($R^2 = 0.945$).




**(a)** Fit of strain-rate results **(b)** Fit of temperature results

**Figure 8.2:** Johnson-Cook plasticity model fit to experimental results of stainless steel 304L; all results fitted together; the residuals of the fitting process have also been plotted.




**(a)** Fit of strain-rate results **(b)** Fit of temperature results

**Figure 8.3:** Johnson-Cook plasticity model fit to experimental results of copper C110; all results fitted together; the residuals of the fitting process have also been plotted.

The downwards trend at high strain-rate is an effect produced by the model, and it cannot be improved by changing the fitting approach. On the other hand, in order to improve the yield and low plasticity modelling, the same fitting process has been tried without considering the data relative to the martensitic transformation ($\bar{\varepsilon}_{pl} < 0.25$ in the $T = -80°C$ case). The results obtained from this revised fitting approach have produced a slight improvement, however, the fit is very similar leading to a $R^2 = 0.948$.[1] An alternative would be to consider the use of a hardening model that takes into account this cryogenic martensitic transformation, such as those proposed by Lee et al. [133, 134]; however, it has been decided that it would add unnecessary complexity to the current research, and consequently it has not been implemented.

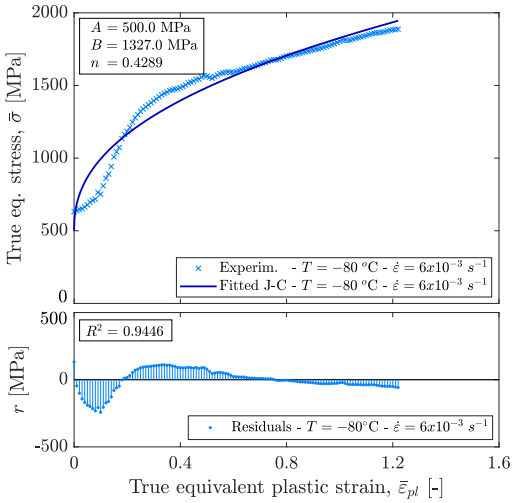
Regarding the results for copper C110, the fitting of this material is complicated due to the changes in hardening rate with temperature, and especially, at the highest strain-rate studied. The experimental data of the region of material degradation beyond its maximum equivalent stress point is not considered, since the formulation of Johnson-Cook model cannot handle that behaviour. An overall $R^2$ value of 0.829 has been achieved, being the fit very satisfactory at high temperature and high strain-rate conditions.

#### 8.2.1.2 Fit of Conditions Separately

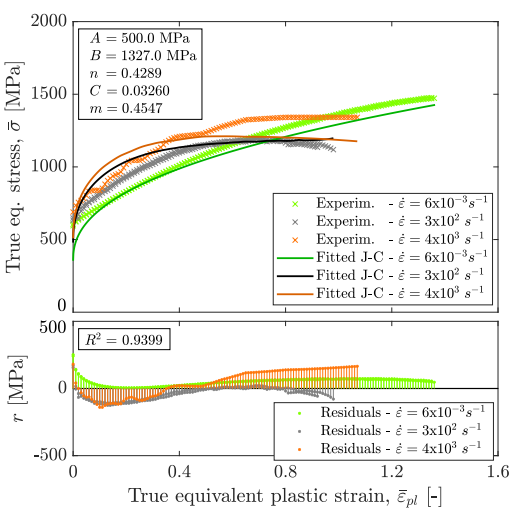
Another similar Matlab script has been written, in which instead of attempting a direct least-square fit of the data to the full Equation 2.6, the parameters that correspond to the different conditions have been fitted separately. Firstly, the base hardening term has been fitted using the experimental results of the reference conditions (lowest strain-rate and lowest temperature conditions tested), and from this process parameters $A$, $B$ and $n$ have been obtained. Then, the temperature term has been fitted using the previously fitted reference hardening term and the results of the varying temperature tests, providing the temperature parameter $m$. Finally, the same procedure has been followed to calibrate the strain-rate parameter $C$, using the varying strain-rate results. The three steps of the model calibration are represented in Figure 8.4 for stainless steel 304L and in Figure 8.5 for copper C110.

Although a better fit of the reference conditions is achieved for both materials ($R^2 = 0.945$ for 304L and $R^2 = 0.988$ for C110 if only those conditions are considered), when the whole model calibration is assessed the fitting results are poorer than those obtained in the previous section ($R^2 = 0.940$ for 304L and $R^2 = 0.771$ for C110). For stainless steel 304L, the same approach has also been followed without considering the

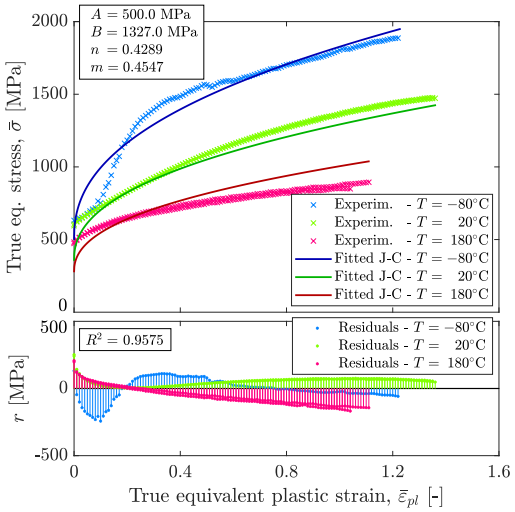
[1] The curve fitting results of Johnson-Cook plastic model fitting all the data together without considering $\bar{\varepsilon}_{pl} < 0.25$ at $T = -80°C$ are included in Figure B.13 of Appendix B.




**(a)** Fit of standard results




**(b)** Fit of strain-rate results




**(c)** Fit of temperature results

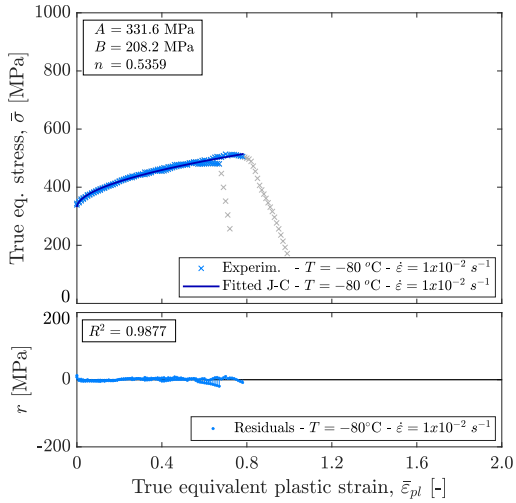
**Figure 8.4:** Johnson-Cook plasticity model fit to experimental results of stainless steel 304L; standard, strain-rate and temperature results fitted separately.

data of the low temperature martensitic transformation, but again an even worse fit has been achieved (overall $R^2 = 0.890$).[2]

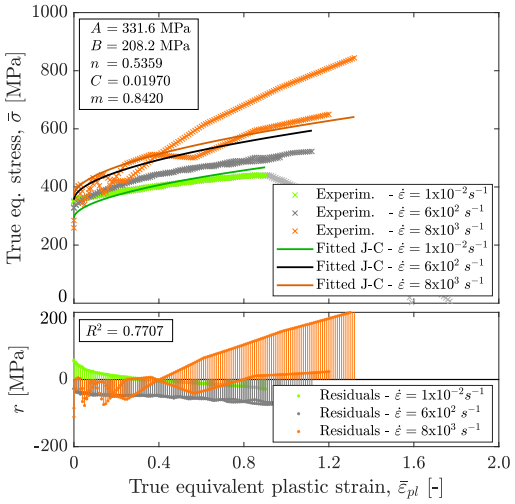
#### 8.2.1.3 Comparison of Fitting Strategies

Fitting all the experimental data at the same time to the full model provides a higher quality fit than calibrating separately the effect of the different conditions. Also, not

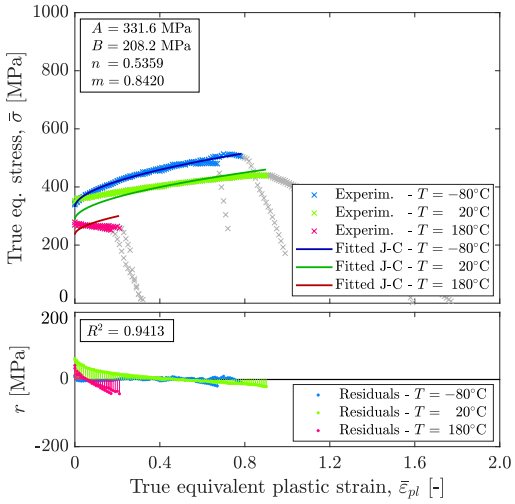
[2]The curve fitting results of Johnson-Cook plastic model fitting the data separately without considering $\bar{\varepsilon}_{pl} < 0.25$ at $T = -80°C$ are included in Figure B.14 of Appendix B.




**(a)** Fit of standard results




**(b)** Fit of strain-rate results




**(c)** Fit of temperature results

**Figure 8.5:** Johnson-Cook plasticity model fit to experimental results of copper C110; standard, strain-rate and temperature results fitted separately.

considering the martensitic transformation region for stainless steel 304L in cryogenic conditions has improved slightly the fit when all the results are calibrated together.

| Material | Together | Together (w/o mart.) | Separat. | Separat.(w/o mart.) |
|---|---|---|---|---|
| s/s 304L | 0.9447 | 0.9483 | 0.9399 | 0.8900 |
| copper C110 | 0.8286 | - | 0.7707 | - |

**Table 8.2:** $R^2$ values of Johnson-Cook model calibration using different fitting approaches.

Table 8.2 presents a summary of the $R^2$ values obtained with all the fitting strategies considered. The final model parameters obtained are presented in Table 8.3.

If large amounts of experimental data from many different conditions need to be fitted the separate approach could be advantageous, since the step-by-step calibration would ease the data handling. Nevertheless, it has been demonstrated that using that approach does not suppose an improvement in the quality of the fit over fitting all the results together. It is therefore advisable to fit all the data together, so that the importance of every data point is equally weighted in the whole equation of the model.

| Material | $A$ [MPa] | $B$ [MPa] | $n$ [-] | $C$ [-] | $m$ [-] |
|---|---|---|---|---|---|
| s/s 304L | 616.9 | 1240.8 | 0.5353 | 0.03373 | 0.4500 |
| copper C110 | 380.7 | 219.7 | 1.3265 | 0.02000 | 0.7326 |

**Table 8.3:** Calibrated parameters of Johnson-Cook plastic hardening model.

## 8.3 Ductile Fracture Modelling

In order to represent ductile fracture, the model developed by Johnson and Cook has been considered [1]. Several models that deal with ductile fracture were analysed in Section 2.2.2 of the Literature Review but this one has been selected, since it incorporates the effects of strain-rate and temperature, and because it deals with the effect of stress triaxiality on fracture strain, which is the parameter that has been experimentally tested in this research. The outcome of the fitting of this model is presented in Section 8.3.1, however, as the results are not entirely satisfactory, a modification of the model has been developed and fitted in Section 8.3.2. This new model considers the same concepts of baseline Johnson-Cook model, nevertheless, the strain-rate and temperature effects are improved allowing for more flexibility when representing variable conditions.

### 8.3.1 Johnson-Cook Model Fit

Johnson-Cook ductile fracture model represents the equivalent fracture strain of the material as a function of stress triaxiality, and incorporates two additional terms that include the effects of strain-rate and temperature respectively. The model was explained in Equation 2.18 of the Literature Review, and includes five parameters that have to be calibrated from experimental data: three are relative to the base effect of triaxiality ($D_1$, $D_2$ and $D_3$), one to the strain-rate effect ($D_4$) and another one to the temperature effect ($D_5$). As in the previous section, different fitting approaches have

been tried, fitting all the experimental data at once, or fitting the stress triaxiality, strain-rate and temperature terms separately. The experimental equivalent fracture strain ($\bar{\varepsilon}_f$) - stress triaxiality ($\eta$) data used for the models fitting are those obtained in previous chapters. The average stress triaxiality and average strain-rate obtained from the values measured along each of the tests have been used for the fitting. The lowest strain-rate and temperature conditions tested for each material have been taken as reference conditions for the model fit and were shown in Table 8.1.

A Matlab script similar to the one used for the plasticity model fitting has been created. For ductile fracture models calibration groups of ($\bar{\varepsilon}_f$, $\eta$, $\dot{\bar{\varepsilon}}_{pl}$, $T$) values, each corresponding to a test, have been used to fit Equation 2.18. The results of the fitting process are represented in Figure 8.6 for stainless steel 304L and in Figure 8.7 for copper C110. In each of the figures both the effects of strain-rate and temperature are represented separately; the experimental data points are plotted along with the model fit and the residuals of the fitting process. These results correspond to the simultaneous fitting approach, which has provided a better fit than the separate fitting process, as it occurred with the plasticity model fitting.[3] The parameters obtained for this model are summarised in Table 8.4 for both materials.

| Material | $D_1$ | $D_2$ | $D_3$ | $D_4$ | $D_5$ |
|---|---|---|---|---|---|
| s/s 304L | 0.6338 | 1.324 | −1.316 | −0.01481 | 0.2216 |
| copper C110 | −0.1862 | 4.324 | −0.8531 | −0.02568 | −2.403 |

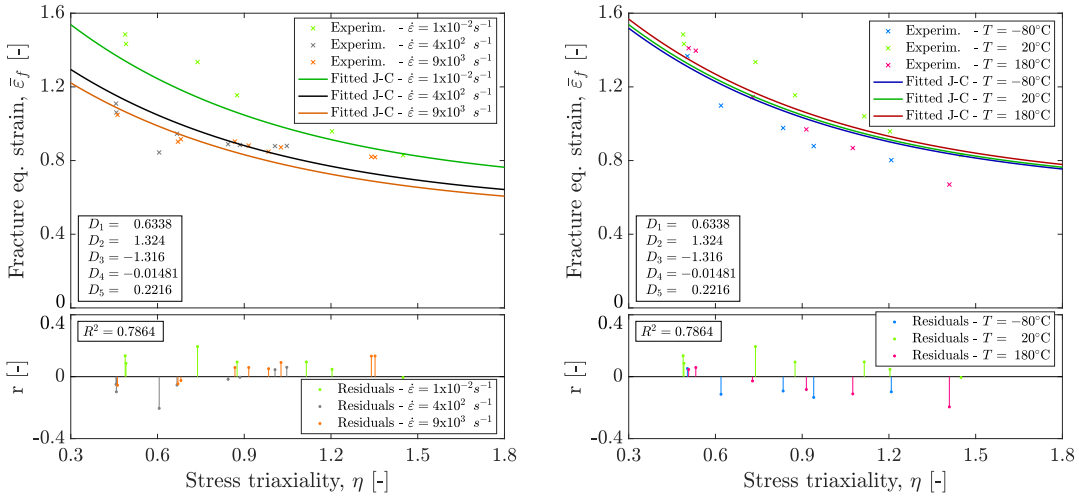
**Table 8.4:** Calibrated parameters of Johnson-Cook ductile fracture model.

The $R^2$ values obtained with both fitting approaches are summarised in Table 8.5, where a clear improvement when all the results are fitted together is observed. Nevertheless, the fitting is not as good as desired, especially because the model is not able to capture some of the non-linear responses that have been observed in the strain-rate and temperature experiments. A modified Johnson-Cook ductile fracture model able to represent all these non-linearities at varying conditions has been proposed.

### 8.3.2 Proposed Ductile Fracture Model

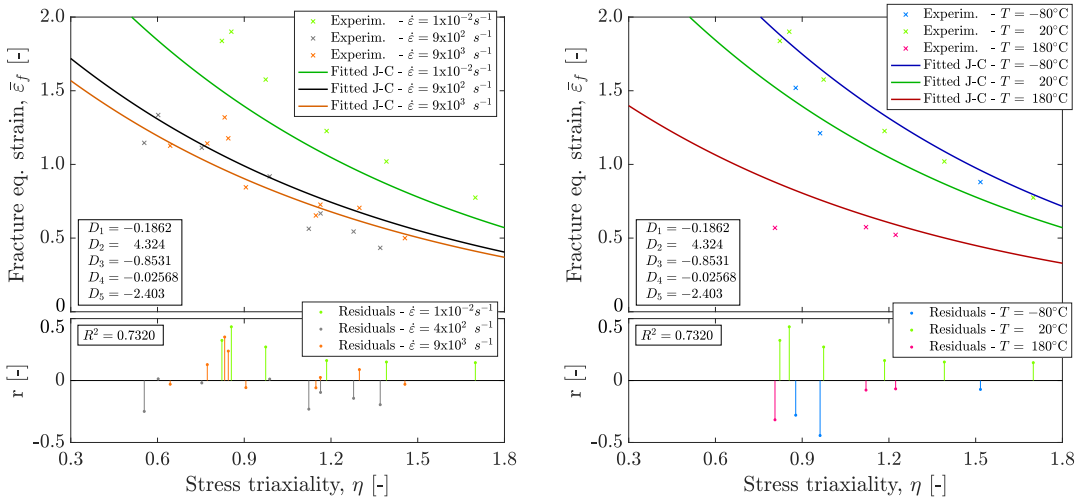
From the experimental results, it has been observed that the $\bar{\varepsilon}_f$ - $\eta$ curve changes its shape radically at certain conditions; e.g. it changes from the typical exponentially decreasing shape to almost flat and horizontal in the studied stainless steel at high strain-rate or copper at high temperature. Also, the displacement of the curve is not always linear, a downwards displacement for both high and low temperatures has been

[3]The curve fitting results of Johnson-Cook ductile fracture model fitting the data separately are included in Figure B.15 and Figure B.16 of Appendix B.




**(a)** Fit of strain-rate results **(b)** Fit of temperature results

**Figure 8.6:** Johnson-Cook ductile fracture model fit to experimental results of stainless steel 304L; the residuals of the fitting process have also been plotted.




**(a)** Fit of strain-rate results **(b)** Fit of temperature results

**Figure 8.7:** Johnson-Cook ductile fracture model fit to experimental results of copper C110; the residuals of the fitting process have also been plotted.

observed in the two materials analysed. The proposed model is able to represent all these non-linearities at varying strain-rate and temperature conditions.

#### 8.3.2.1 Model Development

If the equation of the original Johnson-Cook model is studied (Equation 2.18), strain-rate and temperature are represented by terms that multiply the base exponential equation, and therefore, scale up or down the response curve. In the proposed model, the base exponential equation has been used (Equation 8.1), and the effect of strain-rate and temperature has been included within the three model parameters $D_1$, $D_2$ and $D_3$, as observed in Equations 8.2. This enables the variation of the location and shape of the curve by making the parameters of the exponential strain-rate and temperature dependent, instead of multiplying the exponential equation by separate scaling terms.

$$\bar{\varepsilon}_f = D_1 + D_2 \exp\left(D_3 \eta\right) \tag{8.1}$$

$$\begin{aligned} D_1 &= \left[\xi_1 + (\dot{\varepsilon}^*)^{\gamma_1} + \exp\left[-\frac{(T^*-\psi_1)^2}{{\psi_2}^2}\right]\right] \\ D_2 &= \xi_2 \left[1 + \psi_3 T^*\right] \\ D_3 &= \xi_3 (\dot{\varepsilon}^*)^{\gamma_2} \end{aligned} \tag{8.2}$$

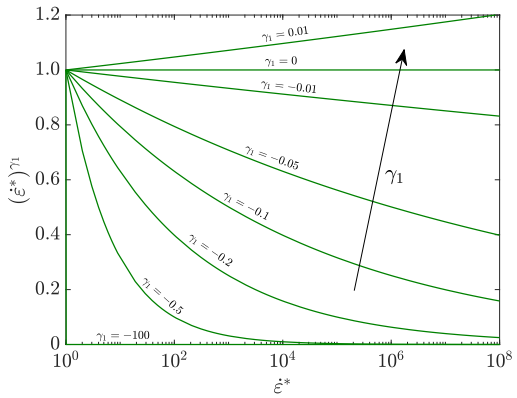
In the equations, $\bar{\varepsilon}_f$ represents the equivalent fracture strain, $\eta$ the stress triaxiality, $\dot{\varepsilon}^*$ the non-dimensional strain-rate, $T^*$ the non-dimensional temperature, $\xi_1$, $\xi_2$ and $\xi_3$ the base model parameters, $\gamma_1$ and $\gamma_2$ the strain-rate effect parameters and $\psi_1$, $\psi_2$ and $\psi_3$ the temperature effect parameters. The non-dimensional strain-rate and temperature are defined as for the original Johnson-Cook model (Equations 2.7 and 2.8).

The equation of $D_1$ translates the curve up or down by means of a base parameter ($\xi_1$), a strain-rate dependent term and a temperature dependent term. The strain-rate dependent term can be tuned through parameter $\gamma_1$, as observed in Figure 8.8a, to produce the effects of Figure 8.8b on the model for varying strain-rate. The same occurs with the temperature dependent term, tuned by parameters $\psi_1$ and $\psi_2$. In this case a Gaussian equation has been considered, which allows the model response to be displaced downwards for both increasing and decreasing temperatures. Parameter $\psi_1$ displaces the peak of the curve within the $T^*$ range (Figure 8.9a) and $\psi_2$ modifies the sharpness of the curve (Figure 8.9c). The different values of $\psi_1$ can produce increasing, decreasing or increasing up to a point and then decreasing values of fracture strain for increasing temperature, depending on the location of the peak, as observed in Figure 8.9b. On the other hand, $\psi_2$ scales the rate of decrease (Figure 8.9d) by modifying the slope of the Gaussian term.

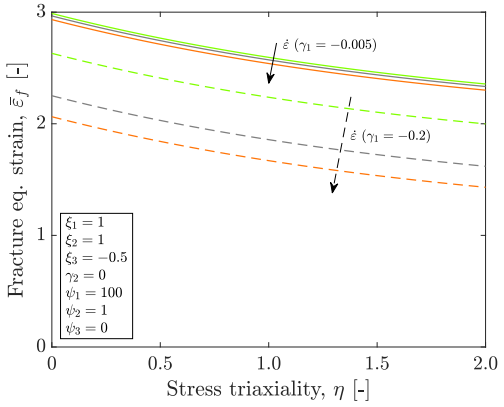
The equations for $D_2$ and $D_3$ modify the shape of the exponential curve using two base parameters ($\xi_2$ and $\xi_3$), a strain-rate dependent term and a temperature dependent

term. The strain-rate dependent term has the same form as the one included in $D_1$ equation, but it is included in this case in the exponent of the exponential equation, multiplying the stress triaxiality. The calibration of parameter $\gamma_2$ produces the model slope variation with strain-rate exemplified in Figure 8.8c, that combined with the model displacement provided by the term in $D_1$ allows for a total flexibility of response representation. The temperature dependent term is included in $D_3$ equation, outside the exponent, as this has provided a better fitting for the materials studied. The variation of the term by adjustment of $\psi_3$ is represented in Figure 8.9e and its effect on the shape of the model is shown in Figure 8.9f.

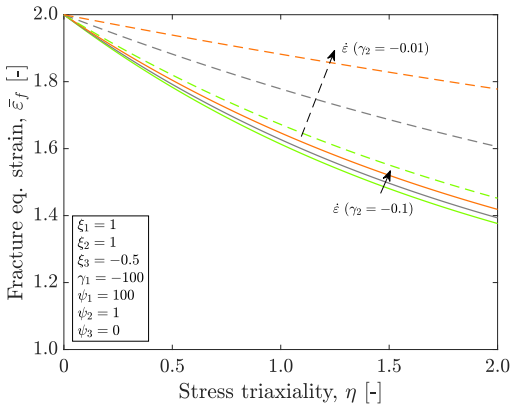
The full equation of the stress triaxiality, strain-rate and temperature dependent ductile fracture model, with the meaning of the parameters and variables explained




**(a)** Term to modify the response with $\dot{\varepsilon}$ controlled by parameter $\gamma_1$ (or $\gamma_2$).

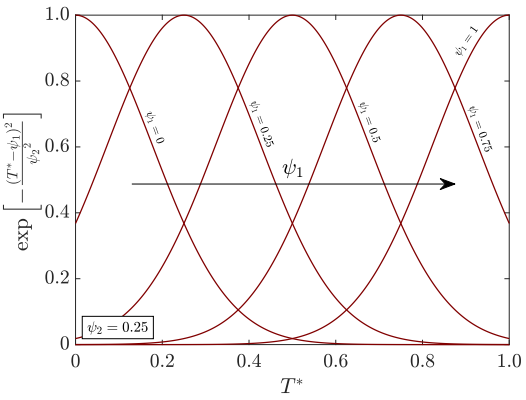



**(b)** Effect of $\gamma_1$ parameter on the vertical displacement of the curve for varying $\dot{\varepsilon}$.

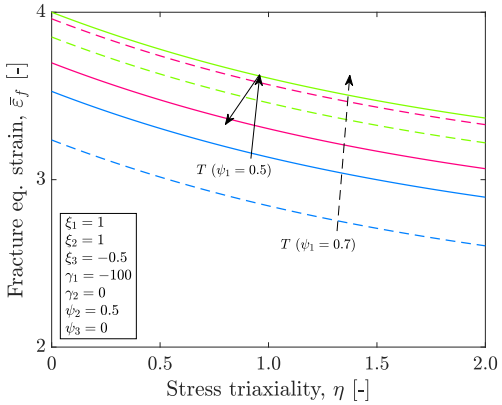



**(c)** Effect of $\gamma_2$ parameter on the curve slope for varying $\dot{\varepsilon}$.

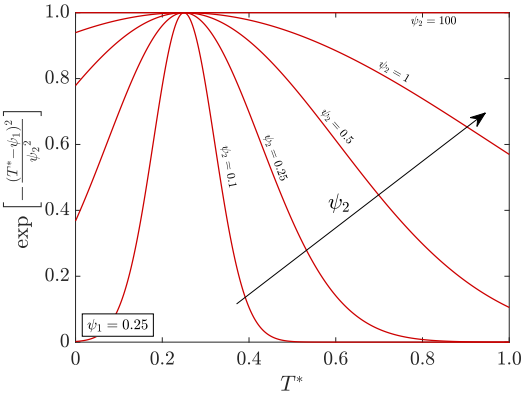
**Figure 8.8:** Analysis of the vertical displacement and slope change of the curve for varying strain-rate controlled by the parameters $\gamma_1$ and $\gamma_2$ in the proposed ductile fracture model.



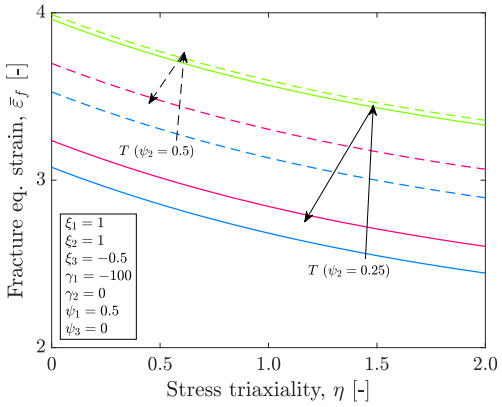

**(a)** Term to control the direction of the curve displacement with $T$ controlled by $\psi_1$.



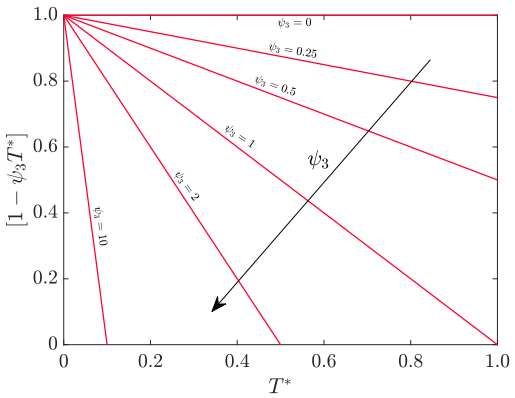

**(b)** Effect of $\psi_1$ parameter on the vertical displacement of the curve for varying $T$.



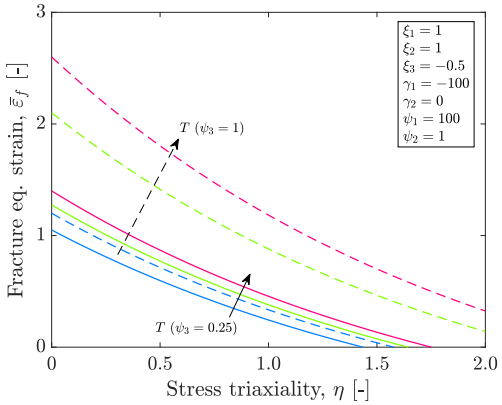

**(c)** Term to scale the vertical displacement of the curve with $T$ controlled by $\psi_2$.




**(d)** Effect of $\psi_2$ parameter on the vertical displacement of the curve for varying $T$.




**(e)** Term to modify the curve shape with $T$ controlled by $\psi_3$.




**(f)** Effect of $\psi_3$ parameter on the curve slope for varying $T$.

**Figure 8.9:** Analysis of the vertical displacement and slope change of the curve for varying temperature controlled by the parameters $\psi_1$, $\psi_2$ and $\psi_3$ in the proposed ductile fracture model.

above, presents the following form:

$$\bar{\varepsilon}_f = \left[\xi_1 + (\dot{\varepsilon}^*)^{\gamma_1} + \exp\left[-\frac{(T^* - \psi_1)^2}{{\psi_2}^2}\right]\right] + \xi_2 \exp\left[\xi_3 \eta (\dot{\varepsilon}^*)^{\gamma_2}\right] \left[1 + \psi_3 T^*\right] \tag{8.3}$$

#### 8.3.2.2 Model Fit

The procedure followed for the fitting of the proposed model has been analogous to that used with the Johnson-Cook model in the previous section. The same experimental data points have been used and all the conditions have been considered at the same time for the model fitting. The resulting curves are represented in Figure 8.10 for stainless steel and Figure 8.11 for copper, along with the experimental data and the residuals of the fitting.

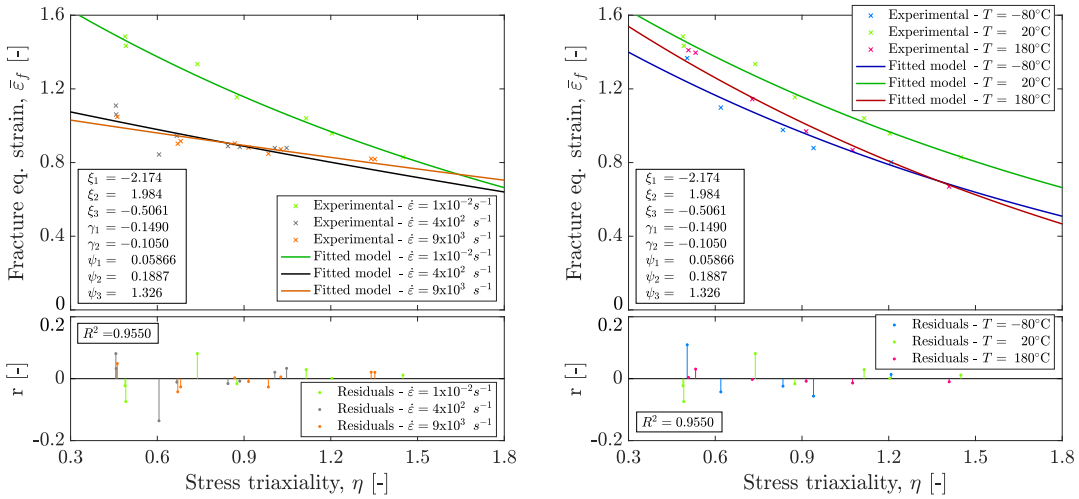
The flexibility of this model can be clearly observed in the fitted curves since, unlike the original Johnson-Cook model, it can radically change the shape and slope of the curves at different strain-rates and temperatures, as well as displace them non-linearly. In the temperature study, the displacement of curves downwards for both low and high temperature is observed, combined with the shape and position adjustment of the curve mentioned in the previous section. The quality of the model fit achieved is good, with $R^2$ values of 0.96 and 0.90 for stainless steel and copper respectively. The improvement compared to the fits obtained with Johnson-Cook model is considerable, as observed in Table 8.5. A summary of the calibrated model parameters is presented in Table 8.6.

| Material | JC model | | Proposed model |
|---|---|---|---|
| | Together | Separately | Together |
| s/s 304L | 0.7864 | 0.6222 | 0.9550 |
| copper C110 | 0.7320 | −0.9392 | 0.9004 |

**Table 8.5:** $R^2$ values of Johnson-Cook and proposed ductile fracture models calibration using different fitting approaches.

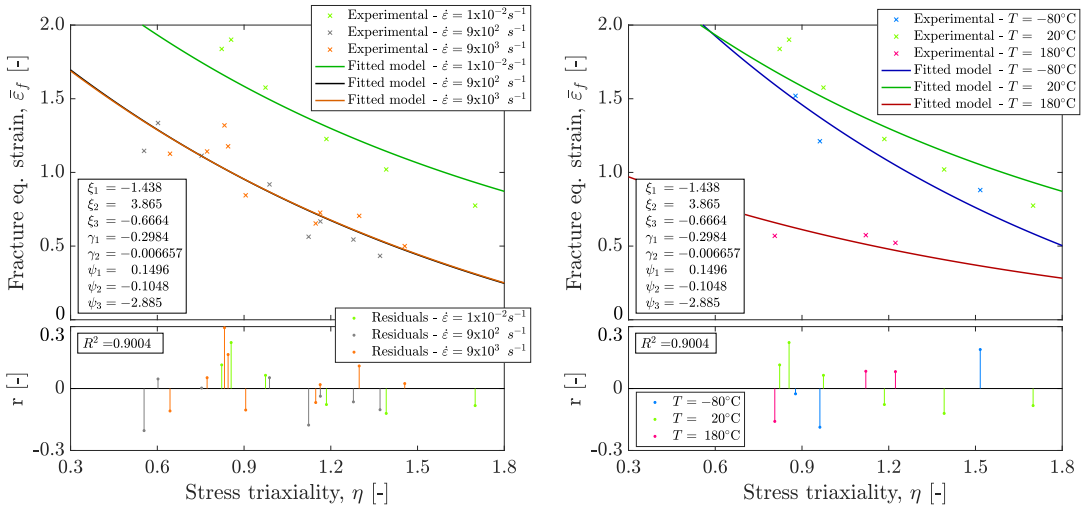
| Material | | | | $\dot{\varepsilon}$ effect | | $T$ effect | | |
|---|---|---|---|---|---|---|---|---|
| | $\xi_1$ | $\xi_2$ | $\xi_3$ | $\gamma_1$ | $\gamma_3$ | $\psi_1$ | $\psi_2$ | $\psi_3$ |
| s/s 304L | −2.174 | 1.984 | −0.5061 | −0.1490 | −0.1050 | 0.05866 | 0.1887 | 1.326 |
| copper C110 | −1.438 | 3.865 | −0.6664 | −0.2984 | −0.006657 | 0.1496 | −0.1048 | −2.885 |

**Table 8.6:** Calibrated parameters of the proposed ductile fracture model.




**(a)** Fit of strain-rate results **(b)** Fit of temperature results

**Figure 8.10:** Proposed ductile fracture model fit to experimental results of stainless steel 304L; the residuals of the fitting process have also been plotted.




**(a)** Fit of strain-rate results **(b)** Fit of temperature results

**Figure 8.11:** Proposed ductile fracture model fit to experimental results of copper C110; the residuals of the fitting process have also been plotted.

## 8.4 Ductile Damage Modelling

As explained in Section 2.2.2 of the Literature Review, many damage models deal only with the ductile fracture behaviour but assume a linear accumulation of damage from yield to final fracture [1, 6]. Other models, such as that proposed by Bonora [83] or Xue and Wierzbicki [54], introduce the concept of non-linear damage accumulation. However, the non-linear modelling of ductile damage accumulation including the effects of strain-rate and temperature has not been attempted before, due to the complications of experimental measurements in those conditions and because of the inherent difficulties involved in the modelling. In this section, the aforementioned Bonora model is firstly assessed in standard quasi-static and room temperature conditions, and then a new model which includes non-linear accumulation, strain-rate and temperature effects is proposed and calibrated for the materials studied.

### 8.4.1 Bonora Model

The ductile damage model proposed by Bonora [83] is based on continuum damage mechanics theory, and its key capability is the incorporation of non-linear damage accumulation. This model was described in detail in Section 2.2.2.3 of the Literature Review. The model aims to represent jointly the material fracture conditions, including the effect of stress triaxiality, and the ductile damage accumulation. Nevertheless, from the fitting process of the available experimental data it has been observed that it is not possible to obtain a reasonable fit of both behaviours with the same set of parameters; therefore, this unified approach has been discarded and a separate representation of ductile fracture (Section 8.3.2) and damage accumulation (Section 8.4.2) has been considered. The attempts to calibrate Bonora model are summarised below.

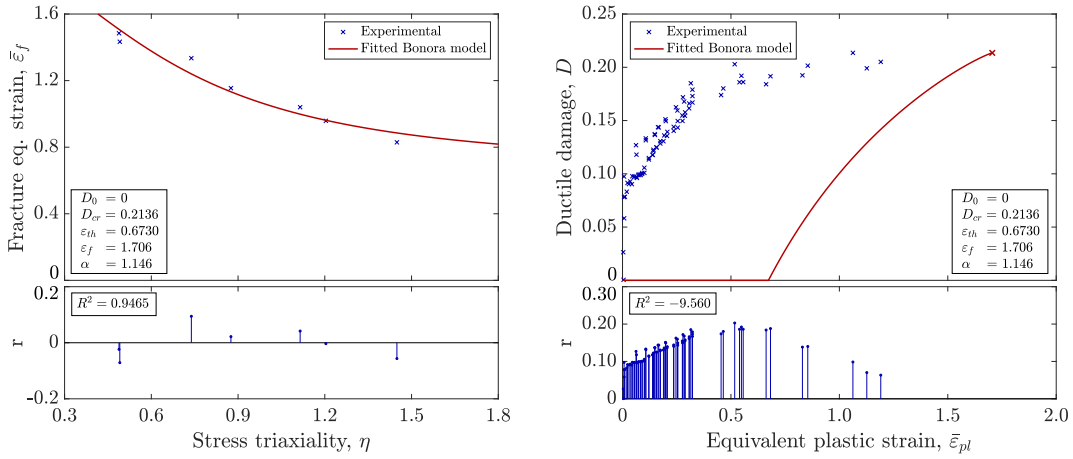
#### 8.4.1.1 Model Fit Attempts

As said before, Bonora model attempts to include ductile fracture and non-linear damage accumulation in a unified formulation. In order to calibrate the model, the experimentally obtained results of $\bar{\varepsilon}_f$ - $\eta$ for ductile fracture and $D$ - $\bar{\varepsilon}_{pl}$ for damage accumulation of the two studied materials in quasi-static and room temperature conditions have been used.

The model fitting procedure suggested in [90] has been followed, which consists of firstly fitting the $\bar{\varepsilon}_f$ - $\eta$ data to Equation 2.25 of the model, and then using the $D$ - $\bar{\varepsilon}_{pl}$ data to fit the parameter $\alpha$, which controls the shape of the damage accumulation curve in Equation 2.24. The results of this fitting process for stainless steel 304L are presented in Figure 8.12. Figure 8.12a shows the ductile fracture part of the model, which defines

parameters $\varepsilon_{th}$ and $\varepsilon_f$, and for which a good quality fit has been achieved ($R^2 = 0.95$). However, when these values of $\varepsilon_{th}$ and $\varepsilon_f$ are used to obtain parameter $\alpha$, the poor fit of Figure 8.12b is obtained for the damage accumulation, which is constrained by the threshold and fracture strain values already defined. Since the fit for damage accumulation is unacceptable ($R^2 = -9.56$), an alternative approach has been tried, which consists of fitting the parameters of the model (including $\varepsilon_{th}$ and $\varepsilon_f$) to the damage accumulation experimental results, and studying the predicted ductile fracture response afterwards. This technique has provided the results of Figure 8.13, where Figure 8.13b shows and improved damage accumulation representation ($R^2 = 0.58$), but the change of parameters modifies unreasonably the ductile fracture response of Figure 8.13a ($R^2 = -14.99$). The fitting results for copper C110 are available in Figures B.17 and B.18 of Appendix B, and present the same problems as the results discussed above for stainless steel.

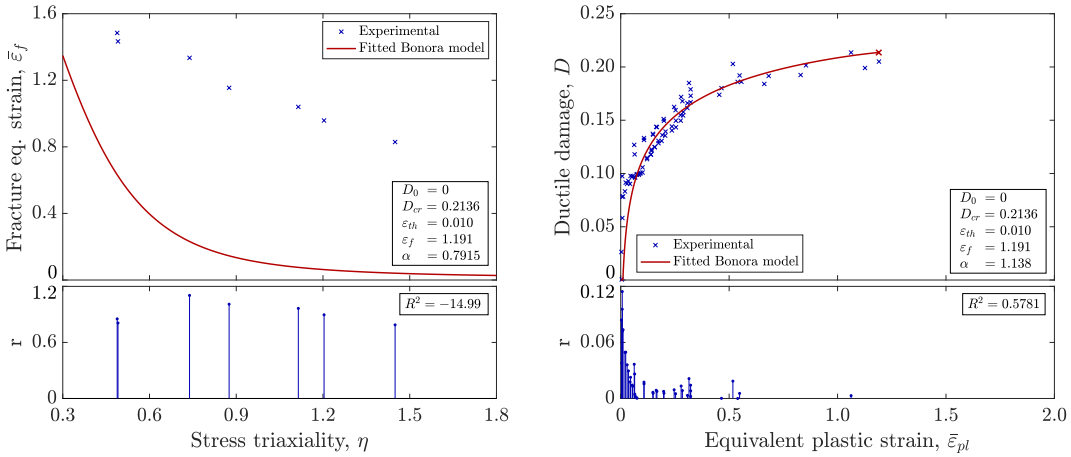
As observed, a satisfactory fit of the model has not been achieved and it has been concluded that it is not reasonable to use it for damage estimation if a relatively good representation of both ductile fracture and damage accumulation phenomena is desired. Alternatively, a model has been created which represents ductile damage accumulation and also includes the effects of strain-rate and temperature, and which can be used in combination with the ductile fracture model described in Section 8.3.2 in order to have a full representation of the degradation process. Some of the concepts involved in Bonora model have been retained when developing the new model, such as the appearance of parameters $\varepsilon_{th}$, $\varepsilon_f$ and $D_{cr}$ or the use of damage exponent parameters to control the non-linearity of the damage accumulation shape.




**(a)** Fit of the ductile fracture part

**(b)** Fit of the damage accumulation part

**Figure 8.12:** Bonora ductile damage model fit attempt of stainless steel 304L following the fitting process recomended in [90].




**(a)** Fit of the ductile fracture part

**(b)** Fit of the damage accumulation part

**Figure 8.13:** Bonora ductile damage model fit attempt of stainless steel 304L fitting the damage accumulation shape firstly.

### 8.4.2 Proposed Damage Model

The model proposed for ductile damage is fundamentally empirical, although it takes concepts from continuum damage mechanics so that most of the parameters have a physical meaning. The model has been developed bearing in mind the results obtained for the two materials tested in different conditions and is able to represent a varying damage accumulation shape when strain-rate and temperature are modified. It also adjusts the damage initiation strain point, the critical damage and the fracture conditions as a function of strain-rate and temperature.

#### 8.4.2.1 Model Development

The proposed model presents the power law form represented in Equation 8.4, in which the argument represents the strain range along which damage takes place and the exponent modifies the shape of the damage accumulation, allowing a tunable non-linear shape of the model curve. A similar power law damage accumulation was used by Cortese et al. [60] on their model to represent ductile damage, in which a direct parallelism with the high cycle fatigue damage law proposed by Palmgrem [61] was made.

$$D = D_{cr}\left[\frac{\bar{\varepsilon}_{pl} - \bar{\varepsilon}_{th}}{\bar{\varepsilon}_f - \bar{\varepsilon}_{th}}\right]^{\left[\nu_1 + \nu_2 \bar{\varepsilon}_{pl}\right]} \tag{8.4}$$

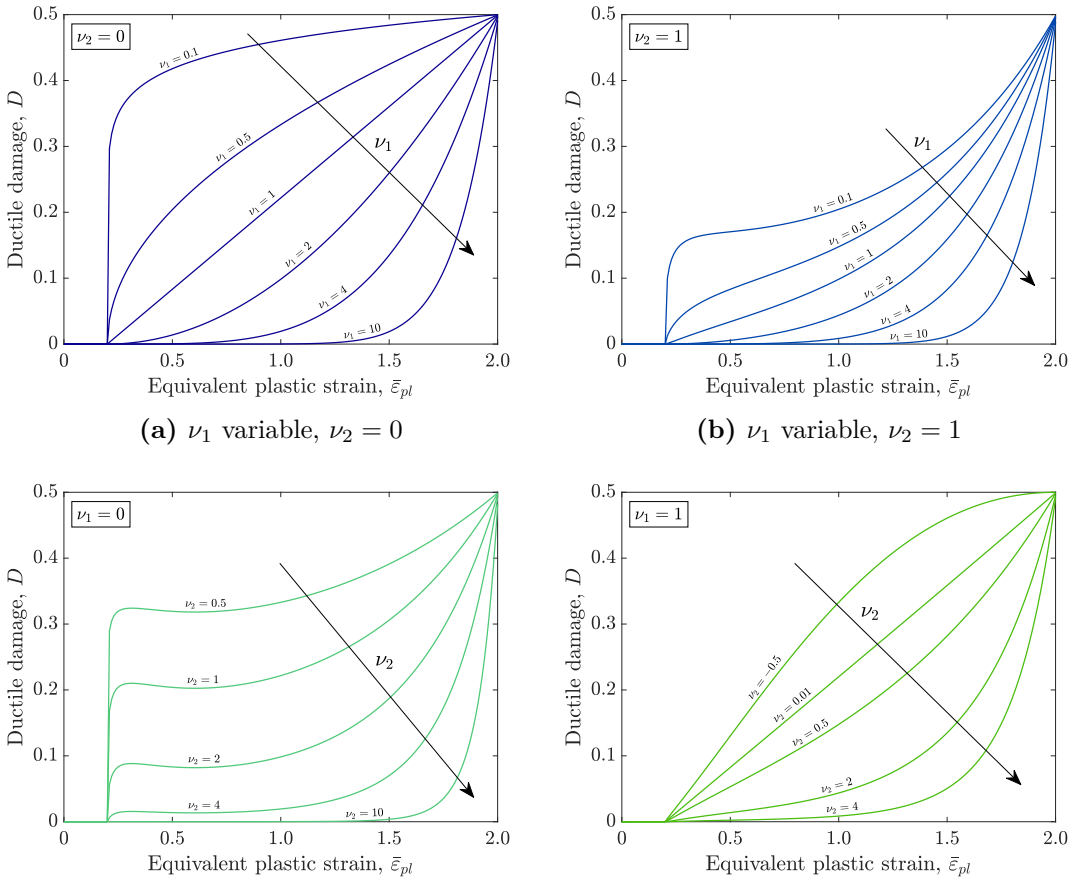
The present model takes some concepts from the continuum damage mechanics approach, since it is based on the macroscopic damage measurements discussed in previous chapters of this work. The threshold strain $\bar{\varepsilon}_{th}$, fracture strain $\bar{\varepsilon}_f$ and critical damage $D_{cr}$ parameters were introduced by Kachanov [68] and used by Lemaitre in his ductile damage model [74]. As explained in the Litreature Review, $\bar{\varepsilon}_{th}$ represents the strain at which the first voids producing ductile damage appear in the material, $\bar{\varepsilon}_f$ is the strain at which ductile damage produces a macroscopic fracture in the material and $D_{cr}$ is the critical damage value that produces that final failure. As said before, the exponent of Equation 8.4 modifies the shape of the curve, and this can be tuned by means of two parameters ($\nu_1$ and $\nu_2$), the second one multiplied by the equivalent plastic strain $\bar{\varepsilon}_{pl}$ to allow a control of the curve shape at low and high plastic strains separately. A similar concept with parameteres in the exponent was used by Cortese et al. [60] and Bonora [83] on their models to introduce a non-linear damage accumulation. The flexibility of the curve shape when $\nu_1$ and $\nu_2$ parameters are varied in the proposed model can be observed in Figure 8.14.

The model described so far represents the accumulation of damage as a function of plastic strain, however, strain-rate and temperature do not appear in the formulation. Rather than including them directly in the base equation, the effects of strain-rate and temperature have been included in the parameters $\bar{\varepsilon}_{th}$, $\bar{\varepsilon}_f$, $D_{cr}$, $\nu_1$ and $\nu_2$, as suggested in [135]. By doing this, the same damage response of Equation 8.4 is maintained for all conditions, and strain-rate and temperature dependent relationships are proposed for each of the parameters involved in the damage function.

The fracture strain parameter has already been studied in the previous section, and the proposed model of Equation 8.3 is used, which apart from the effects of strain-rate and temperature introduces the effect of stress triaxiality on the model. The critical damage and threshold strain are represented by Equations 8.5 and 8.6 respectively. The relationships used present the same form already described in Section 8.3.2.1 for the ductile fracture strain modelling. The temperature effect is represented by a Gaussian term and the strain-rate effect by a power law term. A base parameter, two parameters for the temperature effect and a parameter for the strain-rate effect are included in each of the equations. The shape of these models has been designed based on the experimental observations, where a decrease in properties for both low and high temperature has been observed, as it happened with fracture strain.

$$D_{cr} = \phi_1 \exp\left[-\frac{(T^* - \phi_2)^2}{{\phi_3}^2}\right](\dot{\varepsilon}^*)^{\phi_4} \tag{8.5}$$

$$\bar{\varepsilon}_{th} = \chi_1 \exp\left[-\frac{(T^* - \chi_2)^2}{{\chi_3}^2}\right](\dot{\varepsilon}^*)^{\chi_4} \tag{8.6}$$




**(a)** $\nu_1$ variable, $\nu_2 = 0$ **(b)** $\nu_1$ variable, $\nu_2 = 1$

**(c)** $\nu_1 = 0$, $\nu_2$ variable **(d)** $\nu_1 = 1$, $\nu_2$ variable

**Figure 8.14:** Analysis of the shape change of the damage accumulation curve controlled by the parameters $\nu_1$ and $\nu_2$ in the proposed ductile damage accumulation model ($\bar{\varepsilon}_{th} = 0.2$, $\bar{\varepsilon}_f = 2.0$ and $D_{cr} = 0.5$).

Considerable variation in the shape of damage accumulation has also been observed in the test results when strain-rate and temperature are modified, and Equations 8.7 and 8.8 have been proposed to consider these changes. Equation 8.8 has been designed with the same structure, based on Gaussian and power law terms, previously described for parameters $\bar{\varepsilon}_{th}$ and $D_{cr}$. However, in Equation 8.7 the temperature term has been simplified to a linear variation. Although both parameters are affected by each other, $\nu_1$ has a greater effect on the shape of the curve at low plasticity, where a linear variation with temperature has been considered accurate enough; on the other hand, $\nu_2$ adjusts the model at high plasticity, and a more flexible variation in those conditions has been maintained.

$$\nu_1 = \nu_{11} \left[1 - T^* \nu_{12}\right] (\dot{\varepsilon}^*)^{\nu_{13}} \tag{8.7}$$

$$\nu_2 = \nu_{21}\left[-\frac{(T^* - \nu_{22})^2}{{\nu_{23}}^2}\right](\dot{\varepsilon}^*)^{\nu_{24}} \tag{8.8}$$

As a summary, the model presents a base power law equation (Equation 8.4), including the five parameters $\bar{\varepsilon}_f$ (Equation 8.3), $\bar{\varepsilon}_{th}$ (Equation 8.6), $D_{cr}$ (Equation 8.5), $\nu_1$ (Equation 8.7) and $\nu_2$ (Equation 8.8), each with its own strain-rate and temperature dependent equation. All the parameters and sub-parameters involved in the modelling are presented in Table 8.7.

| | | Parameter | | |
|---|---|---|---|---|
| Feature | Equation | | $\dot{\varepsilon}$ effect | $T$ effect |
| $\bar{\varepsilon}_f$ | 8.3 | $\xi_1$ $\xi_2$ $\xi_3$ | $\gamma_1$ $\gamma_2$ | $\psi_1$ $\psi_2$ $\psi_3$ |
| $\bar{\varepsilon}_{th}$ | 8.6 | $\chi_1$ | $\chi_4$ | $\chi_2$ $\chi_3$ |
| $D_{cr}$ | 8.5 | $\phi_1$ | $\phi_4$ | $\phi_2$ $\phi_3$ |
| $\nu_1$ | 8.7 | $\nu_{11}$ | $\nu_{13}$ | $\nu_{12}$ |
| $\nu_2$ | 8.8 | $\nu_{21}$ | $\nu_{24}$ | $\nu_{22}$ $\nu_{23}$ |

**Table 8.7:** Parameters involved in the damage modelling.

#### 8.4.2.2 Model Fit

The procedure followed to calibrate the model has consisted on fitting firstly the different sub-equations that represent $\bar{\varepsilon}_f$, $\bar{\varepsilon}_{th}$ and $D_{cr}$ making use of the collected experimental data. The obtained results have then been imputed in the main equation of the model to finally calibrate the shape of the damage accumulation by means of the equations for $\nu_1$ and $\nu_2$. In all the cases, all the data available at different strain-rate and temperature conditions has been used simultaneously to fit the models. Automated Matlab scripts have been written to fit the experimental data using non-linear least squares fitting algorithms.

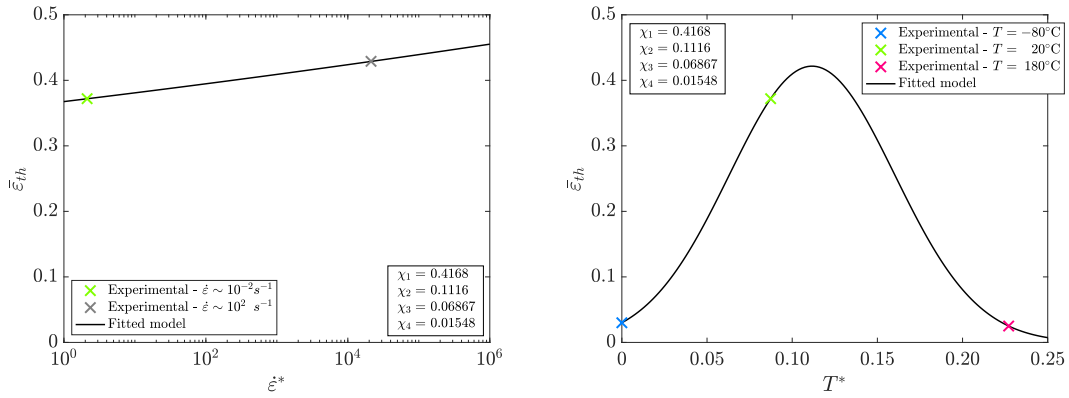
- **Fracture strain.**

  The fitting of the fracture strain model has already been discussed in Section 8.3.2.2, and the parameters obtained there (Table 8.6) have directly been used here for the ductile damage modelling.

- **Threshold strain.**

  The experimental data of threshold strain at each strain-rate and temperature conditions have been obtained by observation of the results of the stiffness reduction tests. For copper C110 a reasonable $\bar{\varepsilon}_{th}$ variation has been observed, and that information has been used to fit Equation 8.6 and obtain the fitting presented in Figure 8.15. On the other hand, no variation of $\bar{\varepsilon}_{th}$ with strain-rate or

temperature has been observed for stainless steel 304L. A summary of the model parameters obtained is available in Table 8.8.




**(a)** Fit of strain-rate results **(b)** Fit of temperature results

**Figure 8.15:** Threshold strain model fit to experimental results of copper C110.

| Material | $T$ effect | | | $\dot{\varepsilon}$ effect |
|---|---|---|---|---|
| | $\chi_1$ | $\chi_2$ | $\chi_3$ | $\chi_4$ |
| s/s 304L | 0.006 | 0 | 1000 | 0 |
| copper C110 | 0.4168 | 0.1116 | 0.06867 | 0.01548 |

**Table 8.8:** Calibrated parameters of the threshold strain part of the model.

- **Critical damage.**

  The experimental critical damage points have been obtained from the metallographic study of the already fractured specimens and from elastic modulus tests. These strain-rate and temperature dependent values have been fitted to Equation 8.5, producing the fitting results presented in Figure 8.16 for stainless steel and Figure 8.17 for copper. Table 8.9 shows the parameters obtained from the model fitting process.

| Material | $T$ effect | | | $\dot{\varepsilon}$ effect |
|---|---|---|---|---|
| | $\phi_1$ | $\phi_2$ | $\phi_3$ | $\phi_4$ |
| s/s 304L | 0.2053 | 0.08054 | 0.2225 | 0.08769 |
| copper C110 | 2.528 | −0.8988 | −0.5830 | 0.01481 |

**Table 8.9:** Calibrated parameters of the critical damage part of the model.

- **Damage accumulation shape.**

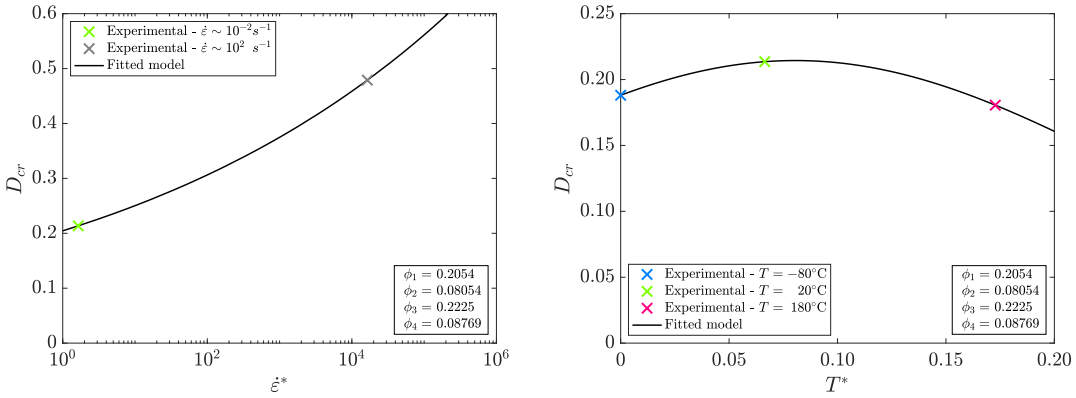
  Once $\bar{\varepsilon}_f$, $\bar{\varepsilon}_{th}$ and $D_{cr}$ have been fitted, their equations have been introduced in the general equation of the model, and the functions that define the shape of damage accumulation have been fitted to obtain the final representation of ductile damage.

The experimental data used for this fitting are those obtained from the elastic modulus reduction tests and the porosity analysis in the case of high strain-rate. The values of the sub-parameters obtained for $\nu_1$ and $\nu_2$ equations are presented in Table 8.10.

| Material | | | | $T$ effect | | $\dot{\varepsilon}$ effect | |
|---|---|---|---|---|---|---|---|
| | $\nu_{11}$ | $\nu_{21}$ | $\nu_{12}$ | $\nu_{22}$ | $\nu_{23}$ | $\nu_{13}$ | $\nu_{24}$ |
| s/s 304L | 0.1704 | 0.7002 | −2.185 | 0.06642 | 0.08240 | 0.09155 | 1.697 |
| copper C110 | 0.4580 | 10.80 | −3.888 | 0.2491 | 0.3992 | 0.03279 | −6.465 |

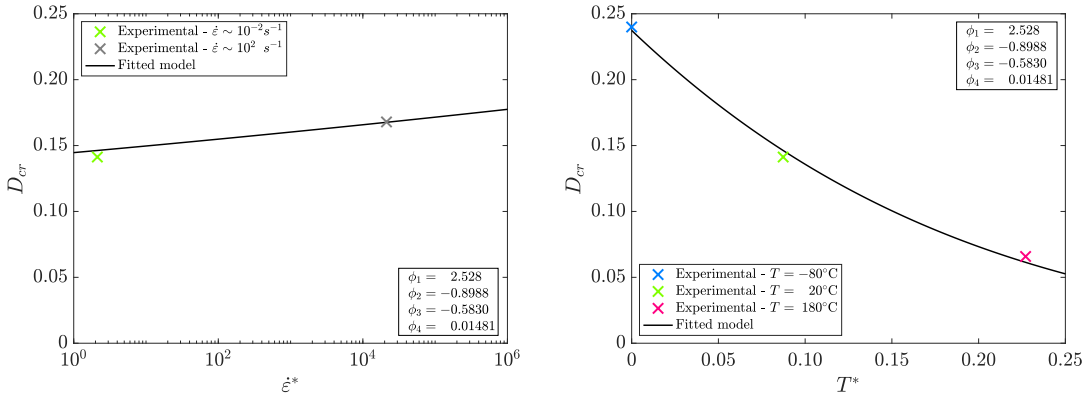
**Table 8.10:** Calibrated parameters of the damage accumulation part of the model.

With all the sub-models involved in the damage characterisation calibrated as a function of strain-rate and temperature, the main equation of the model (Equation 8.4)




**(a)** Fit of strain-rate results **(b)** Fit of temperature results

**Figure 8.16:** Critical damage model fit to experimental results of stainless steel 304L.




**(a)** Fit of strain-rate results **(b)** Fit of temperature results

**Figure 8.17:** Critical damage model fit to experimental results of copper C110.

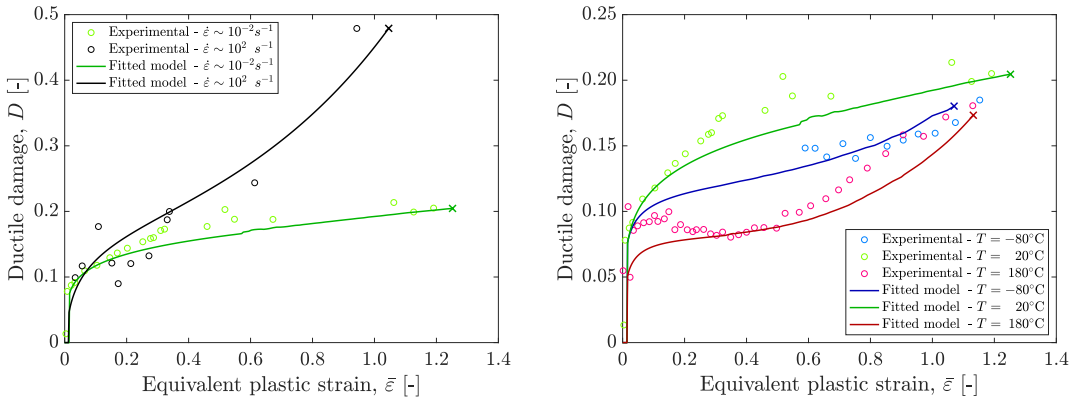
can be used to predict ductile damage accumulation in different conditions. The comparison of the experimental data and the fitted model prediction is presented in Figure 8.18 for stainless steel 304L and in Figure 8.19 for copper C110, showing in both cases the strain-rate and temperature analysis separately. As observed in the plots, very different curve shapes can be produced by the model and the fit quality obtained for both materials is good, considering the differences that take place when strain-rate and temperature are changed.

## 8.5 Conclusions

In this chapter, material models have been developed, analysed and calibrated to represent the three aspects of ductile metals studied experimentally in previous chapters: plasticity, ductile fracture and ductile damage. For the plasticity modelling, Johnson-Cook [1] model has been used, since it incorporates the effects of strain-rate and temperature on hardening and it is relatively simple to fit and use. Its calibration has been satisfactory and an $R^2$ value of 0.95 has been achieved for stainless steel 304L and 0.83 for copper C110.

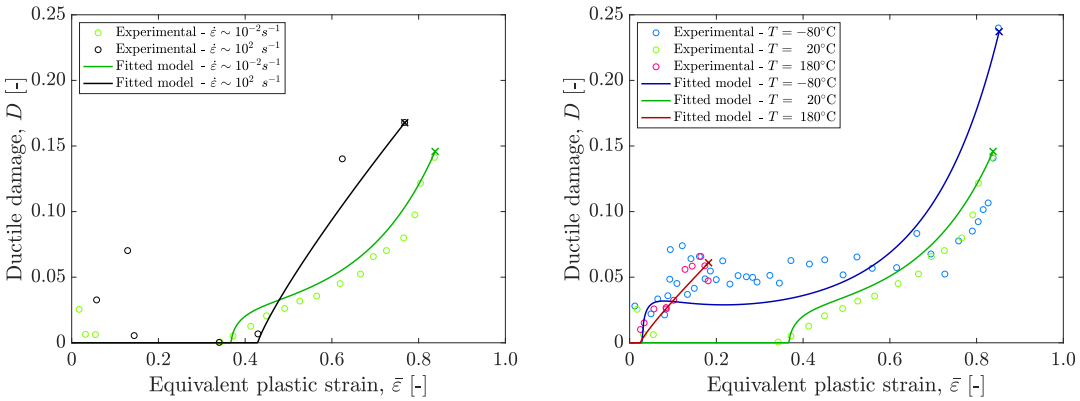
Fitting of the model also proposed by Johnson and Cook to represent ductile fracture [1] has been attempted, nevertheless, its performance has not been as successful as that of the hardening model, obtaining $R^2$ values of 0.79 for stainless steel and 0.73 for copper. The reason is the simplicity of the model, which considers the effect of strain-rate and temperature by means of terms that multiply the base exponential equation and only scale it up or down, while its shape remains unchanged. An alternative model has been proposed to improve the representation of strain-rate and temperature on ductile fracture. This model modifies directly the parameters inside the exponential equation by transforming them into strain-rate and temperature dependent terms. The $R^2$ values obtained in this case are significantly higher, with 0.96 for the austenitic steel and 0.90 for copper. The only drawback of the proposed model compared to Johnson-Cook is the addition of parameters, which is increased from five to eight. However, additional experiments are not required for the calibration of the model, and since the basic approach proposed by Johnson and Cook is not able to represent all the non-linear trends followed by the results, a small increase in model fitting complexity results in a great increase in fracture prediction accuracy without increasing the experimental cost.

Two different approaches have been attempted when fitting the plasticity and ductile fracture models, either considering the experimental data of all the conditions studied together and fitting it to the complete equation, or fitting separately the results in standard conditions, different strain-rates and temperatures to the respective parts of the models. Although the fitting process can be simpler when parts of the model are




**(a)** Fit of strain-rate results **(b)** Fit of temperature results

**Figure 8.18:** Proposed ductile damage model fit to experimental results of stainless steel 304L.




**(a)** Fit of strain-rate results **(b)** Fit of temperature results

**Figure 8.19:** Proposed ductile damage model fit to experimental results of copper C110.

calibrated individually, the quality of the fit has always been better when all the information has been considered together, therefore, it is advisable to follow this approach when it is possible.

For the ductile damage representation Bonora model [83] was initially considered, since it aims to represent ductile fracture and damage accumulation shape together with a very limited number of parameters. However, its calibration has been utterly unsuccessful, and an alternative ductile damage model has been required. A ductile damage model has been developed, that unlike any other model of this characteristics available in literature, incorporates the effects of strain-rate and temperature on damage accumulation. This has been achieved by means of rate and temperature de-

pendent sub-models that represent the different aspects of damage, such as threshold strain of damage initiation, fracture strain, critical damage and the shape of damage accumulation. A good model fit has been achieved thanks to its flexibility, making it possible to adjust the curve to widely changing conditions. The number of parameters required for the model is relatively large, nonetheless, many effects taking place in the damage phenomenon are considered in the model and an accurate estimation in different strain-rate and temperature conditions would be impossible without them.

# Chapter 9

# Conclusions

The fundamental aim of this thesis was to develop a verified methodology to predict ductile damage and fracture of metals at different strain-rate and temperature conditions. Experiments were designed and stainless steel 304L and copper C110 specimens were tested to study their plasticity, ductile fracture and ductile damage behaviour. A neck monitoring method was implemented to account for the material necking, and ductile damage was quantified through the measurement of elastic modulus reduction, and also performing micrographic porosity analyses. The same methodology was applied at high and low temperature, performing the tests inside an environmental chamber; and at high speed including some modifications, such as an experimental rig for interrupted high-speed tests that was designed, built and tested. The experimental results were used for the assessment of plasticity, ductile fracture and damage accumulation models. A damage model was developed that captures the behaviours observed, includes strain-rate and temperature effects and presents non-linear damage accumulation.

## 9.1 Experimental Methodology

Firstly, some comments can be made about the materials and specimen geometries used for this research:

**Materials.** Stainless steel 304L and copper C110 materials were studied in this thesis. The reasons for choosing these materials are that they are very ductile and readily available, perfect for plasticity and ductile damage analyses and for models development. They have been extensively studied in the past and standard information about them can easily be found in literature. The required test specimens were manufactured using these materials, and although the whole project was focused on isotropic

materials, the specimens were machined out of bars that had been produced by cold drawing, which inherently may introduce some anisotropy. Nevertheless, the isotropy of the specimens was checked by studying the fractured neck of the specimens using a shadowgraph, and this study revealed regular diametrical deformation, and hence isotropic behaviour.

**Specimens Geometry.** Round bar (RB), round notched bar (RNB) and hourglass shaped round specimens (HGR) were used in this work for the study of plasticity, ductile fracture and ductile damage respectively. The geometry of the first two is fairly standard, while the hourglass specimens were designed to concentrate damage in their centre without affecting the material behaviour. The aim was to maintain the stress and strain fields uniform in that gauge region, behaving similarly to the smooth round specimens and developing an equivalent neck. This was checked by means of finite elements simulations, and also experimentally comparing the flow curves of RB and HGR specimens, which were coincident.

The experiments that were later used at different conditions were firstly designed in quasi-static strain-rate and room temperature conditions. Below are some comments that can be extracted from the design process of the experiments:

**Imaging Methodology for Neck Monitoring.** A simple and economical method of characterising accurately the flow curve of isotropic metals including the necking effects up to fracture was proposed. It is based on taking images of the specimen during the test, however, specific DIC equipment and a complex calibration process are not required, and tests can be performed using a conventional DSLR camera. The method is more beneficial for materials that develop a pronounced neck, such as copper, for which the uniform deformation approximation would lead to an unacceptable error. The technique is limited to isotropic materials, since the calculations are based on pictures taken from only one direction, while anisotropic materials form a non-uniform neck of elliptical cross-section that could not be characterised with 2D information. In general, the method proved to be robust, and gave repeatable results that were validated with post-test shadowgraph measurements.

**Imaging Methodology for Stress Triaxiality Analysis.** The imaging methodology was also used to measure the evolution of the notch in round notched specimens (RNB). These tests that are normally performed to study the ductile fracture of the material have been improved by the method, since it provides the stress triaxiality history of the notch. This allows for the calculation of the average stress triaxiality of the test, whose use for ductile fracture models calibration is more representative than the initial or final value. In literature, some authors have used finite elements simulations to estimate the stress triaxiality history and obtain its average value [58], nonetheless,

in this work it was obtained purely experimentally, avoiding any possible errors derived from inaccurate FE models calibration.

**Damage Accumulation.** An improved methodology was implemented for damage quantification based on the measurement of elastic modulus variations using a small extensometer during continuous tests. The use of strain gauges was considered, however, the extensometer reduces the duration and cost of the tests. More importantly, the origin of measurement is lost when strain gauges are replaced, making it almost impossible to obtain accurate results using that approach. Many techniques have been proposed to measure ductile damage, being their application very sensitive and producing in general scattered results. The elastic modulus reduction method was selected because there is more experience about its use in literature and it provides relatively good results if the tests are performed carefully. This includes taking into account the geometrical changes of the specimen during the test, which in this methodology was done entirely experimentally using the corrections obtained from the analysis of the neck. Although the method is sensitive, repeatable results were obtained and they were validated through a metallographic study. It must be noted though, that the quality of the results obtained is highly dependent on the skills and experience of the person that sets the test up.

Some conclusions were also drawn when the methodology was modified so that it could be applied at high strain-rate and different temperatures:

**Strain Measurement at High Speed.** Three non-contact imaging methods were tried for strain measurement at high speed and all of them gave good results, however, only the one based in the shadowgraph concept and Bridgman relationships considered material necking. Also, these techniques were compared at a velocity of 1 m/s, and if higher velocities were tested, problems derived from the paint detaching from the surface would be expected for video-extensometer and DIC techniques. On the other hand, paint was not required for the shadowgraph method, and images of the neck of excellent quality were obtained at high speed using a very simple experimental arrangement. The limitation of the method is the resolution and maximum frame rate of the camera, nevertheless, when a sub-pixel edge detection algorithm was implemented for the post-processing good results were obtained even from low resolution images. Therefore, the only real limitation of the method is the maximum frame rate of the camera used, which can be increased to an extent sacrificing image resolution, but can only be addressed by using better equipment.

**Damage at High Speed.** A novel experimental rig was designed for the interruption of high-speed tests and the subsequent damage quantification. The performance of the experiment was better than expected, showing an improved alignment compared to the conventional tests. No additional plasticity was introduced in the sample after

the shear pin broke, which was one of the main concerns. This was checked with FE simulations during the design process, and validated with DIC measurements during the experiment calibration. The method to control the amount of deformation applied to the sample is reasonably precise in the uniform deformation phase, although it becomes more complicated near fracture, when a small adjustment results in considerable deformation. A practical difficulty of the use of the rig appeared when the samples had to be removed after they had been tested. The specimens can always be removed by disassembling the top plate of the rig's frame, however, that is impractical and an additional connection element was included below the specimen in order to ease its extraction.

A hybrid method consisting in damaging the material at high speed and measuring damage at low speed was proposed. Although the validation test of this methodology in quasi-static conditions gave good results, in practice it only worked relatively well with the copper specimens. In this case, the extensometer was attached independently for each specimen and small changes from one test to other, such as a slight misalignment, might have produced considerable changes in the elastic modulus measured, and therefore, scatter in the results. Additional damage measurements were performed based on the microstructure of the damaged material, which in the case of copper validated the trend observed from the hybrid method. The use of only the hybrid methodology for damage measurement would allow to apply multiple deformation steps to the same sample, reducing the cost of tests. However, it would be impractical because the damage measurements would have to be taken in between loading stages, requiring the process the use of both machines at the same time, increasing the duration and complexity of the whole experiment.

**Experiments at Temperature.** The methodology followed to study the temperature effects was the same but the tests were run inside an environmental chamber. All the equipment used must resist the high and low temperatures that were applied inside the chamber, including sensitive components such as the extensometer, whose maximum temperature of operation limited the maximum temperature of the tests. Lighting of the sample supposed a complication, and methods of illuminating the specimen inside the chamber should be explored in the future. However, the main difficulties came from ice formation and paint cracking at low temperature. In the end, it was opted for unpainted specimens testing, although the quality of the images obtained was poor and considerable manual image processing was required in order to obtain good results. The door was kept open for very short periods of time to avoid humid air entering the chamber, and a few minutes were left for the mist to disappear before starting the test. Nevertheless, this procedure did not entirely avoid the slow formation of ice in the surface of the specimen after some time had passed, and if images were not corrected it could have been regarded as a false diameter increase during the post-processing.

## 9.2 Results in Standard Conditions

Some conclusions can be drawn from each of the three material properties studied experimentally:

**Plasticity Analysis.** The technique proposed for plasticity analysis produced consistent results in standard conditions, and was validated by comparison with conventional tensile tests that provided equivalent results in the uniform deformation region. Stainless steel presented a region of uniform deformation up to $\bar{\varepsilon}_{pl} \sim 0.35$ after which a neck developed, while copper necked almost from the yield condition ($\bar{\varepsilon}_{pl} \sim 0.05$) due to its very ductile properties. It was observed that the hardening curve presents an almost linear shape for most of the cases studied, and therefore, an approximation could be made extending the curve of the uniform deformation region up to the fracture point, if this was known. Although the neck imaging technique is easy to apply, this approximation could also be used to have a first estimation of the real flow curve.

**Ductile Fracture Analysis.** The imaging technique was applied to notched specimens of both materials, and the decreasing fracture strain with stress triaxiality reported in the literature was observed. Similar yield stress, similar hardening rate and decreasing fracture strain were observed when stress triaxiality was increased. The stress triaxiality history of each experiment depended on the material and notch geometry, generally increasing as the test developed, but also decreasing for the very sharp notches of stainless steel. In this case, instead of becoming sharper, the notch tended to open increasing its radius of curvature. The trends observed were consistent with those reported in literature and the calculated values of average stress triaxiality improved the fracture models calibration.

**Ductile Damage Analysis.** Ductile damage accumulation was measured using the elastic modulus reduction technique. Very different damage evolution trends were observed for the two materials studied. Stainless steel presented damage from the beginning of the plastic region which then stabilised, while copper nucleated voids at a later plastic strain and then accumulated damage almost linearly. Both materials studied have a similar crystalline structure, however, the nucleation of voids is driven by the presence of inclusions in the metal matrix and by the relative softness of the matrix and the particles. Growth and coalescence is also highly dependent on the material properties, therefore, each material has to be studied independently and an accurate damage accumulation model should be flexible to represent the different non-linear trends.

As an alternative method for damage measurement, flat specimens were tested exploring DIC as an option for elastic modulus measurement. The objective would have been to apply the technique at high strain-rate for in-situ elastic modulus measurements. However, the scatter of results was relatively high, which combined with the

facts that paint detaches from the specimen's surface at high speed and tests cannot be easily stopped in those conditions, resulted in the dismiss of the method for damage quantification.

**Microstructural Analysis.** The measurement of ductile damage through the degradation of elastic modulus was validated by means of a microstructural study of the stainless steel 304L samples. Qualitative studies revealed higher concentration of damage in the centre of the neck of highly damaged specimens, as would be expected since that is the region of highest stress triaxiality. From the quantitative study of void density evolution with plastic strain, the trend of damage accumulation observed from elastic modulus measurements was validated. However, the scale of the macroscopic degradation is much higher than that of the microstructural net cross-section reduction. This means that the degradation not only comes from internal geometrical effects, but also from the strongly plastified material surrounding voids, which has undergone damage that produces further degradation of macroscopic properties. Although the microstructural analysis provided the actual measurements of voids that drive the damage accumulation trends, for a modelling approach interested in the study of macroscopic mechanical properties the values of degradation obtained from stiffness reduction, are considered more representative and were used for the models development.

Another observation is that the void density values measured near fracture correspond to much higher damage levels than those measured with the modulus reduction technique. At that level of material degradation, it became difficult to perform loading and unloading cycles without breaking the specimen. The variability of fracture strain also made it difficult to select the plastic strain for the unloading cycle. In any case, in those conditions the neck would have been extremely developed and the measurement of modulus would have been averaged within the gauge region, and not local as that obtained from the microstructure. Therefore, for damage quantification near fracture elastic modulus reduction technique is not appropriate, and a local method such as microstructure or microindentation is recommended instead.

## 9.3 Strain-Rate Effect

A general difficulty in the high strain-rate analysis was the lack of data points, caused by the limited frame rate of high-speed cameras. The scatter was higher than that of the quasi-static case, produced by the dynamic effects like stress spikes or system ringing. Also, the two high-speed conditions studied were somewhat similar, presenting only an order of magnitude of difference between them, and for some of the tests it was difficult to observe a clear difference between them. In spite of these difficulties, the following conclusions were obtained from the results:

**Strain-Rate Values.** The strain-rate measured was not constant during the tests, presenting the specimens an approximately constant region when the deformation was uniform, and rising when necking appeared. This effect was caused by the rapid increase of local stresses and strains when localisation was taking place, during which a strain-rate increase of about one order of magnitude was observed in most of the tests. For the calibration of plasticity and damage accumulation models the strain-rate information of each data point was used, and for the fracture model the average of the whole test was considered, in order to be consistent with the average stress triaxiality data also used. It must be noted that the average values of strain-rate obtained were significantly higher than those reported in literature. Usually localised strains are not calculated, whereas in this work the higher strain-rates of the neck are considered in the calculation of the average. In the interrupted tests, higher average strain-rates were achieved in the specimens that were deformed to higher plastic strains, due to the aforementioned strain-rate increase during the localised deformation. If more uniform strain-rate values were desired, decreasing values of ram velocity for increasing plastic deformation should be applied, and the velocity for each test should be calibrated by means of FE simulations or trial and error calibration tests.

**Plasticity Strain-Rate Analysis.** It was difficult to extract clear conclusions about the neck development from high-speed tests because of the noise and the lack of data points. In general, a reduction of ductility and an increase of strength was observed at high strain-rate, caused by the lack of time for crystalline planes to slip at high-speed deformation. A small hardening rate increase was observed for increasing strain-rate, however, softening appeared in the high plastic strain region. This was caused by the heating of the specimen which produced the opposite effect to the slight hardening for low values of plastic strain.

**Ductile Fracture Strain-Rate Analysis.** Notched specimens of different geometry were tested at different strain-rates. When the stress-strain curves of all the tests were analysed, a combination of all the effects observed so far appeared: strain-rate increase during the necking process, upwards movement of the maximum axial stress curves and ductility decrease for increasing stress triaxiality and for increasing strain-rate. For copper the ductility reduction was approximately uniform in the whole stress triaxiality range, whereas for stainless steel the decrease was considerable for low triaxialities and almost non-existent for high triaxialities, becoming the fracture curve flat and the material triaxiality independent at high strain-rate fracture. These two very different behaviours proved the different fracture performance of various materials at high strain-rate.

**Ductile Damage Strain-Rate Analysis.** Interrupted tensile tests were performed at high speed to study the effect of strain-rate on damage. Each test provided

a ($D$-$\bar{\varepsilon}_{pl}$) point, and the difficulty involved and the time required for each test resulted in a very limited number of points to construct the curves, complicating the extraction of trends from results. The elastic modulus measurements provided an ascending trend for copper, similar to that observed in the quasi-static case, however, no clear trend was obtained for stainless steel, for which the scatter was significant. Therefore, this technique cannot be directly used for all materials or all conditions, and a complementary porosity analysis was performed on the same samples. A more clear trend was observed from the microstructural study, showing the stainless steel a similar trend to the one that it presented in quasi-static conditions, but losing the plateau and displaying continuous damage accumulation that finished at a lower maximum value. This limited development of voids at fracture might be caused by the lack of time for microstrains to develop around defects and for voids to grow, resulting in an early fracture at limited ductility. Almost no porosity was observed in the copper specimens until high plasticity was achieved, when very high porosity, and in some cases macroscopic holes and cracks, were observed. This study validated the trend obtained with the elastic modulus method on copper, proving the usefulness of that technique for certain materials. The microstructural analysis also revealed a radial distribution of damage in stainless steel during localisation. Damage presented a maximum in the centre that decreased towards the surface of the sample. On the other hand, copper showed a random damage distribution up to fracture explained by the more sudden appearance of bigger defects in random locations at a later stage.

## 9.4 Temperature Effect

Some conclusions can be drawn from the experiments performed at varying temperature:

**Plasticity Temperature Analysis.** As it was expected, an increase in strength and hardening rate for decreasing temperature was observed. Stainless steel at $-80°$C also presented a sudden further rise of flow stress and hardening rate at early plasticity stages caused by a martensitic transformation. Ductility reduction was observed at both high and low temperature. While this was foreseen in the low temperature case, an increase was expected in the high temperature tests. The observed behaviour may have occurred in stainless steel because the temperature analysed was far from its melting temperature ($T_m = 1698$K), and therefore too cold to observe clear softening. Strong degradation was observed in the high temperature copper specimens, which developed an almost instantaneous neck and fracture. The sudden appearance of macroscopic defects may have led to the early fracture before any plastic slip mechanism could have taken place.

**Ductile Fracture Temperature Analysis.** The study of the fracture surface of the specimens revealed brittle cracks in stainless steel at $-80°C$, probably produced by the presence of martensite in the otherwise austenitic matrix. The bigger defects present in copper at $180°C$ relate to its reduced ductility in those conditions. The study performed on notched samples at different temperatures showed the combined effects of stress triaxiality and temperature: reduction of yield stress and hardening rate with temperature, reduction of ductility at low and high temperatures and also for increasing stress triaxiality, and martensitic transformation of stainless steel at cryogenic temperatures. Stainless steel presented a uniform slight decrease of ductility across the stress triaxiality range, because the temperatures tested were low compared to its melting temperature. Copper also showed a small reduction of fracture strain at low temperature, but a massive degradation at high temperature. The reduction was especially pronounced at low stress triaxiality, becoming the fracture curve almost linear and independent of stress triaxiality.

**Ductile Damage Temperature Analysis.** Damage was measured using the elastic modulus reduction technique inside an environmental chamber. The trends changed significantly for both materials studied when temperature was modified, highlighting the need of a non-linear temperature dependent model. Damage in copper did not appear until $\bar{\varepsilon}_{pl} = 0.3$ at room temperature, while voids slowly appeared from the beginning of the plastic region at low and high temperature. The change in mechanical properties of the material matrix and inclusion particles when temperature is modified affects the dynamics of voids nucleation and growth, hence producing changes in the damage accumulation trends. It was also observed that the martensitic transformation of stainless steel at low temperature produced an abrupt fall of the elastic modulus, that recovered its initial value after the phase transformation had been completed. Although normally the measured changes in elastic modulus are produced by ductile damage, other internal phenomena may occur that modify it and must be taken into account, like the phase change that occurs in this case.

## 9.5 Material Models

Some comments can be made about the development and fit of plasticity, ductile fracture and ductile damage models:

**Plasticity Modelling.** Johnson-Cook plasticity model was selected to represent the flow curve because it includes the effects of strain-rate and temperature and because of its simplicity, as plasticity was not the main topic of the present research and only a proper representation of hardening without added complexity was required. Different fitting approaches were followed, calibrating all the data together or the different con-

ditions separately, and the best model fit was achieved with a simultaneous fit. The number of data points available may vary depending of the test conditions, however, a similar number of data points should be used from every test for the models calibration. Therefore, it is advised to preprocess the data so that all the conditions are weighted equally during the calibration process. Following this procedure, an overall $R^2$ value of 0.95 was achieved for stainless steel 304L and 0.83 for copper, which was considered adequate, although a more complex model should be used if additional effects have to be represented, such as the martensitic transformation of stainless steel.

**Ductile Fracture Modelling.** Johnson-Cook ductile fracture model was considered for the representation of fracture strain, again because it incorporates strain-rate and temperature on its formulation; however, the representation of these effects was not that successful in this case. The model includes a temperature dependant term and a strain-rate dependent term that multiply the baseline exponential curve, but do not change its shape. Since a highly non-linear variation of the curve shape with temperature and strain-rate was observed experimentally, only a mediocre fit of experimental data was possible ($R^2 = 0.79$ for stainless steel and $R^2 = 0.73$ for copper). In order to improve the temperature and strain-rate representation, it was considered that a new model based on Johnson-Cook base equation could be proposed, in which these effects appear both in the linear and exponential terms of the equation modifying the position and shape of the curve respectively. The fit of this model resulted in an improved calibration of the experimental data, with $R^2 = 0.96$ for stainless steel and $R^2 = 0.90$ for copper. In the proposed model three parameters were added when compared to the original Johnson-Cook formulation, however, this increased the flexibility of the model and the non-linear dependencies on strain-rate and temperature were better represented. Moreover, no additional tests are required to fit these parameters and only the complexity of the fitting process increases slightly due to the greater number of parameters, nonetheless, the accuracy of the modelling also increases.

**Ductile Damage Modelling.** After researching literature, it was observed that most ductile damage models assume a linear damage accumulation, while it has been proved experimentally that the general case is highly non-linear. The model proposed by Bonora is based on continuum damage mechanics theory and it includes non-linear damage accumulation. It also proposes a joint representation of ductile fracture and damage, however, it was not possible to attain an acceptable fit of both behaviours at the same time, and therefore, the model was not considered further, and fracture and damage accumulation were represented separately. Also, the effects of strain-rate and temperature on damage accumulation have not been included in models proposed in literature. Bearing this in mind, a non-linear strain-rate and temperature dependent damage accumulation model was proposed. The model is based on a power law equation whose exponent controls the non-linear shape of damage accumulation. The depend-

ency of strain-rate and temperature was introduced through each of the parameters, allowing to keep the baseline shape of the equation and at the same time enabling the modification of the parameters.

A simultaneous model fit approach was used, as for the rest of models considered in the thesis, however, the different parameters of the model ($\bar{\varepsilon}_{th}$, $\bar{\varepsilon}_f$, $D_{cr}$, $\nu_1$ and $\nu_2$) were fitted to their respective expressions separately, due to the complexity of the full model equation. A good fit of the proposed model was achieved, nonetheless, it has already been mentioned that the experimental data of some conditions should be treated carefully, and therefore, running more tests would be recommendable for an improved calibration. The proposed model proved to be very flexible to represent different conditions with various curve shapes, but given the variety of damage accumulation trends that are possible, a more extensive study on other materials would be desirable to further validate the model. As it occurred with the fracture model, this damage accumulation model includes many parameters, however, no additional tests are required for their calibration, only more experiments would be desirable to increase the confidence in the experimental data.

## 9.6 Further Work

Throughout this research some areas for further investigation have been identified. Limitations in the duration and scope of the project have prevented their study, nevertheless, the most interesting topics along with some recommendations for their investigation are summarised below.

**Materials and Processing Techniques.** The experimental methodology and modelling approaches discussed in this thesis were developed for stainless steel 304L and copper C110. The same techniques could be applied in the future to a wider range of metals, in order to prove the usefulness of the experiments and the applicability of the material models developed in this thesis. Although the models were designed to be flexible to fit different materials and conditions, they were created based on the limited experimental results obtained in this thesis, and data from other materials could be used to adapt or modify them making them even more flexible.

Not only different materials, but also different material processing techniques could be studied. The analysed materials were drawn and machined, however, other less conventional techniques, such as additive manufacturing, have a great potential for different applications. Particularly, the material produced using this technique is characterised by an initial porosity higher than that presented by other conventional methods. Being ductile damage based on the evolution of microdefects, it would be interesting to apply the techniques proposed in this thesis to specimens produced by additive manufactur-

ing, which inherently should present higher values of initial damage and different trends of damage accumulation.

**Additional Methods for Ductile Damage Measurement.** Successful measurements of ductile damage along the plastic range were obtained making use of the elastic modulus reduction method and microstructure analysis. However, other methods were presented in the Literature Review, and some of them could be of special interest. The use of X-Ray CT was attempted as part of this project, but a thorough study was not conducted since the resolution of the facilities available was not accurate enough to detect the voids of sub-micron size that appear in early stages of damage. This technique has great potential though, as it could even be applied during a tensile test to obtain in-situ void evolution measurements, and in a synchrotron facility to perform similar measurements at higher strain-rate. Nevertheless, the feature minimum size that can be detected by the equipment is the limiting factor, and the adequacy should be firstly assessed with a preliminary 2D microstructural study, from which the order of magnitude of defects can be estimated.

Another technique that could easily be used to further validate the results obtained in this thesis is the indentation method presented in Section 2.3.2 of the Literature Review. A map of indentations and hardness measurements could be performed on the samples whose microstructure was studied in this research, and a comparison of the results with the available porosity maps could be made. The results should present the same areas of damage concentration and proportional trends. Finally, a comparison of the results with finite elements simulations of the tests, including the calibrated damage models, could be made for a final validation of the damage evolution and the behaviour of the models.

**Effect of Lode Angle and Anisotropy.** Lode angle parameter is related to the second and third invariants of the deviatoric stress tensor, and it introduces in the models the effect of the various possible loading conditions (tension, compression, shear, etc.). In this research the effect of stress triaxiality on fracture strain was studied, while the effect of Lode angle was not considered, as it would have required an amount of time beyond the scope of the project. Nevertheless, the effect of Lode angle on fracture strain at different temperatures and strain-rates should be studied experimentally and included in the models, in order to have a complete representation of the state of the material. For that purpose, different tests applying combinations of tensile, compressive and shear loads on various specimen configurations could be run, and these same tests could be performed at different temperatures and strain-rates. Models such as that proposed by Bai and Wierzbicki [55], which considers the effects of both stress triaxiality and Lode parameter on fracture strain, could be used as starting point to modify the model presented in Section 8.3.2. Regarding stress triaxiality, the whole thesis analysed the ductile damage mechanism controlled by voids, that appears at moderate and high stress triaxiality, while the shear controlled ductile damage was not

considered. The effects of this damage mechanism that appears in states of low and negative stress triaxiality would also be studied by running some of the compressive experiments mentioned for the Lode angle analysis.

Another topic of further study to improve the methodology proposed in this thesis is the consideration of anisotropic behaviour. The experiments conducted assume isotropic behaviour of the material, as many of the techniques are based on pictures of the sample taken with a single camera from a single direction. For anisotropic materials the deformation observed would be different from different angles, generally producing an elliptical neck. For the study of anisotropic materials images from at least three different angles are required, increasing the complexity of experiments. CT X-Rays technique would be an interesting option for the characterisation of anisotropic ductile damage, since it could provide an internal 3D map of voids with information about their spatial distribution in different directions. Alternatively, other 2D destructive methods such as the aforementioned microstructure or indentation studies could be performed in different slices and directions.

**Strain-Rate and Temperature Conditions.** The effect of strain-rate and temperature on plasticity and damage was analysed experimentally in this research, however, for an improved representation of the trends that these properties follow a wider range of conditions could be studied. The highest temperature tested was 180°C, and it was limited by the maximum temperature of operation of the extensometer. This temperature is quite low compared to the melting temperatures of the materials studied, and although a trend was observed, a wider temperature difference would have helped to draw quantitative conclusions. Further investigation of the ductility results at 180°C is required, since an increase of fracture strain was expected and the opposite occurred, especially for copper specimens that presented extremely high degradation at that temperature.

Damage accumulation at higher strain-rates could also be tested using the experimental rig designed as part of this research. Some tests were performed at velocities around 8 m/s, but a thorough study was not pursued because of time constraints. It was concluded that a redesign of the shear pin would be required to withstand the dynamic loads that appear at these higher speeds. This could be done by modifying the materials or cross-section of the shear pin.

All the experiments performed in this research modify either the temperature or the strain-rate keeping the other one constant at room temperature or quasi-static rate. Ultimately, in order to collect more information about the effects of these conditions on materials, both could be changed at the same time. Tests at combined high speed and different temperatures could be performed for an improved calibration or further validation of the models. These tests could easily be done for the necking and fracture experiments by running the high-speed tests inside an environmental chamber. The ductile damage analysis would be more complicated because of the bulky dimensions of

the experimental rig required for interrupted tests, which would be difficult to install inside an oven.

**Models Calibration and Validation.** Johnson-Cook model [1] was selected to represent plasticity in this research, nevertheless, this is not the only option available. The experimental results obtained in this research could be used to fit other models in the future, such as Zerilli-Armstrong [18] or MTS [19], which are also appropriate for high-speed applications. The user subroutines written for the models studied in this thesis could easily be modified to implement these or other models just by changing the equations that define the hardening law of the material.

Regarding the ductile fracture and damage accumulation behaviours, new models that include temperature and strain-rate were proposed in this research. Their development is based on the observation of previous models from the literature and on the experimental results obtained in this research. Nonetheless, the information available is limited due to the complexity of some of the experiments, and therefore, the application of these models to other materials would enrich their quality. The models were also implemented in user subroutines that can be directly applied to Abaqus/standard or Abaqus/explicit simulations. The following step of the analysis of the models would involve their application in a campaign of FE simulations that reproduce the same tests that were run in the laboratories. For a final validation of the models, a series of crack propagation tests on compact tension (CT) specimens could be run and also be simulated with FE models. If the behaviour predicted by the simulations was similar to that observed in the experiments, it would serve as validation of the material models accuracy in a more realistic environment.

# References

[1] G. R. Johnson and W. H. Cook, "Fracture characteristics of three metals subjected to various strains, strain rates, temperatures and pressures," *Engineering Fracture Mechanics*, vol. 21, no. 1, pp. 31–48, 1985.

[2] C. Roth and D. Mohr, "Effect of strain rate on ductile fracture initiation in advanced high strength steel sheets: Experiments and modeling," *International Journal of Plasticity*, vol. 56, pp. 19–44, 2014.

[3] Official SpaceX Photos, "Bangabandhu Satellite-1 Mission," 2018.

[4] Official SpaceX Photos, "Falcon Heavy Demo Mission," 2018.

[5] F. McClintock, "A criterion for ductile fracture by the growth of holes," *Journal of Applied Mechanics*, vol. 35, no. 2, pp. 363–371, 1968.

[6] J. R. Rice and D. M. Tracey, "On the ductile enlargement of voids in triaxial stress fields," *Journal of the Mechanics and Physics of Solids*, vol. 17, no. 3, pp. 201–217, 1969.

[7] H. Tresca, *Comptes Rendus Acad. Sci. Paris v. 59.* 1864.

[8] R. von Mises, *Göttinger Nachrichten Math-Phys. Klasse.* 1913.

[9] J. Ewing and W. Rosenhain, "The crystalline structure of metals. Second paper," in *Proceedings of the Royal Society of London 67*, pp. 112–117, 1900.

[10] G. Taylor, "The mechanism of plastic deformation of crystals. Part I: theoretical," *Proceedings of the Royal Society A: Mathematical, Physical and Engineering Sciences*, vol. 145, no. 855, pp. 362–387, 1934.

[11] M. Polanyi, "Über eine Art Gitterstörung, die einen Kristall plastisch machen könnte," *Zeitschrift für Physik*, vol. 89, no. 9-10, pp. 660–664, 1934.

[12] E. Orowan, "Zur Kristallplastizität. III - über den Mechanismus des Gleitvorganges," *Zeitschrift für Physik*, vol. 89, no. 9-10, pp. 634–659, 1934.

[13] D. Stouffer and L. Dame, *Inelastic Deformation of Metals.* New York: John Wiley & Sons, 1996.

[14] R. Hooke, *De Potentia Restitutiva.* 1678.

[15] J. Lemaitre and J. Chaboche, *Mechanics of Solid Materials.* Cambridge: Cambridge University Press, 1990.

[16] A. Khan and S. Huang, *Continuum Theory of Plasticity.* New York: John Wiley & Sons, 1995.

[17] J. Chaboche, "A review of some plasticity and viscoplasticity constitutive theories," *International Journal of Plasticity*, vol. 24, no. 10, pp. 1642–1693, 2008.

[18] F. Zerilli and R. Armstrong, "Dislocation-mechanics-based constitutive relations for material dynamics calculations," *Journal of Applied Physics*, vol. 61, no. 5, pp. 1816–1825, 1987.

[19] P. S. Follansbee and U. F. Kocks, "A constitutive description of the deformation of copper based on the use of the mechanical treshold stress as an internal state variable," *Acta Metallurgica*, vol. 36, no. 1, pp. 81–93, 1988.

[20] M. Achouri, G. Germain, P. Dal Santo, and D. Saidane, "Experimental characterization and numerical modeling of micromechanical damage under different stress states," *Materials and Design*, vol. 50, pp. 207–222, 2013.

[21] A. Weck and D. S. Wilkinson, "Experimental investigation of void coalescence in metallic sheets containing laser drilled holes," *Acta Materialia*, vol. 56, no. 8, pp. 1774–1784, 2008.

[22] D. Tracey, "Strain-hardening and interaction effects on the growth of voids in ductile fracture," *Engineering Fracture Mechanics*, vol. 3, no. 3, pp. 301–315, 1971.

[23] A. Needleman, "Void growth in an elastic-plastic medium," *Journal of Applied Mechanics*, vol. 1, 1972.

[24] A. Gurson, "Continuum theory of ductile rupture by void nucleation and growth: Part I - Yield criteria and flow rules for porous ductile media," *Journal of Engineering Materials and Technology*, vol. 99, no. 1, pp. 2–15, 1977.

[25] V. Tvergaard, "Influence of voids on shear band instabilities under plane strain conditions," *International Journal of Fracture*, vol. 17, no. 4, pp. 389–407, 1981.

[26] V. Tvergaard, "On localization in ductile materials containing spherical voids," *International Journal of Fracture*, vol. 18, no. 4, pp. 237–252, 1982.

[27] V. Tvergaard and A. Needleman, "Analysis of the cup-cone fracture in a round tensile bar," *Acta Metallurgica*, vol. 32, no. 1, pp. 157–169, 1984.

[28] A. Needleman and V. Tvergaard, "An analysis of ductile rupture in notched bars," *Journal of the Mechanics and Physics of Solids*, vol. 32, no. 6, pp. 461–490, 1984.

[29] K. Siruguet and J.-B. Leblond, "Effect of void locking by inclusions upon the plastic behavior of porous ductile solids - I: theoretical modeling and numerical study of void coalescence," *International Journal of Plasticity*, vol. 20, no. 2, pp. 255–268, 2004.

[30] C. Chu and A. Needleman, "Void nucleation effects in biaxially stretched sheets," *Journal of Engineering Materials and Technology*, vol. 102, no. 3, pp. 249–256, 1980.

[31] M. Saje, J. Pan, and A. Needleman, "Void nucleation effects on shear localization in porous plastic solids," *International Journal of Fracture*, vol. 19, no. 3, pp. 163–182, 1982.

[32] A. Dalloz, J. Besson, A. F. Gourgues-Lorenzon, T. Sturel, and A. Pineau, "Effect of shear cutting on ductility of a dual phase steel," *Engineering Fracture Mechanics*, vol. 76, no. 10, pp. 1411–1424, 2009.

[33] P. Thomason, *Ductile Fracture of Metals*. Oxford, UK: Pergamon Press, 1990.

[34] P. Thomason, "A three-dimensional model for ductile fracture by the growth and coalescence of microvoids," *Acta Metallurgica*, vol. 33, no. 6, pp. 1087–1095, 1985.

[35] T. Pardoen and J. Hutchinson, "An extended model for void growth and coalescence," *Journal of the Mechanics and Physics of Solids*, vol. 48, no. 12, pp. 2467–2512, 2000.

[36] F. Scheyvaerts, P. R. Onck, C. Tekoğlu, and T. Pardoen, "The growth and coalescence of ellipsoidal voids in plane strain under combined shear and tension," *Journal of the Mechanics and Physics of Solids*, vol. 59, no. 2, pp. 373–397, 2011.

[37] A. Benzerga and J.-B. Leblond, "Effective yield criterion accounting for microvoid coalescence," *Journal of Applied Mechanics*, vol. 81, no. 3, pp. 031009–1–031009–7, 2014.

[38] M. Gologanu, J.-B. Leblond, and J. Devaux, "Approximate models for ductile metals containing nonspherical voids — case of axisymmetric prolate ellipsoidal cavities," *Journal of Engineering Materials and Technology*, vol. 41, no. 11, pp. 1723–1754, 1993.

[39] C. L. Hom and R. M. McMeeking, "Void growth in elastic-plastic materials," *Journal of Applied Mechanics*, vol. 56, no. 2, pp. 309–317, 1989.

[40] T. Pardoen and F. Delannay, "Assessment of void growth models from porosity measurements in cold-drawn copper bars," *Metallurgical and Materials Transactions A*, vol. 29, no. 7, pp. 1895–1909, 1998.

[41] J. Wen, Y. Huang, K. Hwang, C. Liu, and M. Li, "The modified Gurson model accounting for the void size effect," *International Journal of Plasticity*, vol. 21, no. 2, pp. 381–395, 2005.

[42] V. Monchiet and G. Bonnet, "A Gurson-type model accounting for void size effects," *International Journal of Solids and Structures*, vol. 50, no. 2, pp. 320–327, 2013.

[43] M. Gologanu, J.-B. Leblond, G. Perrin, and J. Devaux, "Recent extensions of Gurson's model for porous ductile metals," in *Continuum Micromechanics* (P. Suquet, ed.), Springer-Verlag, 1995.

[44] K. Madou and J. Leblond, "A Gurson-type criterion for porous ductile solids containing arbitrary ellipsoidal voids - I: Limit-analysis of some representative cell," *Journal of the Mechanics and Physics of Solids*, vol. 60, no. 5, pp. 1020–1036, 2012.

[45] J.-B. Leblond, G. Perrin, and J. Devaux, "An improved Gurson-type model for hardenable ductile metals," *European Journal of Mechanics A/Solids*, vol. 14, no. 4, pp. 499–527, 1995.

[46] U. Mühlich and W. Brocks, "On the numerical integration of a class of pressure-dependent plasticity models including kinematic hardening," *Computational Mechanics*, vol. 31, no. 6, pp. 479–488, 2003.

[47] V. Tvergaard, "Material failure by void growth to coalesce," in *Advances in Applied Mechanics, vol. 27*, pp. 83–151, Elsevier, 1989.

[48] K. Nahshon and J. Hutchinson, "Modification of the Gurson model for shear failure," *European Journal of Mechanics, A/Solids*, vol. 27, no. 1, pp. 1–17, 2008.

[49] L. Xue, "Constitutive modeling of void shearing effect in ductile fracture of porous materials," *Engineering Fracture Mechanics*, vol. 75, no. 11, pp. 3343–3366, 2008.

[50] A. Benzerga and J. Besson, "Plastic potentials for anisotropic porous solids," *European Journal of Mechanics, A/Solids*, vol. 20, no. 3, pp. 397–434, 2001.

[51] A. Benzerga, J. Besson, and A. Pineau, "Anisotropic ductile fracture: Part II: Theory," *Acta Materialia*, vol. 52, no. 15, pp. 4639–4650, 2004.

[52] J. Hancock and A. Mackenzie, "On the mechanisms of ductile failure in high-strength steels subjected to multi-axial stress-states," *Journal of the Mechanics and Physics of Solids*, vol. 24, no. 2-3, pp. 147–160, 1976.

[53] R. Becker, A. Needleman, O. Richmond, and V. Tvergaard, "Void growth and failure in notched bars," *Journal of the Mechanics and Physics of Solids*, vol. 36, no. 3, pp. 317–351, 1988.

[54] L. Xue and T. Wierzbicki, "Ductile fracture initiation and propagation modeling using damage plasticity theory," *Engineering Fracture Mechanics*, vol. 75, no. 11, pp. 3276–3293, 2008.

[55] Y. Bai and T. Wierzbicki, "A new model of metal plasticity and fracture with pressure and Lode dependence," *International Journal of Plasticity*, vol. 24, no. 6, pp. 1071–1096, 2008.

[56] M. Wilkins, R. Streit, and J. Reaugh, "Cumulative-Strain-Damage model of ductile fracture: Simulation and prediction of engineering fracture tests," tech. rep., 1980.

[57] M. G. Cockcroft and D. J. Latham, "Ductility and the workability of metals," *Journal of the Institute of Metals*, vol. 96, no. 1, pp. 33–39, 1968.

[58] T. Wierzbicki, Y. Bao, Y.-W. Lee, and Y. Bai, "Calibration and evaluation of seven fracture models," *International Journal of Mechanical Sciences*, vol. 47, no. 4-5, pp. 719–743, 2005.

[59] X. Teng and T. Wierzbicki, "Evaluation of six fracture models in high velocity perforation," *Engineering Fracture Mechanics*, vol. 73, no. 12, pp. 1653–1678, 2006.

[60] L. Cortese, F. Nalli, and M. Rossi, "A nonlinear model for ductile damage accumulation under multiaxial non-proportional loading conditions," *International Journal of Plasticity*, vol. 85, pp. 77–92, 2016.

[61] A. Palmgren, "Die lehensdauer von kugellagern," vol. 68, pp. 339–341, 1924.

[62] F. Šebek, J. Petruška, and P. Kubík, "Lode dependent plasticity coupled with nonlinear damage accumulation for ductile fracture of aluminium alloy," *Materials and Design*, vol. 137, pp. 90–107, 2018.

[63] Y. Bao and T. Wierzbicki, "A comparative study on various ductile crack formation criteria," *Journal of Engineering Materials and Technology*, vol. 126, no. 3, pp. 314–324, 2004.

[64] Y. Bai and T. Wierzbicki, "A comparative study of three groups of ductile fracture loci in the 3D space," *Engineering Fracture Mechanics*, vol. 135, pp. 147–167, 2015.

[65] Y. Bai and T. Wierzbicki, "Application of extended Mohr-Coulomb criterion to ductile fracture," *International Journal of Fracture*, vol. 161, no. 1, pp. 1–20, 2010.

[66] Y. Lou, H. Huh, S. Lim, and K. Pack, "New ductile fracture criterion for prediction of fracture forming limit diagrams of sheet metals," *International Journal of Solids and Structures*, vol. 49, no. 25, pp. 3605–3615, 2012.

[67] L. Kachanov, "Time of the rupture process under creep conditions," *Izvestia Academii Nauk USSR Otd Tekh.*, 1958.

[68] L. Kachanov, *Introduction to Continuum Damage Mechanics*. Springer Science & Business Media, 1986.

[69] J.-L. Chaboche, "Continuous damage mechanics — A tool to describe phenomena before crack initiation," *Nuclear Engineering and Design*, vol. 64, no. 2, pp. 233–247, 1981.

[70] J.-L. Chaboche, "Anisotropic creep damage in the framework of continuum damage mechanics," *Nuclear Engineering and Design*, vol. 79, no. 3, pp. 309–319, 1984.

[71] J. Lemaitre, "How to use damage mechanics," *Nuclear Engineering and Design*, vol. 80, no. 2, pp. 233–245, 1984.

[72] J. Lemaitre, "Local approach of fracture," *Engineering Fracture Mechanics*, vol. 25, no. 5-6, pp. 523–537, 1986.

[73] J. Lemaitre and R. Desmorat, *Engineering Damage Mechanics*. Berlin Heidelberg New York: Springer, 2005.

[74] J. Lemaitre, "A continuous damage mechanics model for ductile fracture," *Journal of Engineering Materials and Technology*, vol. 107, no. 1, pp. 83–89, 1985.

[75] T. Cao, A. Gaillac, P. Montmitonnet, and P. Bouchard, "Identification methodology and comparison of phenomenological ductile damage models via hybrid numerical-experimental analysis of fracture experiments conducted on a zirconium alloy," *International Journal of Solids and Structures*, vol. 50, no. 24, pp. 3984–3999, 2013.

[76] T. Cao, J. Gachet, P. Montmitonnet, and P. Bouchard, "A Lode-dependent enhanced Lemaitre model for ductile fracture prediction at low stress triaxiality," *Engineering Fracture Mechanics*, vol. 124-125, pp. 80–96, 2014.

[77] J. Lian, Y. Feng, and S. Münstermann, "A modified Lemaitre damage model phenomenologically accounting for the Lode angle effect on ductile fracture," *Procedia Materials Science*, vol. 3, pp. 1841–1847, 2014.

[78] P. Bouchard, L. Bourgeon, S. Fayolle, and K. Mocellin, "An enhanced Lemaitre model formulation for materials processing damage computation," *International Journal of Material Forming*, vol. 4, no. 3, pp. 299–315, 2011.

[79] W. Tai and B. Yang, "A new microvoid-damage model for ductile fracture," *Engineering Fracture Mechanics*, vol. 25, no. 3, pp. 377–384, 1986.

[80] W. Tai, "Plastic damage and ductile fracture in mild steels," vol. 37, no. 4, pp. 853–880, 1990.

[81] T. Wang, "A continuum damage model for ductile fracture of weld heat affected zone," *Engineering Fracture Mechanics*, vol. 40, no. 6, pp. 1075–1082, 1991.

[82] S. Chandrakanth and P. Pandey, "A new ductile damage evolution model," *International Journal of Fracture*, vol. 60, no. 5, pp. 73–76, 1993.

[83] N. Bonora, "A nonlinear CDM model for ductile failure," *Engineering Fracture Mechanics*, vol. 58, no. 1-2, pp. 11–28, 1997.

[84] C. Chow and J. Wang, "An anisotropic theory of continuum damage mechanics for ductile fracture," *Engineering Fracture Mechanics*, vol. 27, no. 5, pp. 547–558, 1987.

[85] N. Bonora, "On the effect of triaxial state of stress on ductility using nonlinear CDM model," *International Journal of Fracture*, vol. 88, no. 1968, pp. 359–371, 1998.

[86] G. Testa, A. Ruggiero, G. Iannitti, N. Bonora, and D. Gentile, "Modification of the Bonora damage model for shear failure," *Frattura ed Integritá Strutturale*, vol. 44, pp. 140–150, 2018.

[87] P. Bridgman, *Studies in Large Plastic Flow and Fracture*. Cambridge, Massachusetts: Harvard University Press, 2nd ed., 1964.

[88] J. Lemaitre and J. Dufailly, "Damage measurements," *Engineering Fracture Mechanics*, vol. 28, no. 5-6, pp. 643–661, 1987.

[89] N. Bonora, "Identification and measurement of ductile damage parameters," *The Journal of Strain Analysis for Engineering Design*, vol. 34, no. 6, pp. 463–478, 1999.

[90] N. Bonora, D. Gentile, and A. Pirondi, "Identification of the parameters of a non-linear continuum damage mechanics model for ductile failure in metals," *The Journal of Strain Analysis for Engineering Design*, vol. 39, no. 6, pp. 639–651, 2005.

[91] N. Bonora, A. Ruggiero, S. De Meo, D. Gentile, and L. Esposito, "A revised approach to damage measurement based on stiffness loss technique," *Proceedings of PVP2008*, pp. 1–5, 2008.

[92] N. Bonora, A. Ruggiero, D. Gentile, and S. De Meo, "Practical applicability and limitations of the elastic modulus degradation technique for damage measurements in ductile metals," *Strain*, vol. 47, no. 3, pp. 241–254, 2011.

[93] M. Alves, J. Yu, and N. Jones, "On the elastic modulus degradation in continuum damage mechanics," *Computers & Structures*, vol. 76, no. 6, pp. 703–712, 2000.

[94] M. Alves, "Measurement of ductile material damage," *Mechanics of Structures and Machines*, vol. 29, no. 4, pp. 451–476, 2001.

[95] T. Wu, M. Coret, and A. Combescure, "Strain localisation and damage measurement by full 3D digital image correlation: Application to 15-5PH stainless steel," *Strain*, vol. 47, no. 1, pp. 49–61, 2011.

[96] C. Tasan, J. Hoefnagels, and M. Geers, "Identification of the continuum damage parameter: An experimental challenge in modeling damage evolution," *Acta Materialia*, vol. 60, no. 8, pp. 3581–3589, 2012.

[97] W. Oliver and G. Pharr, "An improved technique for determining hardness and elastic modulus using load and displacement sensing indentation experiments," *Journal of Materials Research*, vol. 7, no. 6, pp. 1564–1583, 1992.

[98] W. Oliver and G. Pharr, "Measurement of hardness and elastic modulus by instrumented indentation. Advances in understanding and refinements to methodology," *Materials Research Society*, vol. 19, no. 1, pp. 3–20, 2004.

[99] B. Guelorget, M. François, and J. Lu, "Microindentation as a local damage measurement technique," *Materials Letters*, vol. 61, no. 1, pp. 34–36, 2007.

[100] S. Zhang, Q. Xia, W. Li, and X. Zhou, "Ductile damage measurement and necking analysis of metal sheets based on digital image correlation and direct current potential drop methods," *International Journal of Damage Mechanics*, vol. 23, no. 8, pp. 1133–1149, 2014.

[101] D. Boccaccini and A. Boccaccini, "Dependence of ultrasonic velocity on porosity and pore shape in sintered materials," *Journal of Nondestructive Evaluation*, vol. 16, no. 4, pp. 1–6, 1997.

[102] K.-Y. Jhang, "Nonlinear ultrasonic techniques for non-destructive assessment of micro damage in material: a review," *International Journal of Precision Engineering and Manufacturing*, vol. 10, no. 1, pp. 123–135, 2009.

[103] L. Salvo, M. Suéry, A. Marmottant, N. Limodin, and D. Bernard, "3D imaging in material science: Application of X-ray tomography," *Comptes Rendus Physique*, vol. 11, no. 9-10, pp. 641–649, 2010.

[104] T. S. Cao, E. Maire, C. Verdu, C. Bobadilla, P. Lasne, P. Montmitonnet, and P. O. Bouchard, "Characterization of ductile damage for a high carbon steel using 3D X-ray micro-tomography and mechanical tests - Application to the identification of a shear modified GTN model," *Computational Materials Science*, vol. 84, pp. 175–187, 2014.

[105] C. Landron and E. Maire, "Validation of void growth models using X-ray micro-tomography characterization of damage in dual phase steels," *Acta Materialia*, vol. 59, no. 20, pp. 7564–7573, 2011.

[106] E. Maire, T. Morgeneyer, C. Landron, J. Adrien, and L. Helfen, "Bulk evaluation of ductile damage development using high resolution tomography and laminography," *Comptes Rendus Physique*, vol. 13, no. 3, pp. 328–336, 2012.

[107] N. Tada, Y. Hayashi, T. Kitamura, and R. Ohtani, "Analysis on the applicability of direct current electrical potential method to the detection of damage by multiple small internal cracks," *International Journal of Fracture*, vol. 85, pp. 1–9, 1997.

[108] J. Liu, G. Li, G. Liu, and X. Hao, "Damaged evaluation of ferrite ductile iron with electric resistance," *Materials Letters*, vol. 58, no. 6, pp. 1051–1055, 2004.

[109] J. Kumar, S. Padma, B. Srivathsa, N. Vyaghreswara Rao, and V. Kumar, "Evolution of damage in near $\alpha$ IMI-834 titanium alloy under monotonic loading condition: a continuum damage mechanics approach," *Journal of Engineering Materials and Technology*, vol. 131, no. 3, pp. 031012–1–031012–6, 2009.

[110] V. Brinnel, B. Döbereiner, and S. Münstermann, "Characterizing ductile damage and failure: application of the direct current potential drop method to uncracked tensile specimens," *Procedia Materials Science*, vol. 3, pp. 1161–1166, 2014.

[111] R. Farris, "Dilatation of granular filled elastomers under high rates of strain," *Journal of Applied Polymer Science*, vol. 8, pp. 25–35, 1964.

[112] J. Harding, *Effect of High Strain Rate on Material Properties*. Elsevier Applied Science, 1987.

[113] B. Hopkinson, "A method of measuring the pressure produced in the detonation of high explosives or by the impact of bullets," *Philosophical Transactions of the Royal Society A: Mathematical, Physical and Engineering Sciences*, vol. 213, pp. 437–456, 1914.

[114] R. Davies, "A critical study of the Hopkinson pressure bar," *Philosophical Transactions of the Royal Society A: Mathematical, Physical and Engineering Sciences*, vol. 240, pp. 375–457, 1948.

[115] G. Gray, "Classic Split Hopkinson Pressure Bar Technique," in *ASM V8 Mechanical Testing. ASM Handbook*, 1999.

[116] G. Taylor, "The use of flat-ended projectiles for determining dynamic yield stress. I. Theoretical considerations," *Proceedings of the Royal Society A: Mathematical, Physical and Engineering Sciences*, vol. 194, pp. 289–299, 1948.

[117] M. Cox, *Development of High Strain Rate Mechanical Testing for Metallic Materials*. Phd thesis, Imperial College London, 2013.

[118] J. Field, S. Walley, W. Proud, H. Goldrein, and C. Siviour, "Review of experimental techniques for high rate deformation and shock studies," *International Journal of Impact Engineering*, vol. 30, no. 7, pp. 725–775, 2004.

[119] ASTM (American Society for Testing and Materials), "Standard Specification for Chromium and Chromium-Nickel Stainless Steel Plate, Sheet, and Strip for Pressure Vessels and for General Applications," tech. rep., 2015.

[120] ASTM (American Society for Testing and Materials), "Standard Specification for Copper Sheet, Strip, Plate, and Rolled Bar," tech. rep., 2013.

[121] R. Thomson and J. Hancock, "Ductile failure by void nucleation, growth and coalescence," *International Journal of Fracture*, vol. 26, no. 2, pp. 99–112, 1984.

[122] K. Mogi, "Effect of the intermediate principal stress on rock failure," *Journal of Geophysical Research*, vol. 72, no. 20, pp. 5117–5131, 1967.

[123] M. Brünig, O. Chyra, D. Albrecht, L. Driemeier, and M. Alves, "A ductile damage criterion at various stress triaxialities," *International Journal of Plasticity*, vol. 24, no. 10, pp. 1731–1755, 2008.

[124] L. Malcher, F. Andrade Pires, and J. César De Sá, "An assessment of isotropic constitutive models for ductile fracture under high and low stress triaxiality," *International Journal of Plasticity*, vol. 30-31, pp. 81–115, 2012.

[125] A. Khan and H. Liu, "A new approach for ductile fracture prediction on Al 2024-T351 alloy," *International Journal of Plasticity*, vol. 35, pp. 1–12, 2012.

[126] D. Bonorchis, *Implementation of Material Models for High Strain Rate Applications as User-subroutines in Abaqus/Explicit*. MSc Thesis, University of Cape Town, 2003.

[127] A. Trujillo-Pino, K. Krissian, M. Alemán-Flores, and D. Santana-Cedrés, "Accurate subpixel edge location based on partial area effect," *Image and Vision Computing*, vol. 31, no. 1, pp. 72–90, 2013.

[128] J. Fitoussi, F. Meraghni, Z. Jendli, G. Hug, and D. Baptiste, "Experimental methodology for high strain-rates tensile behaviour analysis of polymer matrix composites," *Composites Science and Technology*, vol. 65, no. 14, pp. 2174–2188, 2005.

[129] M. Dongfang, C. Danian, W. Shanxing, W. Huanran, H. Yanjun, and C. Canyuan, "An interrupted tensile testing at high strain rates for pure copper bars," *Journal of Applied Physics*, vol. 108, no. 11, pp. 114902–1–114902–13, 2010.

[130] X. Yang, X. Xiong, Z. Yin, H. Wang, J. Wang, and D. Chen, "Interrupted test of advanced high strength steel with tensile split Hopkinson bar method," *Experimental Mechanics*, vol. 54, no. 4, pp. 641–652, 2014.

[131] T. S. DeSisto and F. Carr, "Low temperature mechanical properties of 300 series stainless steels and titanium," 1961.

[132] S. Park, S. Yoo, M. Kim, and J. Lee, "Strain-rate effects on the mechanical behavior of the AISI 300 series of austenitic stainless steel under cryogenic environments," *Materials and Design*, vol. 31, no. 8, pp. 3630–3640, 2010.

[133] K. Lee, M. Chun, M. Kim, and J. Lee, "A new constitutive model of austenitic stainless steel for cryogenic applications," *Computational Materials Science*, vol. 46, no. 4, pp. 1152–1162, 2009.

[134] C.-S. Lee, B.-M. Yoo, M.-H. Kim, and J.-M. Lee, "Viscoplastic damage model for austenitic stainless steel and its application to the crack propagation problem at cryogenic temperatures," *International Journal of Damage Mechanics*, vol. 22, no. 1, pp. 95–115, 2013.

[135] N. Bonora and P. Milella, "Constitutive modeling for ductile metals behevior incoporating strain rate, temperature and damage mechanics," *International Journal of Impact Engineering*, vol. 26, no. 1-10, pp. 53–64, 2001.

# Appendix A

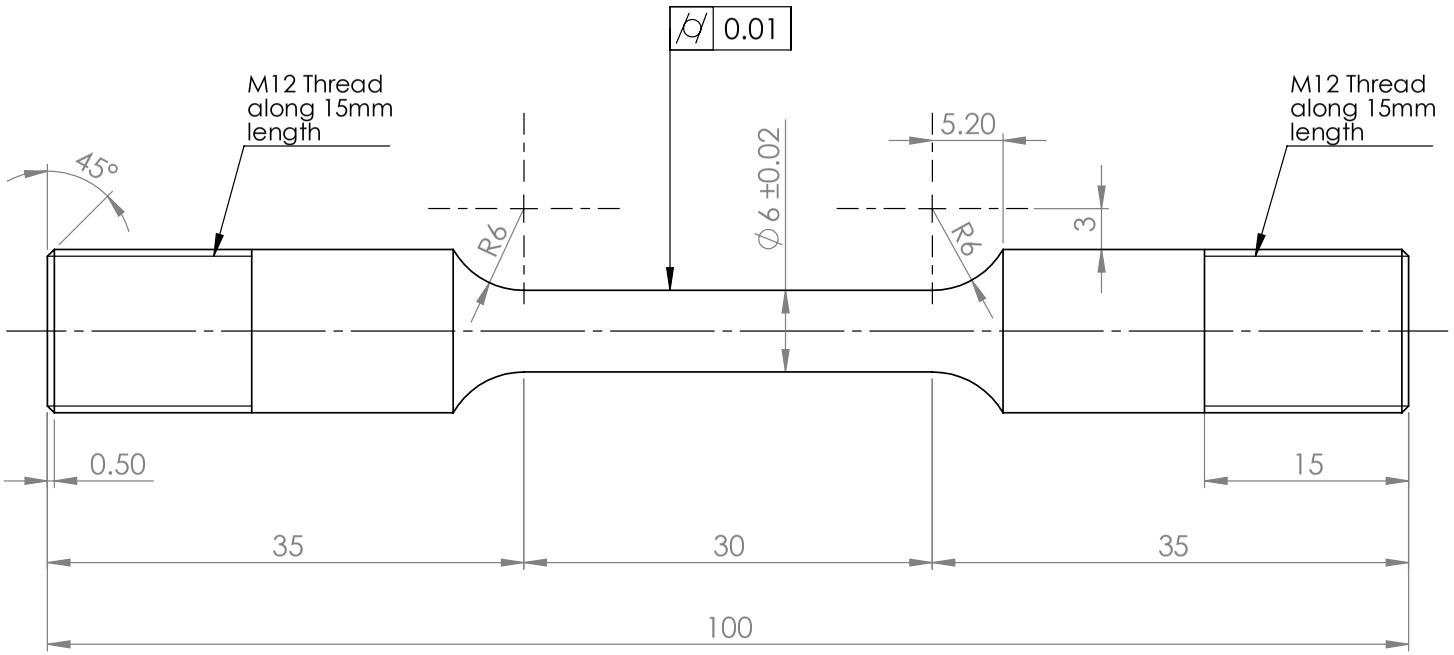
# Drawings

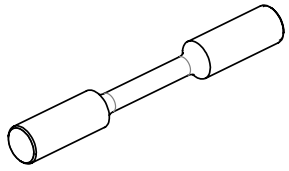
## A.1 Sample Drawings

The technical drawings of all the specimen geometries used in this research are presented in this appendix.

| Specimen drawing | Curvature, $\rho$ [mm] | Diameter, $2a$ [mm] |
|---|---|---|
| RB6 | $\infty$ | 6 |
| HGR6 | $\infty$ | 6 |
| HGF6 | $\infty$ | 6 x 3 |
| RNB6-1 | 8 | 4 |
| RNB6-2 | 8 | 5 |
| RNB6-3 | 6 | 5 |
| RNB6-4 | 3 | 5 |
| RNB6-5 | 2 | 5 |
| RNB6-6 | 1 | 5 |
| RB3.5 | $\infty$ | 3.5 |
| HGR3.5 | $\infty$ | 3.5 |
| RNB3.5-1 | 4 | 2.5 |
| RNB3.5-2 | 1.5 | 2.5 |
| RNB3.5-3 | 1 | 2.5 |
| RNB3.5-4 | 0.5 | 2.5 |

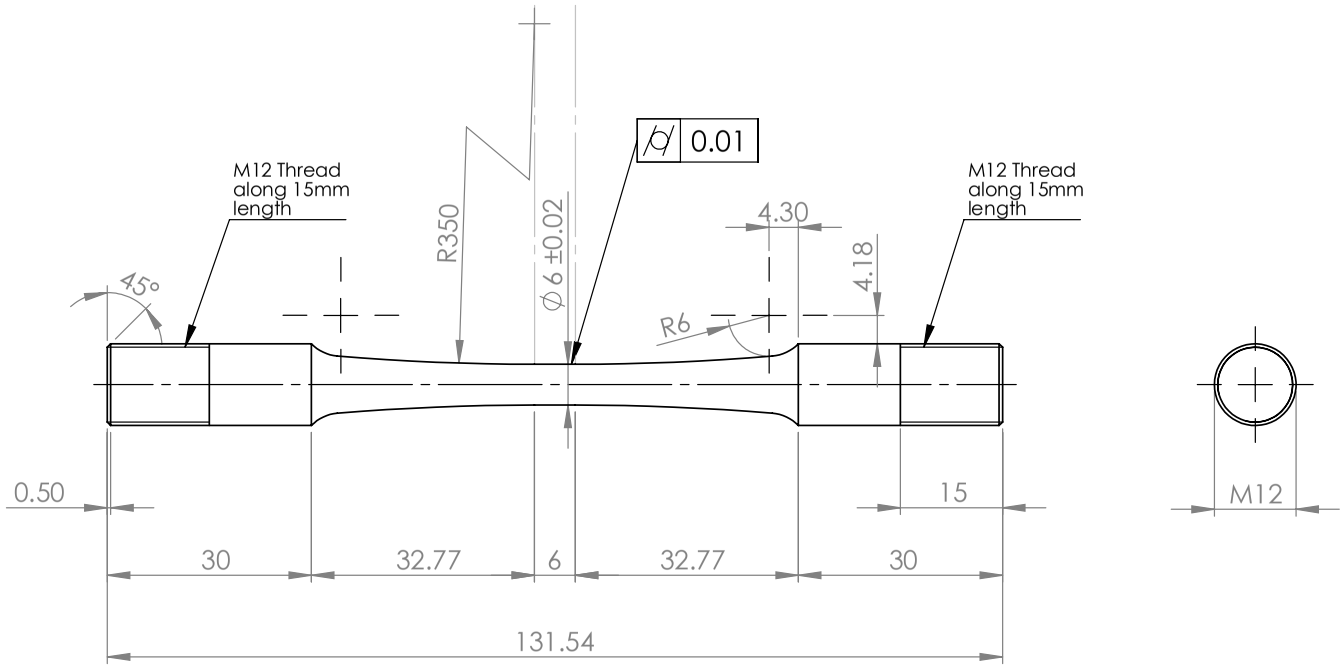
**Table A.1:** List of specimen drawings included in the appendix.

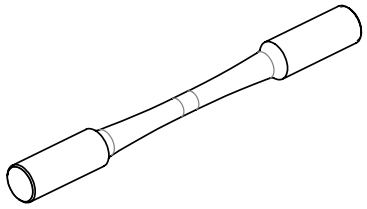


Isometric view - Scale 1:2

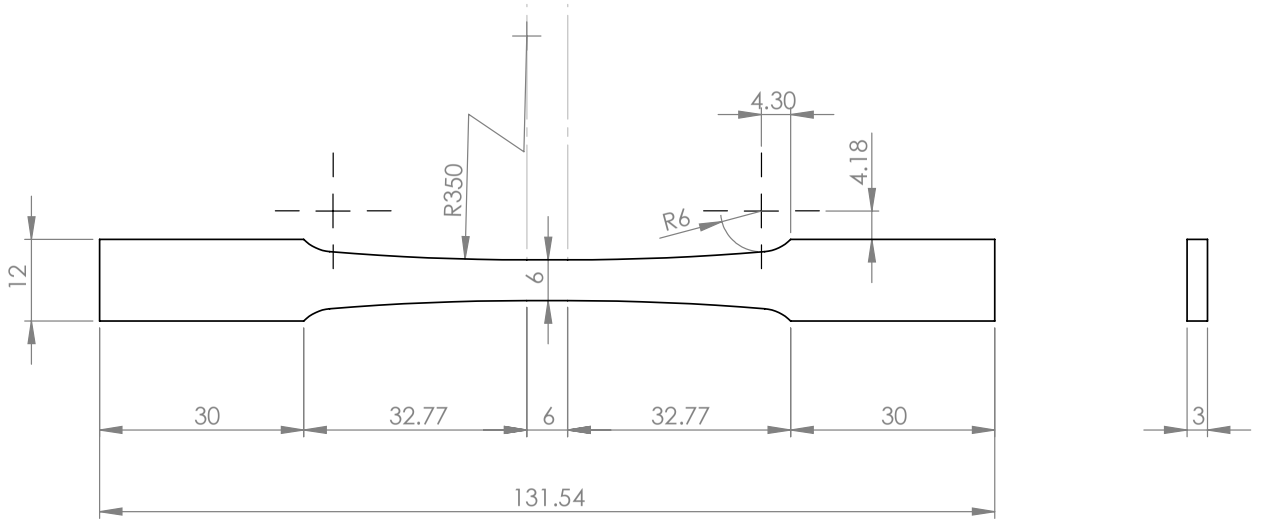
| | | | | | |
|---|---|---|---|---|---|
| UNLESS OTHERWISE SPECIFIED: DIMENSIONS ARE IN MILLIMETERS | | | Imperial College London | | TITLE: RB6 (gauge diameter = 6mm) |
| | NAME | SIGNATURE | DATE | MATERIAL: | |
| DRAWN | Alexander Sancho | | 9/11/16 | 304L stainless steel / C110 copper | A4 |
| | | | | SCALE 2:1 | SHEET 1 OF 1 |

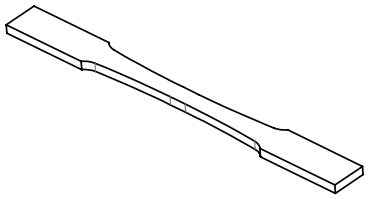


Isometric view - Scale 1:2

| | | | | | |
|---|---|---|---|---|---|
| UNLESS OTHERWISE SPECIFIED: DIMENSIONS ARE IN MILLIMETERS | | | Imperial College London | TITLE: HGR6 (gauge diameter = 6mm) | |
| | NAME | SIGNATURE | DATE | MATERIAL: | |
| DRAWN | Alexander Sancho | | 9/11/16 | 304L stainless steel / C110 copper | A4 |
| | | | | SCALE 1:1 | SHEET 1 OF 1 |



Isometric view - Scale 1:2

UNLESS OTHERWISE SPECIFIED:
DIMENSIONS ARE IN MILLIMETERS

Imperial College London

TITLE:

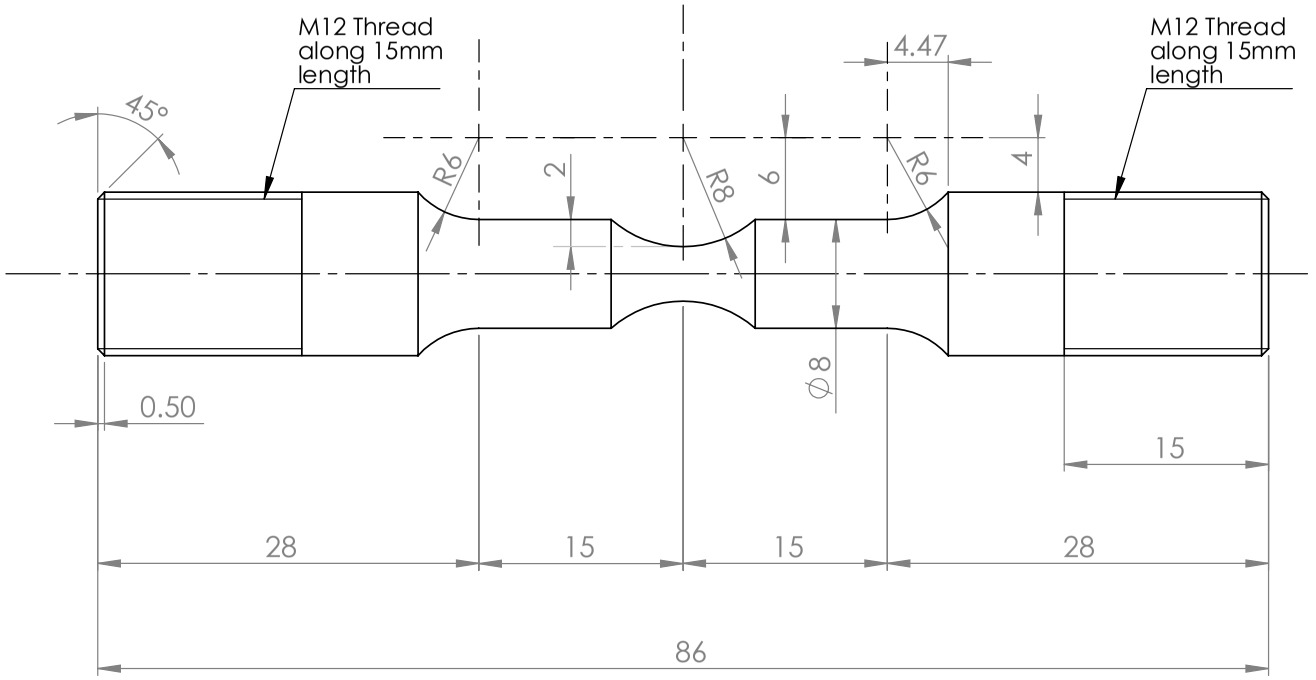
# HGF6
(gauge diameter = 6mm)

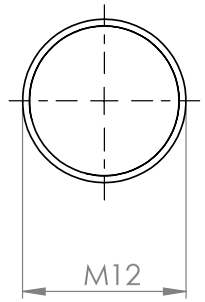
| | NAME | SIGNATURE | DATE | MATERIAL: |
|---|---|---|---|---|
| DRAWN | Alexander Sancho | | 29/5/15 | 304L stainless steel / C110 copper |

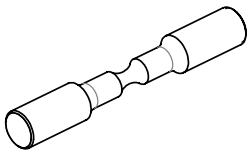
A4

SCALE 1:1

SHEET 1 OF 1

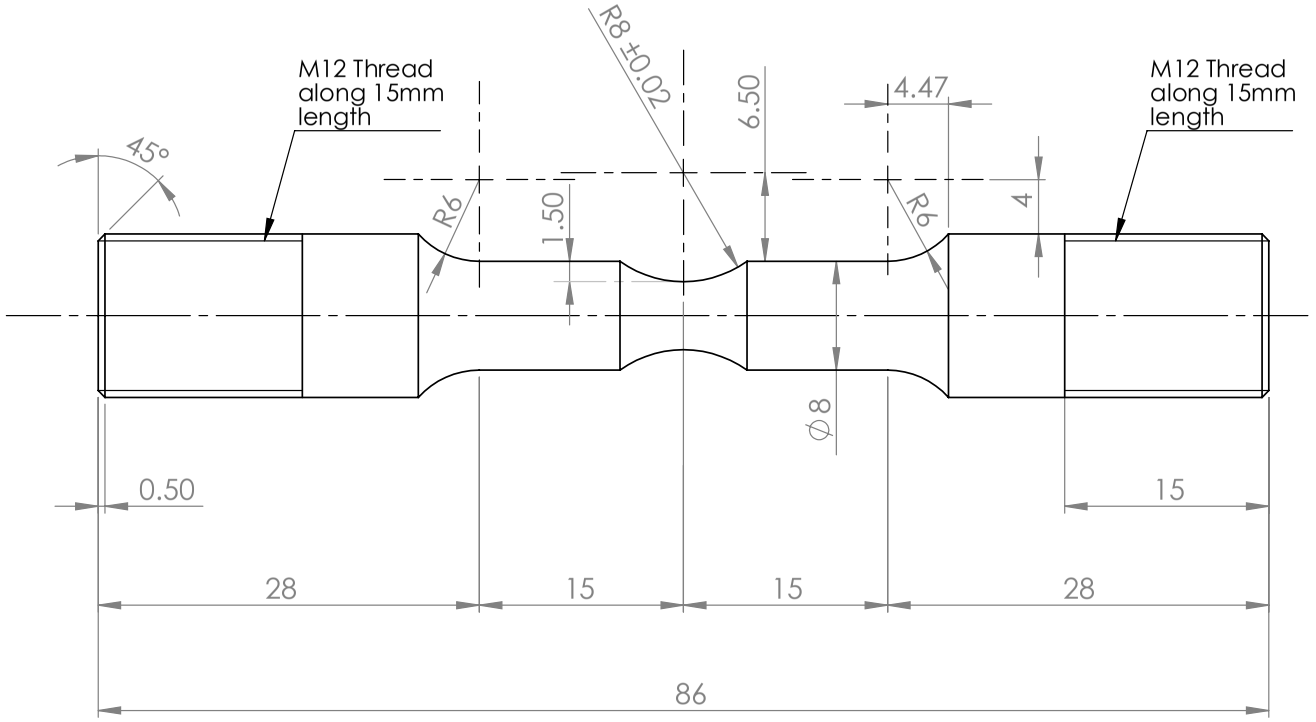


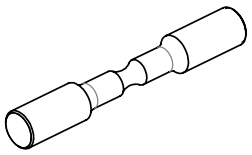



Isometric view - Scale 1:2

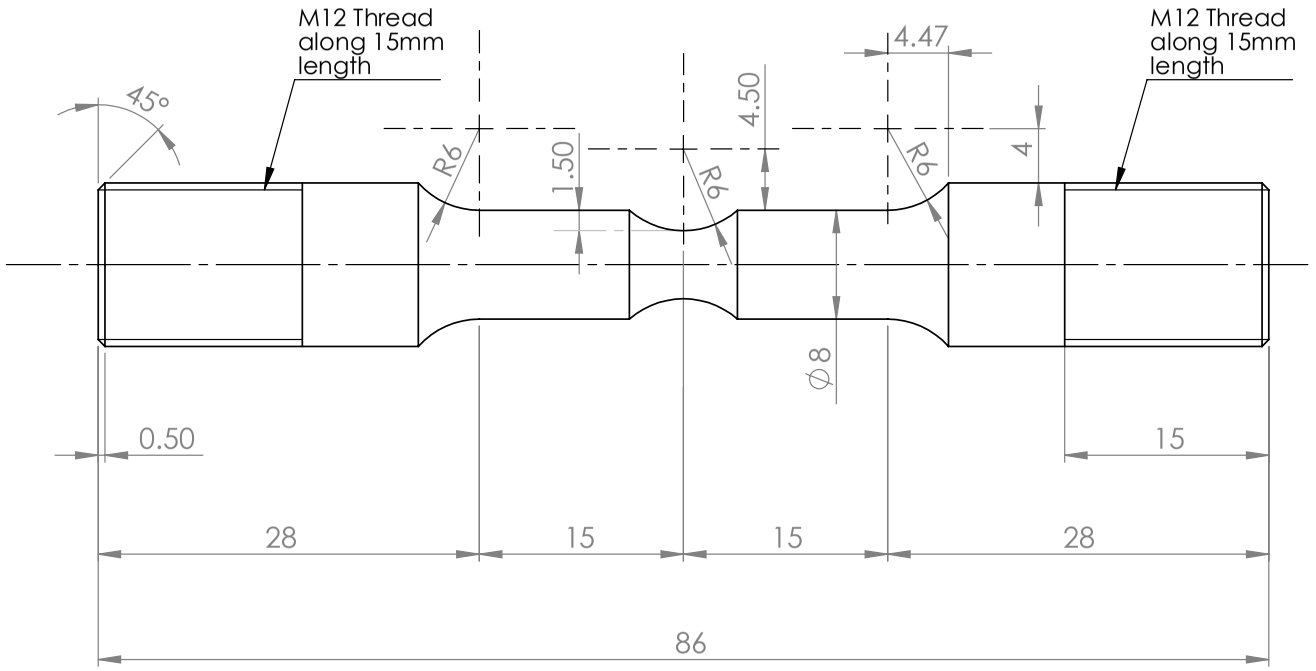
| | | | | | |
|---|---|---|---|---|---|
| UNLESS OTHERWISE SPECIFIED: DIMENSIONS ARE IN MILLIMETERS | | | Imperial College London | TITLE: RNB6-1 (gauge diameter = 4mm; notch curvature = 8mm) | |
| | NAME | SIGNATURE | DATE | MATERIAL: | |
| DRAWN | Alexander Sancho | | 05/5/16 | 304L stainless steel / C110 copper | A4 |
| | | | | SCALE 2:1 | SHEET 1 OF 1 |

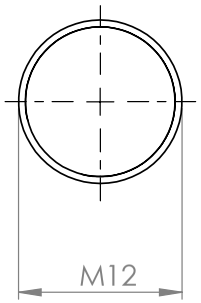


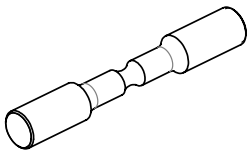



Isometric view - Scale 1:2

| | | | | | |
|---|---|---|---|---|---|
| UNLESS OTHERWISE SPECIFIED: DIMENSIONS ARE IN MILLIMETERS | | | Imperial College London | TITLE: RNB6-2 (gauge diameter = 5mm; notch curvature = 8mm) | |
| | NAME | SIGNATURE | DATE | MATERIAL: | |
| DRAWN | Alexander Sancho | | 9/11/16 | 304L stainless steel / C110 copper | A4 |
| | | | | SCALE 2:1 | SHEET 1 OF 1 |

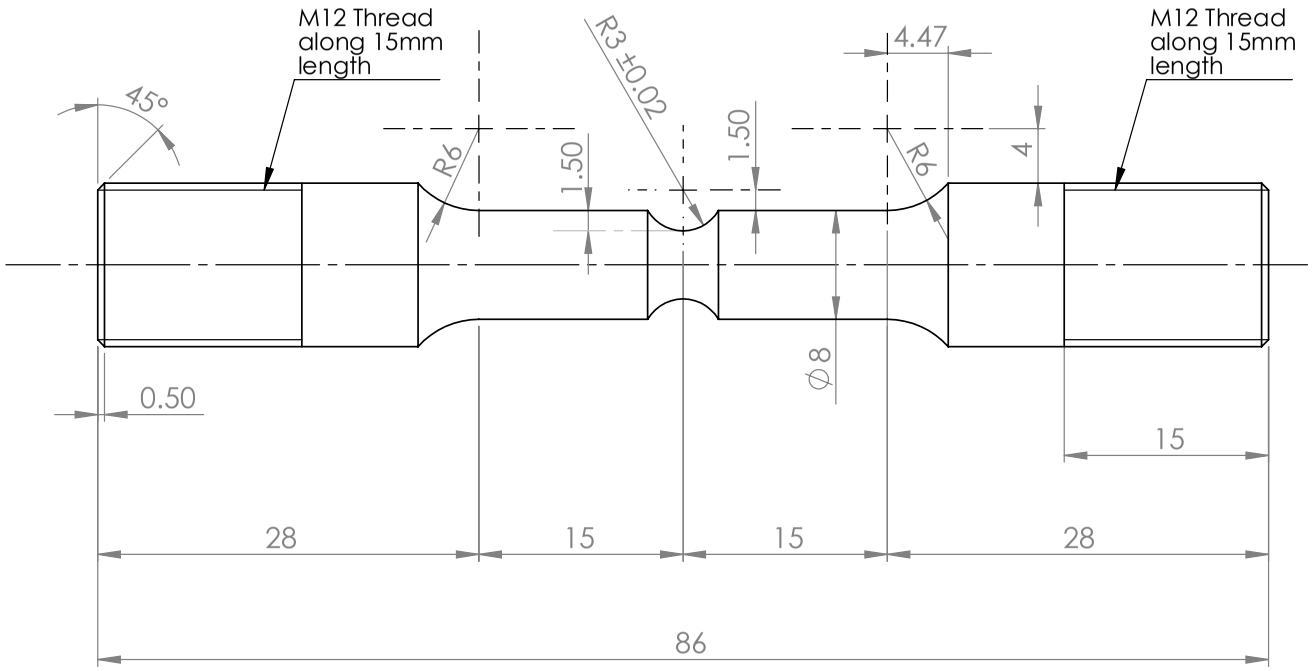


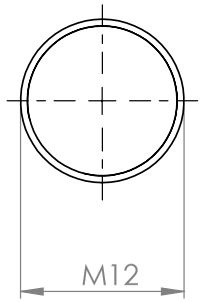



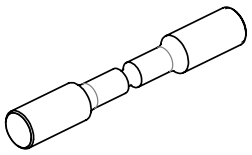



Isometric view - Scale 1:2

| | | | | | |
|---|---|---|---|---|---|
| UNLESS OTHERWISE SPECIFIED: DIMENSIONS ARE IN MILLIMETERS | | | Imperial College London | TITLE: RNB6-3 (gauge diameter = 5mm; notch curvature = 6mm) | |
| | NAME | SIGNATURE | DATE | MATERIAL: | |
| DRAWN | Alexander Sancho | | 05/5/16 | 304L stainless steel / C110 copper | A4 |
| | | | | SCALE 2:1 | SHEET 1 OF 1 |

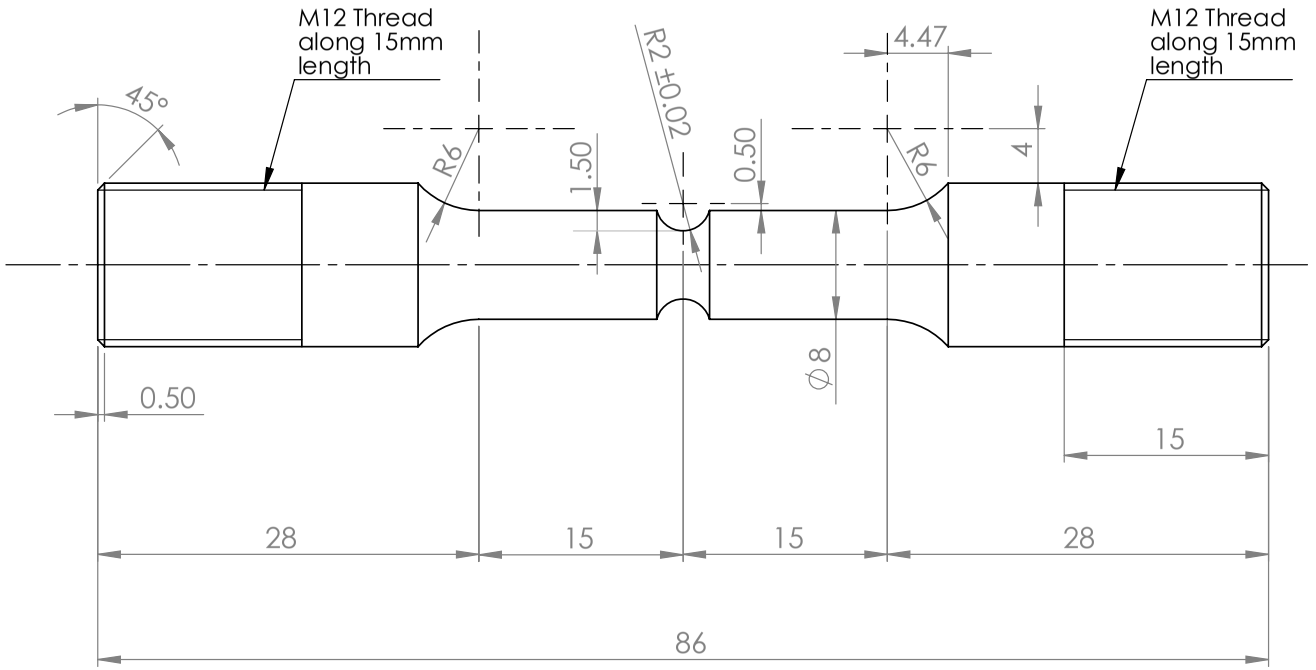


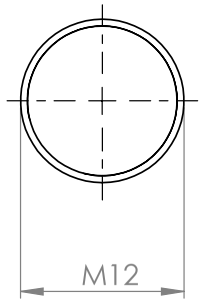



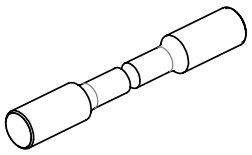



Isometric view - Scale 1:2

| | | | | | |
|---|---|---|---|---|---|
| UNLESS OTHERWISE SPECIFIED: DIMENSIONS ARE IN MILLIMETERS | | | Imperial College London | TITLE: RNB6-4 (gauge diameter = 5mm; notch curvature = 3mm) | |
| | NAME | SIGNATURE | DATE | MATERIAL: | |
| DRAWN | Alexander Sancho | | 9/11/16 | 304L stainless steel / C110 copper | A4 |
| | | | | SCALE 2:1 | SHEET 1 OF 1 |

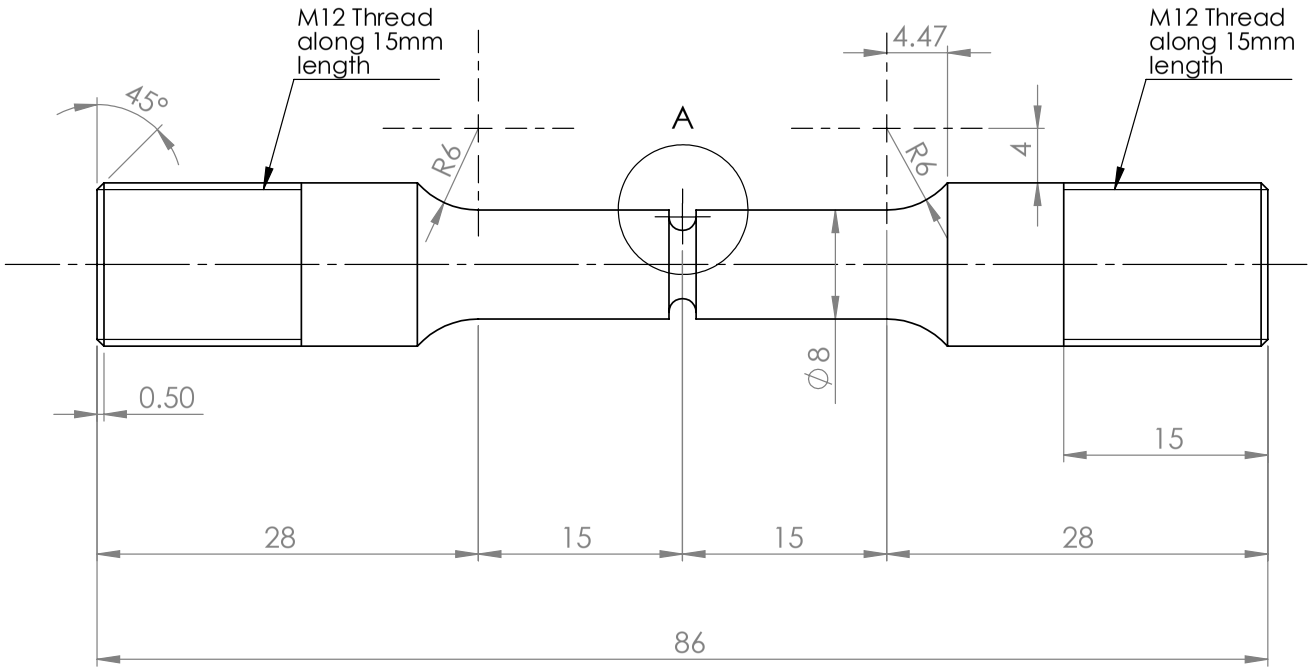


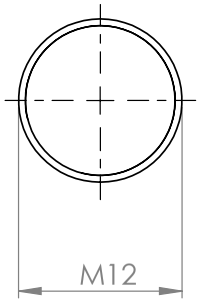



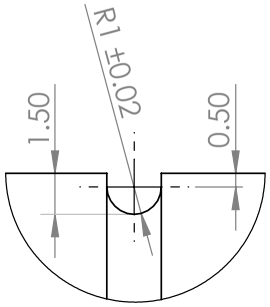



Isometric view - Scale 1:2

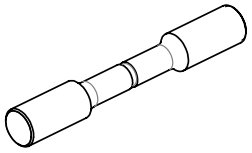
| | | | | | |
|---|---|---|---|---|---|
| UNLESS OTHERWISE SPECIFIED: DIMENSIONS ARE IN MILLIMETERS | | | Imperial College London | TITLE: RNB6-5 (gauge diameter = 5mm; notch curvature = 2mm) | |
| | NAME | SIGNATURE | DATE | MATERIAL: | |
| DRAWN | Alexander Sancho | | 9/11/16 | 304L stainless steel / C110 copper | A4 |
| | | | | SCALE 2:1 | SHEET 1 OF 1 |



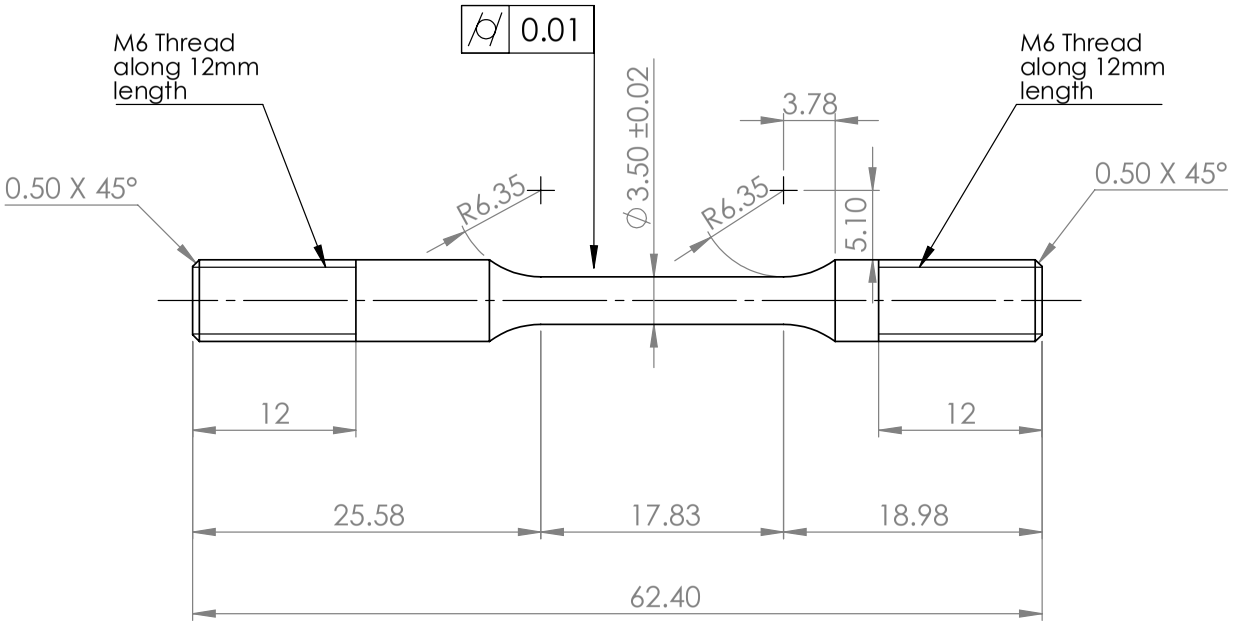



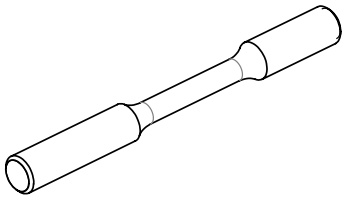

DETAIL A
SCALE 4 : 1



Isometric view - Scale 1:2

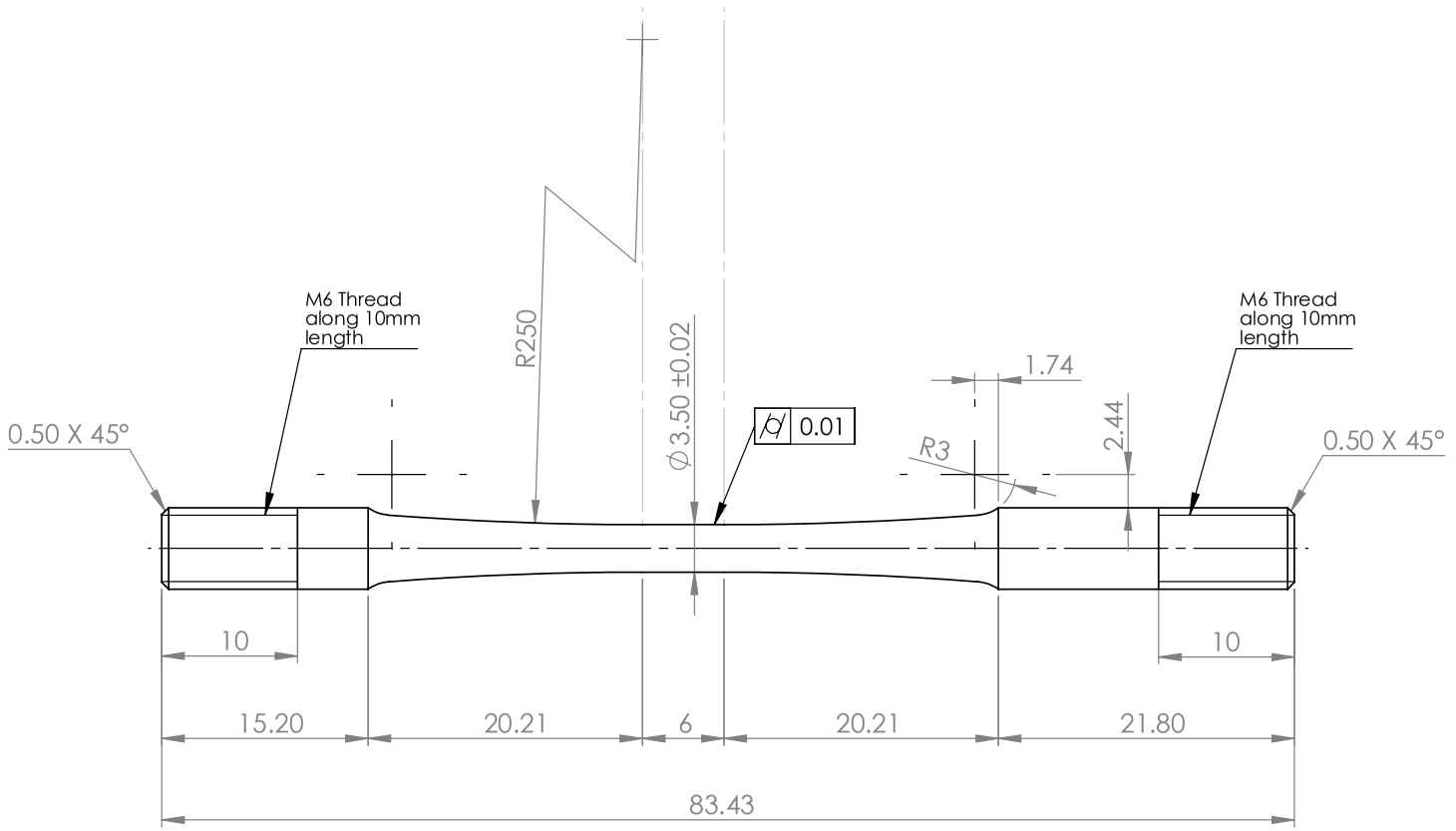
| | | | | | |
|---|---|---|---|---|---|
| UNLESS OTHERWISE SPECIFIED: DIMENSIONS ARE IN MILLIMETERS | | | Imperial College London | TITLE: RNB6-6 (gauge diameter = 5mm; notch curvature = 1mm) | |
| | NAME | SIGNATURE | DATE | MATERIAL: | |
| DRAWN | Alexander Sancho | | 9/11/16 | 304L stainless steel / C110 copper | A4 |
| | | | | SCALE 2:1 | SHEET 1 OF 1 |

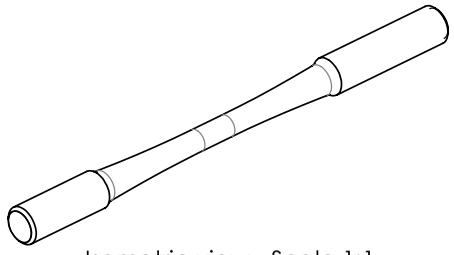


Isometric view - Scale 1:1

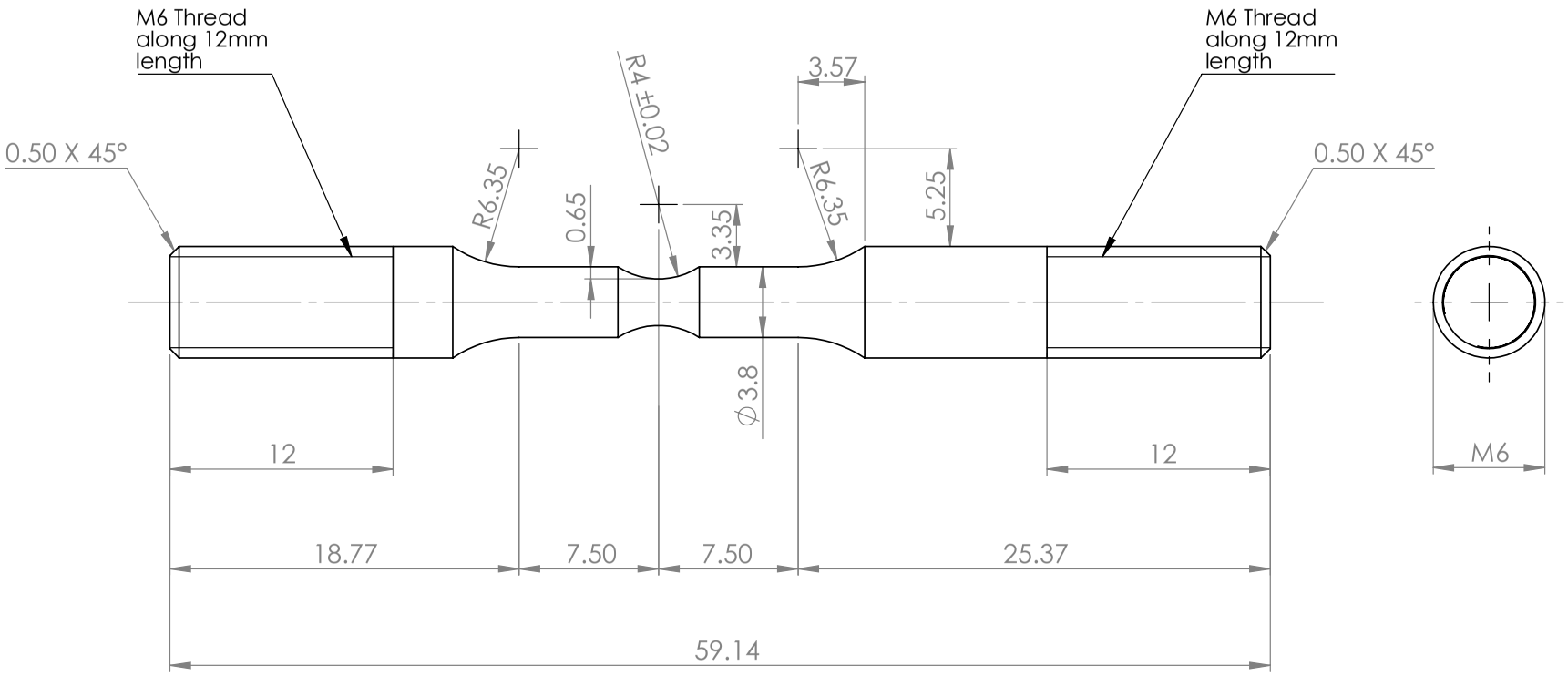
| | | | | | |
|---|---|---|---|---|---|
| UNLESS OTHERWISE SPECIFIED: DIMENSIONS ARE IN MILLIMETERS | | | Imperial College London | TITLE: RB3.5 (gauge diameter = 3.5mm) | |
| | NAME | SIGNATURE | DATE | MATERIAL: | |
| DRAWN | Alexander Sancho | | 9/11/16 | 304L stainless steel / C110 copper | A4 |
| | | | | SCALE 2:1 | SHEET 1 OF 1 |

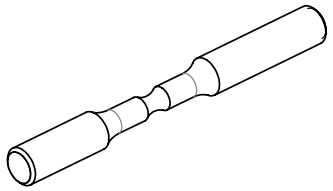


Isometric view - Scale 1:1

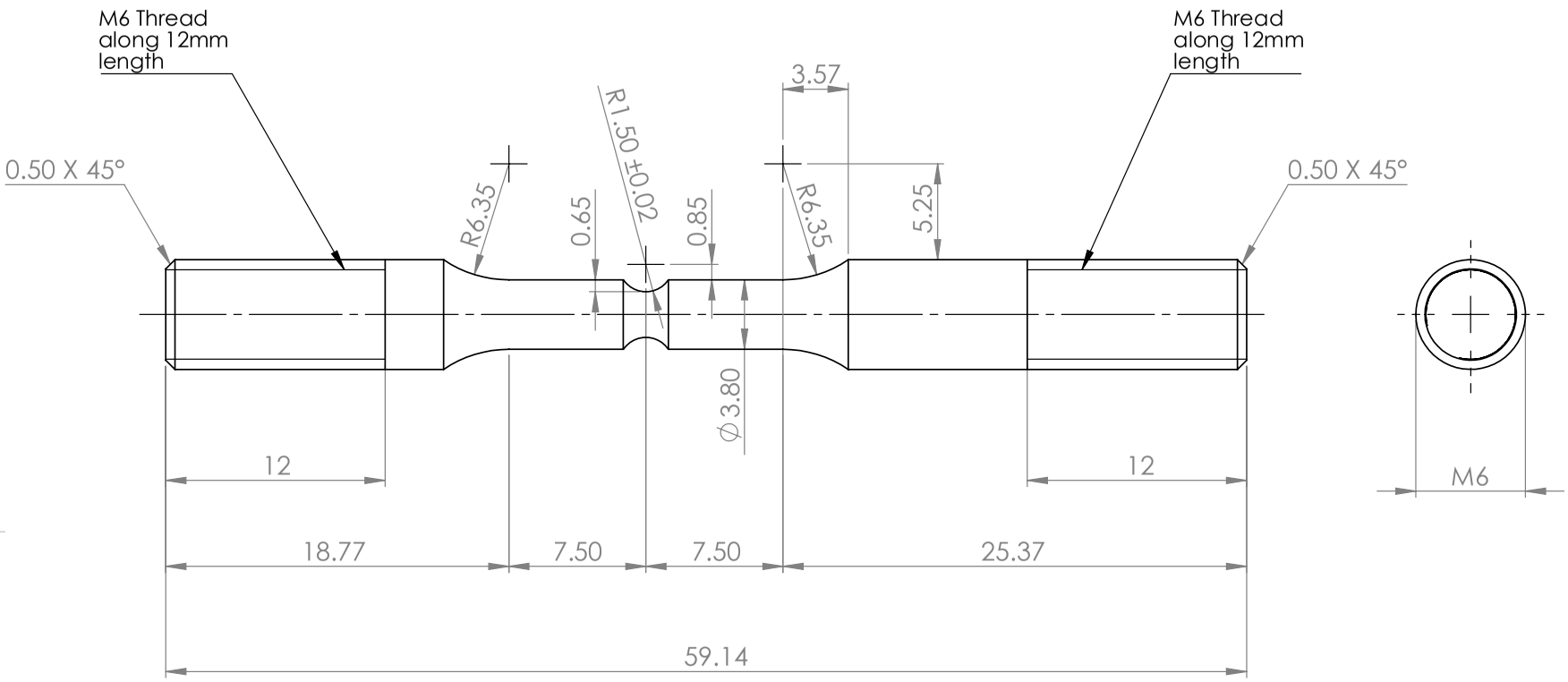
| | | | | | |
|---|---|---|---|---|---|
| UNLESS OTHERWISE SPECIFIED: DIMENSIONS ARE IN MILLIMETERS | | | Imperial College London | TITLE: HGR3.5 (gauge diameter = 3.5mm) | |
| | NAME | SIGNATURE | DATE | MATERIAL: | |
| DRAWN | Alexander Sancho | | 9/11/16 | 304L stainless steel / C110 copper | A4 |
| | | | | SCALE 2:1 | SHEET 1 OF 1 |

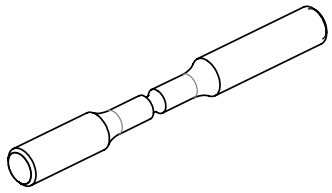


Isometric view - Scale 1:1

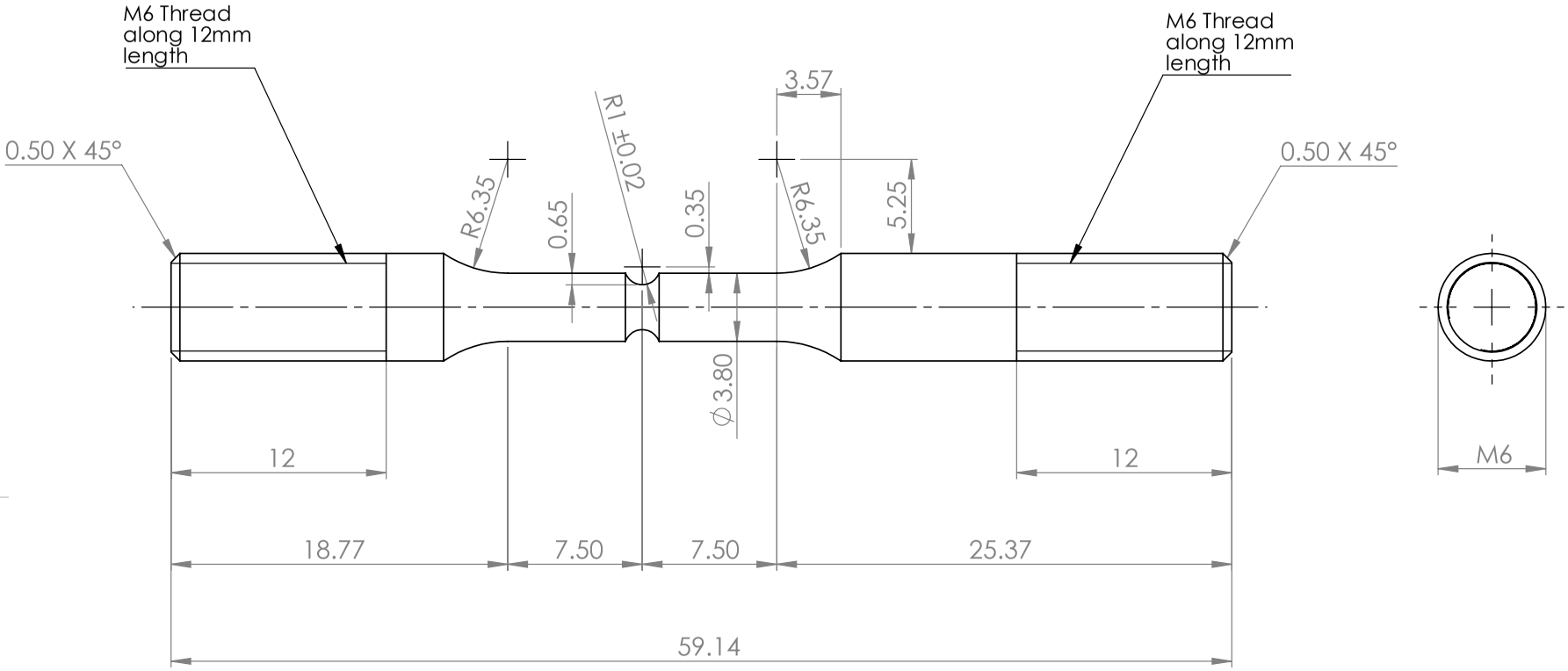
| | | | | | |
|---|---|---|---|---|---|
| UNLESS OTHERWISE SPECIFIED: DIMENSIONS ARE IN MILLIMETERS | | | Imperial College London | TITLE: RB3.5-1 (gauge diameter = 2.5mm; curvature = 4mm) | |
| | NAME | SIGNATURE | DATE | MATERIAL: | |
| DRAWN | Alexander Sancho | | 9/11/16 | 304L stainless steel / C110 copper | A4 |
| | | | | SCALE 3:1 | SHEET 1 OF 1 |

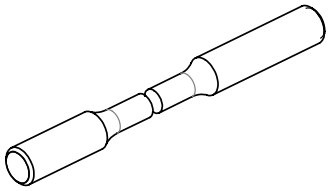


Isometric view - Scale 1:1

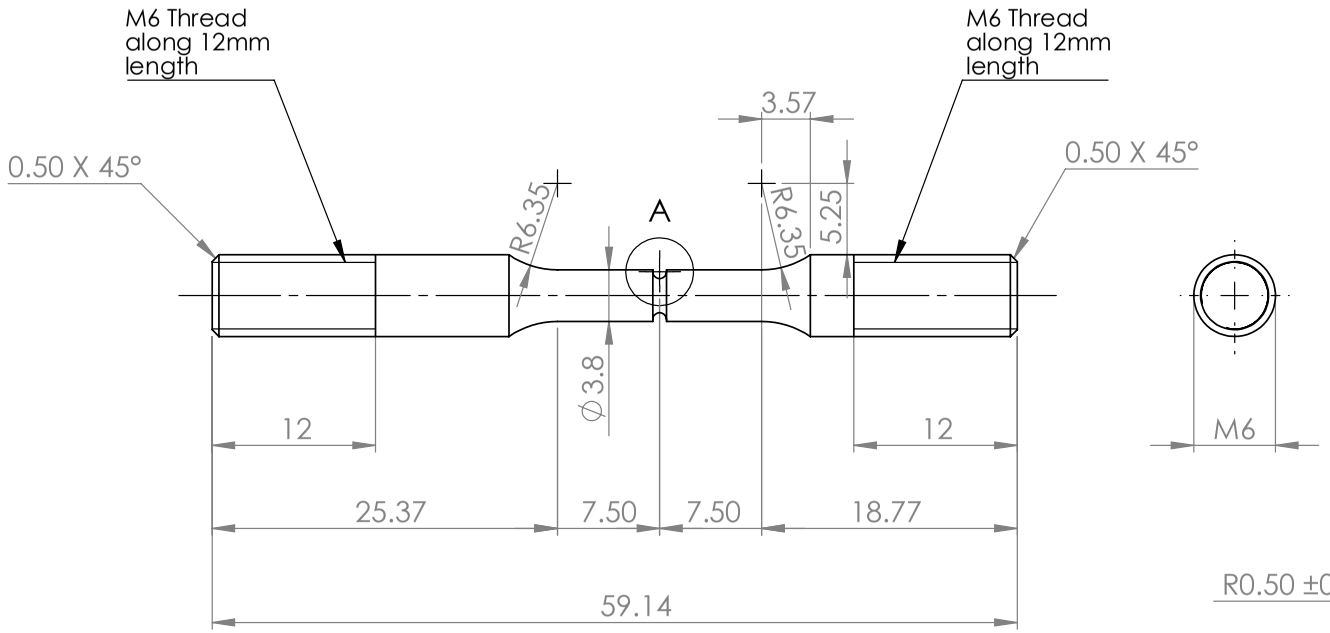
| | | | | | |
|---|---|---|---|---|---|
| UNLESS OTHERWISE SPECIFIED: DIMENSIONS ARE IN MILLIMETERS | | | Imperial College London | TITLE: RB3.5-2 (gauge diameter = 2.5mm; curvature = 1.5mm) | |
| | NAME | SIGNATURE | DATE | MATERIAL: | |
| DRAWN | Alexander Sancho | | 9/11/16 | 304L stainless steel / C110 copper | A4 |
| | | | | SCALE 3:1 | SHEET 1 OF 1 |

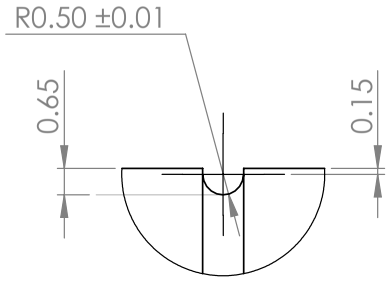


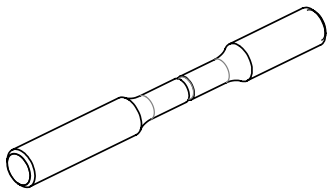
Isometric view - Scale 1:1

| | | | | | |
|---|---|---|---|---|---|
| UNLESS OTHERWISE SPECIFIED: DIMENSIONS ARE IN MILLIMETERS | | | Imperial College London | TITLE: RB3.5-3 (gauge diameter = 2.5mm; curvature = 1mm) | |
| | NAME | SIGNATURE | DATE | MATERIAL: | |
| DRAWN | Alexander Sancho | | 9/11/16 | 304L stainless steel / C110 copper | A4 |
| | | | | SCALE 3:1 | SHEET 1 OF 1 |




DETAIL A
SCALE 6 : 1



Isometric view - Scale 1:1

UNLESS OTHERWISE SPECIFIED:
DIMENSIONS ARE IN MILLIMETERS

Imperial College London

TITLE:

# RB3.5-4
(gauge diameter = 2.5mm;
curvature = 0.5mm)

| | NAME | SIGNATURE | DATE | MATERIAL: |
|---|---|---|---|---|
| DRAWN | Alexander Sancho | | 28/2/17 | 304L stainless steel / C110 copper |

A4

SCALE 2:1

SHEET 1 OF 1

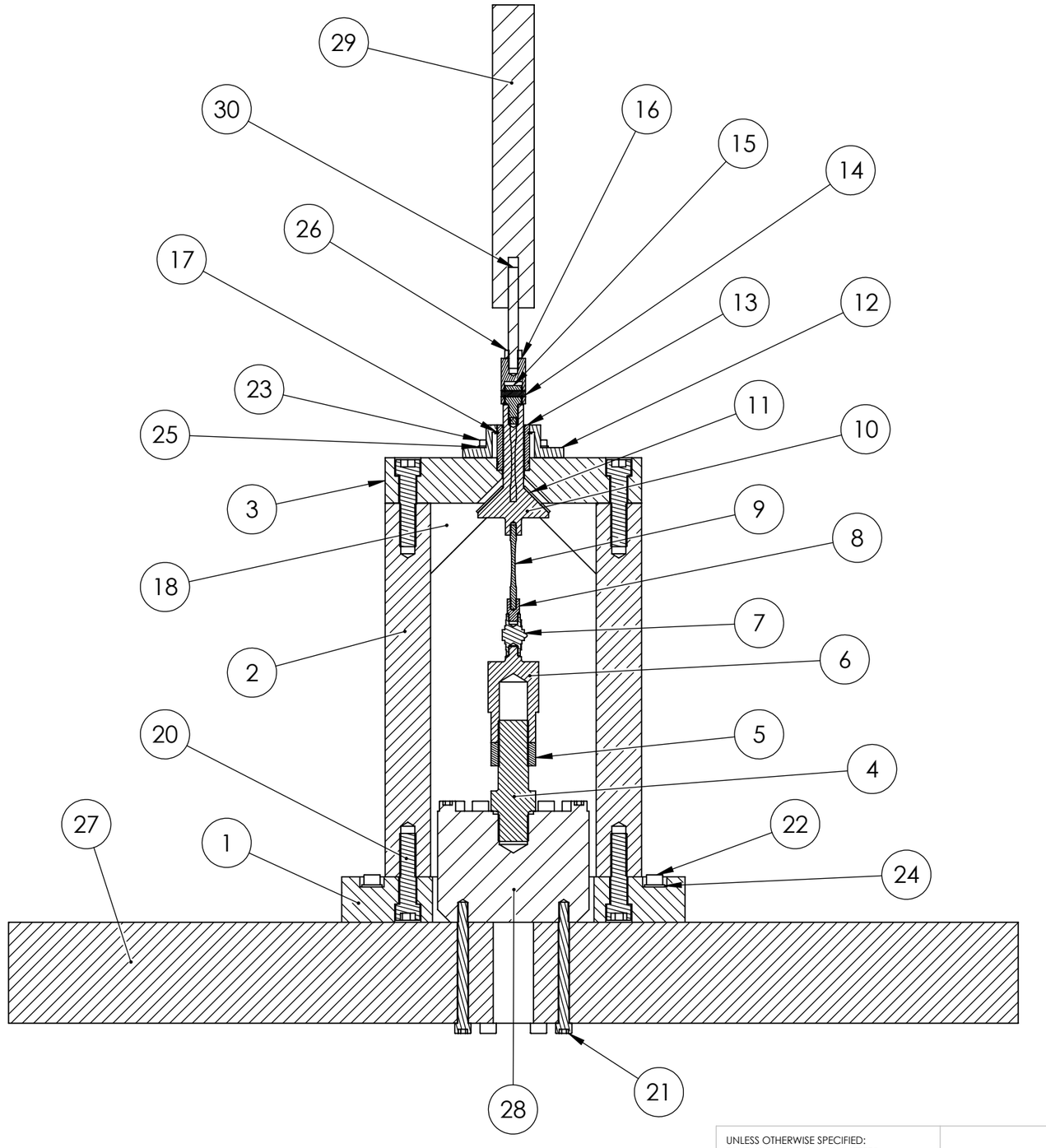
## A.2 Rig Drawings

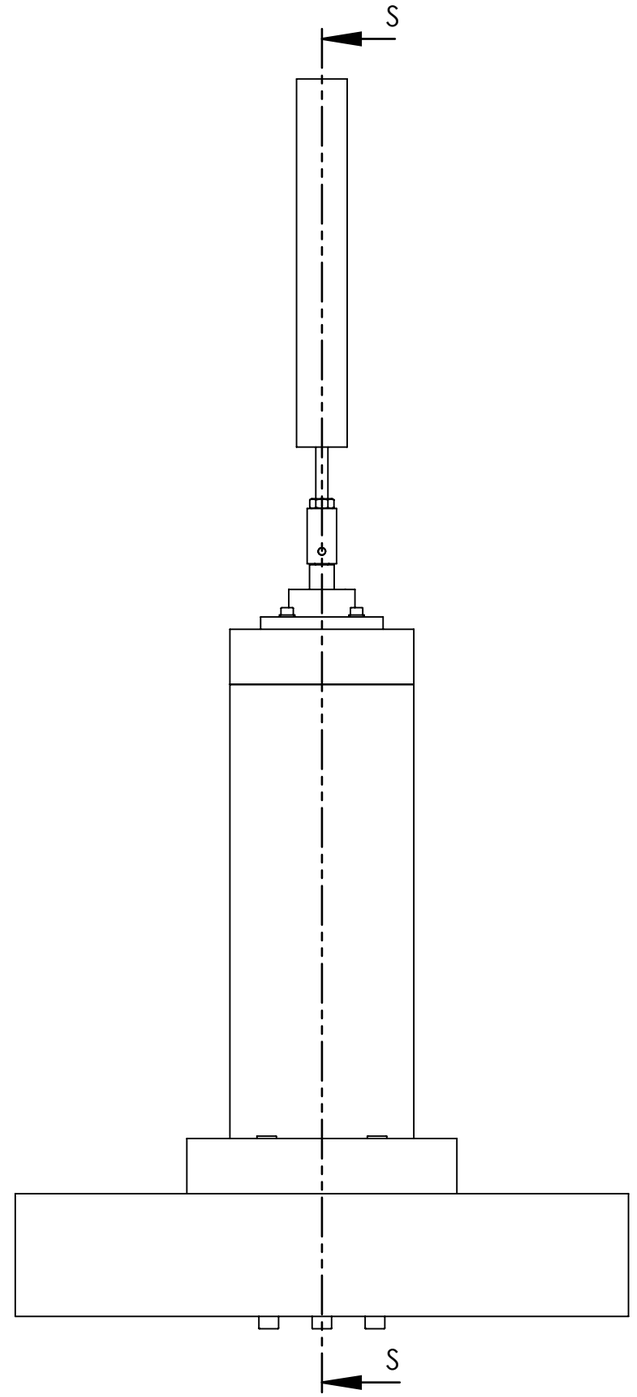
The drawings of the interrupted high-speed tensile experimental rig are presented in this appendix. A technical drawing of the assembly of the rig is firstly included and detail drawings of the main components are then presented.

| Item number | Part name |
|---|---|
| - | Rig assembly |
| 1 | Base |
| 2 | Column |
| 3 | Top |
| 4 | Length selector 2 |
| 6 | Length selector 1 |
| 10 | Conical part |
| 12 | Bearing housing |
| 14 | Shear pin |
| 15 | Shear pin adaptor 1 |
| 16 | Shear pin adaptor 2 |
| 18 | Reinforcing bracket |

**Table A.2:** List of rig part drawings included in the appendix.

| ITEM NO. | PART NUMBER | QTY. |
|---|---|---|
| 1 | Base | 1 |
| 2 | Column | 2 |
| 3 | Top | 1 |
| 4 | Length selector 2 | 1 |
| 5 | M30x2 nut | 1 |
| 6 | Length selector 1 | 1 |
| 7 | Piezo load cell | 1 |
| 8 | Load cell adapter | 1 |
| 9 | HGR-3.5 sample | 2 |
| 10 | Conical part | 1 |
| 11 | Rubber cone | 1 |
| 12 | Bearing housing | 1 |
| 13 | Bearing | 1 |
| 14 | Shear pin | 1 |
| 15 | Shear pin adaptor 1 | 1 |
| 16 | Shear pin adaptor 2 | 1 |
| 17 | Circlip bearing | 1 |
| 18 | Reinforcing bracket | 4 |
| 19 | 8x40 dowel pin | 6 |
| 20 | M16x70 bolt | 12 |
| 21 | M10x120 bolt | 6 |
| 22 | M10x50 bolt | 4 |
| 23 | M6x25 bolt | 20 |
| 24 | M10 washer | 4 |
| 25 | M6 washer | 20 |
| 26 | M10 nut | 1 |
| 27 | VHS Instron base | 1 |
| 28 | Load cell | 1 |
| 29 | Lost motion device | 1 |
| 30 | Lost motion device 2 | 1 |




UNLESS OTHERWISE SPECIFIED:
DIMENSIONS ARE IN MILLIMETERS

Imperial College London

TITLE:

# Interrupted High-Speed Rig

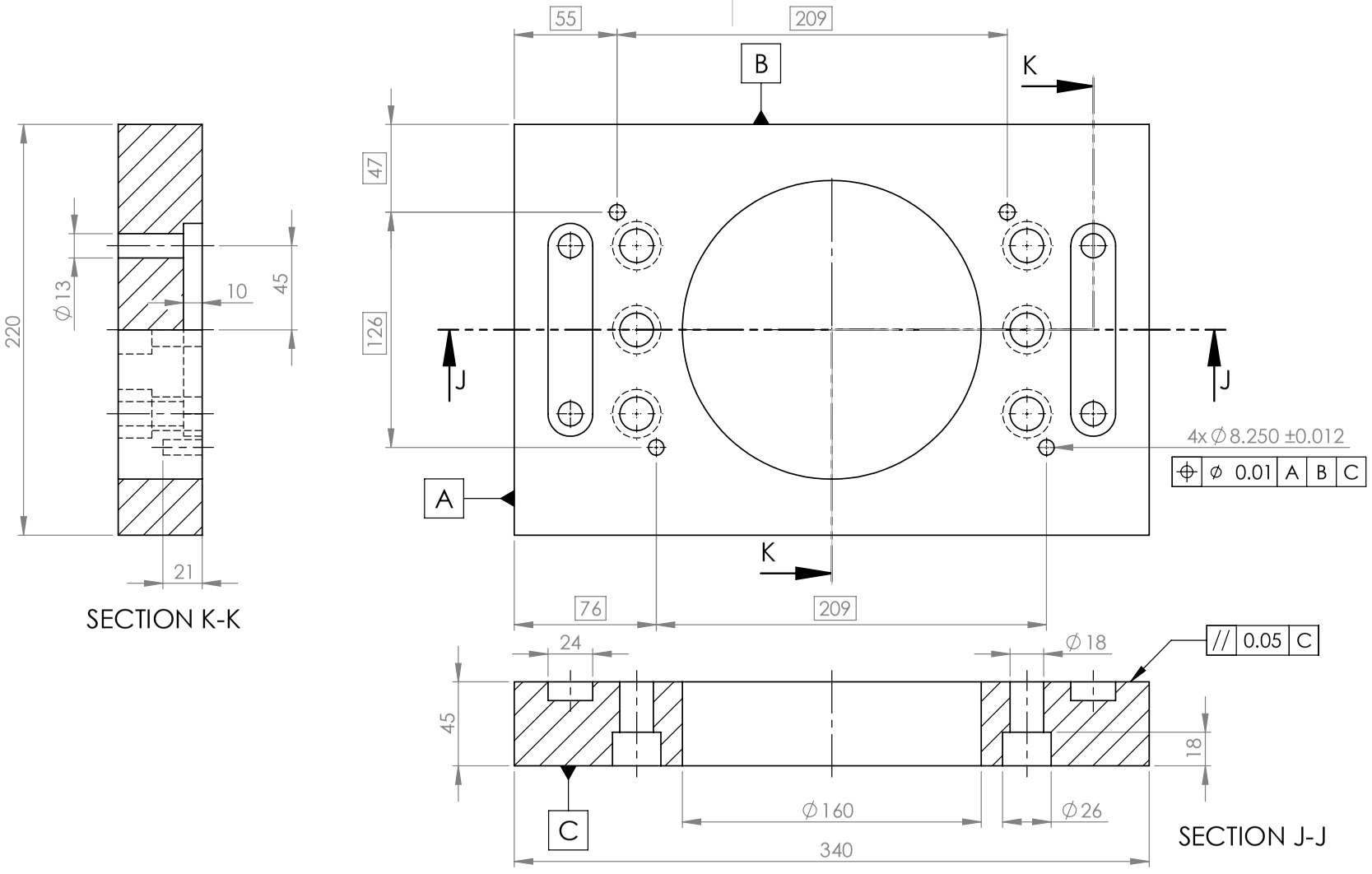
| | NAME | SIGNATURE | DATE |
|---|---|---|---|
| DRAWN | Alexander Sancho | | 09/09/16 |

Rig Assembly

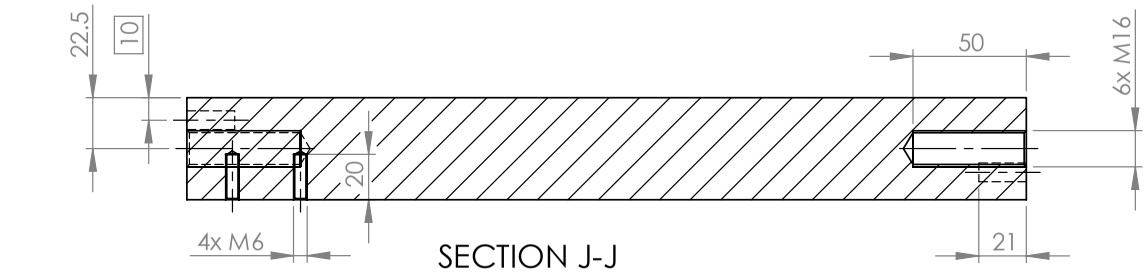
A3

SCALE 1:5

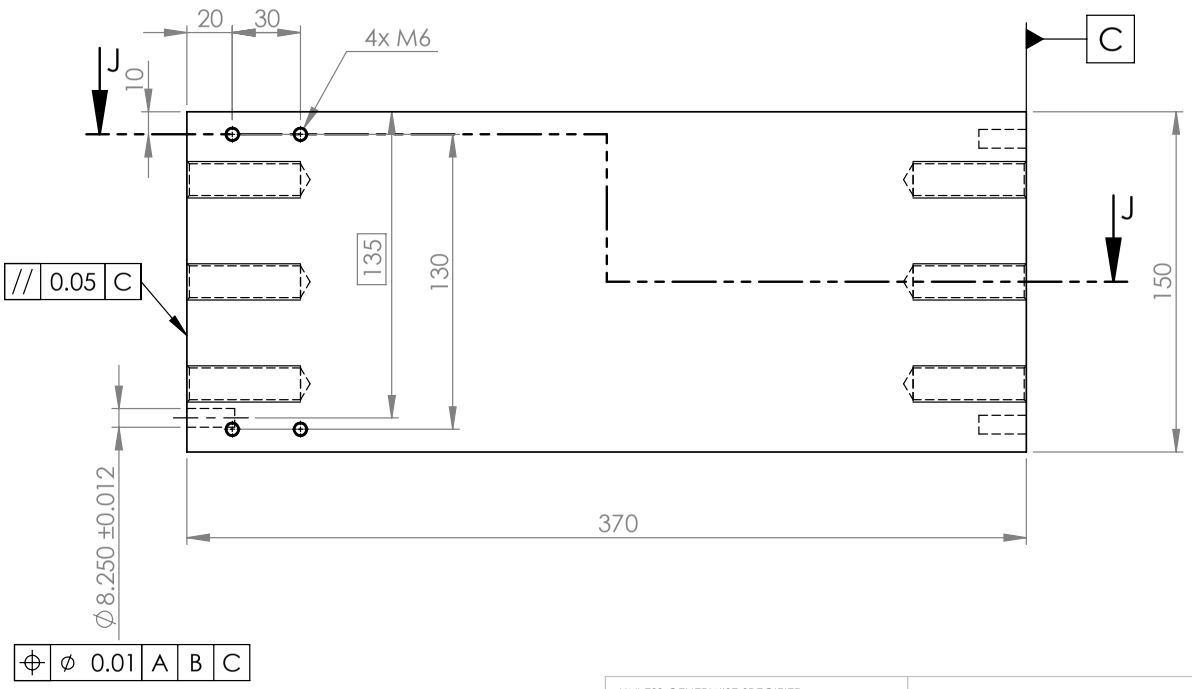
SHEET 1 OF 1

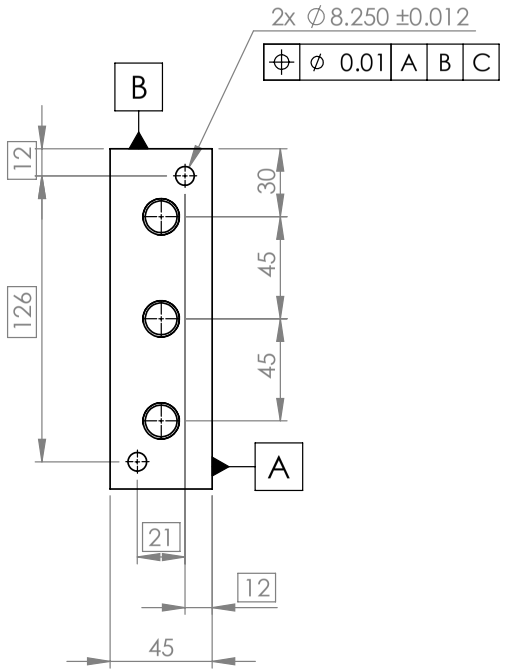



| | | | | | | |
|---|---|---|---|---|---|---|
| UNLESS OTHERWISE SPECIFIED: DIMENSIONS ARE IN MILLIMETERS | | | | Imperial College London | TITLE: Base (Interrupted high-speed rig) | |
| | NAME | SIGNATURE | DATE | MATERIAL: | ITEM NO. | |
| DRAWN | Alexander Sancho | | 02/09/16 | EN24T | 1 | A4 |
| | | | | | SCALE 1:3 | SHEET 1 OF 1 |

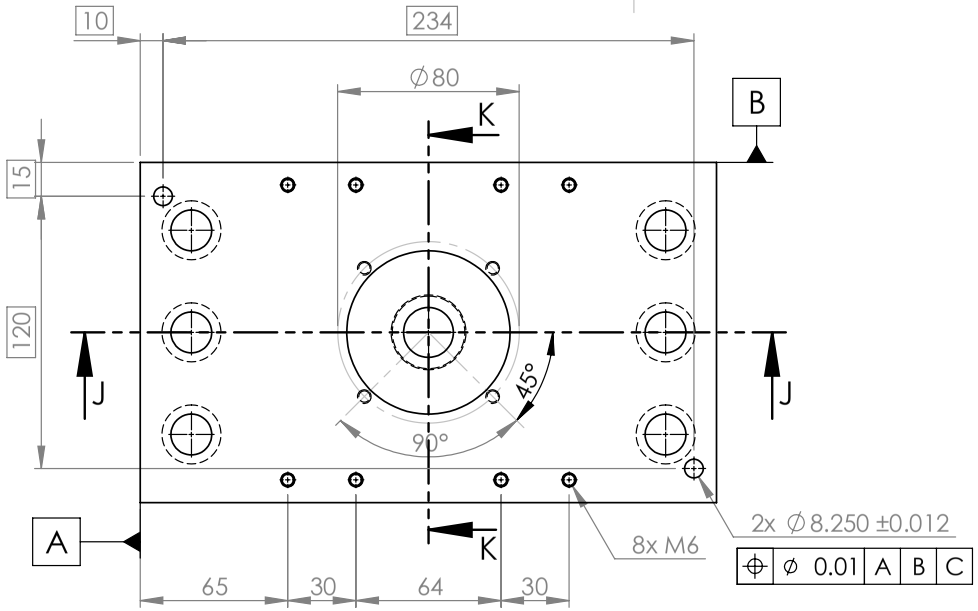


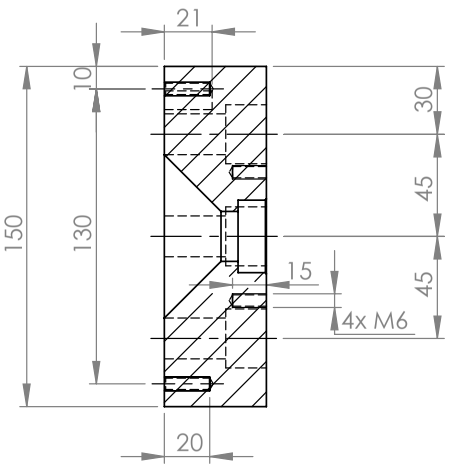

SECTION J-J



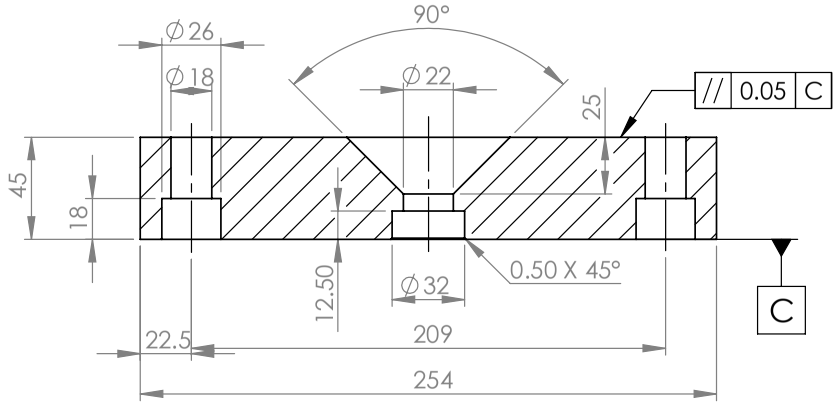




| | | | | | | |
|---|---|---|---|---|---|---|
| UNLESS OTHERWISE SPECIFIED: DIMENSIONS ARE IN MILLIMETERS | | | | Imperial College London | TITLE: Column (Interrupted high-speed rig) | |
| | NAME | SIGNATURE | DATE | MATERIAL: | ITEM NO. | A4 |
| DRAWN | Alexander Sancho | | 02/09/16 | EN24T | 2 | |
| | | | | | SCALE 1:3 | SHEET 1 OF 1 |




SECTION K-K




SECTION J-J

UNLESS OTHERWISE SPECIFIED:
DIMENSIONS ARE IN MILLIMETERS

Imperial College London

TITLE:
Top
(Interrupted high-speed rig)

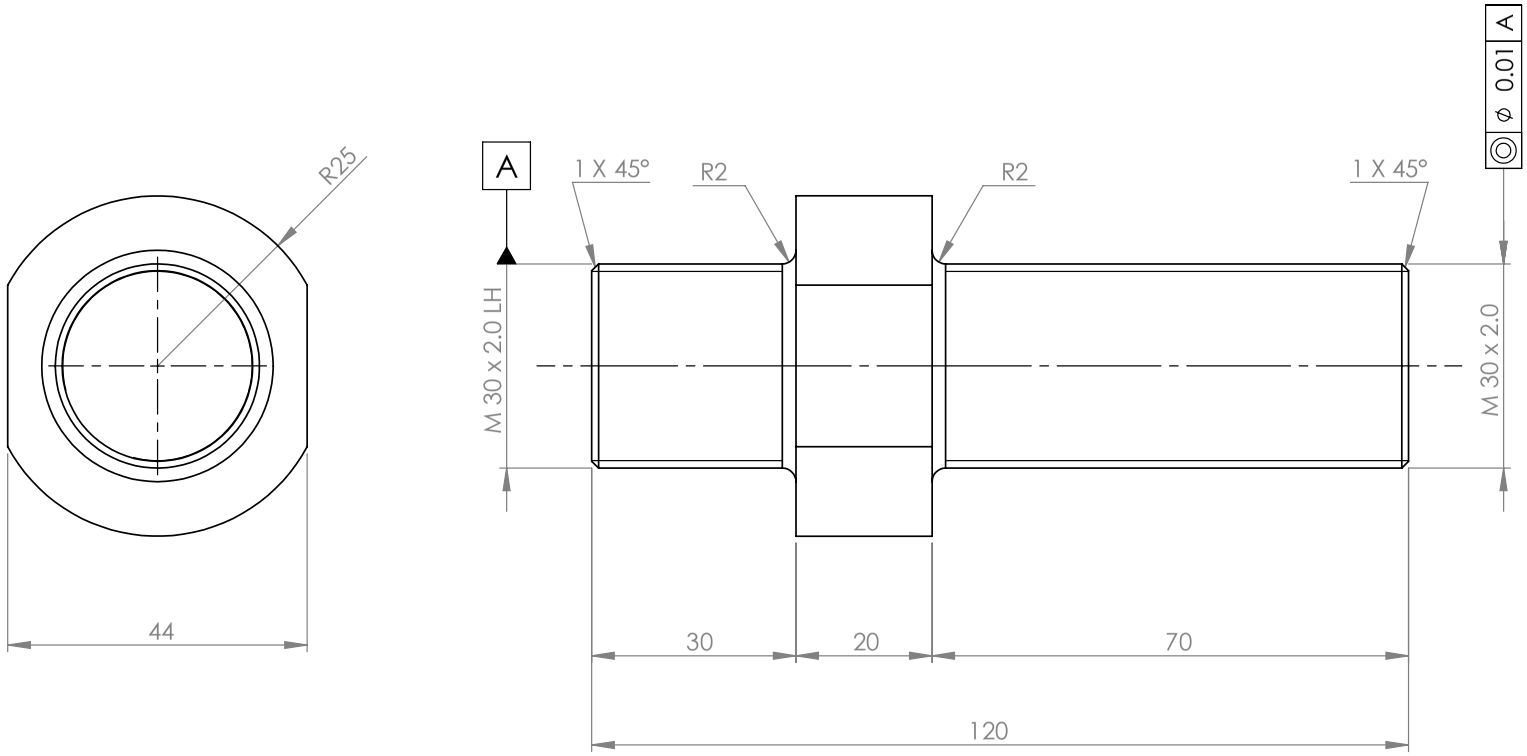
| | NAME | SIGNATURE | DATE | MATERIAL: |
|---|---|---|---|---|
| DRAWN | Alexander Sancho | | 09/09/16 | EN24T |

ITEM NO. 3

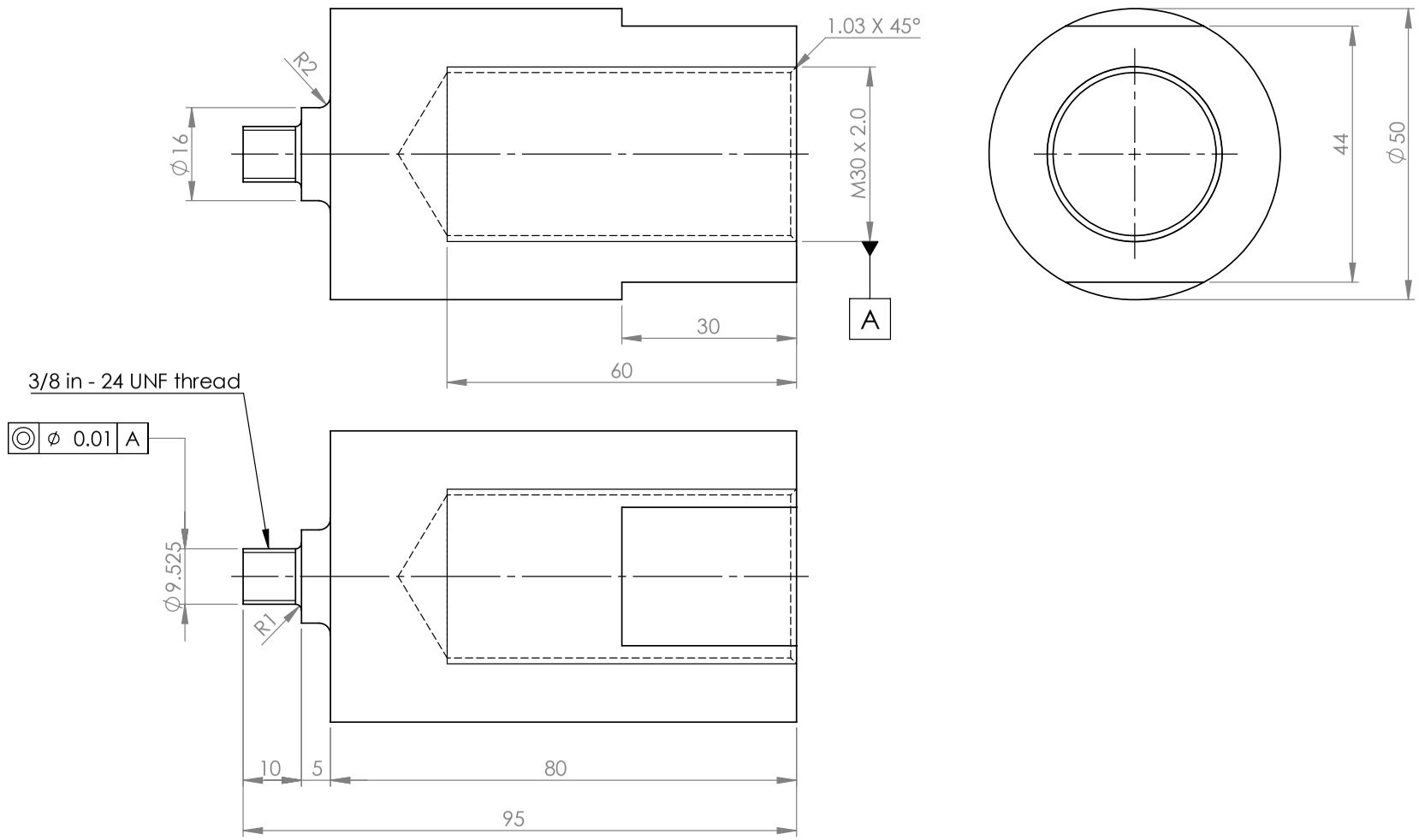
A4

SCALE 1:3

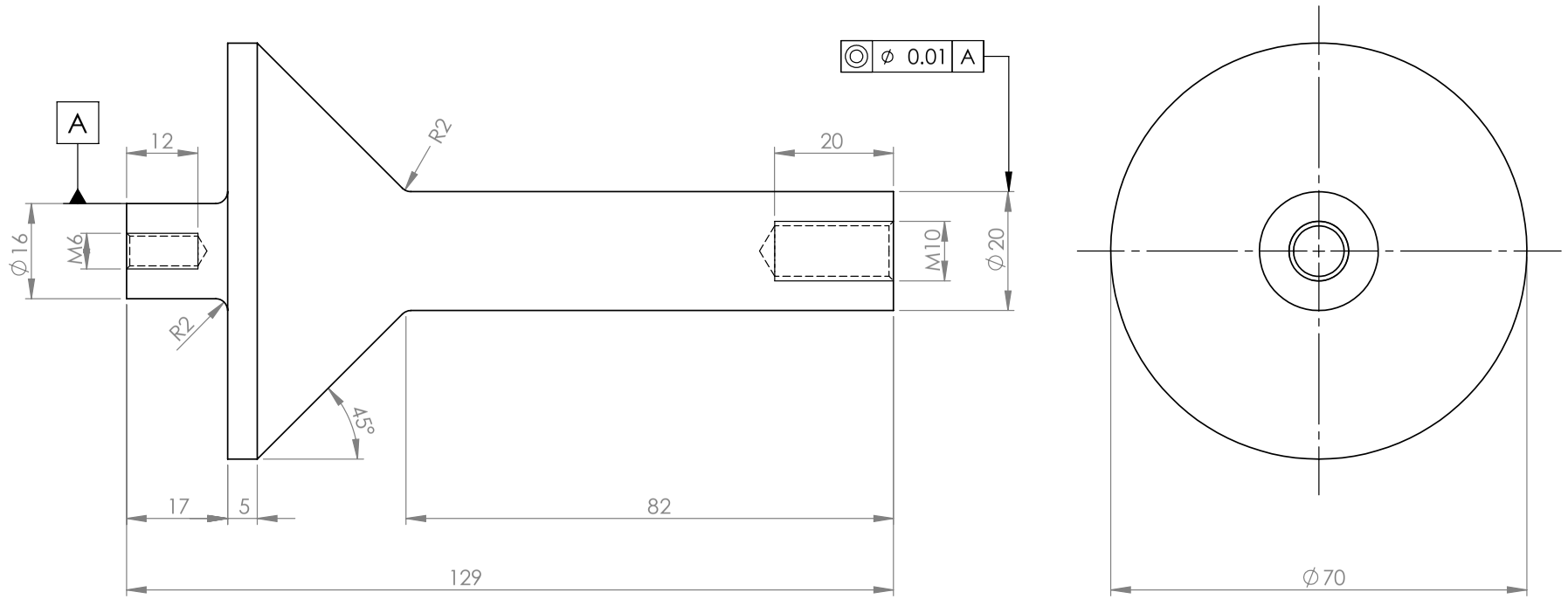
SHEET 1 OF 1



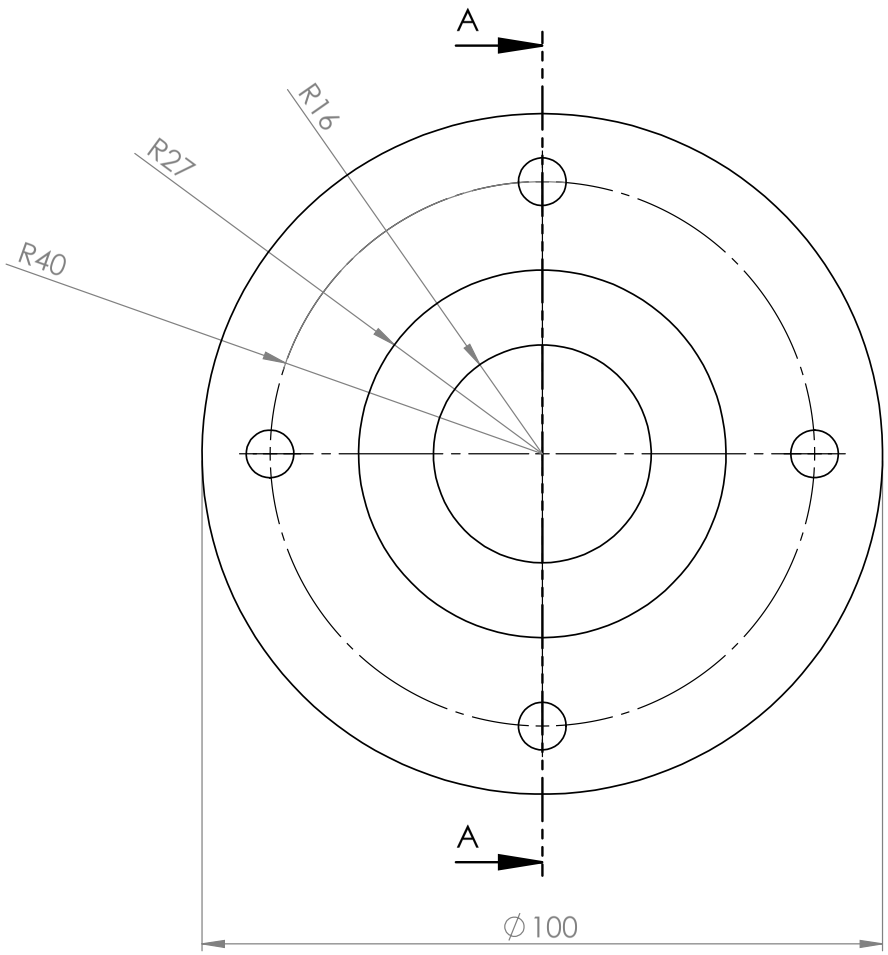

| | | | | | |
|---|---|---|---|---|---|
| UNLESS OTHERWISE SPECIFIED: DIMENSIONS ARE IN MILLIMETERS | | | Imperial College London | | TITLE: Length selector 2 (Interrupted high-speed rig) |
| | NAME | SIGNATURE | DATE | MATERIAL: | ITEM NO. 4 / A4 |
| DRAWN | Alexander Sancho | | 09/09/16 | 17-4PH | |
| | | | | | SCALE 1:1 / SHEET 1 OF 1 |

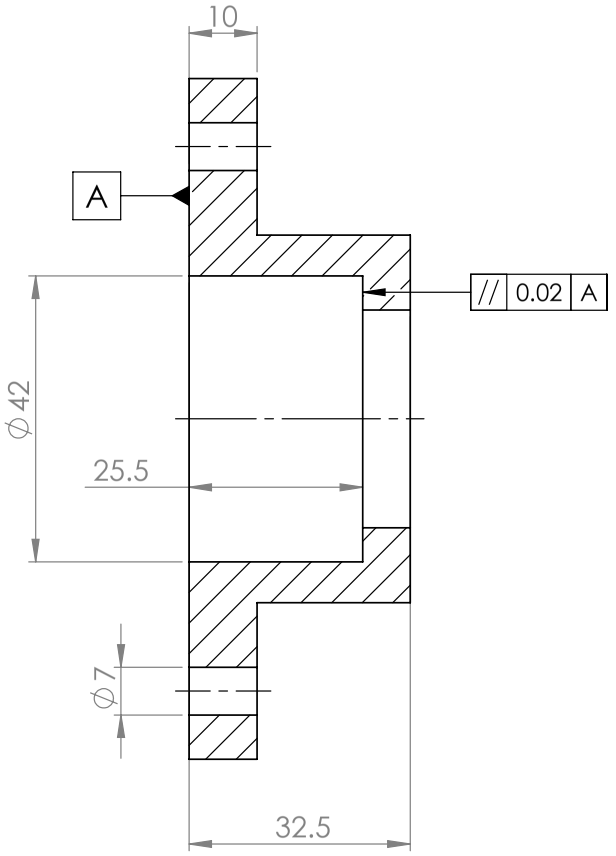



| | | | | | |
|---|---|---|---|---|---|
| UNLESS OTHERWISE SPECIFIED: DIMENSIONS ARE IN MILLIMETERS | | | | Imperial College London | TITLE: Length selector 1 (Interrupted high-speed rig) |
| | NAME | SIGNATURE | DATE | MATERIAL: | ITEM NO. 6 / A4 |
| DRAWN | Alexander Sancho | | 12/09/16 | 17-4PH | |
| | | | | | SCALE 1:1 / SHEET 1 OF 1 |




| | | | | | | |
|---|---|---|---|---|---|---|
| UNLESS OTHERWISE SPECIFIED: DIMENSIONS ARE IN MILLIMETERS | | | | Imperial College London | TITLE: Conical part (Interrupted high-speed rig) | |
| | NAME | SIGNATURE | DATE | MATERIAL: | ITEM NO. 10 | A4 |
| DRAWN | Alexander Sancho | | 12/09/16 | Ti-6Al-4V | | |
| | | | | | SCALE 1:1 | SHEET 1 OF 1 |

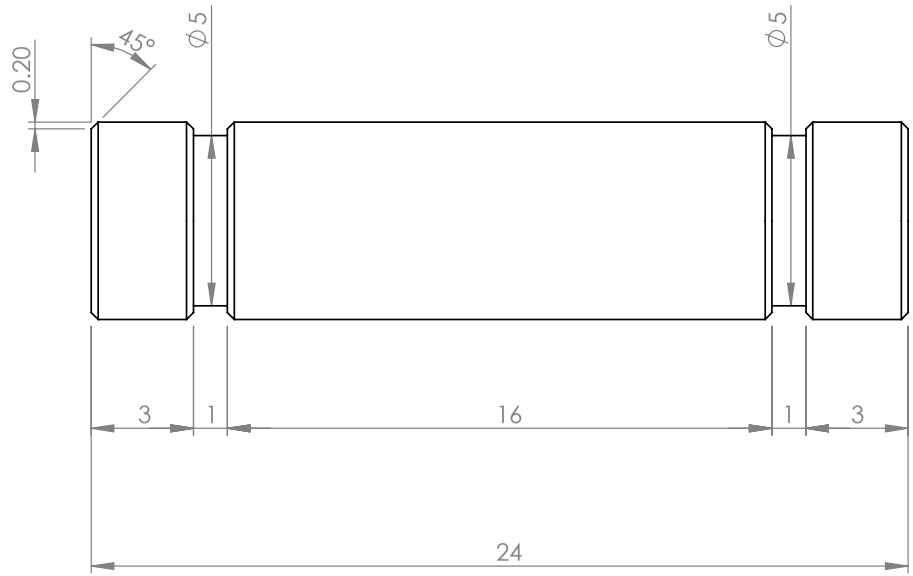


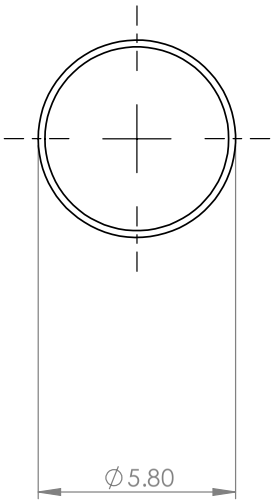



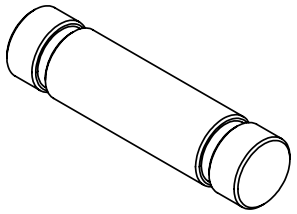

SECTION A-A

| | | | | | |
|---|---|---|---|---|---|
| UNLESS OTHERWISE SPECIFIED: DIMENSIONS ARE IN MILLIMETERS | | Imperial College London | | TITLE: Bearing housing (Interrupted high-speed rig) | |
| | NAME | SIGNATURE | DATE | MATERIAL: | ITEM NO. |
| DRAWN | Alexander Sancho | | 12/09/16 | 17-4PH | 12 |
| | | | | SCALE 1:1 | SHEET 1 OF 1 |

A4



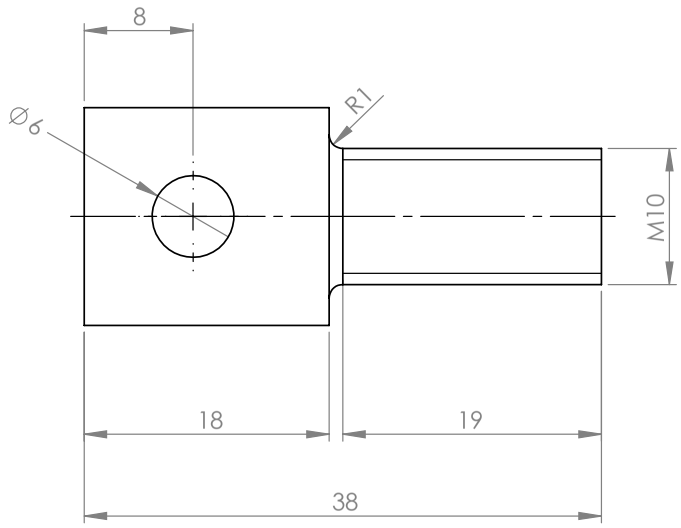



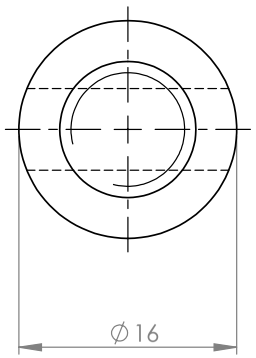



Isometric view - Scale 2:1

| | | | | | |
|---|---|---|---|---|---|
| UNLESS OTHERWISE SPECIFIED: DIMENSIONS ARE IN MILLIMETERS | | | Imperial College London | TITLE: Shear pin (Ø5mm) (Interrupted high-speed rig) | |
| | NAME | SIGNATURE | DATE | MATERIAL: | ITEM NO. |
| DRAWN | Alexander Sancho | | 25/05/17 | Al 7075 | 14 |
| | | | | SCALE 5:1 | SHEET 1 OF 1 |

A4




UNLESS OTHERWISE SPECIFIED:
DIMENSIONS ARE IN MILLIMETERS

Imperial College London

TITLE:

# Shear pin adaptor 1
(Interrupted high-speed rig)

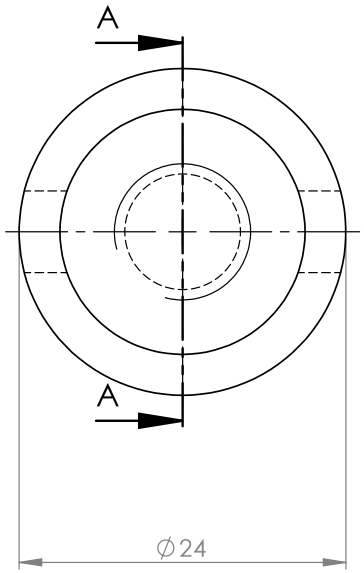
| | NAME | SIGNATURE | DATE | MATERIAL: |
|---|---|---|---|---|
| DRAWN | Alexander Sancho | | 12/09/16 | Ti-6Al-4V |

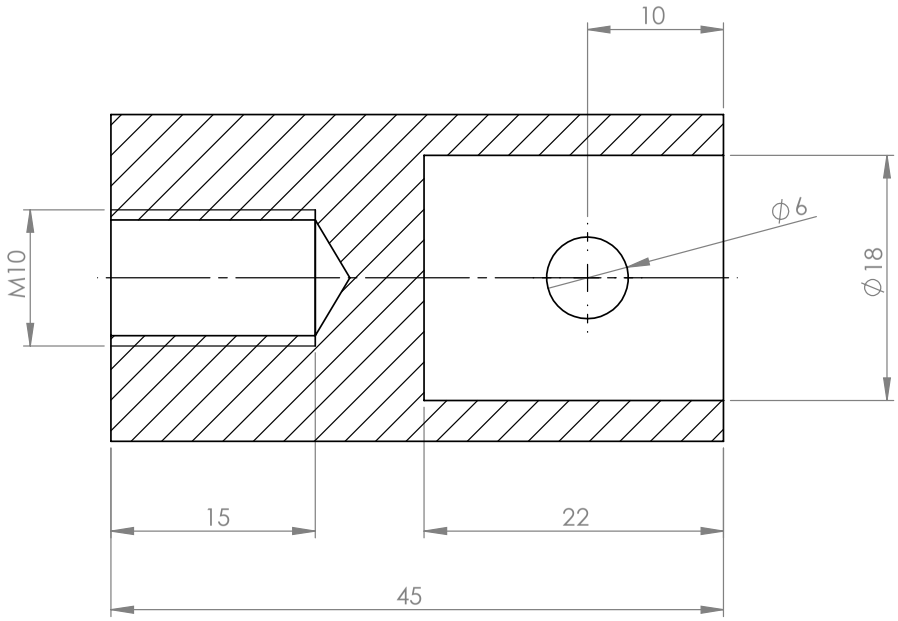
ITEM NO. 15

A4

SCALE 2:1

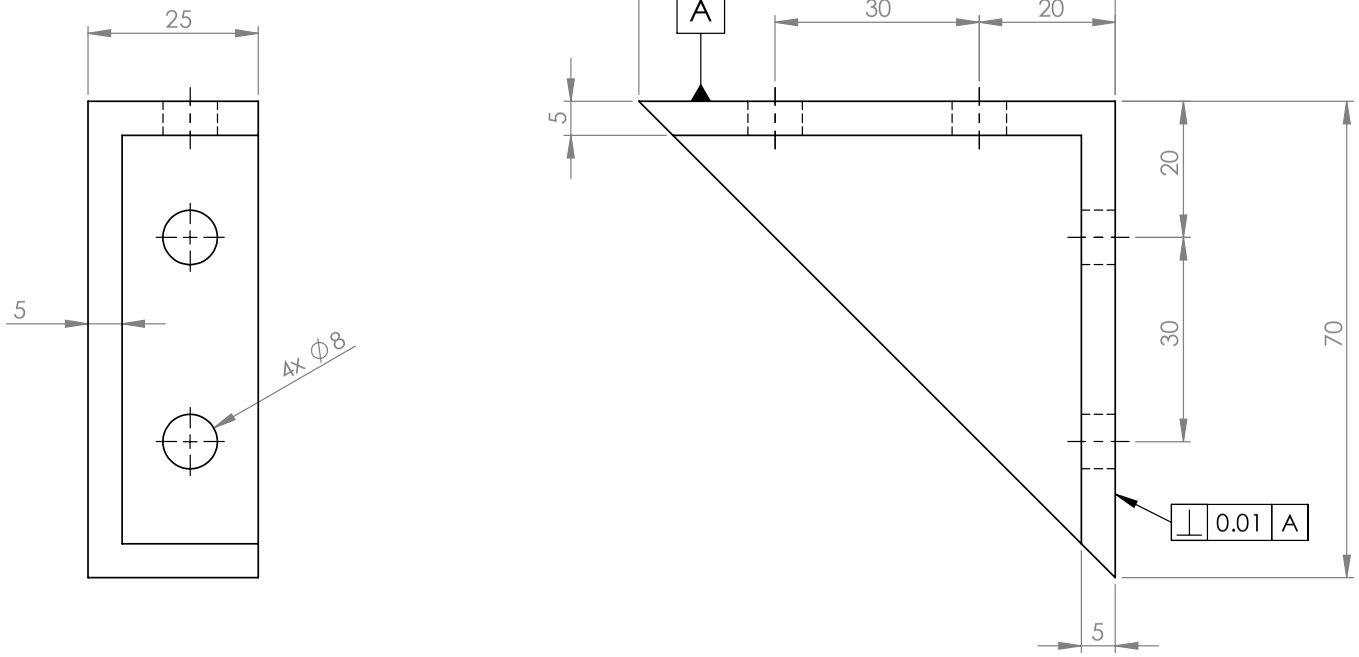
SHEET 1 OF 1




SECTION A-A

| | | | | | |
|---|---|---|---|---|---|
| UNLESS OTHERWISE SPECIFIED: DIMENSIONS ARE IN MILLIMETERS | | | Imperial College London | | TITLE: Shear pin adaptor 2 (Interrupted high-speed rig) |
| | NAME | SIGNATURE | DATE | MATERIAL: | ITEM NO. 16 / A4 |
| DRAWN | Alexander Sancho | | 12/09/16 | Ti-6Al-4V | |
| | | | | | SCALE 2:1 / SHEET 1 OF 1 |




| | | | | | | |
|---|---|---|---|---|---|---|
| UNLESS OTHERWISE SPECIFIED: DIMENSIONS ARE IN MILLIMETERS | | | Imperial College London | | TITLE: Reinforcing bracket (Interrupted high-speed rig) | |
| | NAME | SIGNATURE | DATE | MATERIAL: | ITEM NO. | |
| DRAWN | Alexander Sancho | | 09/09/16 | EN24T | 18 | A4 |
| | | | | | SCALE 1:1 | SHEET 1 OF 1 |

# Appendix B

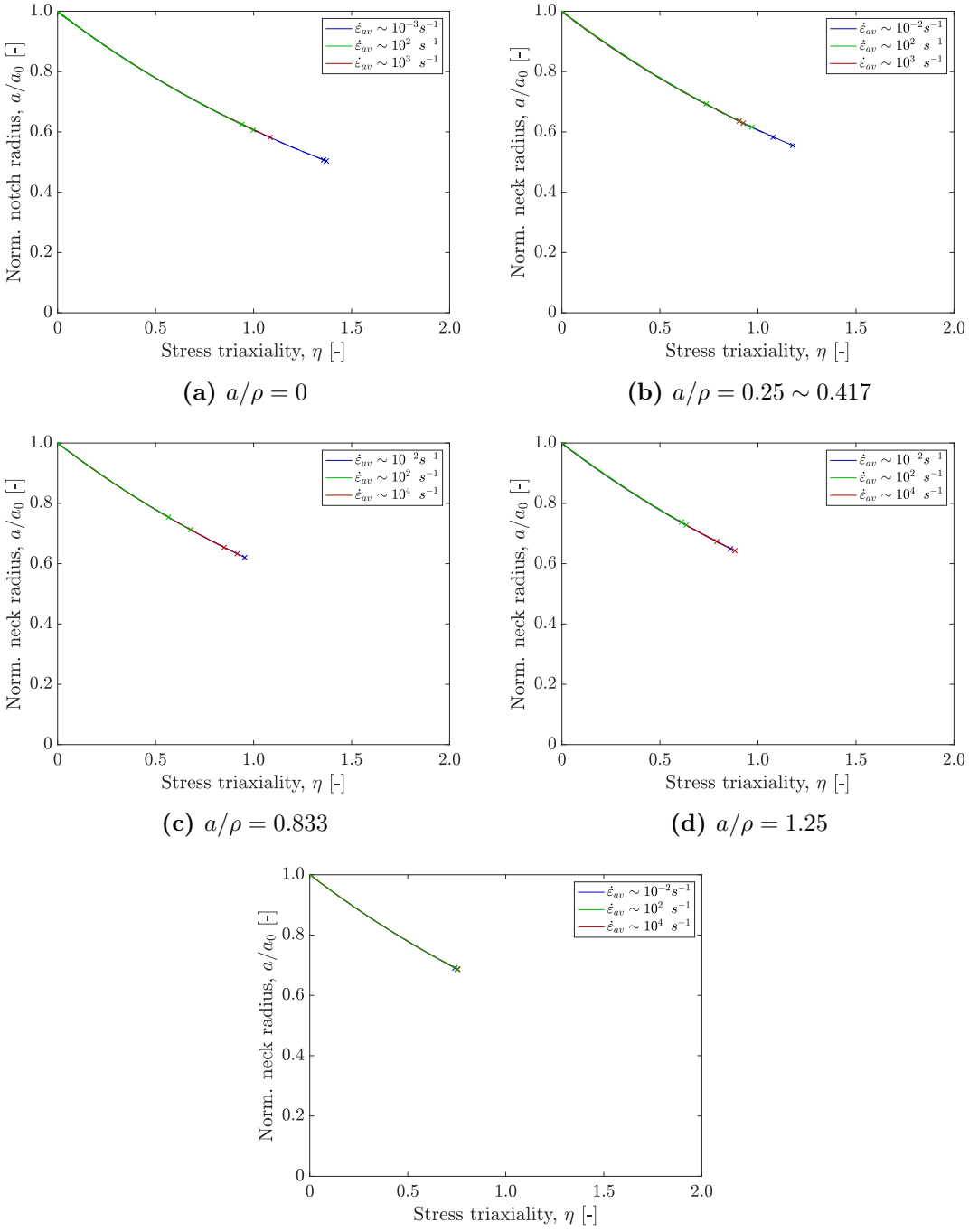
# Additional Results

Some additional results are presented in this appendix in the form of tables and diagrams. Results from the strain-rate analysis can be found in Section B.1, from the temperature study in Section B.2 and from the model fitting process in Section B.3.

## B.1 Additional Strain-Rate Results

| Av. rate, $\dot{\varepsilon}_{av}$ $[s^{-1}]$ | Geometry | Notch acuity, $a/\rho$ | Spec. | Theor. | Imaging | | | |
|---|---|---|---|---|---|---|---|---|
| | | | | $\eta_0$ | $\eta_0$ | $\eta_f$ | $\eta_{av}$ | $\bar{\varepsilon}_f$ |
| $6.28\text{x}10^{-3}$ | RB6 | 0 | #14 | 0.333 | 0.333 | 0.787 | 0.488 | 1.37 |
| $6.15\text{x}10^{-3}$ | | | #16 | 0.333 | 0.333 | 0.796 | 0.491 | 1.36 |
| $1.18\text{x}10^{-2}$ | RNB6-1 | 0.25 | #19 | 0.546 | 0.582 | 0.905 | 0.738 | 1.18 |
| $9.95\text{x}10^{-3}$ | RNB6-3 | 0.417 | #15 | 0.660 | 0.726 | 1.001 | 0.875 | 1.08 |
| $1.09\text{x}10^{-2}$ | RNB6-4 | 0.833 | #11 | 0.892 | 1.084 | 1.144 | 1.115 | 0.95 |
| $1.11\text{x}10^{-2}$ | RNB6-5 | 1.25 | #7 | 1.110 | 1.225 | 1.203 | 1.204 | 0.86 |
| $1.23\text{x}10^{-2}$ | RNB6-6 | 2.5 | #3 | 1.540 | 1.614 | 1.346 | 1.449 | 0.74 |
| $3.03\text{x}10^{2}$ | RB3.5 | 0 | #2 | 0.333 | 0.333 | 0.747 | 0.457 | 1.00 |
| $2.94\text{x}10^{2}$ | | | #3 | 0.333 | 0.333 | 0.690 | 0.458 | 0.94 |
| $5.06\text{x}10^{2}$ | RNB3.5-2 | 0.313 | #16 | 0.594 | 0.597 | 0.839 | 0.667 | 0.97 |
| $3.09\text{x}10^{2}$ | | | #17 | 0.606 | 0.602 | 0.632 | 0.606 | 0.74 |
| $3.88\text{x}10^{2}$ | RNB3.5-4 | 0.833 | #12 | 0.924 | 0.922 | 0.936 | 0.885 | 0.57 |
| $4.32\text{x}10^{2}$ | | | #13 | 0.935 | 0.928 | 0.800 | 0.844 | 0.68 |
| $4.56\text{x}10^{2}$ | RNB3.5-5 | 1.25 | #7 | 1.119 | 1.185 | 1.068 | 1.047 | 0.63 |
| $4.96\text{x}10^{2}$ | | | #8 | 1.102 | 1.131 | 0.965 | 1.006 | 0.61 |
| $4.69\text{x}10^{2}$ | RNB3.5-6 | 2.5 | #3 | 1.573 | 1.593 | 1.336 | 1.376 | 0.75 |
| $3.79\text{x}10^{3}$ | RB3.5 | 0 | #5 | 0.333 | 0.333 | 0.730 | 0.462 | 1.08 |
| $4.37\text{x}10^{3}$ | | | #6 | 0.333 | 0.333 | 0.655 | 0.457 | 1.06 |
| $8.28\text{x}10^{3}$ | RNB3.5-2 | 0.313 | #19 | 0.598 | 0.572 | 0.917 | 0.671 | 0.92 |
| $9.27\text{x}10^{3}$ | | | #20 | 0.588 | 0.580 | 0.921 | 0.681 | 0.90 |
| $1.05\text{x}10^{4}$ | RNB3.5-4 | 0.833 | #14 | 0.921 | 0.887 | 0.965 | 0.868 | 0.85 |
| $1.15\text{x}10^{4}$ | | | #15 | 0.909 | 0.892 | 1.079 | 0.916 | 0.92 |
| $1.05\text{x}10^{4}$ | RNB3.5-5 | 1.25 | #9 | 1.131 | 1.081 | 1.142 | 1.027 | 0.88 |
| $1.02\text{x}10^{4}$ | | | #10 | 1.150 | 1.081 | 0.982 | 0.984 | 0.79 |
| $1.03\text{x}10^{4}$ | RNB3.5-6 | 2.5 | #4 | 1.572 | 1.583 | 1.313 | 1.340 | 0.75 |
| $1.10\text{x}10^{4}$ | | | #5 | 1.574 | 1.567 | 1.271 | 1.352 | 0.76 |

**Table B.1:** Stress triaxiality results of stainless steel 304L at different strain-rates. Theoretical initial stress triaxiality ($\eta_0$) obtained using Equation 3.5; initial ($\eta_0$), final ($\eta_f$) and average ($\eta_{av}$) stress triaxiality throughout the test obtained using the proposed imaging method; and fracture equivalent strain ($\bar{\varepsilon}_f$) obtained using the proposed imaging technique.

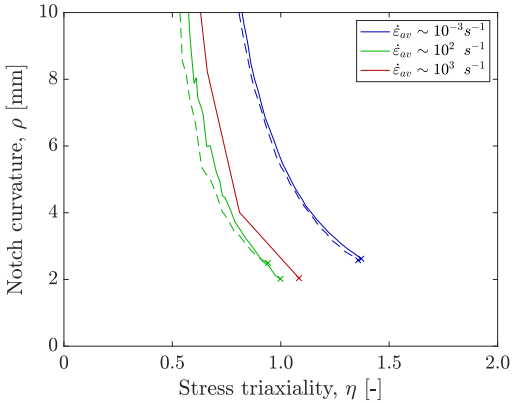



**(a)** $a/\rho = 0$ **(b)** $a/\rho = 0.25 \sim 0.417$

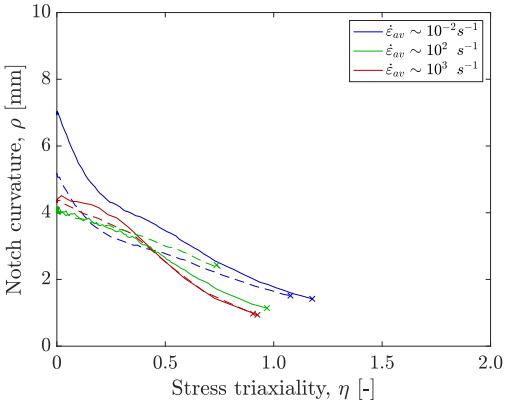
**(c)** $a/\rho = 0.833$ **(d)** $a/\rho = 1.25$

**(e)** $a/\rho = 2.5$

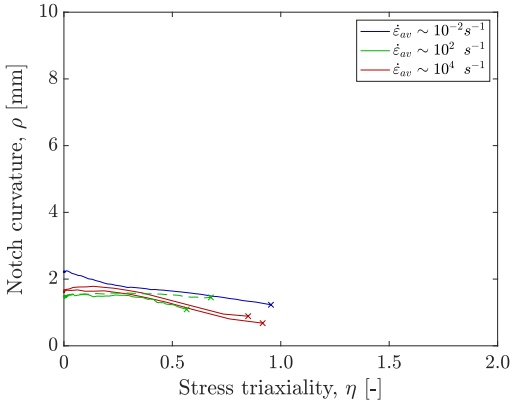
**Figure B.1:** Strain-rate effect on normalised minimum cross-sectional radius - equivalent plastic strain ($a/a_0$ - $\bar{\varepsilon}_{pl}$) for stainless steel 304L specimens with different notch acuities.



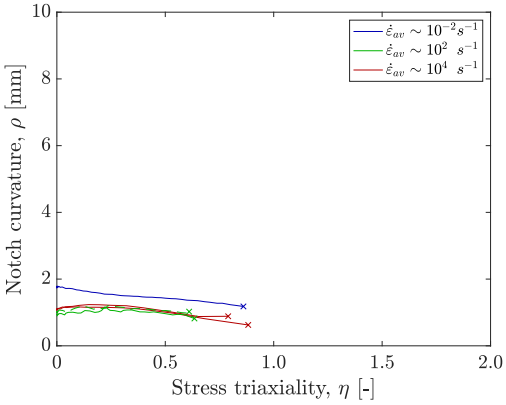

**(a)** $a/\rho = 0$



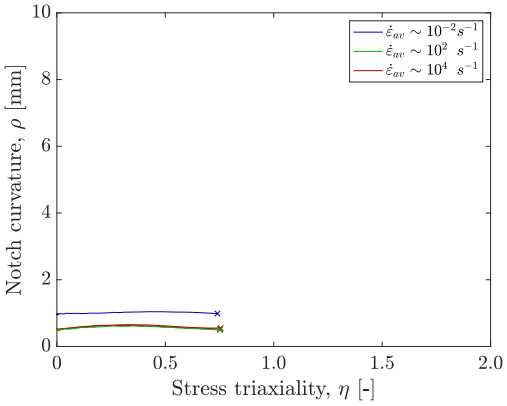

**(b)** $a/\rho = 0.25 \sim 0.417$




**(c)** $a/\rho = 0.833$

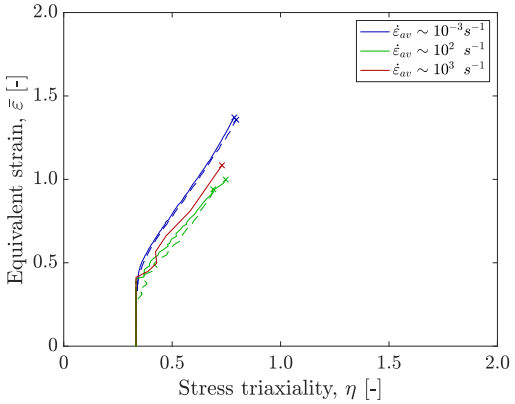



**(d)** $a/\rho = 1.25$

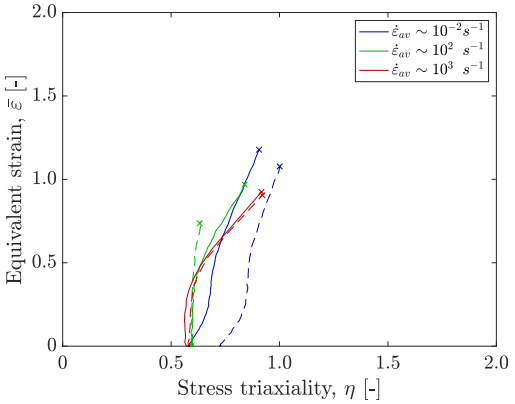



**(e)** $a/\rho = 2.5$

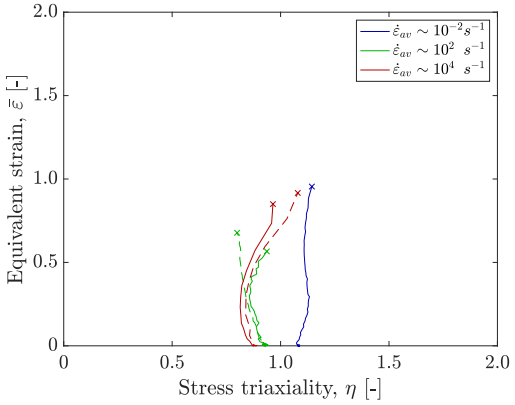
**Figure B.2:** Strain-rate effect on notch curvature - equivalent plastic strain ($\rho$ - $\bar{\varepsilon}_{pl}$) for stainless steel 304L specimens with different notch acuities.



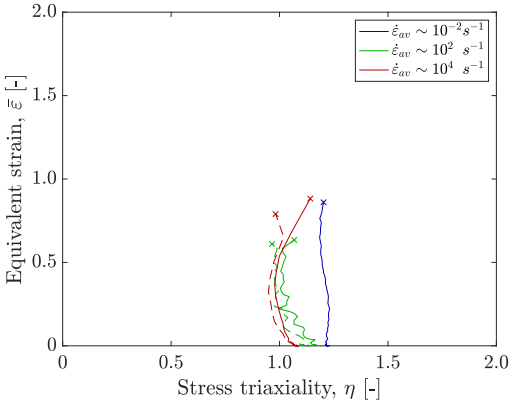

**(a)** $a/\rho = 0$



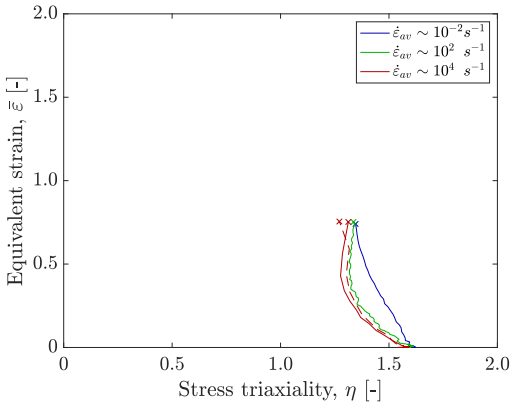

**(b)** $a/\rho = 0.25 \sim 0.417$




**(c)** $a/\rho = 0.833$




**(d)** $a/\rho = 1.25$

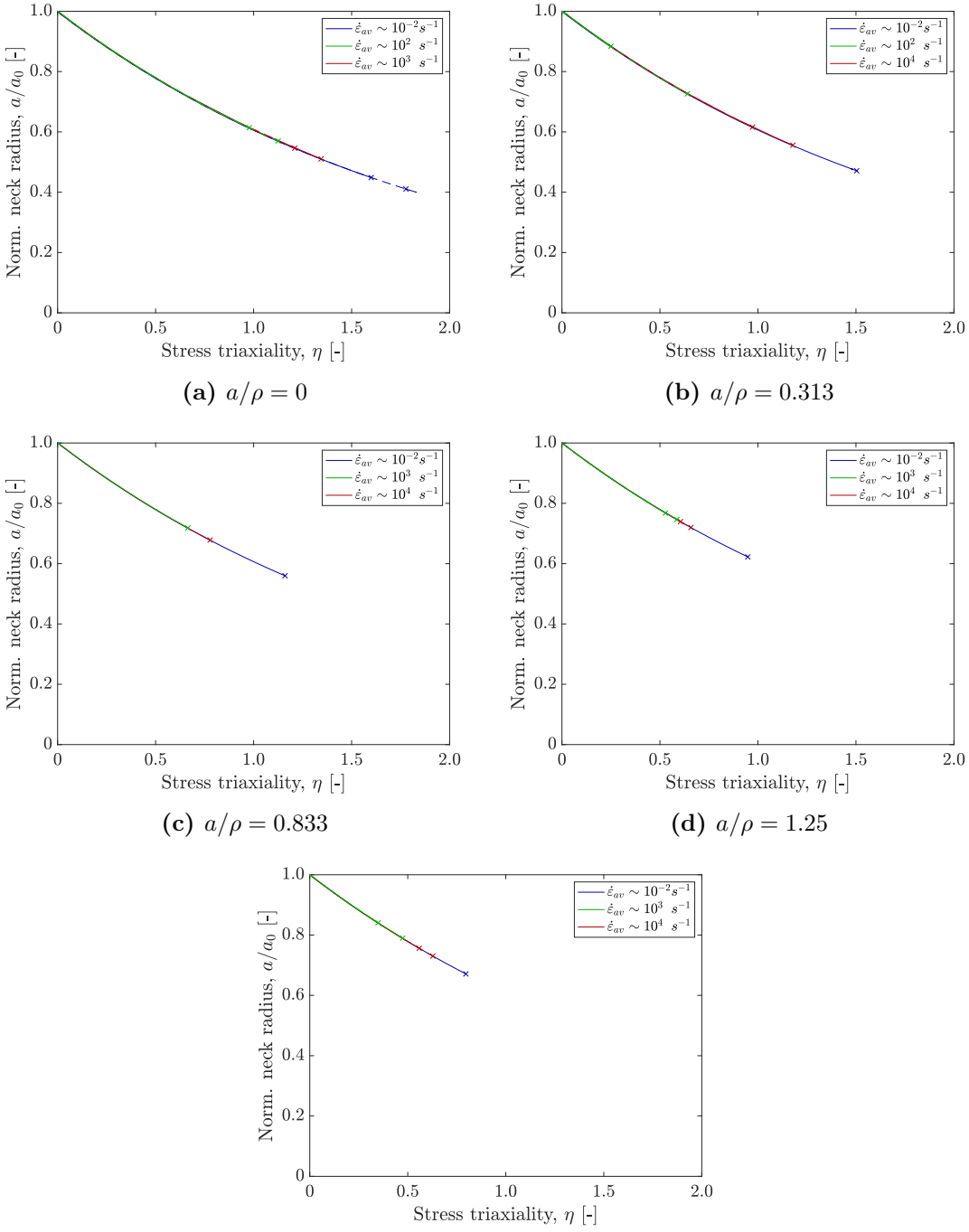



**(e)** $a/\rho = 2.5$

**Figure B.3:** Strain-rate effect on equivalent strain - stress triaxiality ($\bar{\varepsilon}$ - $\eta$) for stainless steel 304L specimens with different notch acuities.

| Av. rate, $\dot{\varepsilon}_{av}$ $[s^{-1}]$ | Geometry | Notch acuity, $a/\rho$ | Spec. | Theor. | Imaging | | | |
|---|---|---|---|---|---|---|---|---|
| | | | | $\eta_0$ | $\eta_0$ | $\eta_f$ | $\eta_{av}$ | $\bar{\varepsilon}_f$ |
| $1.07\text{x}10^{-2}$ | RB6 | 0 | #1 | 0.333 | 0.333 | 1.329 | 0.823 | 1.60 |
| $1.12\text{x}10^{-2}$ | | | #2 | 0.333 | 0.333 | 1.316 | 0.855 | 1.78 |
| $1.35\text{x}10^{-2}$ | RNB6-2 | 0.313 | #11 | 0.602 | 0.602 | 1.247 | 0.974 | 1.50 |
| $1.42\text{x}10^{-2}$ | RNB6-4 | 0.833 | #8 | 0.958 | 0.936 | 1.470 | 1.185 | 1.16 |
| $1.39\text{x}10^{-2}$ | RNB6-5 | 1.25 | #5 | 1.173 | 1.147 | 1.808 | 1.392 | 0.95 |
| $1.98\text{x}10^{-2}$ | RNB6-6 | 2.5 | #2 | 1.532 | 1.586 | 2.194 | 1.699 | 0.80 |
| $4.80\text{x}10^{2}$ | RB3.5 | 0 | #1 | 0.333 | 0.333 | 0.845 | 0.554 | 0.98 |
| $6.34\text{x}10^{2}$ | | | #2 | 0.333 | 0.333 | 0.952 | 0.602 | 1.13 |
| $2.09\text{x}10^{2}$ | RNB3.5-2 | 0.313 | #13 | 0.601 | 0.586 | 0.658 | 0.620 | 0.25 |
| $9.47\text{x}10^{2}$ | | | #14 | 0.602 | 0.573 | 1.167 | 0.753 | 0.64 |
| $1.00\text{x}10^{3}$ | RNB3.5-4 | 0.833 | #10 | 0.921 | 0.941 | 1.146 | 0.988 | 0.66 |
| $1.11\text{x}10^{3}$ | RNB3.5-5 | 1.25 | #5 | 1.168 | 1.163 | 1.208 | 1.164 | 0.59 |
| $1.09\text{x}10^{3}$ | | | #6 | 1.158 | 1.163 | 1.121 | 1.123 | 0.53 |
| $9.22\text{x}10^{2}$ | RNB3.5-6 | 2.5 | #1 | 1.575 | 1.484 | 1.213 | 1.278 | 0.47 |
| $9.05\text{x}10^{2}$ | | | #2 | 1.546 | 1.464 | 1.369 | 1.370 | 0.35 |
| $8.11\text{x}10^{3}$ | RB3.5 | 0 | #4 | 0.333 | 0.333 | 1.226 | 0.832 | 1.34 |
| $7.40\text{x}10^{3}$ | | | #5 | 0.333 | 0.333 | 1.102 | 0.644 | 1.21 |
| $1.26\text{x}10^{4}$ | RNB3.5-2 | 0.313 | #15 | 0.597 | 0.585 | 1.087 | 0.845 | 1.18 |
| $1.03\text{x}10^{4}$ | | | #16 | 0.596 | 0.591 | 1.014 | 0.772 | 0.97 |
| $8.38\text{x}10^{3}$ | RNB3.5-4 | 0.833 | #12 | 0.942 | 0.910 | 1.017 | 0.906 | 0.78 |
| $9.61\text{x}10^{3}$ | RNB3.5-5 | 1.25 | #7 | 1.129 | 1.114 | 1.351 | 1.148 | 0.61 |
| $9.59\text{x}10^{3}$ | | | #8 | 1.173 | 1.113 | 1.336 | 1.163 | 0.66 |
| $8.22\text{x}10^{3}$ | RNB3.5-6 | 2.5 | #3 | 1.577 | 1.566 | 1.438 | 1.456 | 0.56 |
| $9.22\text{x}10^{3}$ | | | #4 | 1.574 | 1.548 | 1.239 | 1.298 | 0.63 |

**Table B.2:** Stress triaxiality results of copper C110 at different strain-rates. Theoretical initial stress triaxiality ($\eta_0$) obtained using Equation 3.5; initial ($\eta_0$), final ($\eta_f$) and average ($\eta_{av}$) stress triaxiality throughout the test obtained using the proposed imaging method; and fracture equivalent strain ($\bar{\varepsilon}_f$) obtained using the proposed imaging technique.

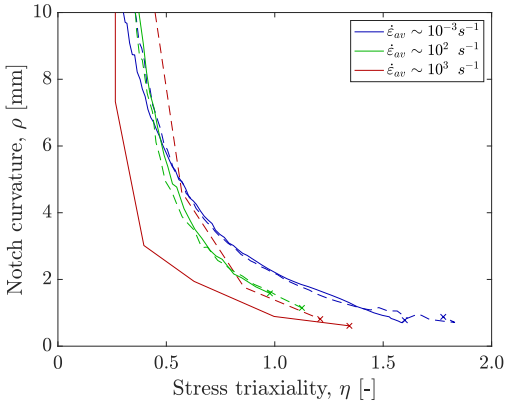



**(a)** $a/\rho = 0$ **(b)** $a/\rho = 0.313$

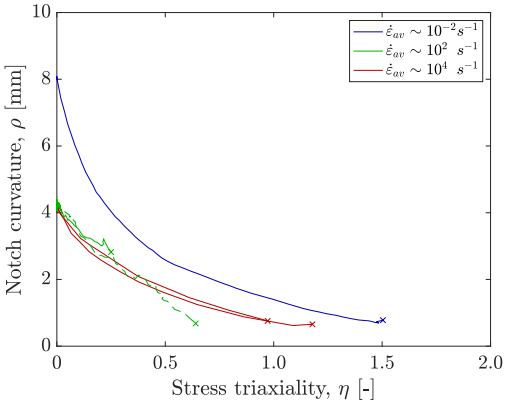
**(c)** $a/\rho = 0.833$ **(d)** $a/\rho = 1.25$

**(e)** $a/\rho = 2.5$

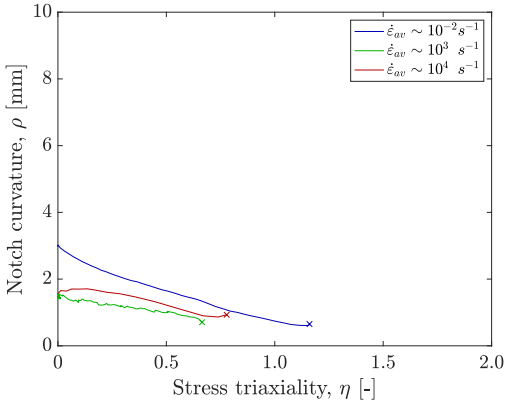
**Figure B.4:** Strain-rate effect on normalised minimum cross-sectional radius - equivalent plastic strain ($a/a_0$ - $\bar{\varepsilon}_{pl}$) for copper C110 specimens with different notch acuities.



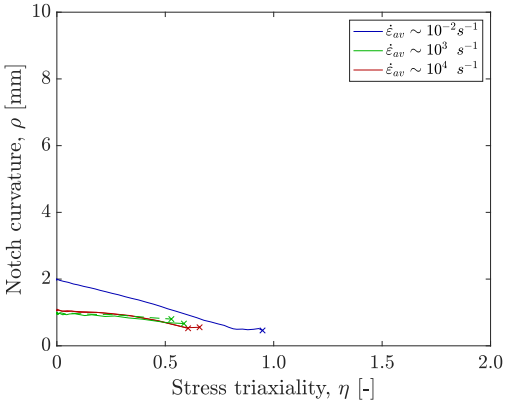

**(a)** $a/\rho = 0$



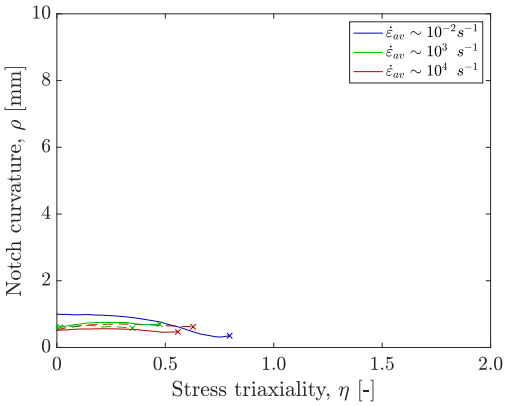

**(b)** $a/\rho = 0.313$




**(c)** $a/\rho = 0.833$

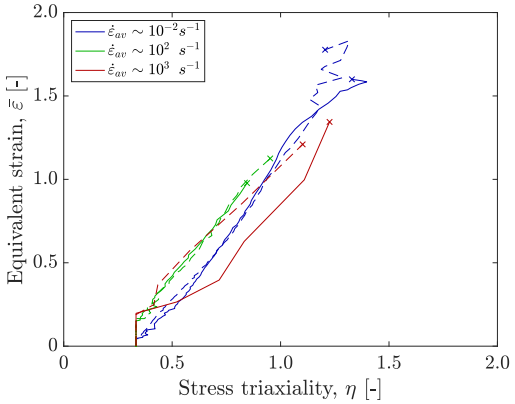



**(d)** $a/\rho = 1.25$

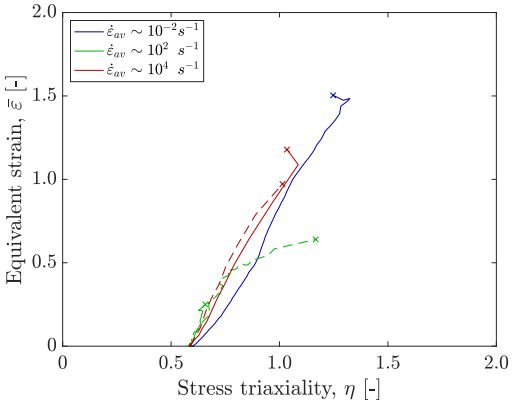



**(e)** $a/\rho = 2.5$

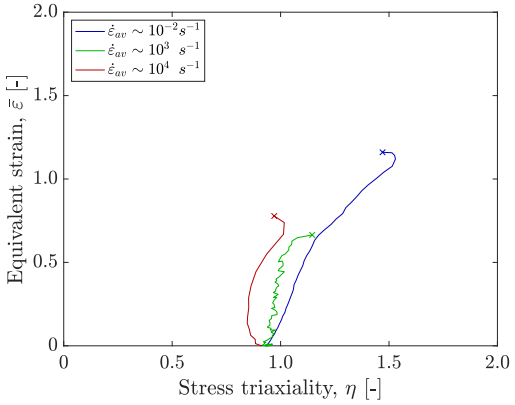
**Figure B.5:** Strain-rate effect on notch curvature - equivalent plastic strain ($\rho$ - $\bar{\varepsilon}_{pl}$) for copper C110 specimens with different notch acuities.



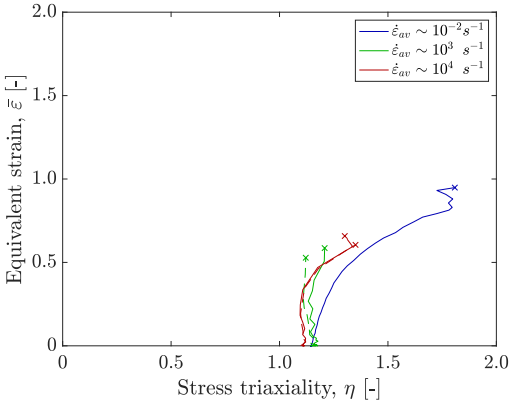

**(a)** $a/\rho = 0$



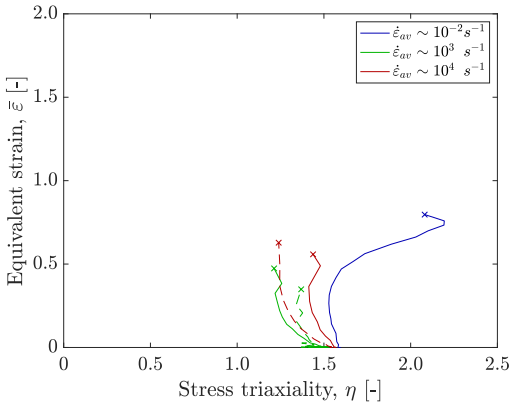

**(b)** $a/\rho = 0.25 \sim 0.417$




**(c)** $a/\rho = 0.833$




**(d)** $a/\rho = 1.25$



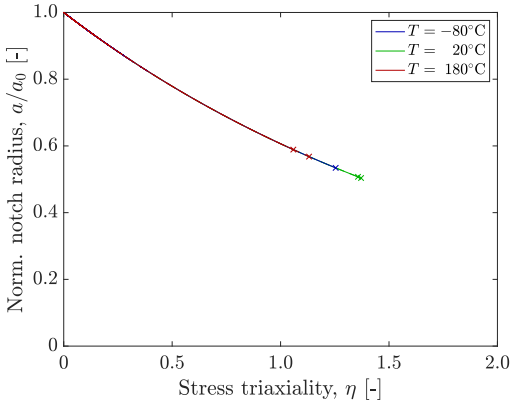

**(e)** $a/\rho = 2.5$

**Figure B.6:** Strain-rate effect on equivalent strain - stress triaxiality ($\bar{\varepsilon}$ - $\eta$) for copper C110 specimens with different notch acuities.

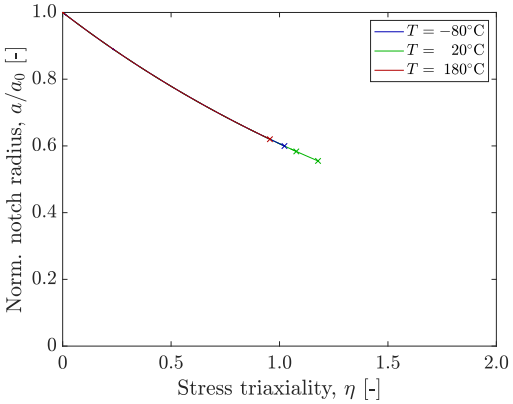
## B.2 Additional Temperature Results

| Temp., $T$ $[K]$ | Geometry | Notch acuity, $a/\rho$ | Spec. | Theor. | Imaging | | | |
|---|---|---|---|---|---|---|---|---|
| | | | | $\eta_0$ | $\eta_0$ | $\eta_f$ | $\eta_{av}$ | $\bar{\varepsilon}_f$ |
| 193 | RB6 | 0 | #24 | 0.333 | 0.333 | 0.810 | 0.503 | 1.25 |
| | RNB6-2 | 0.313 | #28 | 0.610 | 0.635 | 0.751 | 0.619 | 1.02 |
| | RNB6-4 | 0.833 | #26 | 0.951 | 1.005 | 0.870 | 0.834 | 0.88 |
| | RNB6-5 | 1.25 | #24 | 1.114 | 1.144 | 0.859 | 0.940 | 0.80 |
| | RNB6-6 | 2.5 | #22 | 1.537 | 1.596 | 1.047 | 1.208 | 0.67 |
| 293 | RB6 | 0 | #14 | 0.333 | 0.333 | 0.787 | 0.488 | 1.37 |
| | | | #16 | 0.333 | 0.333 | 0.796 | 0.491 | 1.36 |
| | RNB6-1 | 0.25 | #19 | 0.546 | 0.582 | 0.905 | 0.738 | 1.18 |
| | RNB6-3 | 0.417 | #15 | 0.660 | 0.726 | 1.001 | 0.875 | 1.08 |
| | RNB6-4 | 0.833 | #11 | 0.892 | 1.084 | 1.144 | 1.115 | 0.95 |
| | RNB6-5 | 1.25 | #7 | 1.110 | 1.225 | 1.203 | 1.204 | 0.86 |
| | RNB6-6 | 2.5 | #3 | 1.540 | 1.614 | 1.346 | 1.449 | 0.74 |
| 453 | RB6 | 0 | #21 | 0.333 | 0.333 | 0.772 | 0.507 | 1.06 |
| | | | #22 | 0.333 | 0.333 | 0.823 | 0.532 | 1.13 |
| | RNB6-2 | 0.313 | #27 | 0.603 | 0.592 | 0.883 | 0.728 | 0.96 |
| | RNB6-4 | 0.833 | #25 | 0.929 | 0.916 | 0.956 | 0.914 | 0.88 |
| | RNB6-5 | 1.25 | #23 | 1.119 | 1.133 | 1.048 | 1.075 | 0.55 |
| | RNB6-6 | 2.5 | #21 | 1.534 | 1.558 | 1.313 | 1.409 | 0.39 |

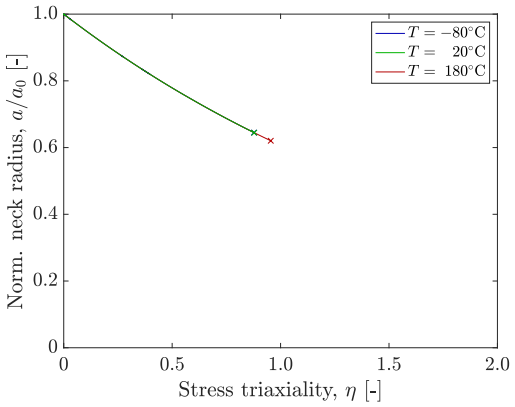
**Table B.3:** Stress triaxiality results of stainless steel 304L at different temperatures. Theoretical initial stress triaxiality ($\eta_0$) obtained using Equation 3.5; initial ($\eta_0$), final ($\eta_f$) and average ($\eta_{av}$) stress triaxiality throughout the test obtained using the proposed imaging method; and fracture equivalent strain ($\bar{\varepsilon}_f$) obtained using the proposed imaging technique.



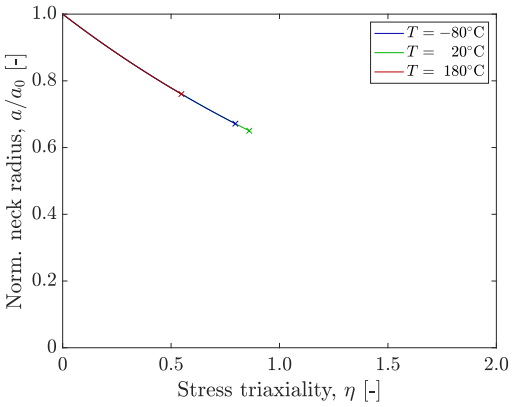

**(a)** $a/\rho = 0$



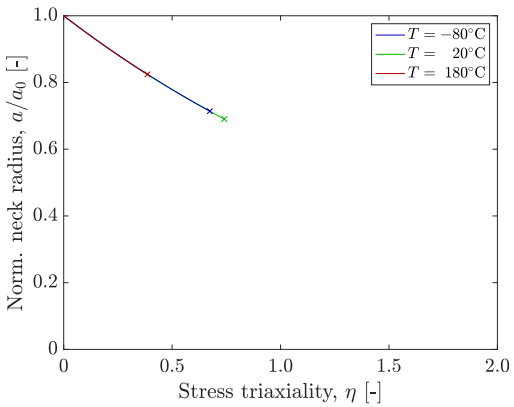

**(b)** $a/\rho = 0.25 \sim 0.417$




**(c)** $a/\rho = 0.833$

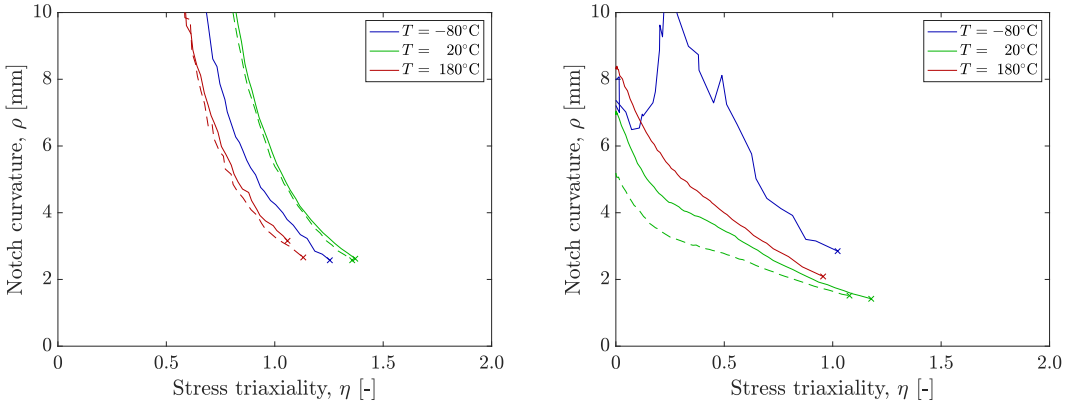



**(d)** $a/\rho = 1.25$

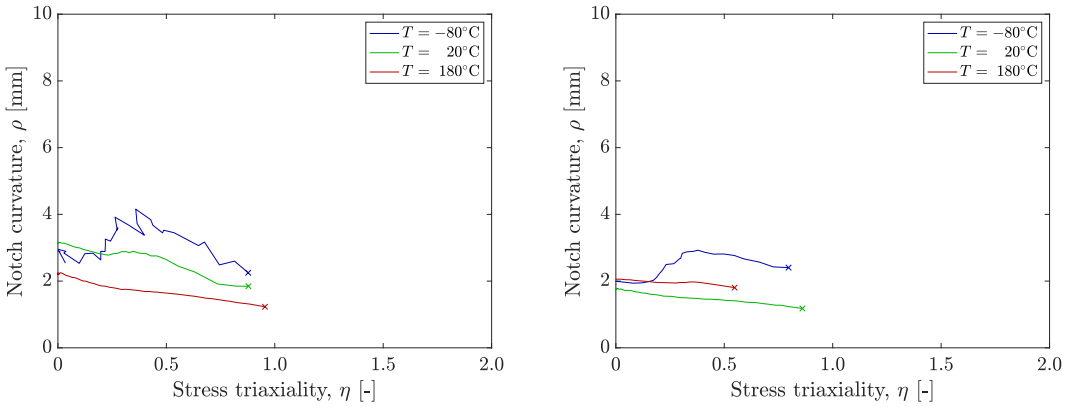



**(e)** $a/\rho = 2.5$

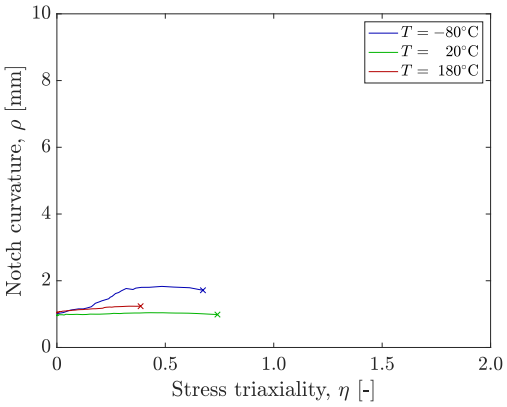
**Figure B.7:** Temperature effect on normalised minimum cross-sectional radius - equivalent plastic strain ($a/a_0$ - $\bar{\varepsilon}_{pl}$) for stainless steel 304L specimens with different notch acuities.




**(a)** $a/\rho = 0$ **(b)** $a/\rho = 0.25 \sim 0.417$

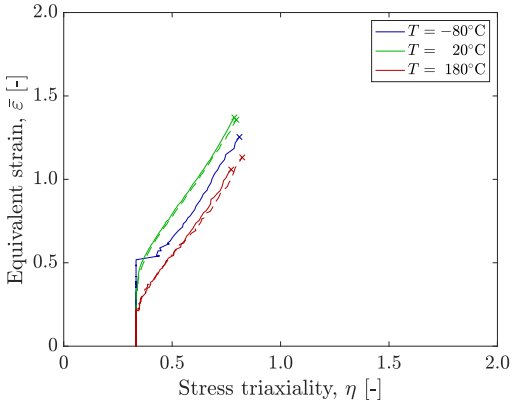



**(c)** $a/\rho = 0.833$ **(d)** $a/\rho = 1.25$

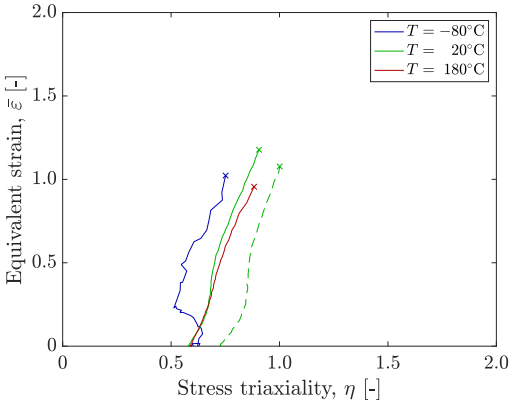



**(e)** $a/\rho = 2.5$

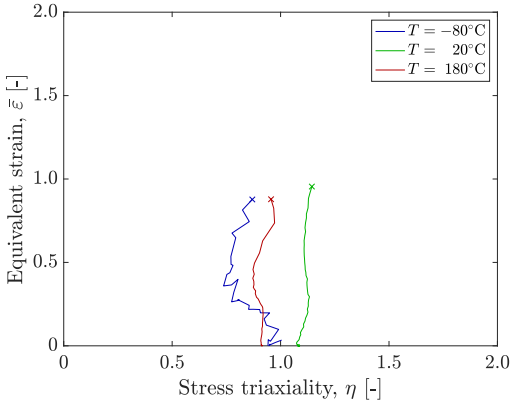
**Figure B.8:** Temperature effect on notch curvature - equivalent plastic strain ($\rho$ - $\bar{\varepsilon}_{pl}$) for stainless steel 304L specimens with different notch acuities.



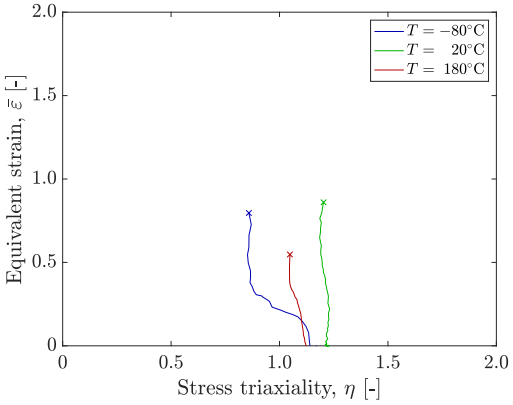

**(a)** $a/\rho = 0$



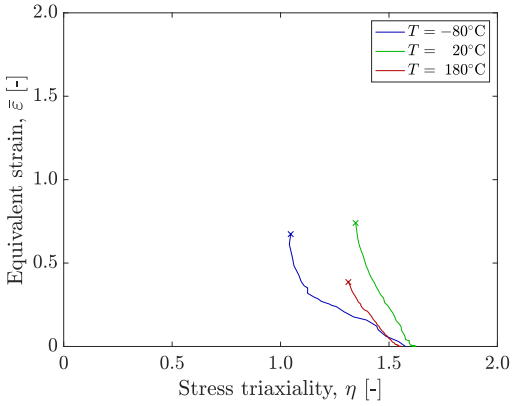

**(b)** $a/\rho = 0.25 \sim 0.417$




**(c)** $a/\rho = 0.833$




**(d)** $a/\rho = 1.25$

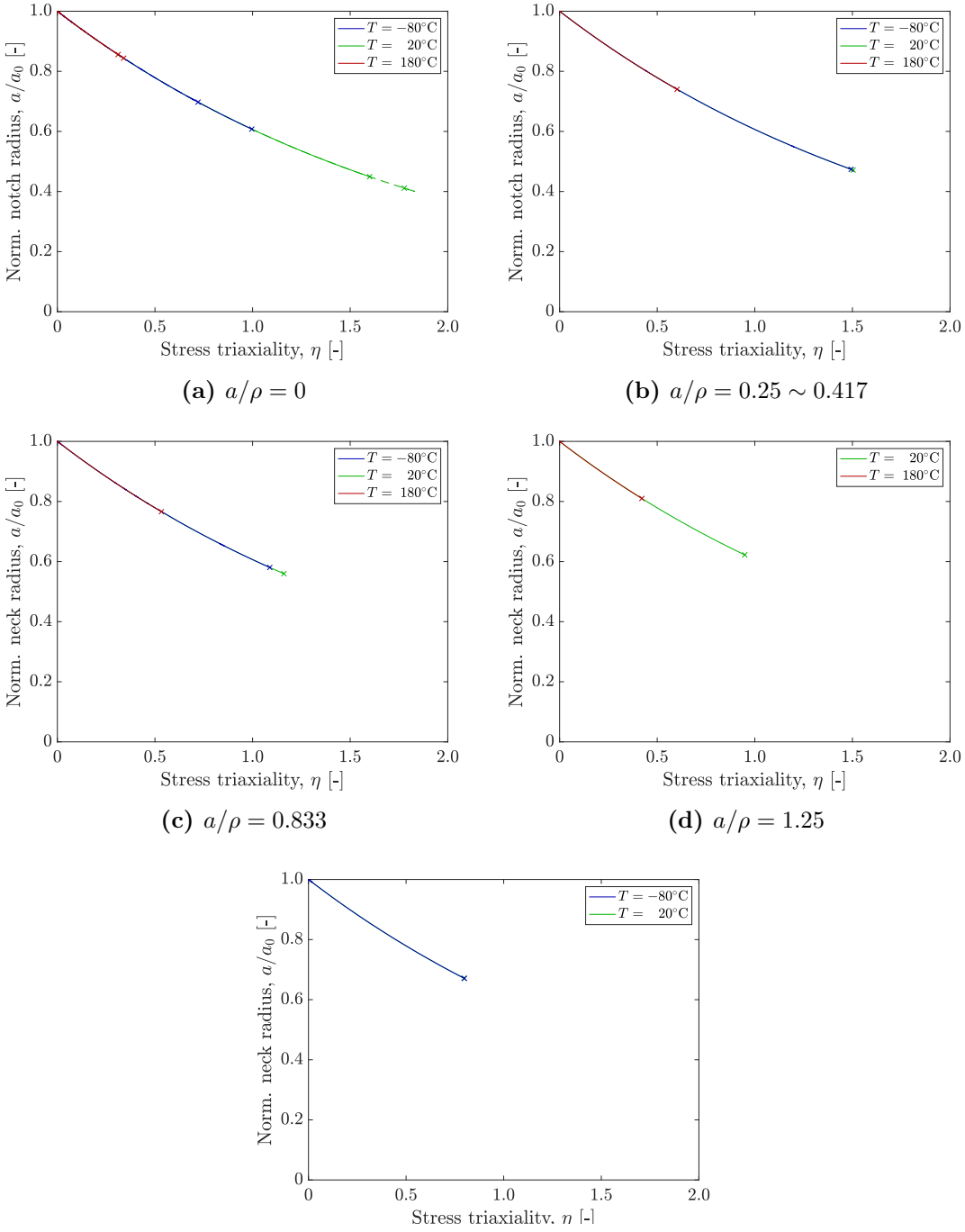



**(e)** $a/\rho = 2.5$

**Figure B.9:** Temperature effect on equivalent strain - stress triaxiality ($\bar{\varepsilon}$ - $\eta$) for stainless steel 304L specimens with different notch acuities.

| Temp., $T$ $[K]$ | Geometry | Notch acuity, $a/\rho$ | Spec. | Theor. | Imaging | | | |
|---|---|---|---|---|---|---|---|---|
| | | | | $\eta_0$ | $\eta_0$ | $\eta_f$ | $\eta_{av}$ | $\bar{\varepsilon}_f$ |
| 193 | RB6 | 0 | #7 | 0.333 | 0.333 | 0.785 | 0.527 | 1.00 |
| | | | #8 | 0.333 | 0.333 | 0.649 | 0.456 | 0.72 |
| | RNB6-2 | 0.313 | #10 | 0.606 | 0.601 | 1.006 | 0.878 | 1.49 |
| | RNB6-4 | 0.833 | #7 | 0.948 | 0.952 | 1.060 | 0.962 | 1.09 |
| | RNB6-6 | 2.5 | #1 | 1.544 | 1.586 | 1.586 | 1.517 | 0.80 |
| 293 | RB6 | 0 | #1 | 0.333 | 0.333 | 1.329 | 0.823 | 1.60 |
| | | | #2 | 0.333 | 0.333 | 1.316 | 0.855 | 1.78 |
| | RNB6-2 | 0.313 | #11 | 0.602 | 0.602 | 1.247 | 0.974 | 1.50 |
| | RNB6-4 | 0.833 | #8 | 0.958 | 0.936 | 1.470 | 1.185 | 1.16 |
| | RNB6-5 | 1.25 | #5 | 1.173 | 1.147 | 1.808 | 1.392 | 0.95 |
| | RNB6-6 | 2.5 | #2 | 1.532 | 1.586 | 2.194 | 1.699 | 0.80 |
| 453 | RB6 | 0 | #5 | 0.333 | 0.333 | 0.815 | 0.532 | 0.34 |
| | | | #6 | 0.333 | 0.333 | 0.691 | 0.530 | 0.31 |
| | RNB6-2 | 0.313 | #12 | 0.602 | 0.594 | 0.992 | 0.806 | 0.60 |
| | RNB6-4 | 0.833 | #9 | 0.959 | 0.932 | 1.304 | 1.121 | 0.53 |
| | RNB6-5 | 1.25 | #6 | 1.158 | 1.121 | 1.341 | 1.223 | 0.42 |

**Table B.4:** Stress triaxiality results of copper C110 at different temperatures. Theoretical initial stress triaxiality ($\eta_0$) obtained using Equation 3.5; initial ($\eta_0$), final ($\eta_f$) and average ($\eta_{av}$) stress triaxiality throughout the test obtained using the proposed imaging method; and fracture equivalent strain ($\bar{\varepsilon}_f$) obtained using the proposed imaging technique

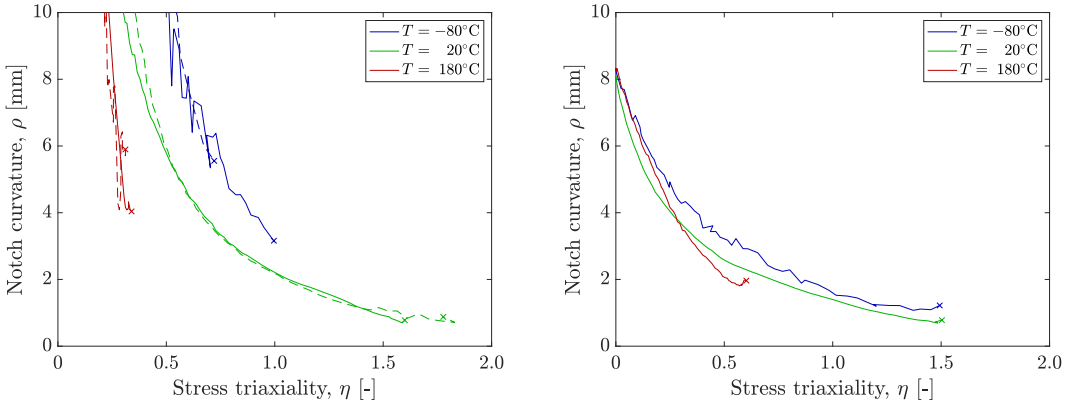



**(a)** $a/\rho = 0$ **(b)** $a/\rho = 0.25 \sim 0.417$

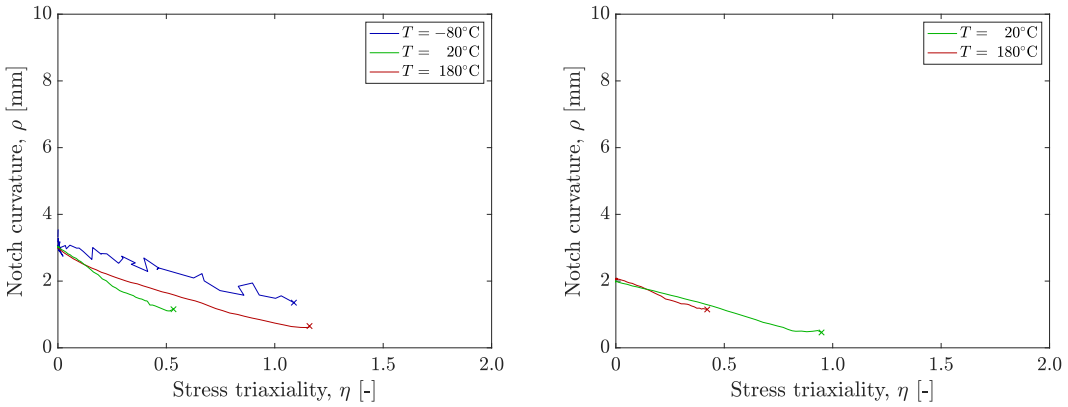
**(c)** $a/\rho = 0.833$ **(d)** $a/\rho = 1.25$

**(e)** $a/\rho = 2.5$

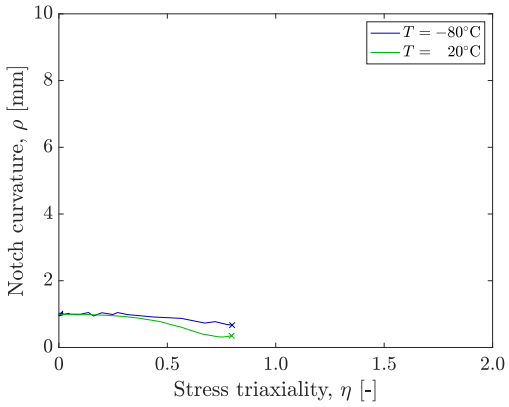
**Figure B.10:** Temperature effect on normalised minimum cross-sectional radius - equivalent plastic strain ($a/a_0$ - $\bar{\varepsilon}_{pl}$) for copper C110 specimens with different notch acuities.




**(a)** $a/\rho = 0$ **(b)** $a/\rho = 0.25 \sim 0.417$

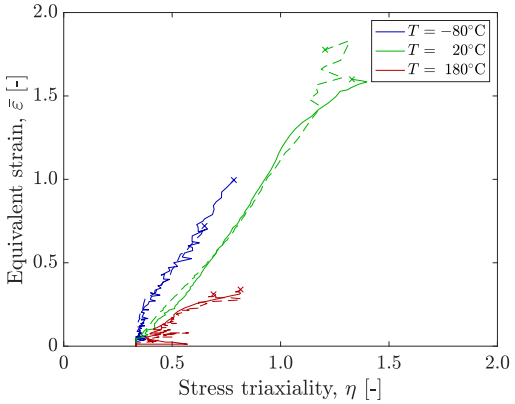



**(c)** $a/\rho = 0.833$ **(d)** $a/\rho = 1.25$

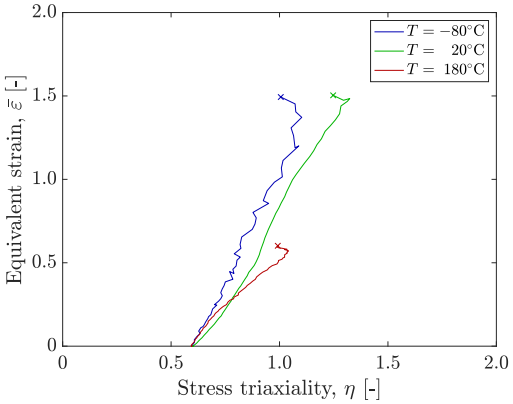



**(e)** $a/\rho = 2.5$

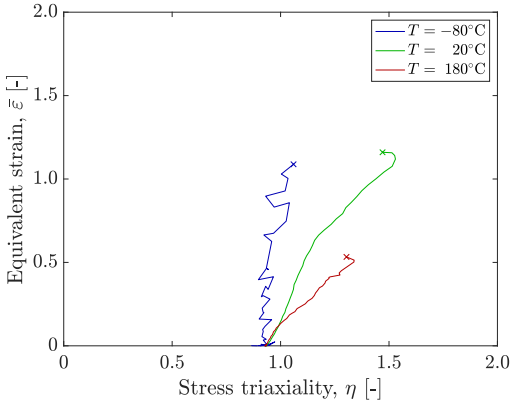
**Figure B.11:** Temperature effect on notch curvature - equivalent plastic strain ($\rho$ - $\bar{\varepsilon}_{pl}$) for copper C110 specimens with different notch acuities.



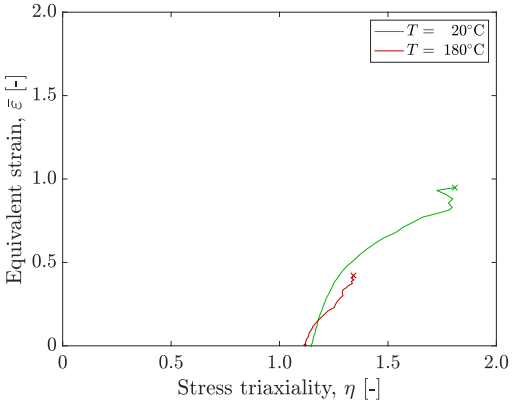

**(a)** $a/\rho = 0$



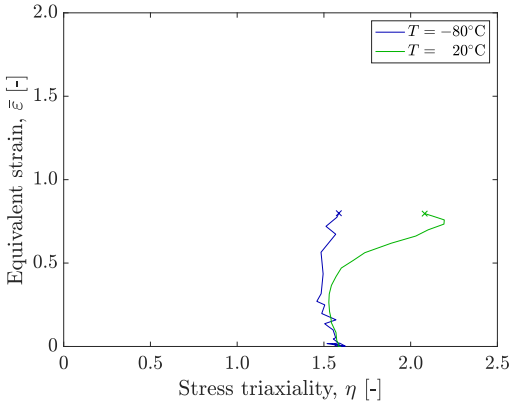

**(b)** $a/\rho = 0.25 \sim 0.417$




**(c)** $a/\rho = 0.833$



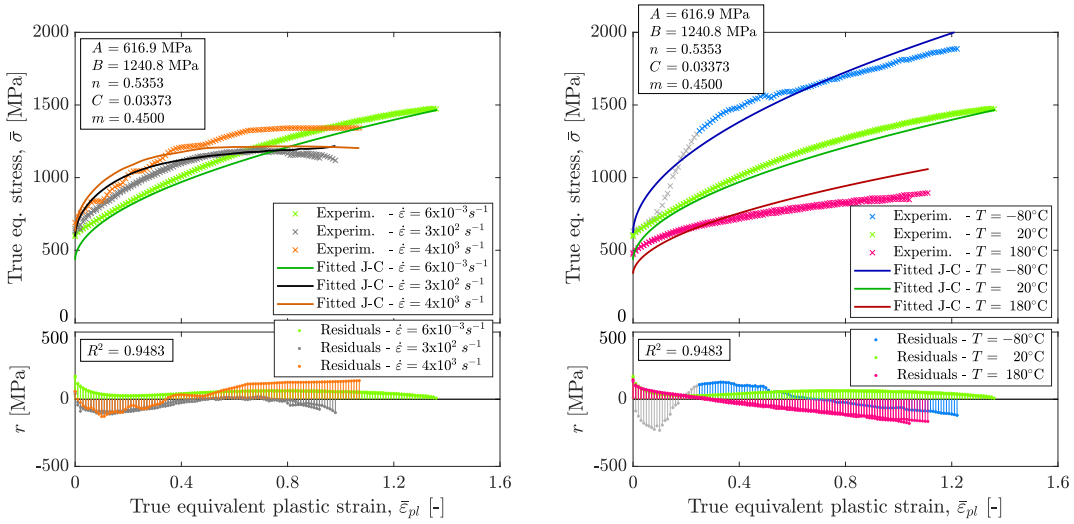

**(d)** $a/\rho = 1.25$




**(e)** $a/\rho = 2.5$

**Figure B.12:** Temperature effect on equivalent strain - stress triaxiality ($\bar{\varepsilon}$ - $\eta$) for copper C110 specimens with different notch acuities.

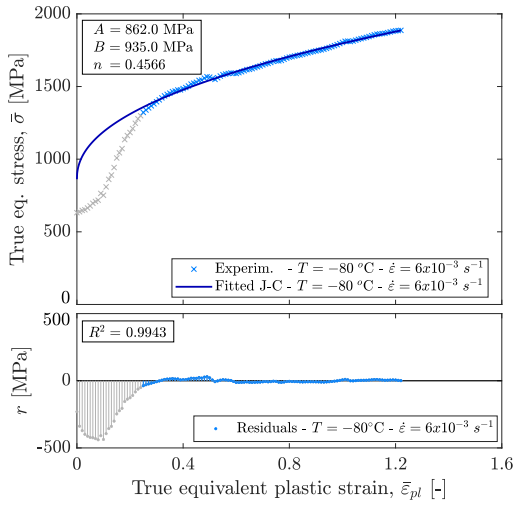
## B.3 Additional Modelling Results



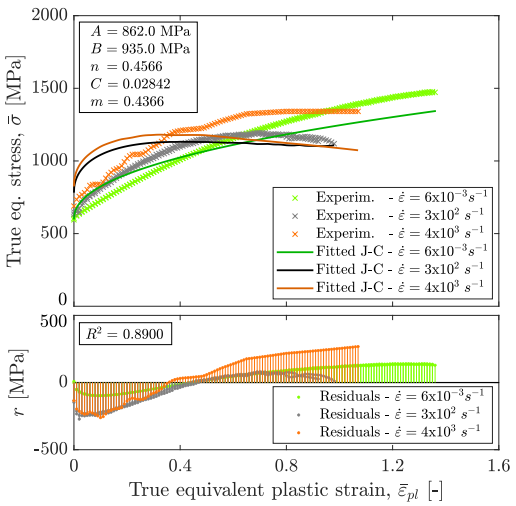

**(a)** Fit of strain-rate results

**(b)** Fit of temperature results

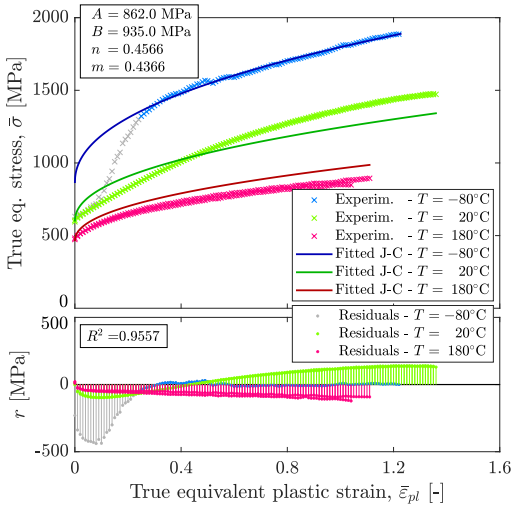
**Figure B.13:** Johnson-Cook plasticity model fit to experimental results of stainless steel 304L; all experimental data fitted together; low plasticity at low temperature has not been used in the fitting.




**(a)** Fit of standard results

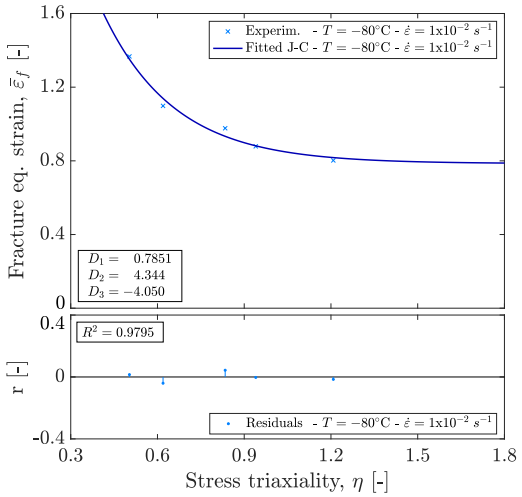



**(b)** Fit of strain-rate results

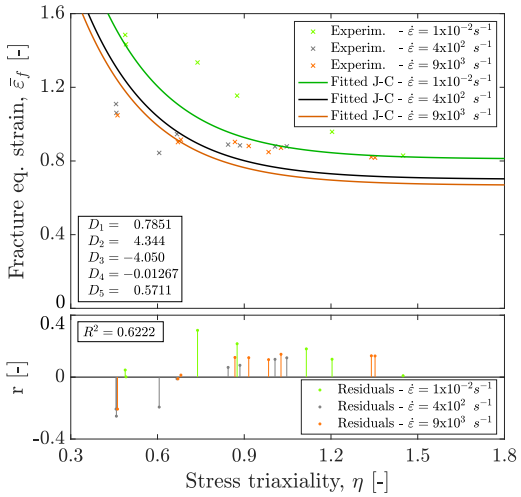



**(c)** Fit of temperature results

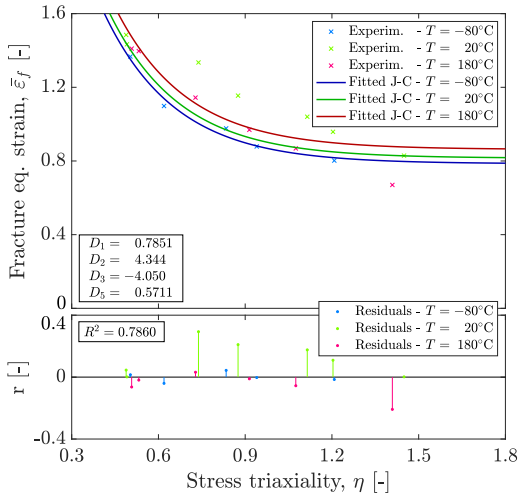
**Figure B.14:** Johnson-Cook plasticity model fit to experimental results of stainless steel 304L; standard, strain-rate and temperature results fitted separately; low plasticity at low temperature has not been used in the fitting.




**(a)** Fit of standard results

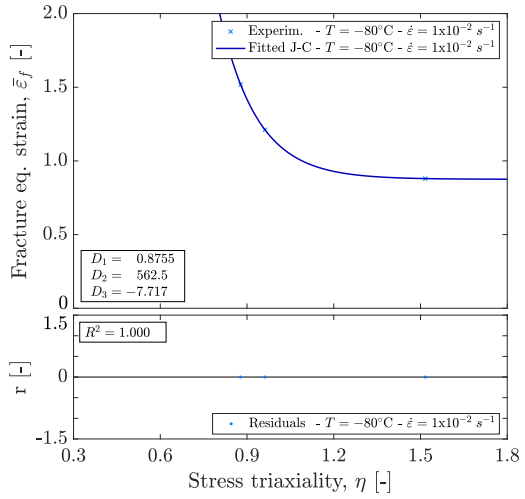



**(b)** Fit of strain-rate results

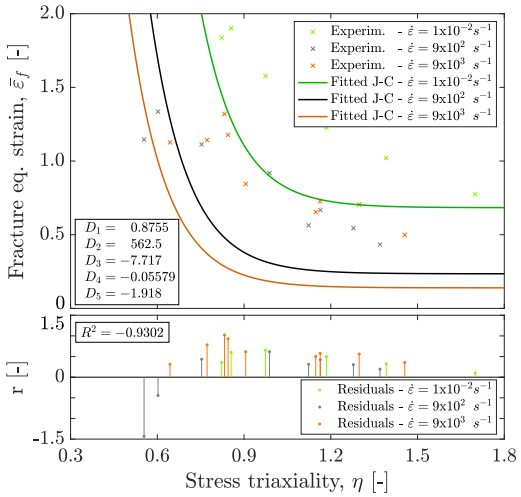



**(c)** Fit of temperature results

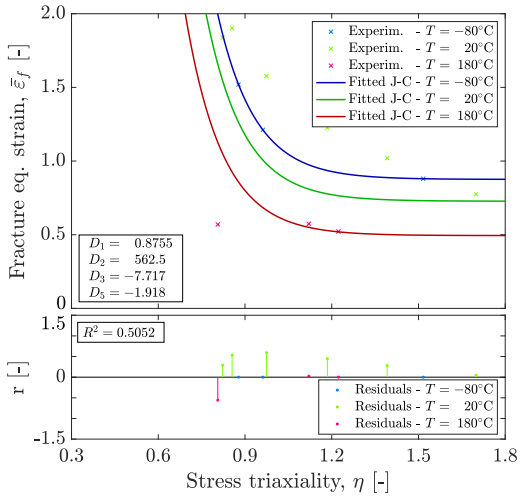
**Figure B.15:** Johnson-Cook fracture model fit to experimental results of stainless steel 304L; standard, strain-rate and temperature results fitted separately.




**(a)** Fit of standard results

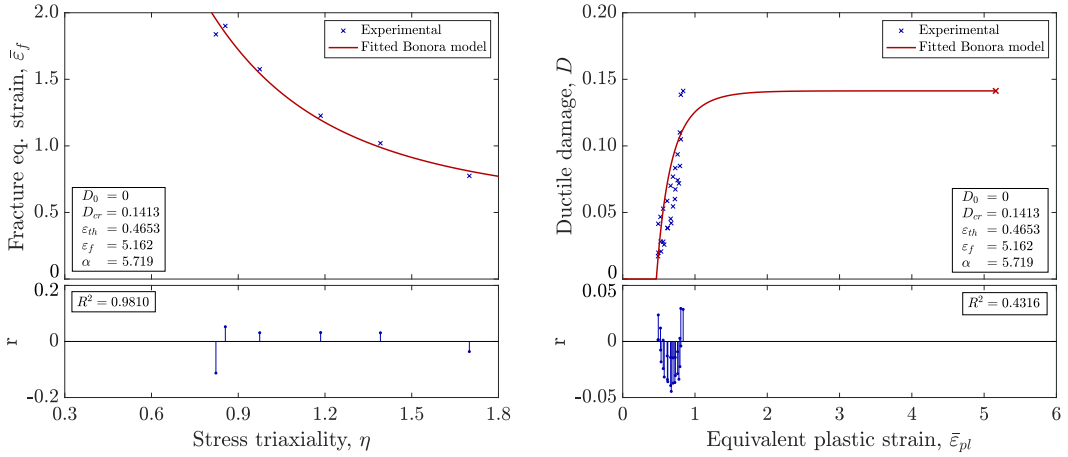



**(b)** Fit of strain-rate results



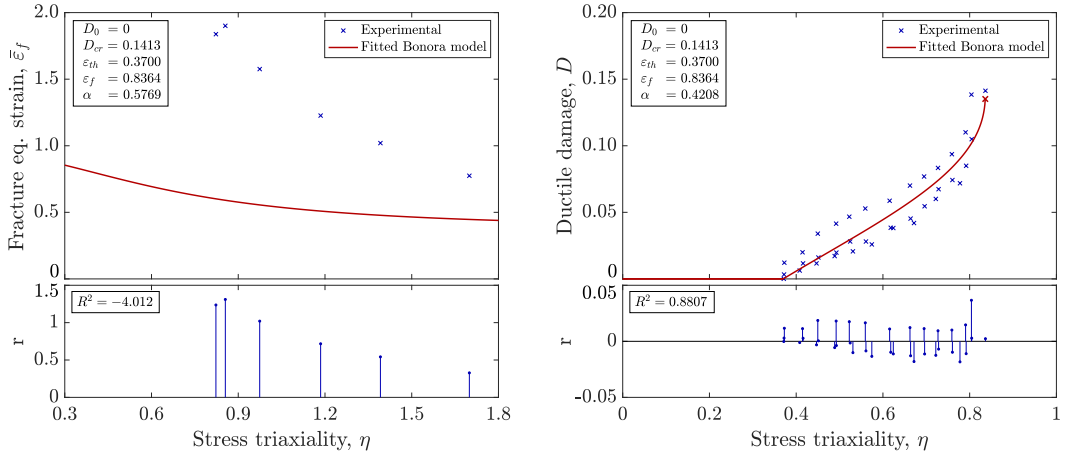

**(c)** Fit of temperature results

**Figure B.16:** Johnson-Cook fracture model fit to experimental results of copper C110; standard, strain-rate and temperature results fitted separately.




**(a)** Fit of the ductile fracture part **(b)** Fit of the damage accumulation part

**Figure B.17:** Bonora ductile damage model fit attempt of copper C110 following the fitting process recomended in [90].




**(a)** Fit of the ductile fracture part **(b)** Fit of the damage accumulation part

**Figure B.18:** Bonora ductile damage model fit attempt of copper C110 fitting the damage accumulation shape firstly.

# Appendix C

# User Subroutines

An example of UMAT (user defined material subroutine) written in Fortran for its implementation in Abaqus/Standard finite elements code is presented in this appendix. A VUMAT subroutine (vectorised user defined material subroutine) has also been coded for Abaqus/Explicit. However, only the UMAT is presented here since the principles of the models implementation are equivalent.

## C.1 UMAT Material model subroutine

A UMAT (user defined material subroutine) containing Johnson-Cook plasticity modelling, the proposed ductile fracture criterion (Equation 8.3) and damage accumulation law (Equation 8.4) is presented for its use in Abaqus/Standard:

```
C ************************************************************
C
C     UMAT subroutine for material isotropic elasticity and
C      isotropic Johnson-Cook plasticity.
C      Proposed strain-rate and temperature dependent
C      fracture model.
C      Proposed strain-rate and temperature dependent
C      non-linear damage accumulation model.
C      Adiabatic heating is used to consider the increase
C      in temperature due to plastic strain energy.
C
C     Valid for: 3D, plane strain and axisymmetric
C                simulations
C     ABAQUS/Standard
C
C     By: Alexander Sancho, Imperial College London
C     (a.sancho15@imperial.ac.uk)
C
C     Date: 04/08/2018
C
C ************************************************************

      SUBROUTINE UMAT( STRESS, STATEV, DDSDDE, SSE, SPD,
     1  SCD, RPL, DDSDDT, DRPLDE, DRPLDT, STRAN, DSTRAN,
     2  TIME, DTIME, TEMP, DTEMP, PREDEF, DPRED, CMNAME,
     3  NDI, NSHR, NTENS, NSTATV, PROPS, NPROPS, COORDS,
     4  DROT, PNEWDT, CELENT, DFGRD0, DFGRD1, NOEL, NPT,
     5  LAYER, KSPT, KSTEP, KINC )

      INCLUDE 'ABA_PARAM.INC'

      DIMENSION STRESS(NTENS), STATEV(NSTATV),
     1  DDSDDE(NTENS, NTENS), DDSDDT(NTENS), DRPLDE(NTENS),
     2  STRAN(NTENS), DSTRAN(NTENS), PREDEF(1), DPRED(1),
     3  PROPS(NPROPS), COORDS(3), DROT(3,3), DFGRD0(3,3),
     4  DFGRD1(3,3), stress_dev(NTENS)

      DIMENSION EELAS(6), EPLAS(6), sig(6), de(6),
     1  s_old(6), FLOW(6), ehat(6), ehat_old(6), s(6),
     2  xnormal(6), s_trial(6), HARD(3)
```

```
      CHARACTER*8 CMNAME

      PARAMETER( ZERO = 0.D0, ONE = 1.D0, TWO = 2.D0,
     1  THREE = 3.D0, SIX = 6.D0, third = ONE/THREE,
     2  twoThirds = TWO/THREE, threeHalfs = THREE/TWO,
     3  ENUMAX = .4999D0, NEWTON = 10, TOL_YIE = 1.0D-6,
     4  Tol_Bis = 1.0d5 )

C     CONVERGENCE TOLERANCE FOR BISECTION METHOD SET IN Pa.
C       IF THE MODEL'S PRESSURE UNITS ARE MPa, THIS NUMBER
C       HAS TO BE CHANGED TO 0.1.

C -------------------------------------------------------------
C                       Local arrays
C -------------------------------------------------------------

C      EELAS    : Elastic strains
C      EPLAS    : Plastic strains
C      sig      : Trial stresses
C      de       : Deviatoric strain increments
C      s_old    : Old total deviatoric stresses
C      FLOW     : Direction of plastic flow
C      ehat     : New total deviatoric strains
C      ehat_old : Old deviatoric strains
C      s        : Deviatoric stresses
C      xnormal  : Direction of deviatoric stresses
C      s_trial  : New trial stresses
C      HARD     : Hardening dependence on plastic strain,
C                 temperature and rate


C -------------------------------------------------------------
C                      State variables
C -------------------------------------------------------------

C      STATEV(1)        : Total Equivalent Plastic Strain
C      STATEV(2)        : Temperature
C      STATEV(3)        : Accumulated Ductile Damage
C      STATEV(4)        : Stress Triaxiality
```

```
C       STATEV(5)         : Equivalent Strain to Fracture
C       STATEV(6)         : Elastic Modulus
C       STATEV(7)         : Failure - Element deletion flag
C       STATEV(8)         : Elastic Modulus of dt (i-1)
C       STATEV(9) - STATEV(8+NTENS)     : Elastic Strain
C                                         components
C       STATEV(9+NTENS) - STATEV(8+2*NTENS) : Plastic Strain
C                                             components


C ------------------------------------------------------------
C              Material property definitions
C ------------------------------------------------------------

C     Elastic properties:
C       props(1)    : E
        E_0         = ZERO
        E_0         = PROPS(1)
C       props(2)    : nu
        ENU         = ZERO
        ENU         = MIN( PROPS(2), ENUMAX )
C       props(3) : Density
        density    = zero
        density    = props(3)

C     Johnson-Cook plastic model parameters:
C       props(4)    : A
        A           = zero
        A           = props(4)
C       props(5)    : B
        B           = zero
        B           = props(5)
C       props(6)    : n
        xn          = zero
        xn          = props(6)
C       props(7)    : m
        xm          = zero
        xm          = props(7)
C       props(8)    : C
        C          = zero
```

```
        C           = props(8)
C       props(9)    : Reference temperature
        T_trans     = zero
        T_trans     = props(9)
C       props(10)    : Melting temperature
        T_melt      = zero
        T_melt      = props(10)
C       props(11)   : Reference strain rate
        edot_0      = zero
        edot_0      = props(11)

C     Heat transfer parameters:
C       props(12) : eta (net heat transfer)
        xneta       = zero
        xneta       = props(12)
C       props(13) : Cp
        s_heat      = zero
        s_heat      = props(13)

C     Fracture model parameters:
C       props(14)    : xi1
        xi1         = zero
        xi1         = props(14)
C       props(15)    : xi2
        xi2         = zero
        xi2         = props(15)
C       props(16)    : xi3
        xi3         = zero
        xi3         = props(16)
C       props(17)    : gamma1
        gamma1      = zero
        gamma1      = props(17)
C       props(18)    : gamma2
        gamma2      = zero
        gamma2      = props(18)
C       props(19)    : psi1
        psi1         = zero
        psi1         = props(19)
C       props(20)    : psi2
        psi2         = zero
```

```
        psi2        = props(20)
C       props(21)   : psi3
        psi3        = zero
        psi3        = props(21)

C     Ductile damage model parameters:
C     Critical damage:
C       props(22)   : phi1
        phi1        = zero
        phi1        = props(22)
C       props(23)   : phi2
        phi2        = zero
        phi2        = props(23)
C       props(24)   : phi3
        phi3        = zero
        phi3        = props(24)
C       props(25)   : phi4
        phi4        = zero
        phi4        = props(25)
C     Threshold equivalent strain:
C       props(26)   : chi1
        chi1        = zero
        chi1        = props(26)
C       props(27)   : chi2
        chi2        = zero
        chi2        = props(27)
C       props(28)   : chi3
        chi3        = zero
        chi3        = props(28)
C       props(29)   : chi4
        chi4        = zero
        chi4        = props(29)
C     Damage exponent:
C       props(30)   : nu11
        nu11        = zero
        nu11        = props(30)
C       props(31)   : nu12
        nu12        = zero
        nu12        = props(31)
C       props(32)   : nu13
```

```
        nu13         = zero
        nu13         = props(32)
C       props(33)    : nu21
        nu21         = zero
        nu21         = props(33)
C       props(34)    : nu22
        nu22         = zero
        nu22         = props(34)
C       props(35)    : nu23
        nu23         = zero
        nu23         = props(35)
C       props(36)    : nu24
        nu24         = zero
        nu24         = props(36)


C -------------------------------------------------------------
C      WRITE(*,*) '--------------------------------'
C      WRITE(*,*) 'Time: ', TIME, ' - dt: ', DTIME
C      WRITE(*,*) 'Element no.: ', NOEL, ' - Integration
C        point no.: ', NPT

C *************************************************************

C -------------------------------------------------------------
C                Linear elasticity algorithm
C -------------------------------------------------------------

C Load elastic modulus from previous step
      EMOD = STATEV(6)

C Calculate Bulk and Shear moduli
      EBULK3 = EMOD / (ONE-TWO*ENU)
      EG2 = EMOD / (ONE+ENU)
      EG = EG2 / TWO
      EG3 = THREE*EG
      ELAM = (EBULK3-EG2) / THREE

C Elastic stiffness matrix
      DO K1 = 1,NDI
```

```
          DO K2 = 1,NDI
            DDSDDE(K2,K1) = ELAM
          END DO
          DDSDDE(K1,K1) = EG2+ELAM
        END DO
        DO K1 = NDI+1,NTENS
          DDSDDE(K1,K1) = EG
        END DO

C       WRITE(*,*) 'DDSDDE: '
C       WRITE(*,*) DDSDDE(1,1), DDSDDE(1,2), DDSDDE(1,3)
C       WRITE(*,*) DDSDDE(2,1), DDSDDE(2,2), DDSDDE(2,3)
C       WRITE(*,*) DDSDDE(3,1), DDSDDE(3,2), DDSDDE(3,3)
C       WRITE(*,*) DDSDDE(1,4), DDSDDE(1,5), DDSDDE(1,6)
C       WRITE(*,*) DDSDDE(2,4), DDSDDE(2,5), DDSDDE(2,6)
C       WRITE(*,*) DDSDDE(3,4), DDSDDE(3,5), DDSDDE(3,6)
C       WRITE(*,*) DDSDDE(4,1), DDSDDE(4,2), DDSDDE(4,3)
C       WRITE(*,*) DDSDDE(5,1), DDSDDE(5,2), DDSDDE(5,3)
C       WRITE(*,*) DDSDDE(6,1), DDSDDE(6,2), DDSDDE(6,3)
C       WRITE(*,*) DDSDDE(4,4), DDSDDE(4,5), DDSDDE(4,6)
C       WRITE(*,*) DDSDDE(5,4), DDSDDE(5,5), DDSDDE(5,6)
C       WRITE(*,*) DDSDDE(6,4), DDSDDE(6,5), DDSDDE(6,6)

C Load elastic and plastic strains and rotate
        CALL ROTSIG(STATEV(9),        DROT, EELAS, 2, NDI,
     1  NSHR)
        CALL ROTSIG(STATEV(9+NTENS), DROT, EPLAS, 2, NDI,
     1  NSHR)

C Load total equivalent plastic strain
        EQPLAS = STATEV(1)

C       WRITE(*,*) 'EQPLAS: ', EQPLAS
C       WRITE(*,*) 'STRESS: '
C       WRITE(*,*) STRESS(1), STRESS(2), STRESS(3)
C       WRITE(*,*) STRESS(4), STRESS(5), STRESS(6)
C       WRITE(*,*) 'DSTRAN: '
C       WRITE(*,*) DSTRAN(1), DSTRAN(2), DSTRAN(3)
C       WRITE(*,*) DSTRAN(4), DSTRAN(5), DSTRAN(6)
```

```
C Load temperature
      Told = zero
      Told = STATEV(2)

C      WRITE(*,*) '**** Old T: ', Told

C Calculate trial stress and elastic strain
      DO K1 = 1,NTENS
        sig(K1) = STRESS(K1)
      END DO
      DO K1 = 1,NTENS
        DO K2 = 1,NTENS
          sig(K2) = sig(K2) + DDSDDE(K2,K1)*DSTRAN(K1)
        END DO
        EELAS(K1) = EELAS(K1) + DSTRAN(K1)
      END DO

C      WRITE(*,*) 'sig: '
C      WRITE(*,*) sig(1), sig(2), sig(3)
C      WRITE(*,*) sig(4), sig(5), sig(6)
C      WRITE(*,*) 'EELAS: '
C      WRITE(*,*) EELAS(1), EELAS(2), EELAS(3)
C      WRITE(*,*) EELAS(4), EELAS(5), EELAS(6)

C **************************************************************

C -------------------------------------------------------------
C                Yield criterion algorithm
C -------------------------------------------------------------

C Calculate total trial hydrostatic stress
      p = zero
      p = -third * ( sig(1) + sig(2) + sig(3) )
C      WRITE(*,*) 'p: ', p

C Calculate trial equivalent Mises stress
      SMISES = (sig(1)-sig(2))**2 + (sig(2)-sig(3))**2
     1  + (sig(3)-sig(1))**2
      DO K1 = NDI+1,NTENS
        SMISES = SMISES + SIX*sig(K1)**2
```

```
      END DO
      SMISES = SQRT(SMISES/TWO)

      e_pl_old = EQPLAS

C Set up temperature effects for the J-C yield criterion
C check
      IF (Told .lt. T_trans) THEN
        T_star = ZERO
      ELSE IF (T_trans .ge. Told .le. T_melt) THEN
        T_star = (Told - T_trans)/(T_melt - T_trans)
      ELSE
        T_star = ONE
      END IF

C Calculate volumetric strain increment (strain trace
C increment)
      trace = ZERO
      trace = DSTRAN(1) + DSTRAN(2) + DSTRAN(3)

C Calculate deviatoric strain increments
      DO K1 = 1,NDI
        de(K1) = DSTRAN(K1) - third*trace
      END DO
      DO K1 = NDI+1,NTENS
        de(K1) = DSTRAN(K1)
      END DO

C Calculate new equivalent deviatoric strain increment and
C strain rate for the J-C yield criterion check
      deeq = twoThirds* ( de(1)**2 + de(2)**2 + de(3)**2 +
     1  two*de(4)**2 + two*de(5)**2 + two*de(6)**2 )
      deeq = SQRT(deeq)

C      WRITE(*,*) 'deeq: ', deeq

      dedot = deeq/DTIME

C Log trap for dedot
      IF ((dedot/edot_0) .gt. ZERO) THEN
```

```
        dedot_LOG = LOG(dedot/edot_0)
      ELSE
        dedot_LOG = ZERO
      END IF

C Calculate equivalent uniaxial yield stress using
C Johnson-Cook flow rule
      SYIELD0 = ( A + B*(e_pl_old**xn) ) *
     1 ( one + C*dedot_LOG ) * ( one - T_star**xm )

C      WRITE(*,*) 'SYIELD0: ', SYIELD0

C Check for yielding
      IF (SMISES .LE. (ONE+TOL_YIE)*SYIELD0) THEN

        DO K1 = 1,NTENS
          STRESS(K1) = sig(K1)
        END DO

C         WRITE(*,*) 'STRESS: '
C         WRITE(*,*) STRESS(1), STRESS(2), STRESS(3)
C         WRITE(*,*) STRESS(4), STRESS(5), STRESS(6)

        depl = zero

C         WRITE(*,*) 'depl: ', depl

        Tnew = Told
        count = 0
        f_depl = 0.0d0

      ELSE

C ***********************************************************

C ----------------------------------------------------------
C   Algorithm to obtain the Mises equivalent uniaxial form
C ----------------------------------------------------------

        WRITE(*,*) '**********plastic!*************'
```

```
C Calculate old total hydrostatic stress
        sig_mean = zero
        sig_mean = -third * ( STRESS(1) + STRESS(2) +
       1  STRESS(3) )

C Calculate old total deviatoric stresses
        DO K1 = 1,NDI
          s_old(K1) = STRESS(K1) + sig_mean
        END DO
        DO K1 = NDI+1,NTENS
          s_old(K1) = STRESS(K1)
        END DO

C Load elastic modulus used in previous dt
        OLDE = STATEV(8)

C Calculate Bulk and Shear moduli of previous dt
        OLDEBULK3 = OLDE / (ONE-TWO*ENU)
        OLDEG2 = OLDE / (ONE+ENU)
        OLDEG = OLDEG2 / TWO

C Calculate flow directions
        DO K1 = 1,NDI
          FLOW(K1) = (sig(K1)+p) / SMISES
        END DO
        DO K1 = NDI+1,NTENS
          FLOW(K1) = sig(K1) / SMISES
        END DO

C Calculate new total deviatoric strains
        DO K1 = 1,NTENS
          ehat(K1) = s_old(K1) / (two*OLDEG) + de(K1)
        END DO

C Calculate new total equivalent deviatoric strain
        etilde = twoThirds* ( ehat(1)**2 + ehat(2)**2 +
       1  ehat(3)**2 + two*ehat(4)**2 + two*ehat(5)**2 +
       2  two*ehat(6)**2 )
        etilde = SQRT(etilde)
```

```
C ************************************************************

C -------------------------------------------------------------
C    Algorithm to solve for the equivalent deviatoric
C      plastic strain increment (depl). Iterative Bisection
C      method is used.
C -------------------------------------------------------------

C Set initial limits and convergence tolerance
        depl_a = ZERO
        depl_b = 1.0d-1

C Calculation of f_depl with the initial limits to check
C tolerance as first iteration
        depl = (depl_a + depl_b) / TWO
        edot = depl/DTIME

        IF ((edot/edot_0) .gt. zero) THEN
          edot_LOG = LOG(edot/edot_0)
        ELSE
          edot_LOG = zero
        END IF

        SYIELD_depl = ( A + B*( (e_pl_old+depl)**xn) )
     1    * ( one + C*edot_LOG ) * ( one - T_star**xm )

C        WRITE(*,*) 'SYIELD_depl: ', SYIELD_depl

        f_depl = three*EG*(etilde - depl) - SYIELD_depl
        count = 0

C Initial check, if it does not satisfy the check the loop
C starts until the convergence criterion is met or the
C maximum number of iterations reached.

        DO WHILE ( (ABS(f_depl) .gt. Tol_Bis) .AND.
       1  (count .le. 100) )
          count = count + 1

C Find midpoint value
```

```
          depl = (depl_a + depl_b)/two

C If the Bisection method is not expected to converge
C (maximum number of iterations reached), set depl to its
C maximum possible value, i.e. the total equivalent
C deviatoric strain increment.
          IF (count .ge. 100) THEN

C Calculate old total deviatoric strains
            DO K1 = 1,NTENS
              ehat_old(K1) = s_old(K1)/(two*OLDEG)
            END DO

C Calculate the old total equivalent deviatoric strain
            etilde_old = twoThirds* ( ehat_old(1)**2 +
     1        ehat_old(2)**2 + ehat_old(3)**2 +
     2        two*ehat_old(4)**2 + two*ehat_old(5)**2 +
     3        two*ehat_old(6)**2 )
            etilde_old = SQRT(etilde_old)

C Calculate total equivalent deviatoric strain increment
C and assign it to depl
            depl_bb = (etilde - etilde_old)
            depl = depl_bb
          END IF

C Calculation of f_a and f_depl using Johnson-Cook flow
C rule
          edot_a = depl_a/DTIME;

          edot = depl/DTIME;

          IF ((edot_a/edot_0) .gt. zero) THEN
            edot_LOG_a = LOG(edot_a/edot_0)
          ELSE
            edot_LOG_a = zero
          END IF

          IF ((edot/edot_0) .gt. zero) THEN
            edot_LOG = LOG(edot/edot_0)
```

```
            ELSE
              edot_LOG = zero
            END IF

            SYIELD_a = ( A + B*( (e_pl_old+depl_a)**xn) )
     1        * ( one + C*edot_LOG_a ) * ( one - T_star**xm )

            SYIELD_depl = ( A + B*( (e_pl_old+depl)**xn) )
     1        * ( one + C*edot_LOG ) * ( one - T_star**xm )

            f_a    = three*EG*(etilde - depl_a) - SYIELD_a

            f_depl = three*EG*(etilde - depl) - SYIELD_depl

C Find location of the root
            IF ( (f_a * f_depl) .gt. zero) THEN
              depl_a = depl
            ELSE
              depl_b = depl
            END IF

C Calculate deviatoric stresses
            denom = one + (three*EG*depl) / SYIELD_depl
            IF (denom .eq. zero) THEN
              DO K1 = 1,NTENS
                s(K1) = zero
              END DO
            ELSE
              DO K1 = 1,NTENS
                s(K1) = (two*EG/denom) * ehat(K1)
              END DO
            END IF

C Calculate normals to yield surface (direction of
C deviatoric stresses)
            DO K1 = 1,NTENS
              xnormal(K1) = threeHalfs*s(K1)/SYIELD_depl
            END DO

C Calculate new trial stresses
```

```
            DO K1 = 1,NDI
              s_trial(K1) = s(K1) - p
            END DO
            DO K1 = NDI+1,NTENS
              s_trial(K1) = s(K1)
            END DO

C Calculate increase in temperature
            term = (xneta*depl)/(two*density*s_heat)

C            WRITE(*,*) '**** term: ', term

            dtheta = zero
            DO K1 = 1,NDI
              dtheta = dtheta + xnormal(K1)*(STRESS(K1) +
     1          s_trial(K1))
            END DO
            DO K1 = NDI+1,NTENS
              dtheta = dtheta + two*xnormal(K1)*(STRESS(K1) +
     1          s_trial(K1))
            END DO
            dtheta = dtheta * term
            Tnew = Told + dtheta

C Calculate updated temperature effect
            IF (Tnew .lt. T_trans) THEN
              T_star = zero
            ELSEIF ( T_trans .ge. Tnew .le. T_melt) THEN
              T_star = (Tnew - T_trans)/(T_melt - T_trans)
            ELSE
              T_star = one
            ENDIF

C            WRITE(*,*) '**** New Tstar: ', T_star

          END DO

C New stresses in case the material has yielded
          DO K1 = 1,NTENS
            STRESS(K1) = s_trial(K1)
```

```
        END DO

C New elastic strains and plastic strains
        DO K1 = 1,NDI
          STRESS(K1) = FLOW(K1)*SYIELD_depl - p
          EPLAS(K1) = EPLAS(K1) + THREE/TWO*FLOW(K1)*depl
          EELAS(K1) = EELAS(K1) - THREE/TWO*FLOW(K1)*depl
        END DO
        DO K1 = NDI+1,NTENS
          STRESS(K1) = FLOW(K1)*SYIELD_depl
          EPLAS(K1) = EPLAS(K1) + THREE*FLOW(K1)*depl
          EELAS(K1) = EELAS(K1) - THREE*FLOW(K1)*depl
        END DO

C        WRITE(*,*) 'STRESS: '
C        WRITE(*,*) STRESS(1), STRESS(2), STRESS(3)
C        WRITE(*,*) STRESS(4), STRESS(5), STRESS(6)
C        WRITE(*,*) 'EPLAS: '
C        WRITE(*,*) EPLAS(1), EPLAS(2), EPLAS(3)
C        WRITE(*,*) EPLAS(4), EPLAS(5), EPLAS(6)
C        WRITE(*,*) 'EELAS: '
C        WRITE(*,*) EELAS(1), EELAS(2), EELAS(3)
C        WRITE(*,*) EELAS(4), EELAS(5), EELAS(6)

C New equivalent plastic strain
        EQPLAS = EQPLAS + depl

C        WRITE(*,*) 'depl: ', depl
C        WRITE(*,*) 'EQPLAS: ', EQPLAS

C Calculate plastic dissipation
        SPD = depl*(SYIELD0+SYIELD_depl)/TWO

C End of plastic strain increment (depl) algorithm


C ************************************************************

C -------------------------------------------------------------
C             Stress triaxiality calculation
```

```
C -------------------------------------------------------------

C Calculate new hydrostatic stress
        stress_hydro = zero
        stress_hydro = third * ( STRESS(1) + STRESS(2) +
     1    STRESS(3) )

C        WRITE(*,*) 'stress_hydro: '
C        WRITE(*,*) stress_hydro

C Calculate new deviatoric stresses
        DO K1 = 1,NDI
          stress_dev(K1) = zero
          stress_dev(K1) = STRESS(K1) - stress_hydro
        END DO
        DO K1 = NDI+1,NTENS
          stress_dev(K1) = zero
          stress_dev(K1) = STRESS(K1)
        END DO

C        WRITE(*,*) 'stress_dev: '
C        WRITE(*,*) stress_dev(1), stress_dev(2),
C     1     stress_dev(3)
C        WRITE(*,*) stress_dev(4), stress_dev(5),
C     1     stress_dev(6)

C Calculate new equivalent Mises stress
        stress_VM = zero
        DO K1 = 1,NDI
          stress_VM = stress_VM + stress_dev(K1)**2
        END DO
        DO K1 = NDI+1, NTENS
          stress_VM = stress_VM + two*stress_dev(K1)**2
        END DO
        stress_VM = SQRT( threeHalfs*stress_VM )

C        WRITE(*,*) 'stress_VM: '
C        WRITE(*,*) stress_VM

C Calculate stress triaxiality
```

```
        triax = zero
        IF (stress_VM .LT. 1.0E-10) THEN
          triax = 100.0
        ELSE
          triax = stress_hydro / stress_VM
        END IF

C        WRITE(*,*) 'triax: '
C        WRITE(*,*) triax


C ************************************************************

C ------------------------------------------------------------
C   Calculate equivalent plastic strain to fracture using
C     the proposed fracture model
C ------------------------------------------------------------
C
C Calculate adimensional strain-rate
          edot = depl/DTIME

          edot_star = edot/edot_0

C Calculate fracture equivalent plastic strain with the
C proposed model
        D1 = ( xi1 + edot_star**gamma1 +
     1    EXP( - (T_star - psi1)**2 / psi2**2 ) )
        D2 = xi2 * ( 1 + psi3*T_star )
        D3 = xi3 * edot_star**gamma2

        eps_f = D1 + D2 * EXP( D3 * triax )

C        WRITE(*,*) 'eps_f: '
C        WRITE(*,*) eps_f

C End of fracture strain algorithm

C ************************************************************

C ------------------------------------------------------------
```

```
C   Calculate damage accumulation using the proposed
C     ductile damage model
C -------------------------------------------------------------

C Load accumulated damage from previous step
        accumD = zero
        accumD = STATEV(3)

C         WRITE(*,*) 'D: ', accumD

C If the equivalent deviatoric plastic strain increment is
C zero no damage is accumulated. If hydrostatic/mean stress
C is zero or negative (compression) no damage is
C accumulated. Ignore damage calculation if eqepl is zero
C orbellow a threshold.
        IF ( (depl .LE. zero) .OR. (stress_hydro .LE. zero)
     1    .OR. (EQPLAS .LE. eps_th) ) THEN
          accumD = accumD

C           WRITE(*,*) 'dD: 0'

        ELSE

C If the value of eps_f goes below the threshold the
C material would fail in the real life. Nevertheless, in
C this case this check is included because during the
C iterative calculations of every step an intermediate step
C where eps_f<eps_th could occur before the convergence is
C achieved. In this situation the previous value of eps_f
C is used for the step.
          IF (eps_f .LE. eps_th) THEN
            eps_th = STATEV(5)

C             WRITE(*,*) 'eps_f: ', eps_f

          END IF

C Calculate new total damage

C Critical damage
```

```
          Dcr = phi1 *
     1      EXP( - (T_star - phi2)**2 / phi3**2 ) ) *
     2      edot_star**phi4

C Threshold equivalent strain
          eps_th = chi1 *
     1      EXP( - (T_star - chi2)**2 / chi3**2 ) ) *
     2      edot_star**chi4

C Damage exponents
          nu1 = nu11 * ( 1 - T_star*nu12 ) *
     1      edot_star**nu13
          nu2 = nu21 *
     1      EXP( - (T_star - nu22)**2 / nu23**2 ) ) *
     2      edot_star**nu24

C Damage calculation
          accumD = Dcr *
     1      ( (EQPLAS - eps_th)/(eps_f - eps_th) )
     2      **(nu1 + nu2*EQPLAS)

C           WRITE(*,*) 'D: ', accumD

        END IF

C Check if critical damage is reached in calculation point,
C and in that case the element is removed
        IF (accumD .GE. Dcr) THEN
          accumD = Dcr
          EMOD = zero
          STATEV(7) = zero
          WRITE(*,*) '****critical damage reached!****'

C The material point is degraded by means of E for the
C following dt
        ELSE
          EMOD = E_0*(1-accumD)

C Recalculate Bulk and Shear moduli
          EBULK3 = EMOD / (ONE-TWO*ENU)
```

```
          EG2 = EMOD / (ONE+ENU)
          EG = EG2 / TWO
          EG3 = THREE*EG
          ELAM = (EBULK3-EG2) / THREE
        END IF

C End of ductile damage increment (dD) algorithm

C -------------------------------------------------------------
C         Formulate the Jacobian (material tangent)
C -------------------------------------------------------------

C Variation of yield stress with equivalent plastic strain
        HARD(1) = ( B*xn*( (e_pl_old+depl)**(xn-one) ) )
     1      * ( one + C*edot_LOG ) * ( one - T_star**xm )

C Calculate effective Bulk and Shear moduli
        EFFG = EG*SYIELD_depl / SMISES
        EFFG2 = TWO*EFFG
        EFFG3 = threeHalfs * EFFG2
        EFFLAM = (EBULK3-EFFG2) / THREE
        EFFHRD = EG3*HARD(1) / (EG3+HARD(1)) - EFFG3

C Effective elastic stiffness matrix
        DO K1 = 1,NDI
          DO K2 = 1,NDI
            DDSDDE(K2,K1) = EFFLAM
          END DO
          DDSDDE(K1,K1) = EFFG2+EFFLAM
        END DO
        DO K1 = NDI+1,NTENS
          DDSDDE(K1,K1) = EFFG
        END DO
        DO K1 = 1,NTENS
          DO K2 = 1,NTENS
            DDSDDE(K2,K1) = DDSDDE(K2,K1) +
     1        EFFHRD*FLOW(K2)*FLOW(K1)
          END DO
        END DO
```

```
C         WRITE(*,*) 'DDSDDE: '
C         WRITE(*,*) DDSDDE(1,1), DDSDDE(1,2), DDSDDE(1,3)
C         WRITE(*,*) DDSDDE(2,1), DDSDDE(2,2), DDSDDE(2,3)
C         WRITE(*,*) DDSDDE(3,1), DDSDDE(3,2), DDSDDE(3,3)
C         WRITE(*,*) DDSDDE(1,4), DDSDDE(1,5), DDSDDE(1,6)
C         WRITE(*,*) DDSDDE(2,4), DDSDDE(2,5), DDSDDE(2,6)
C         WRITE(*,*) DDSDDE(3,4), DDSDDE(3,5), DDSDDE(3,6)
C         WRITE(*,*) DDSDDE(4,1), DDSDDE(4,2), DDSDDE(4,3)
C         WRITE(*,*) DDSDDE(5,1), DDSDDE(5,2), DDSDDE(5,3)
C         WRITE(*,*) DDSDDE(6,1), DDSDDE(6,2), DDSDDE(6,3)
C         WRITE(*,*) DDSDDE(4,4), DDSDDE(4,5), DDSDDE(4,6)
C         WRITE(*,*) DDSDDE(5,4), DDSDDE(5,5), DDSDDE(5,6)
C         WRITE(*,*) DDSDDE(6,4), DDSDDE(6,5), DDSDDE(6,6)

      END IF

C ************************************************************

C -------------------------------------------------------------
C   Update calculated variables to state variables of
C     subroutine
C -------------------------------------------------------------

C Elastic and plastic strains
      DO K1 = 1,NTENS
        STATEV(K1+8) = EELAS(K1)
        STATEV(K1+8+NTENS) = EPLAS(K1)
      END DO

C Equivalent plastic strain
      STATEV(1) = EQPLAS

C      WRITE(*,*) 'Equivalent plastic strain:  ', STATEV(1)

C Temperature
      STATEV(2) = Tnew

C      WRITE(*,*) 'Final temperature T:        ', STATEV(2)

C Accumulated ductile damage
```

```
      STATEV(3) = accumD

C      WRITE(*,*) 'Accumulated damage D:       ', STATEV(3)

C Stress Triaxiality
      STATEV(4) = triax

C      WRITE(*,*) 'Stress triaxiality:         ', STATEV(4)

C Equivalent plastic strain to fracture
      STATEV(5) = eps_f

C      WRITE(*,*) 'Eq. pl. strain to fracture: ', STATEV(5)

C Failure flag

C      WRITE(*,*) 'Failure flag:               ', STATEV(7)

C Old elastic modulus
      STATEV(8) = STATEV(6)

C      WRITE(*,*) 'Old elastic modulus:        ', STATEV(8)

C New elastic modulus
      STATEV(6) = EMOD

C      WRITE(*,*) 'New elastic modulus:        ', STATEV(6)

      RETURN
      END

C ************************************************************
C                          End of UMAT
C ************************************************************
```

## C.2 Example of Abaqus/Standard Input File

An example of an input file of Abaqus/Standard that uses the UMAT subroutine presented above to perform the material calculations is included here. The geometry modelled is a cube of size 0.01x0.01x0.01 and the model parameters introduced are those obtained for stainless steel 304L. This very simple model has been used to test the subroutine under various loading conditions.

```
*HEADING
One element test for Johnson-Cook plastic model, proposed
fracture model and proposed damage model UMAT
**
** ----------------------------------------------------------
** 1 element - 3D model
**     Tensile Test
**     Johnson-Cook plastic model + adiabatic heating
**     Proposed fracture model (strain-rate and temperature
**       dependent)
**     Proposed damage model (non-linear damage
**       accumulation, strain-rate and temperature
**       dependent)
** ABAQUS Standard analysis
** By: Alexander Sancho, Imperial College London
**     (a.sancho15@imperial.ac.uk)
** Date: 04/08/2018
** ----------------------------------------------------------
**
** --- NODES ---
**
*NODE, nset=all
1,      0.01,        0.,      0.01
2,        0.,        0.,      0.01
3,      0.01,        0.,        0.
4,        0.,        0.,        0.
5,      0.01,      0.01,      0.01
6,        0.,      0.01,      0.01
7,      0.01,      0.01,        0.
8,        .0,      0.01,        0.
**
** --- ELEMENTS ---
**
*ELEMENT, type=C3D8H, elset=ecube
1,   5, 6, 8, 7, 1, 2, 4, 3
**
** --- SECTIONS ---
**
** Section: Solid
```

```
*SOLID SECTION, elset=ecube, material=ss304L-UMAT
,
**
** --- SETS ---
**
*NSET, nset=top
 1,  2,  5,  6
*NSET, nset=bottom
 3,  4,  7,  8
*NSET, nset=side1
 1,  2,  3,  4
*NSET, nset=side2
 2,  4,  6,  8
**
** --- MATERIALS ---
**
** - Stainless steel 304L -
**
*MATERIAL, name=ss304L-UMAT
**
*Density
8030.
**
** - State Variables: -
**
*Depvar, delete=7
   20,
    1,  EQPLS,   "Equivalent plastic strain"
    2,  T,       "Temperature"
    3,  D,       "Accumulated ductile damage"
    4,  TRIAX,   "Stress triaxiality"
    5,  EQPLSF,  "Equivalent plastic strain fracture"
    6,  E,       "Elastic modulus"
    7,  FAIL     "Failure flag"
    8,  E2       "Previous elastic modulus"
    9,  EELAS11, "Elastic strain energy 11"
   10,  EELAS22, "Elastic strain energy 22"
   11,  EELAS33, "Elastic strain energy 33"
   12,  EELAS12, "Elastic strain energy 12"
   13,  EELAS13, "Elastic strain energy 13"
```

```
   14,  EELAS23, "Elastic strain energy 23"
   15,  EPLAS11, "Plastic strain energy 11"
   16,  EPLAS22, "Plastic strain energy 22"
   17,  EPLAS33, "Plastic strain energy 33"
   18,  EPLAS12, "Plastic strain energy 12"
   19,  EPLAS13, "Plastic strain energy 13"
   20,  EPLAS23, "Plastic strain energy 23"
**
** - Material Properties -
**
** Elastic properties
**   Prop. 1: Base elastic modulus, E [Pa]
**   Prop. 2: Poisson ratio, nu [-]
**   Prop. 3: Density, rho [kg/m^3]
** Johnson-Cook plastic model parameters
**   Prop. 4: A [Pa]
**   Prop. 5: B [Pa]
**   Prop. 6: n [-]
**   Prop. 7: m [-]
**   Prop. 8: C [-]
**   Prop. 9: Reference temperature, Tref [K]
**   Prop.10: Melting temperature, Tm [K]
**   Prop.11: Reference strain-rate [s^-1]
** Heat transfer parameters
**   Prop.12: Net heat transfer eta [-]
**   Prop.13: Specific heat, Cp [J/kg K]
** Fracture model parameters
**   Prop.14: xi1 [-]
**   Prop.15: xi2 [-]
**   Prop.16: xi3 [-]
**   Prop.17: gamma1 [-]
**   Prop.18: gamma2 [-]
**   Prop.19: psi1 [-]
**   Prop.20: psi2 [-]
**   Prop.21: psi3 [-]
** Damage model parameters
** Critical damage
**   Prop.22: phi1 [-]
**   Prop.23: phi2 [-]
**   Prop.24: phi3 [-]
```

```
**   Prop.25: phi4 [-]
** Threshold equivalent strain
**   Prop.26: chi1 [-]
**   Prop.27: chi2 [-]
**   Prop.28: chi3 [-]
**   Prop.29: chi4 [-]
** Damage exponent
**   Prop.30: nu11 [-]
**   Prop.31: nu12 [-]
**   Prop.32: nu13 [-]
**   Prop.33: nu21 [-]
**   Prop.34: nu22 [-]
**   Prop.35: nu23 [-]
**   Prop.36: nu24 [-]
**
*User Material, constants=36
16.6e+10,     0.3,   8030., 616.9e+06, 1241e+06,   0.5353,
  0.4500, 0.03373,    193.,     1698., 6.11e-03,      0.9,
    500.,  -2.174,   1.984,   -0.5061,  -0.1490,  -0.1050,
 0.05866,  0.1887,   1.326,    0.2053,  0.08054,   0.2225,
 0.08769,   0.006,       0,      1000,        0,   0.1704,
  0.7002,  -2.185, 0.06642,   0.08240,  0.09155,    1.697
**
** - State variables initial conditions -
**
*Initial Conditions, type=SOLUTION
ecube,     0.0,  293.,   0.0,   0.0,  100., 16.6e+10,   1.0
16.6e+10,  0.0,   0.0,   0.0,   0.0,   0.0,      0.0,   0.0
     0.0,  0.0,   0.0,   0.0,   0.0
**
** ----------------------------------------------------------
**
** --- STEPS ---
**
** STEP: Load
**
*STEP, nlgeom=YES, INC=10000
*Dynamic
0.001, 80, 1e-4, 1
**
```

```
** - BOUNDARY CONDITIONS -
**
** Name: Tensile-1 Type Velocity/Angular velocity
*BOUNDARY, type=VELOCITY
top,      3,   3,  0.001
**
** Name: Tensile-2 Type: Velocity/Angular velocity
*BOUNDARY, type=VELOCITY
bottom,   3,   3, -0.001
**
** Name: Tensile-3 Type: Displacement
*BOUNDARY, type=DISPLACEMENT
side1,    2,   2,    0
**
** Name: Tensile-4 Type: Displacement
*BOUNDARY, type=DISPLACEMENT
side2,    1,   1,    0
**
** - OUTPUT REQUESTS -
**
*RESTART, write, number interval=1, time marks=NO
**
** FIELD OUTPUT: F-Output-1
**
*OUTPUT , field, freq=1
**
*NODE OUTPUT
U,   V,   A
**
*ELEMENT OUTPUT
S,   NE,   LE, ELEN,  SDV,  STATUS
**
** HISTORY OUTPUT: H-Output-1
**
*OUTPUT, history, variable=PRESELECT, freq=1
**
*ELEMENT OUTPUT, elset=ecube
MISES, SDV1, SDV2, SDV3, SDV4, SDV5, SDV6, SDV7
**
*Name END
```